Texas General Land Office

Final Project Report

Prediction of Texas Wetland Erosion through Remote Sensing, Field Surveys, and Numerical Modeling

GLO Contract No. 21-155-006-C878

Project Period (04/01/2021 to 09/30/2023)

Kuang-An Chang, Jens Figlus, Huilin Gao, James Kaihatu, Scott Socolofsky, Soo Bum Bae, Chi-Hsiang Huang, Jin-Young Kim, Fangzhou Tong, Shuai Zhang, and Yao Li

Texas A&M Engineering Experiment Station
3136 TAMU
College Station, TX 77843-3136

This report was funded in part through a grant from the Texas General Land Office (GLO) providing Gulf of Mexico Energy Security Act of 2006 funding made available to the State of Texas and awarded under the Texas Coastal Management Program. The views contained herein are those of the authors and should not be interpreted as representing the views of the GLO or the State of Texas.

October 1, 2023

CONTENTS

Executive Summary

Coastal erosion is a major threat to Bay communities and ecosystems along the Texas coast. Wetlands are an important defense against erosion and provide many beneficial uses, including water quality enhancement, ecosystem habitat, and alteration of storm surge. Wetlands on the Texas coast have been a major focus of the State's coastal protection plan. The dynamics of natural and created wetlands, especially their resilience or erodibility, is very complex, and depends on wave and current forcing, water levels, soil properties, and vegetation type and coverage; hence, reliable models are not available to predict the evolution of Texas coastal wetlands under baseline or future conditions. The purpose of this project was to establish a long-term, comprehensive wetland erosion time-series of observations and to develop a predictive numerical model using this time-series to evaluate short- and long-term wetland erosion for key areas in Galveston Bay, Texas.

This project used Cycle 26 Gulf of Mexico Energy Security Act (GOMESA) funds to create a reliable design and evaluation tool for coastal wetlands in Texas. The project plan comprised two main tasks: 1.) direct observation of wetland evolution over long (using satellite data) and short (using drone and in situ observation) timescales, and 2.) development of a predictive numerical model validated to these observations. This study focused on created wetlands in West Galveston Bay, along the Galveston Bay ship channel, and on natural wetlands in the Mission-Aransas National Estuarine Research Reserve (MANERR), a northern extension of the Corpus Christi Bay system.

Satellite data offer a 3-m spatial resolution for the past 10 years (Cubesat) and 30-m resolution during the last 40 years (Landsat). The project quantified the long-term wetland evolution using Landsat image classification from 1984 to 2020 and Cubesat images in the last 10 years to determine the long- term trend of wetland boundary evolution. Historical water level, weather, wave, and current data were also analyzed to supplement the satellite time-series. The outcome of these activities is a nearly 40-year time series of wetland evolution at these sites coupled to a mechanistic understanding of the drivers for erosion.

For short-term wetland evolution, the project utilized unmanned aerial vehicle (UAV or drone) and real-time kinematic (RTK) differential global positioning system (DGPS) equipment to obtain relevant observations of wetland boundary evolution during the project period. The team also deployed *in-situ* sensors to measure hydrodynamic forcing. The surveys covered four field sites and collected images and boundary feature resolutions of up to 0.01 m in spatial scale. The field surveys included drone surveys at discrete times and simultaneous *in-situ* deployments of instruments for periods of up to a few weeks. Surveys were conducted on a regular schedule to capture seasonal variation and were also initiated to observe the effects of discrete events (e.g., before and after a major storm; termed here "event-based surveying"). These observations help understand fine-scale changes occurring at the storm-event and seasonal time-scales.

The project utilized a high-resolution Delft3D model for the waves, hydrodynamics, sediment transport, and morphological change of the wetlands systems. Employing adaptive grid settings for short-term and long-term predictions, the model was validated using the in-situ hydrodynamic measurements and the temporal wetland evolution results drawn from satellite and UAS imagery analyses. The validated model was used in conjunction with measured erosion estimates from satellite data to determine relationships between wave power (the incident wave metric relevant to marsh evolution) and erosion in the Galveston and Corpus Christi Bay systems. The validated model was used under assumed future sea level and atmospheric forcing to predict wetland erosion through 2100.

1 Introduction

Coastal erosion is a major concern to Bay communities and ecosystems for its potential to impact the ecological balance and the economy along the Texas coast. In West Galveston Bay, the second largest estuary along the northern Gulf of Mexico coast, coastal wetlands play an important role in the ecosystems of Houston (Mukaimi et al., 2018). These wetlands establish a natural inland barrier that helps to reduce the impact of extreme weather events, to lower the probability of flooding, and to protect the city from direct wave erosions (Guannel et al., 2014; Reja et al., 2017), as well as to provide habitats for migrating birds and estuarine species (Rozas et al., 2009; Dahl & Stedman, 2013; Entwistle et al., 2018). In addition, wetlands serve as natural filters and buffers, contributing to absorption and processing of the pollutants produced by the nearby chemical plants to prevent their dispersion to the surrounding ecosystems (Bugica et al., 2020). These significances of wetlands on the coastal ecosystems raise the importance in understanding comprehensive dynamics of wetland evolution to develop optimized wetland protection plans in the state of Texas. However, the coastal wetland evolution presents complex dynamics closely associated with varying factors, including wave and current forces, water levels, soil properties, and the density of vegetation cover. Thus, this project aims to create a comprehensive dataset of wetland erosion and subsequently develop a predictive numerical model based on this dataset to assess both short and long-term wetland erosion trends in Texas.

Over the past several decades, satellite remote sensing has offered remarkable opportunities for observing the earth's surface. Although its accuracy is incomparable with *in-situ* measurements, satellite remote sensing provides observations data over wetlands on a large spatial scale. This is particularly advantageous for coastal settings where comprehensive monitoring benefits from large spatial-scale data. In addition, remote sensing with satellite imagery proves to be highly cost-efficient for wetland monitoring, considering the vast amount of data available from satellite platforms. It also maintains a consistent stream of near-real-time measurements. In contrast, data collected through traditional approaches usually lags several months behind and lacks continuous recording over a long period. All these benefits of satellite-based remote sensing highlight the superiority of wetland monitoring through satellite imagery over traditional in-situ measurement of wetland evolutions.

Despite their strong advantage in large-scale mapping, satellite images suffer from fully-resolving short-term coastal wetland evolution with geomorphic changes smaller than the spatial resolution of the satellite imagery. Also, dense cloud covers often contaminate satellite images (Klemas et al, 2013). The limitations present in satellite imagery triggered the data acquisition via aerial photographs. Recent technological development of Unmanned Aerial System (UAS) and associated digital photogrammetry using structure-from-motion (SfM) technique has overcome these limitations of satellite imagery by providing short-term and high-resolution spatial data. Despite its limitation based on weather, UAS features a broad range of accessibility to research regions (Coops et al., 2019) and low-altitude surveys (up to 120 m by FAA regulation), providing centimeter-level ground sample distance (Toth et al., 2016). Mapping accuracy of UAS photogrammetry has also been significantly enhanced from meter-level to sub-5cm absolute accuracy with the adaptation of direct georeferencing techniques, which are real-time kinematics (RTK) and post-processing kinematics (PPK) (Forlani et al., 2018; Padro et al., 2019). These advantages of UAS mapping have promoted the application of UAS-based remote sensing technique in geomorphological studies in various coastal settings (Gonçalves and Henriques, 2015; Eltner et al., 2015; Dronova et al., 2021).

For wetland monitoring, field measurements are needed to better understand the forcing conditions driving wetland change processes and to validate numerical modeling efforts of hydrodynamics and sediment dynamics near wetland boundaries. Field measurements of water free-surface hydrodynamics and wave-induced sediment suspension near wetlands are critical to quantify the wave energy and estimate the erosion potential. Pressure transducers (PT) are robust instruments commonly used to measure surface fluctuations and wave parameters and were the primary method for collecting the required data for this project. In addition, Acoustic Doppler Velocimeters (ADV) and Current Profilers (ADCP) were used to measure instantaneous velocities at high frequencies. ADV and ADCP offer instantaneous velocity measurements in three dimensions coupled with water pressure using built-in pressure transducers (PT). Optical Backscatter Sensors (OBS) were also used in combination with the acoustic instruments to facilitate turbidity measurements, which allow for estimation of suspended sediment transport rates at the field sites through calibrated suspended sediment concentration (SSC) and measured co-located velocity.

While sophisticated remote sensing platforms and *in-situ* measurements are capable of determining present-day states of erosion along wetland boundaries, their ability to predict erosion in future years is limited to extrapolation of best-fit erosion rates. This approach presupposes the absence of sea level rise, which would have a nonlinear effect on rates projected from prior data. As sea levels rise, the location of wave breaking on the wetland edge would likely move closer to this edge due to

increased water depth, which would amplify the erosive potential. However, as sea levels continue to rise, the wetlands may become partially or completely drowned. In this case, waves which would have previously broken on the wetlands edge may instead pass over them without breaking. In addition, meteorological conditions altered by climate change impacts would also change the incoming wave environment and local wind-induced surge. These complicating factors would need to be captured in the erosion prediction, and as such a computational model is required.

1.1 Goal and objectives

The o*ver-arching* goal of this project was to develop a robust numerical forecasting model to predict the short-term and long-term evolution of coastal wetland in key estuaries along the Texas coast, particularly in Galveston Bay and the Mission-Aransas National Estuarine Research Reserve (MANERR). Our approach to achieve the over-arching goal was to synthesize direct observations of wetland evolution over various timescales, including long-term satellite and short-term UAS observations, with *in-situ* measurements of wave-induced hydrodynamics and sediment suspension as validation methods to aid the numerical modeling effort. To achieve the over-arching goal of this project, we pursued the following specific objectives/tasks:

- **Task 1: Establish historical long-term Galveston Bay and MANERR wetland boundary evolution through satellite imagery.**
  - We conducted wetland erosion evolution mapping using satellite imagery, specifically focusing on the regions of West Galveston Bay, Matagorda Bay, and Espiritu Santo Bay. Utilizing Landsat imagery with 30 m spatial resolution and revisit frequency of 16 days, we thoroughly assessed the long-term trends in wetland boundary evolution from 1984 to 2020 and identified preliminary hotspots of erosion and accretion activity from Landsat water occurrence images in **Chapter 2**, **Section 2.2**. We also analyzed these hotspots by employing CubeSat satellite images with higher spatio-temporal resolution than the Landsat imagery in four specific locations of Galveston wetlands. The error associated with misclassification due to low spatial resolution of the Landsat imagery is significantly reduced using the Cubesat imagery, and the improved wetland evolution analysis with detailed spatial information is discussed in **Section 2.3**. In addition, the Cubesat imagery allows discrete quantification of the influence of sea level rise and sedimentation due to its high spatial and temporal resolution. We focused on changes in sedimentation to further analyze the impact of two recent hurricane events on wetland evolution dynamics, as discussed in **Section 2.4**.

- **Task 2: Establish seasonal and eventful short-term Galveston Bay wetland boundary**
  - We conducted seven field campaigns at four specific wetland sites in Galveston Bay between September 2021 and July 2023 using a small UAS platform to collect wetland boundary images, as discussed in **Chapter 3, Section 3.1**. The first two campaigns were associated with Hurricane Nicholas (Category 1) before and after it made landfall in September 2021, and the following five field campaigns were conducted to explore seasonal variations in shoreline change dynamic at the four Galveston wetland sites. We post-processed the collected UAS imagery to generate mapping products (i.e., DEMs and orthomosaic maps) and evaluated hurricane-induced and seasonal shoreline changes at Galveston wetlands by statistical analysis of temporal boundary movements observed from the UAS-based wetland maps. The associated data processing and data analysis are discussed in **Sections 3.2 and 3.3**.
  - Hydrodynamic field measurements using pressure transducers (PT), acoustic Doppler Velocimeters (ADV), and Current Profilers (ADCP) were conducted at the field sites simultaneously with the UAS surveys during the first four campaigns to better understand the forcing conditions driving changes near the wetland edges and in support of long-term (and short-term) modeling efforts. The instrumentation and deployment plan and the associated data processing are discussed in **Chapter 4, Section 4.2**. We conducted times-series and spectral analyses from times-series of the measured water surface elevation data to acquire wave spectral information. The observation results for elevated wave activities and the correlated increase in water velocity magnitudes during abrupt weather changes, including the prevalent cold fronts and Hurricane Nicholas, are discussed in **Section 4.3**. The link between the hurricane event with the turbidity analysis from the suspended sediment concentration (SSC) measurements using optical sensors is also discussed in **Section 4.3**.

- **Task 3: Numerical simulations – validation and forecast of wetland boundary**
  - Prior studies on wetlands erosion have identified surface waves as a primary erosion agent, with winds, tides and water levels serving to modulate the impact of waves (and thus the erosion). In this task, we predicted future erosion rates by wave impacts on wetlands using the Delft3D-FLOW model, validated by *in-situ* measurement data discussed in **Chapter 4**. The validation process is discussed in **Chapter 5, Section 5.1**. The short-term simulation results during the period of the field campaigns for this report were conducted using

finely-resolved grids. The simulation process, model sensitivity tests, and the results for short-term simulation are discussed in **Section 5.2**. Long-term forecasts of wetland erosion through simulated coastal wave energy flux up to the year of 2100 were also simulated using the validated Delft3D-Flow model with a slightly coarser grid resolution for computation efficiency. The corresponding simulation process and results are discussed in **Section 5.3**.

- **Task 4: Establish Interactive, Web-based Galveston Wetland Boundary Evolution Map**
  - The historical data of wetland boundary evolution obtained in Task 1, and future predictions from numerical simulations under various scenarios (base line water level and weather conditions and future weather pattern and sea level) in Task 3 have been integrated into the existing GIS based website Texas Coastal Atlas (https://www. texascoastalatlas.com/) managed by the Center for Texas Beaches and Shores (CTBS). Users can see the time history of wetland boundary maps by selecting a certain period to see the changes (erosion mostly) in the past 30 years. Erosion/accretion hotspots observed from the UAS-based short-term analysis and the long-term analysis using Landsat imagery are summarized in **Appendix B**. Users can also see predictions of our future wetland extent and compare that to the wetland extent of the present day, and predictions under various scenarios of weather and sea level conditions up to year 2100. This task has been supported by CTBS with data supplied from the research team.

The ultimate outcome of this project is to create a comprehensive understanding of wetland dynamics and erosion mechanisms, which will inform effective wetland management strategies to maximize their benefits, including storm surge reduction, habitat creation, fisheries sustainability, and carbon sequestration. This project will build a strong basis to develop an optimized coastal resiliency program along the Texas Coast and act as the connection point for the public to access the states' Coastal Resiliency Master Plan to maintain the coastal ecosystem through the numerical forecast model integrated with remote sensing data and *in-situ* hydrodynamics measurements.

1.2. Major accomplishments (publications / presentations)

The outcomes of each task were presented through multiple conference presentations and seminar talks, including remote sensing analysis of Texas wetland evolution, hydrodynamic impacts induced by from hurricane, cold-fronts, and vessel-wakes, and numerical analysis to verify wave impact on wetland evolution dynamics. The manuscripts based on these project outcomes are in preparation for future submission to appropriate research journals. The conference presentations, invited talks, and journal manuscripts in preparation are listed as follows:

- **Conference presentations**
  - Bae, S. B., Kim, J. Y., Huang, C., Li, Y., Tong, F., Zhang, S., Chang, K.A., Figlus, J., Gao, H., Kaihatu, J.M. and Socolofsky, S.A., 2022, December. Detecting Changes of Wetland Boundaries by Applying Particle Image Velocimetry to UAS Orthoimagery in Galveston Bay, Texas. In AGU Fall Meeting Abstracts (Vol. 2022, pp. H36D-04).
  - Huang, C., Li, Y., Zhang, S., Bae, S. B., Kim, J. Y., Tong, F., Chang, K.A., Kaihatu, J.M., Figlus, J., Socolofsky, S.A. and Gao, H., 2022, December. High resolution mapping of Texas wetland evolution using Landsat and CubeSat images. In AGU Fall Meeting Abstracts (Vol. 2022, pp. H36D-03).
  - Kim, J.Y., Chang, K.A. and Kaihatu, J., 2021, December. Verification of wave-induced impact on saltmarsh edges based on UAV images and numerical model. In AGU Fall Meeting Abstracts (Vol. 2021, pp. EP35H-1395).
  - Kim, J.Y., Kaihatu, J., Chang, K.A., Huff, T. and Feagin, R., 2021, December. Sediment transport and morphodynamics at salt marsh boundary in the shallow bay during cold front passages. In AGU Fall Meeting Abstracts (Vol. 2021, pp. EP24A-03).
  - Tong, F., Figlus, J., Chang, K.A., Gao, H., Kaihatu, J.M., Socolofsky, S.A., Bae, S. B., Kim, J. Y., Huang, C., Li, Y. and Zhang, S., 2022, December. Hurricane, Cold-Front, and Vessel-Wake Hydrodynamic Impacts on Wetland Edges in Galveston Bay, Texas. In AGU Fall Meeting Abstracts (Vol. 2022, pp. OS53B-03).

- **Invited talks**
  - Bae, S. B., Application of unmanned aerial systems (UAS) imagery to coastal process monitoring, UAS Certification Program, Mar 23, 2023, Montana Technological University, MT, USA

- **Manuscripts in preparation (with tentative title)**
  - Bae S. B., J. Kim, F. Tong, C. Huang, S. Zhang, Y. Li, J. Figlus, J. Kaihatu, H. Gao, S. Socolofsky, and K. Chang,

Enhancing Accuracy in Shoreline Changes Derived from UAS Mapping using Georectification Based on Particle Image Velocimetry.

- Huang, C., Y. Li, S. Zhang, S. Bae, J. Kim, F. Tong, K. Chang, J. Kaihatu, J. Figlus, S. Socolofsky, and H. Gao, Mapping Intertidal Wetland Evolution using Multi-year High Resolution CubeSat Imagery in West Galveston Bay on the Gulf of Mexico.

1.3 Outline of Report

The main objectives and results of Task 1 through 3 are discussed in the main body of this report. **Chapter 2** introduces the observation of large-scale wetland changes in Galveston Bay, specifically focusing on West Galveston Bay, Matagorda Bay, and Espiritu Santo Bay. We utilize satellite imagery to identify historical long-term trends of wetland boundary evolution in these regions and to quantify their wetland erosion rates under the combined influence of both sea-level changes and sediment transportation. Key outcomes of Task 2 through UAS surveys along the wetland boundaries and *in-situ* hydrodynamic measurements through field campaigns are reported in **Chapter 3** and **4**. In **Chapter 3**, we assess hurricane impact on wetland geomorphology and evaluate seasonal variations of shoreline changes from geospatial map data generated using the collected UAS imagery. Identification of forcing conditions that influence the wetland evolution dynamics is conducted through the wave-spectral analysis from *in-situ* measurements at the field sites and is represented in **Chapter 4**. Then, we discuss the synthesis result of numerical simulation of wetland evolution using Delft3D-Flow model with the observation data from remote sensing and field campaigns in the preceding chapters in **Chapter 5**. Lastly, the concluding remarks of the project objectives are addressed in **Chapter 6**.

2 Establish historical long-term Galveston Bay and MANERR wetland boundary evolution through satellite imagery

Significant research efforts have been directed towards understanding the vulnerability of coastal wetlands to climate changes and human activities (Ravens et al., 2009; White et al., 2002). The two driving factors of the wetland change processes are known to be “sea level rise” and “sediment erosion”. Hydrodynamic data collected from Galveston Bay 21 (NOAA, 2021) indicate a consistent upward trend in relative sea level with an annual increase of 12.1 mm/year since 2000 (Paine et al., 2021). In contrast, a decrease of approximately 50% in sediment supply has been reported since the construction of the Texas City Dike (TCD) and 31 major dammed reservoirs (Ravens et al., 2009). Through a comprehensive analysis employing eight Pb (lead) radiochemical assessments, an average vertical sediment accretion with a rate of 2.5 mm/year was identified (Ravens et al., 2009; Mukaimi et al., 2018). This deficiency in sediment supply largely contributes to erosion within West Galveston Bay. Their study, however, lacks detailed spatial data regarding the erosion. While land subsidence is a prominent issue in Galveston Bays, mainly due to human activities (Shirzaei, 2021), subsidence in West Galveston Bay measures less than 0.2 mm/year (Khan et al., 2022). Despite these findings, due to the lack of *in-situ* measurements, the detailed understanding of long-term wetland evolution remains limited, and few investigative measures have been undertaken in previous studies.

The recent advancements in high spatial and temporal satellite remote sensing provide a powerful tool for effective monitoring and identifying large-scale wetland changes over a long historical period. Given the vulnerability of wetlands to both climate change and human activities, the valuable insights obtained through remote sensing about wetland changes can significantly contribute to a better understanding of wetland evolution. This information can also help managers and stakeholders make effective wetland protection strategies.

In this chapter, the evolution of wetlands is observed through satellite images. Firstly, in Section 2.2, long-term wetland evolution from 1984 to 2020 is analyzed using Landsat image classifications which have 30-m spatial resolution and monthly interval. The annual and seasonal wetland boundaries are extracted from the water occurrence maps that are derived from the Landsat classifications. Preliminary hotspots of deposition and erosion can be then identified by comparing the differences between the two water occurrence images (1985-1989 and 2010-2014).

Secondly, to gain a more accurate and comprehensive understanding of the wetland evolution and to avoid misclassification of small islands, CubeSat satellite images from 2009 to 2021 are utilized for detailed analysis at four locations in Section 2.3. These four sites are selected based on the existence of estuarine wetlands in potentially erosive states and accessibility via truck/trailer and towed boat using local boat ramps. Due to the high temporal and spatial resolution of the CubeSat images, we are able not only to capture the detailed changes of the wetland boundary but also to observe the variations in seabed caused by sediment transport.

Thirdly, in Section 2.4, the wetland erosion rate, which is determined under the combined influence of both sea level changes and sediment transport, is quantified using the previous wetland evolution maps from both Landsat and CubeSat water occurrence maps. The average wetland erosion rates are calculated for more than 900 locations from the Landsat images. Wetland regions that have experienced the highest erosion are further investigated using the CubeSat satellite observations. The sediment erosion rate, which is defined as the wetland change purely affected by the sediment transportation, can be specifically derived by utilizing the CubeSat based water occurrence map along with the *in-situ* water levels. The sediment erosion rate can serve as a metric to represent the landscape evolution of seabed (namely bed evolution hereafter). Additionally, the Landsat-based erosion rate are compared with the U.S. Fish and Wildlife Service National Wetlands Inventory (NWI) geospatial dataset to improve our understanding regarding the influences of wetland types. Furthermore, sedimentation during two hurricane events is analyzed, which can provide valuable insights for future shoreline protection efforts.

2.1 Mapping wetland evolution using Landsat satellite images

In this section, the annual and seasonal water occurrence maps from 1984 to 2020 are generated using Landsat images to provide insights into the wetland's evolution. The 30+ years of Landsat images Changes in these annual water occurrence maps are used to detect the preliminary hotspots of this evolution. Wetland evolution is investigated over the three study regions included in three Texas Coastal Regions (**Figure 2.1**) in the Master Plan.

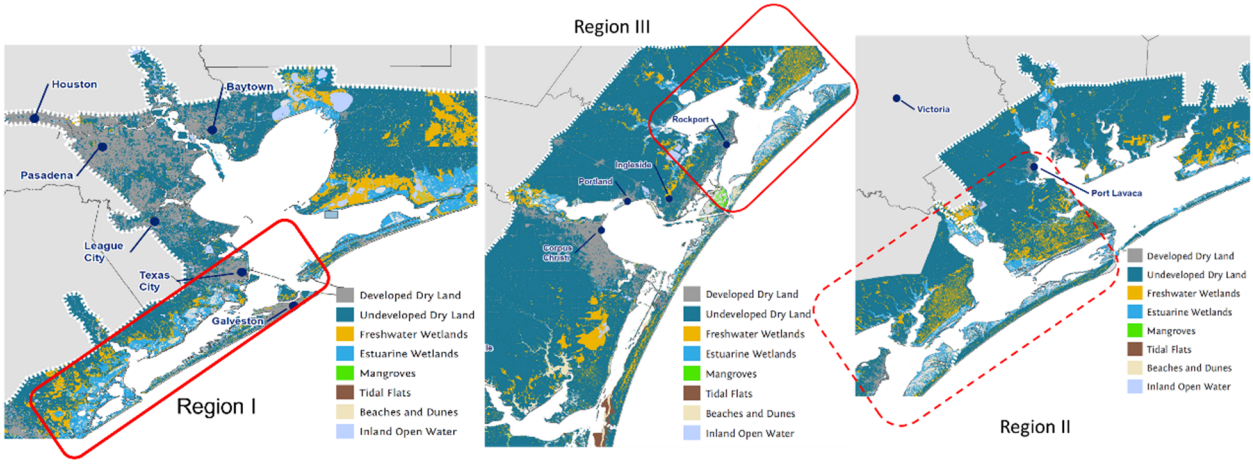

Figure 2.1: Study regions (red boxes) in the three regions of the Master Plan.

2.1.1 Landsat data used for wetland evolution mapping

The Global Surface Water dataset (GSW, Pekel et al., 2016) is adopted to analyze wetland evolution. The GSW dataset generates monthly global classification maps based on Landsat 5, 7, and 8 from 1984 to 2021. These classification maps employ an expert system that identifies pixels as either "no water," "water," or "no data" at a 30 m spatial resolution. The maps have been widely used to depict the seasonal and annual changes of water bodies.

2.1.2 Methods for the long-term wetland evolution mapping

To quantify the hot spots related to wetland evolution and analyze the seasonal change, we generated the annual and the seasonal (i.e., monthly) water occurrence images for each of the three regions (i.e., regions 1, 2, and 3). The water occurrence represents the frequency that a pixel was detected as water for a given period. The annual water occurrence value for a specific pixel is calculated as the proportion of times that pixel is detected as water compared to the total number of observations for that pixel throughout a given year. Similarly, the seasonal (or monthly) water occurrence is calculated in the same manner but use the observations within the given season (or month) from 1984 to 2020.

2.1.3 Landsat based wetland evolution maps

The water occurrence maps can effectively represent the average wetland area for a specific year, which are significantly affected by sea level fluctuations. **Figure 2.2** shows an example of water occurrence maps in 1984 across the three regions. The value of water occurrence is measured on a scale ranging from 0 to 1. The annual and seasonal water occurrence images (in TIF format) are available for each of the three study regions. Additionally, we provide two movie animations (in GIF format) for each study region in this delivery to illustrate the spatio-temporal variations.

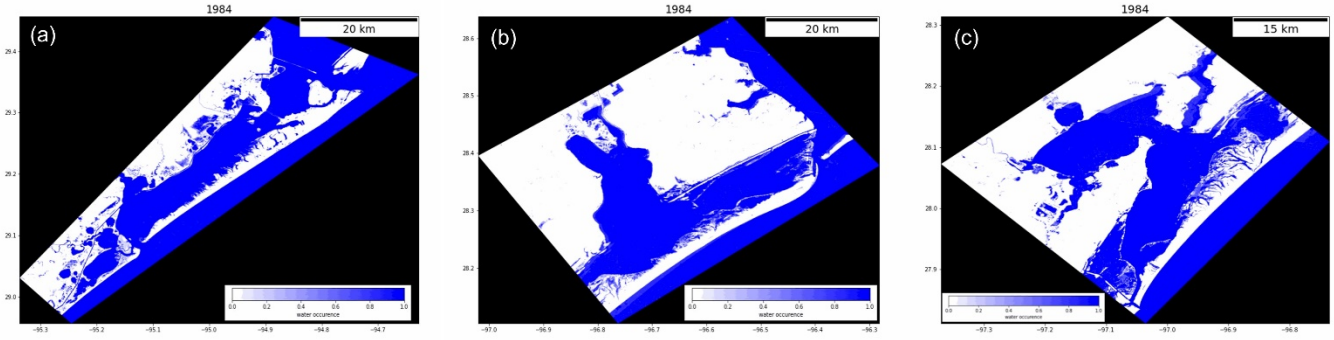

Figure 2.2: The annual water occurrence maps in 1984 for (a) Region 1 (b) Region 2 (c) Region 3.

When quantifying wetland evolution using annual water occurrence maps, there may be high uncertainty due to large sea level fluctuations. According to the interannual variation recorded at Galveston Pier 21 (NOAA, 2021), the sea level fluctuation lies between ±0.15m, while these fluctuations are much lower than the sea level rise from 1984 to 2020, which is around 0.78 meters over 37 years (0.21 mm/year) (NOAA, 2021). Therefore, to reduce the uncertainty caused by the sea level changes, we utilize the 5-year water occurrence images to identify the hot spots in terms of wetland changes. As shown in **Figure 2.3**, the hot spots of long-term wetland evolution are estimated using the difference of water occurrence images between 1985-1989 and 2010-2014. In Region 1 (Figure. 2.3 a), erosion dominates the land cover changes—especially at West Bay, Christmas

Bay, and Pelican Island. The water area within this domain has increased at a rate of about 0.5 km^2/yr (representing a loss of the land). In study region 2 (Fig. 2.3 b), most of the changes are attributed to erosion especially, San Luis Pass Beach [red box in Figure 2.3 (a)] experienced significant erosion. The water area within this domain has increased at a rate of about 0.28 km^2/yr. In study region 3 (Fig. 2.3 c), a small amount of deposition occurs along the coastline, but the wetland is eroded. The rate is around 0.67 km^2/yr within this domain. The identified erosion "hot spots" in **Figure 2.3** are also included in the delivery.

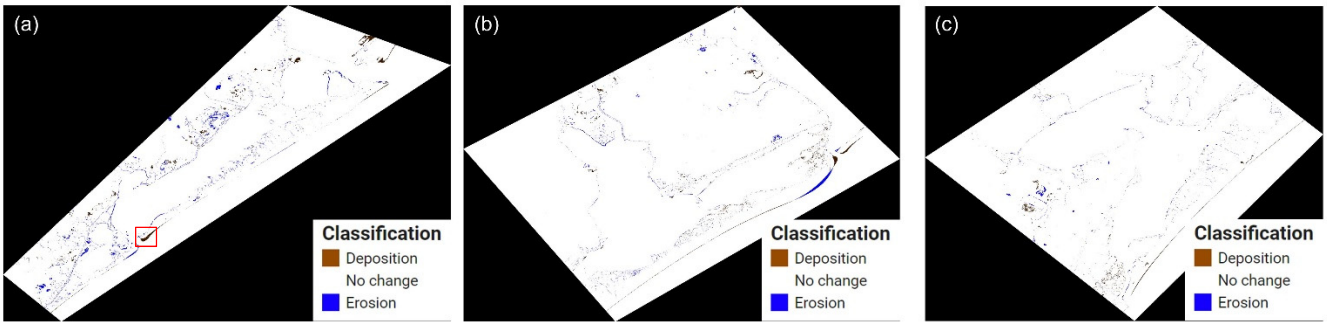

Figure 2.3: The hot spots of long-term wetland evolution between 2010-2014 and 1985-1999 for (a) Region 1 (b) Region 2 (c) Region 3.

2.2 Mapping wetland evolution based on CubeSat imagery

Although the long-term evolution of the wetlands has been inspected through Landsat Images in the previous section, Landsat's 30-meter spatial resolution limits its applicability for conducting finer-scale wetland evolution analysis. To gain a more comprehensive understanding of the evolution and to avoid misclassification on small islands, CubeSat satellite images from 2009 to 2021 are adopted for detailed analysis at the four selected locations (**Figure 2.4)**. The CubeSat satellites can provide data with spatial resolutions of 3-5 meters and near-daily re-visit frequency. Furthermore, due to this high temporal resolution, the bathymetry map can be estimated, allowing the wetland and sediment erosion rates to be calculated separately. The wetland erosion rate is determined by quantifying the horizontal loss of land at the mean water level, while the sediment erosion rate is inferred by analyzing horizontal shifts in bathymetry maps at a specific water level. The four sites are chosen based on the existence of estuarine wetlands in a potentially erosive state and accessibility via truck/trailer and towed boat using local boat ramps. *In-situ* hydrodynamic measurements and unmanned aerial system (UAS) surveys have been conducted at these four locations, and the findings are presented in Chapters 3 and 4.

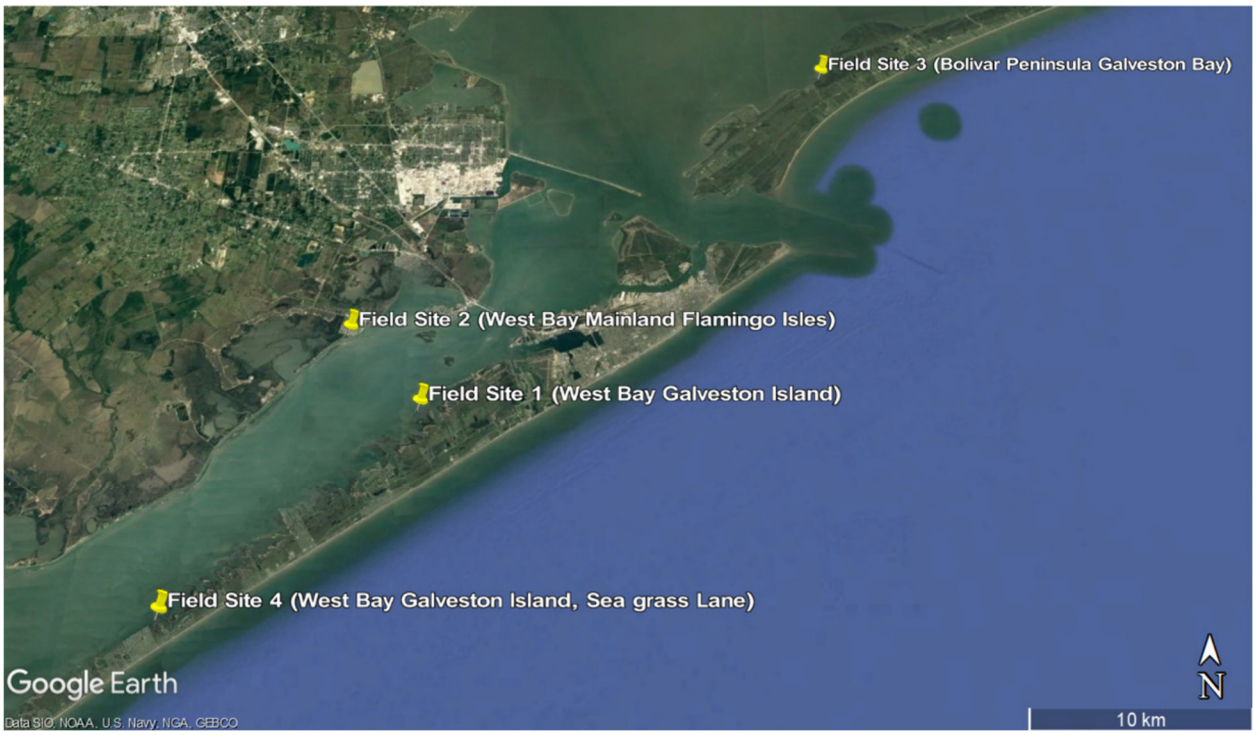

Figure 2.4: Overview of three final field sites in Galveston Bay (FS-1, 3, and 4) and the alternative field side (FS-2) in West Bay.

2.2.1 CubeSat imagery

CubeSat satellite data (mainly including images from RapidEye and PlanetScope) are adopted to estimate wetland evolution at finer spatial scale over the four selected sites. CubeSats, which are miniaturized satellites, offer low-cost opportunities for Earth observation (Poghosyan et al., 2017). With constellations of over 170 CubeSat satellites, CubeSat can provide near-daily high spatial-resolution (3m to 5m) data (Houborg et al., 2018) from 2009 to 2021. Although these images contain less spectral information compared to Landsat imagery, CubeSat satellite data can offer a fresh perspective on coastal regions due to its improved spatial resolution and re-visit frequency.

2.2.2 Method for mapping short-term wetland evolution with high spatial resolution

CubeSat based wetland evolution and bed evolution results from 2009 to 2021 at the four field sites have been submitted as deliverable. The following contains a detailed explanation of the algorithm. The primary data include CubeSat images (https://www.planet.com) and water levels collected at NOAA tide stations.

The flow chart of the algorithm is shown in **Figure 2.5**.

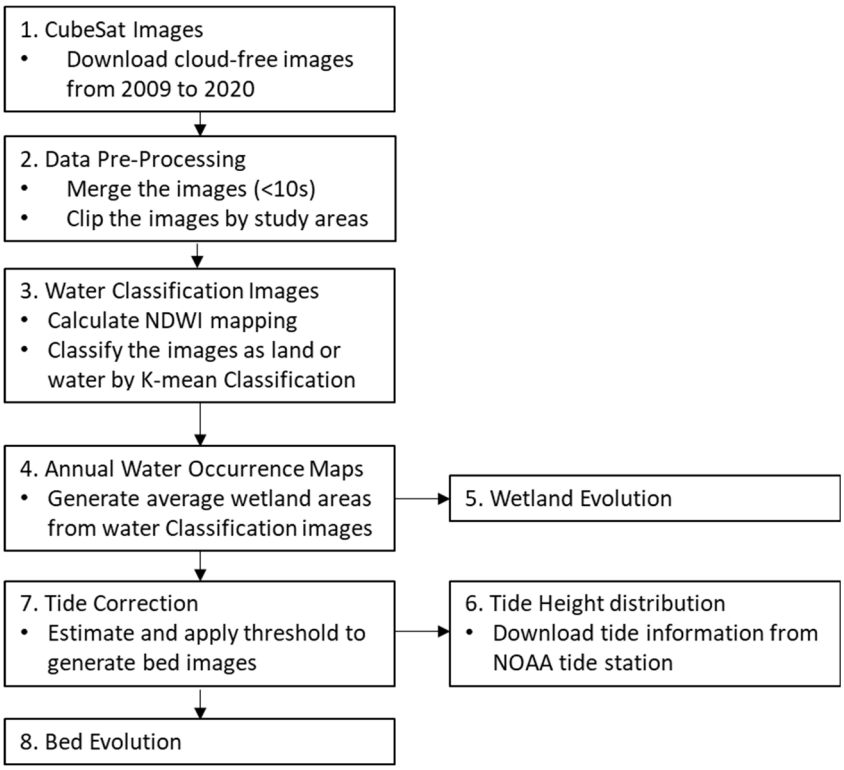

Figure. 2.5: Flow Chart for quantifying wetland evolution and bed evolution.

1) CubeSat images downloading

Over 3,000 cloud-free CubeSat images are downloaded from 2009 to 2021 for evaluating wetland evolution at these four field sites. In this study, RapidEye provides monthly observations at a 5-meter resolution from 2009 to 2016, and PlanetScope provides daily measurement with a resolution of 3 meters from 2017 to 2021.

2) Data pre-processing:

Each Planet image is taken along the orbit every 1-2 seconds—which is about 280 to 630 km^2 in size, depending on the satellite. Clipping these images to extract regions of interest, and then merging to a fixed domain can significantly reduce the computation data amount. However, as explained in Planet (2022), image quality varies significantly due to the different satellite sensors and the different atmospheric effects. Additionally, the tide height varies over time. Therefore, we only merge the images with close acquisition times (<10s apart) from the same satellites (i.e., the same satellite ID). For the overlapping areas, the mean value for each band is adopted.

3) Water classification

The Normalized Difference Water Index (NDWI) (McFeeters, 1996) images are calculated after the following formula: NDWI = [(Green-NIR)/(Green+NIR)]. To extract water pixels from background information on CubeSat images, a two-dimensional K-

mean classification algorithm (Sobiech and Dierking 2013) is applied to the NIR and NDWI bands to classify each pixel into water (1) or non-water (0). **Figure 2.6** shows an example of the RGB image, the NIR image, and the water classification results for the FS-1 site.

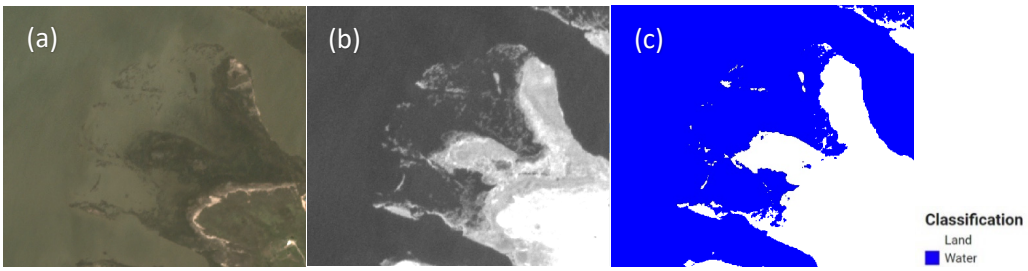

Figure. 2.6: The PlanetScope RGB image (a), NIR image (b), and water classification (c) at the FS-1 site on 09/03/2021.

4) Annual/bi-annual water occurrence calculation

On a water occurrence map, the value of a pixel represents the frequency (probability) of that pixel being classified as water during a certain time period [(∑water detection)/(the total number of images)]. Because RapidEye provides monthly images, only two-year water occurrence maps are generated from 2009 to 2016. Annual water occurrence maps based on other satellite sensors are from 2017 to 2021. The differences between the water occurrence maps in different years can be used for estimating erosion.

5) Wetland evolution estimation

The difference between annual water occurrence in different years can be used to estimate the wetland evolution. In this study, the difference between the water occurrences maps in 2009 and 2021 for the four field sites is demonstrated.

6) Tide height distribution calculation

Figure 2.7 shows the tide height distributions at the four field sites. Based on the data acquisition time of the CubeSat images, the tide height values were acquired from the nearest NOAA tide station (FS1, FS2, FS3: 8771486; FS4:8771972). Some tide height values are not available before 2017. Therefore, we only collected the data after 2017.

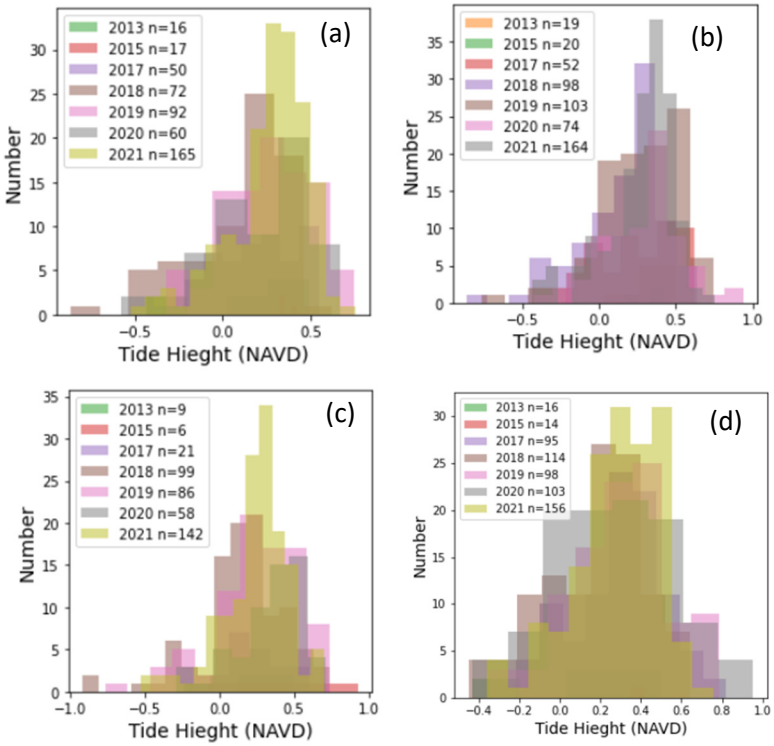

Figure. 2.7: Histogram plot for the corresponding tide heights at the (1) FS-1, (2) FS-2, (3) FS-3, and (4) FS-4 sites. *n* represents the total number of images per year.

7) Bed evolution correction by removing impacts from tides
Water occurrence is affected by the tide height. In water classification, when a given pixel is classified as water (1), the bed elevation should be lower than the tide height. In other words, water occurrence also represents the frequency when the bed elevation is lower than the tide height (1-exceeding probability of height). Tide height distribution is a composite of the tide heights at the acquisition time of the various CubeSat images. Tide height distribution varies during different years.

To quantify the bed erosion at the same water level, water occurrence maps need to be corrected by utilizing tide information. The tide height distribution (**Figure 2.7**) varies at different locations in different years. A cumulative histogram and exceeding probability of height can be calculated from the tide height distribution. Therefore, the relationship between the water occurrence value (1-exceeding probability of height) and the bed height is determined. In other words, we can transfer the water occurrence map to bathymetry. However, the cloud contamination and classification errors result in some problems at the tail of the distribution. In this study, we separate the bathymetry values into land (elevation > 0.2 m) and water (elevation < 0.2 m) to generate "bed" images at 0.2 meters. This is based on the fact that the mean value from all tide height distributions is 0.2 m (North American Vertical Datum of 1988).

8.) Bed Evolution
The difference of the beds in the 0.2- meter images between 2017 and 2021 is calculated for the four field sites.

2.2.3 CubeSat-based short term wetland evolution
Figure 2.8 shows the difference of the water occurrence maps between 2009 and 2021 for the four field sites. Different degrees of erosion have been observed at each of these four locations. The north side of FS-1 was eroded by about 15-20 meters within 12 years, and the wetland and the island in FS-3 were eroded 30-50 meters over 12 years (this is where the most erosion occurred). The coastlines at FS-2 did not show an obvious change (around 5 meters/12 years), but the south side of the island eroded around 10-15 meters over 12 years.

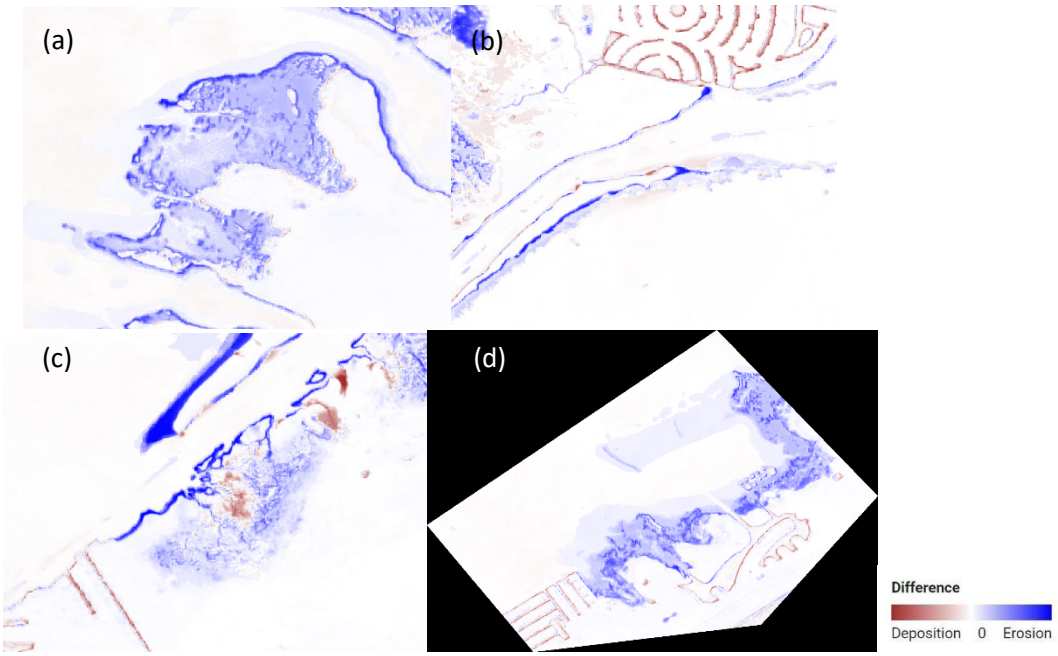

Figure. 2.8: The difference between water occurrence maps in 2009 and 2021 at FS-1, (b) FS-2, (c) FS-3, and (d) FS-4.

Figure 2.9 shows the difference between the beds in the 0.2-meter images in 2017 and 2021. The beds in the 0.2-meter images are water occurrence maps corrected by utilizing tide information. Because the images are at the same elevation, they offer more accurate sediment erosion estimations than the results solely based on occurrence differences discussed above. According to **Figure 2.9a-c**, it is obvious that FS-1, FS-2 and FS-3 are losing sedimentation, which is consistent with their counterparts in **Figure 2.9d**. However, the coastline at FS-4 in **Figure 2.9d** only shows slight erosion, differing from the results in **Figure 2.9d**. This suggests that the increased water occurrence for FS-4 in **Figure 2.9d** is likely driven by the mean water level change (sea-level rise and/or land subsidence), rather than sediment erosion.

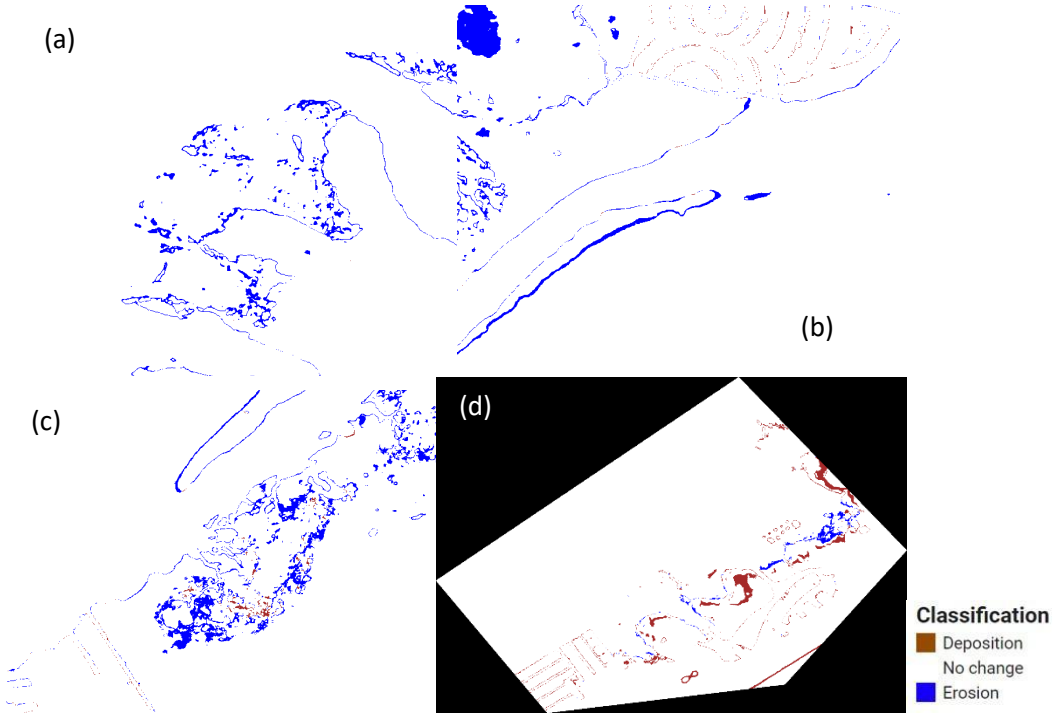

Figure. 2.9: The difference between the beds in the 0.2-meter images in 2017 and 2021. The beds in the 0.2-meter images are water occurrences mapping corrected by the tide information at the (a) FS-1, (b) FS-2, (c) FS-3, and (d) FS-4 sites.

2.3 Analysis of wetland boundary evolution and erosion rates

To quantify the shoreline change, the wetland erosion rate is first calculated using Landsat image classification. The wetland erosion rates are determined by measuring the horizontal loss of land at the mean water level. Hotspots with high erosion rates are further investigated using CubeSat satellite images. Additionally, to separately quantify the impacts from sea level rise and sediment deposition, wetland and sediment erosion rates are calculated in Region 1. This map can be used for identifying the regions with potentially high vulnerability in the future. Besides, we also explore other potential causes of erosion. The wetland erosion rate under different types of wetlands and the erosion occurring after a hurricane are analyzed.

2.3.1 Data for the erosion rate quantification

The water occurrence maps created in section 2.1 and section 2.2 are adopted to quantify the wetland erosion rate.

2.3.2 Methods for quantifying the erosion rate

Accurately mapping wetland changes caused by erosion is essential for coastal management. Two erosion indicators – wetland erosion rate and sediment erosion rate – are estimated using remote sensing images. The wetland erosion rate is used for quantifying the horizontal area changes of wetlands, which are affected by both sea level rise and sedimentation. The sediment erosion rate represents the horizontal changes of wetlands without considering the impact from sea level changes.

2.3.2.1 Wetland erosion rate quantification

The wetland erosion rate is estimated from Landsat and CubeSat images through the following steps:

1) The coastline is delineated by manually deleting rivers and reservoirs from the polygons provided by the National Wetland Inventory (NWI).
2) A masked area is created by buffering 1000 meters on both sides of the coastline.
3) The masked area is divided into smaller segments (every 500 meters) along the coastline. A total of 196 segments are created in Region 1.
4) The annual water area values for each segment are calculated by averaging the monthly area values from Landsat image classifications. We exclude the images which are heavily contaminated by clouds. The annual width change is calculated by comparing the annual total water area change with the coastline at each grid. The annual total water area change is based on the difference of water area between each year and the reference year which is 1984. The length of the coastline in each segment is a constant value estimated from the NWI shapefiles.
5) The rate of wetland evolution (in terms of width) is estimated using a linear trend analysis of the annual width change time series from 1984 to 2020.
6) The rate of wetland evolution is repeated estimated (step 4 and5) by the CubeSat images at the hotspot. The hotspot

area is located by where the Landsat-based erosion rate is smaller than the 15th percentile (-0.25 m/year) or larger than the 85th percentile (2 m/year)

2.3.2.2 Sediment erosion rate quantification

In this study, the sediment erosion rate is calculated by contrasting the bathymetry maps (Section 2.2.2) between the year 2009 and 2020.

2.3.2.3 Erosion vulnerability index (EVI)

In Equation 2.1, the EVI is defined as the absolute ratio of sediment erosion rate to the SLR induced erosion rate (i.e., wetland erosion rate minus sediment erosion rate).

$$Erosion\ Vulnerability\ Index\ (EVI) = \left| \frac{\text{sediment erosion rate}}{\text{wetland erosion rate} - \text{sediment erosion rate}} \right| \quad (2.1)$$

2.3.3 Wetland erosion rate

Due to the scarcity of *in-situ* erosion rates in the wetland region, we only validate the Landsat-based erosion rates over the coastal area in Region 1 by comparing with that calculated by Paine et al. (2021) from 2000 to 2019 based on Lidar images and water level data over the coastal area [**Figure 2.10(a)**]. To match the period in Paine et al. (2021), the Landsat-based erosion rates are recalculated using our method during the same period [**Figure 2.10(b)**]. Two sets of results are in good agreement (**Figure 2.11**), with an r^2 value of 0.78 and a p value of 0.015.

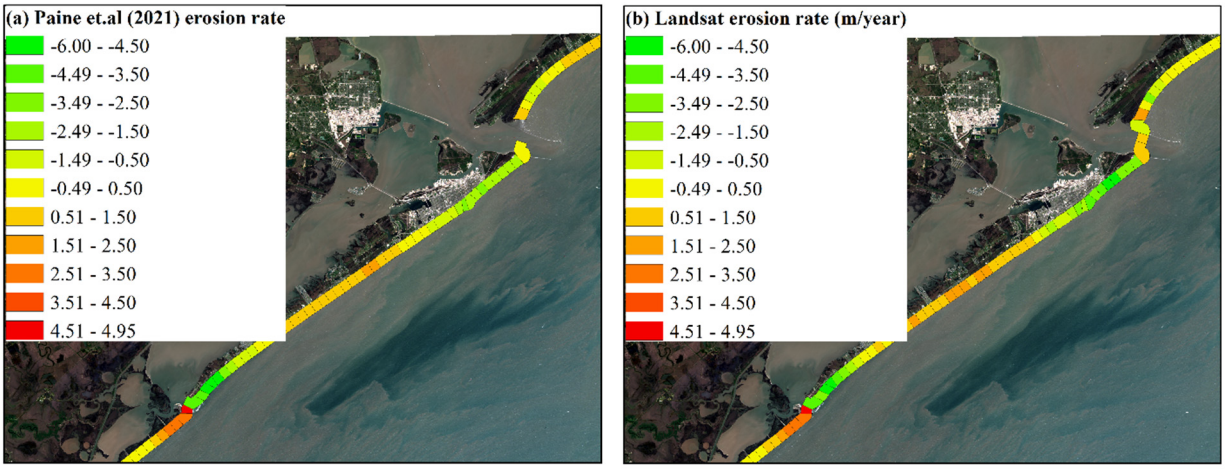

Figure 2.10: The coastal erosion rate from 2000-2019 at the coastal area in Region 1: (a) results reported in Paine et al. (2021); and (b) results based on Landsat imagery

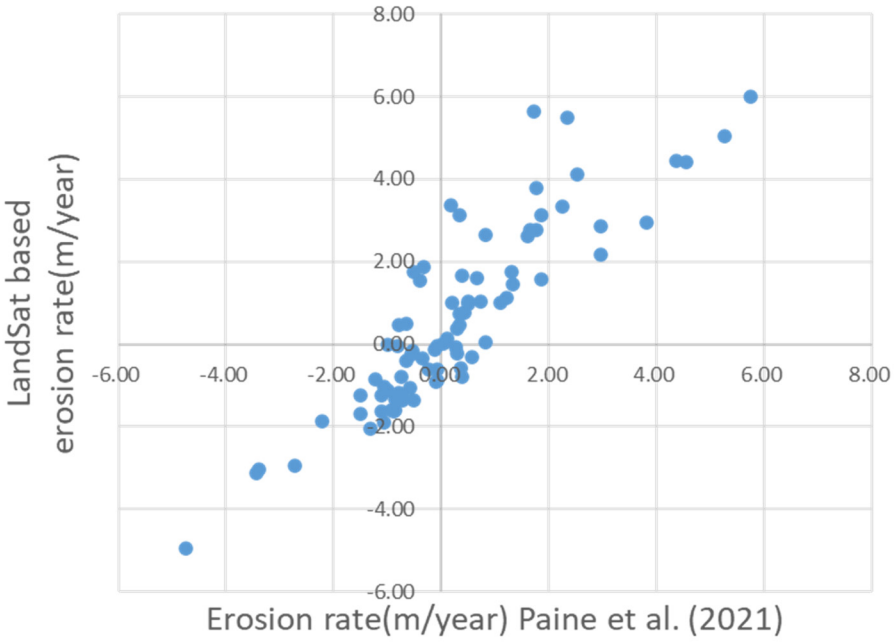

Figure 2.11: The linear relationship of coastal erosion rate between Paine et al. (2021) and Landsat results.

Figure 2.12(a) shows the Landsat-based wetland erosion rate in Region 1, with a mean value of approximate 0.71 m/year. In this context, a negative rate indicates accretion, while a positive rate means erosion. Most wetland areas are experiencing erosion, particularly in the vicinity of Christmas Bay (3-15m/year). This is possibly due to the flat slope in that region. In contrast, industrialized areas such as Texas International Terminals [two red boxes at right corner in Figure 2.12(a)] are witnessing slight deposition (-2.30 m/year). The red box identifies the hotspot area where the erosion rate is smaller than the 15th percentile (-0.25 m/year) or larger than the 85th percentile (2 m/year). **Figure 2.12(b)** illustrates the CubeSat-based wetland erosion rate for these hotspots in Region 1. For industrialized zones like Galveston, the deposition is not detected. We suspect that human impacts (such as a ship passing) may have affected the accuracy of the Landsat images, given their low spatial resolution. Regarding the wetland area, the CubeSat-based erosion rate is slightly higher than the Landsat-based erosion rate. In general, the results across both methods exhibit a similar trend. The r^2 value is 0.79 and p-value is 10^{-5}.

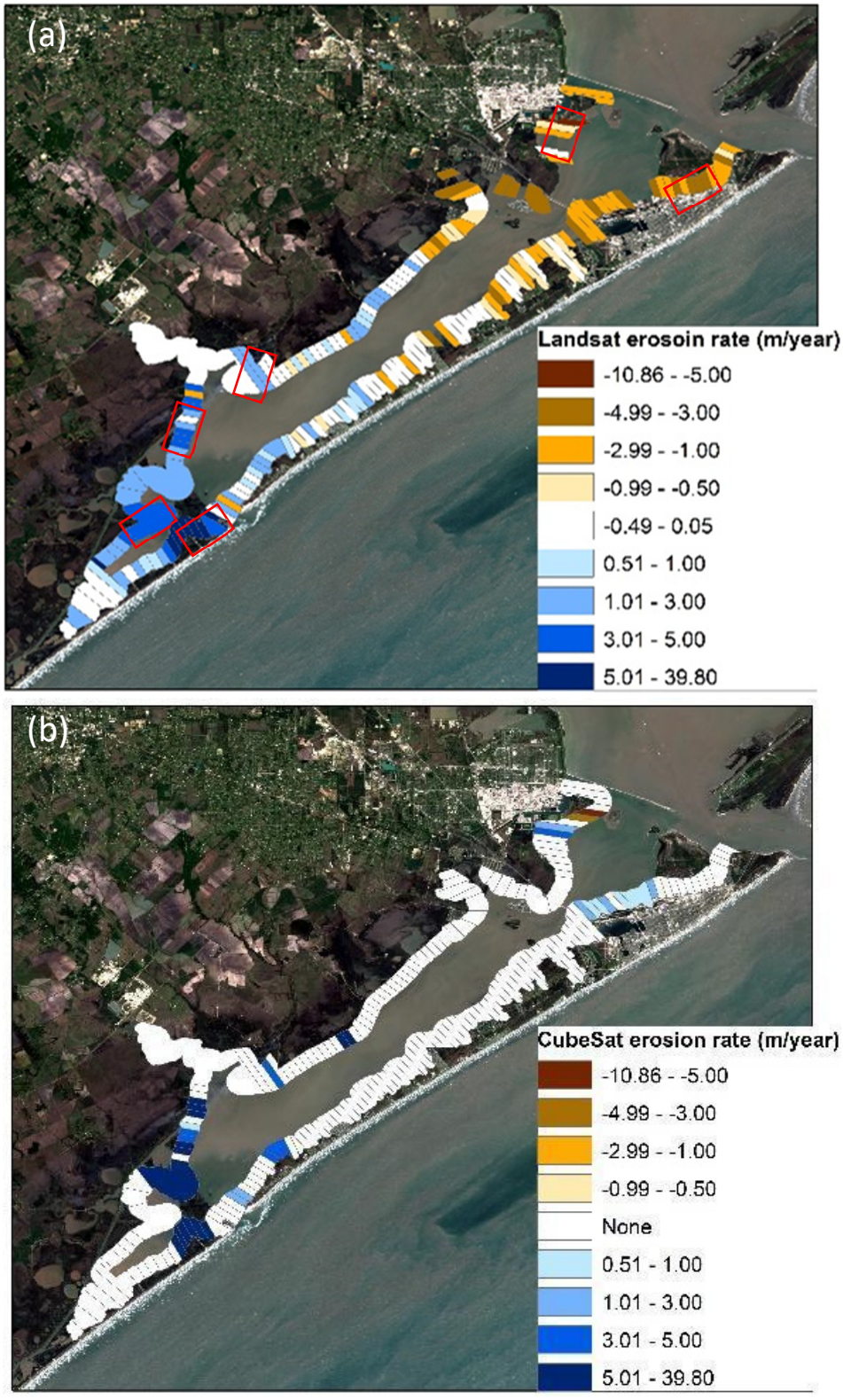

Figure 2.12: The wetland erosion rate in Region 1: (a) Landsat-based erosion rate from 2009 to 2020, (b) CubeSat-based erosion rate from 2009 to 2021.

Wetlands in Regions 2 and 3 are mostly eroded according to the Landsat-based wetland erosion rates as shown in **Figure 2.13 (a)**. Compared to Region 1 (0.71 m/year), the mean value of erosion rate in Regions 2 and 3 (0.68 m/year) is slightly lower. The erosion rate at San Antonio Bay (Region 3) is higher than that at Matagorda Bay (Region 2). The red boxes indicate the hotspots identified based on the same criteria used for Region 1. **Figure 2.13(b)** shows the CubeSat-based erosion rate at these hot spots. CubeSat-based erosion rate is approximately 0.3 times higher than the Landsat-based erosion rate. The

difference is especially evident in San Jose Island and Matagorda Island. These locations are composed of abundant small islands. Due to the low spatial resolution, Landsat-based results are less sensitive to the change of wetlands along those small islands, resulting in a relatively lower Landsat-based erosion rate compared with the CubeSat-based results. If we separate the hotspot into two groups (yellow and red box) in **Figure 2.13(b)**, the r^2 value between Landsat-based wetland erosion rate and CubeSat-based erosion rate is 0.72 for the red box and but only 0.19 in the yellow box. The disagreement in the yellow box might be because the shape of the polygon does not cover all the islands in the location.

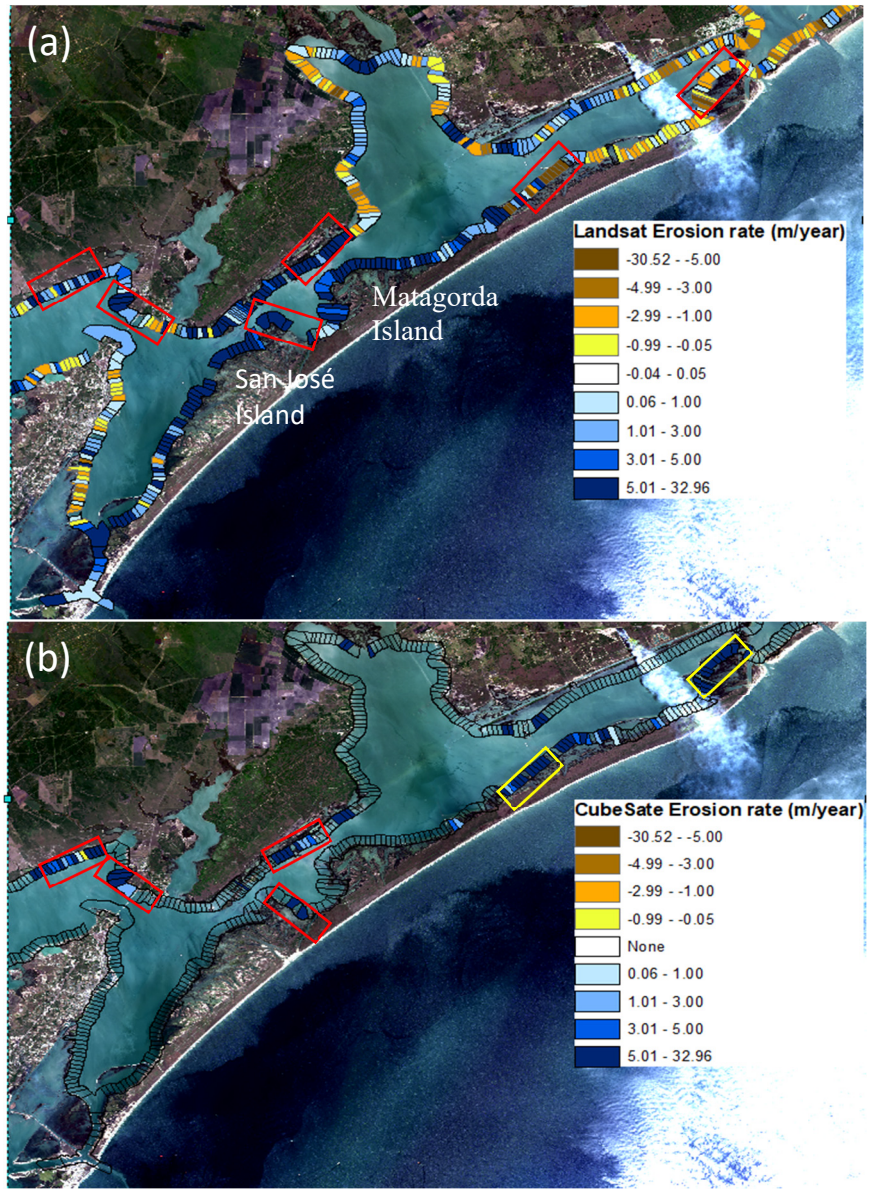

Figure 2.13: The wetland erosion rate in region 2 and region 3: (a) Landsat-based erosion rate from 2009 to 2020, (b) CubeSat-based erosion rate from 2009 to 2021.

2.3.4 Erosion vulnerability analysis

Since areas with EVI values less than 1 are more vulnerable to erosion due to sea level rise, while the land areas with the EVI values higher than 1 are more influenced by sediment accretion, we can see the sediment accretion is insufficient to offset the impact of sea level rise, as the average sediment erosion rate is only about 45% of the average SLR induced erosion rate across the West Galveston Bay from **Figure 2.14**.

Furthermore, the EVI values can be applied for estimating the vertical sediment accretion rate, which is scarce due to the lack of sedimentary measurements. By assuming the sediment accretion rate in the vertical direction is uniform within a given segment, the EVI can also be regarded as the absolute ratio of sediment erosion rate to the SLR induced erosion rate. Therefore, the vertical sediment accretion rate for each segment can be calculated by multiplying the EVI values in **Figure**

2.13 with the rate of sea level rise. To calculate the vertical sediment accretion rate, we have adopted the historic relative sea level rise values reported by Paine et al. (2021), which is 6.8 mm/year from 2009 to 2020. The EVI-based mean sediment accretion rate across the west Galveston Bay (3.08 mm/year) is consistent with the average of the *in-situ* measurements (3.06 mm/year) from Mukaimi et al. (2018). The advantage of this is that it can provide more detailed information about the sedimentary distribution across the region and improve the accuracy of inundation mapping.

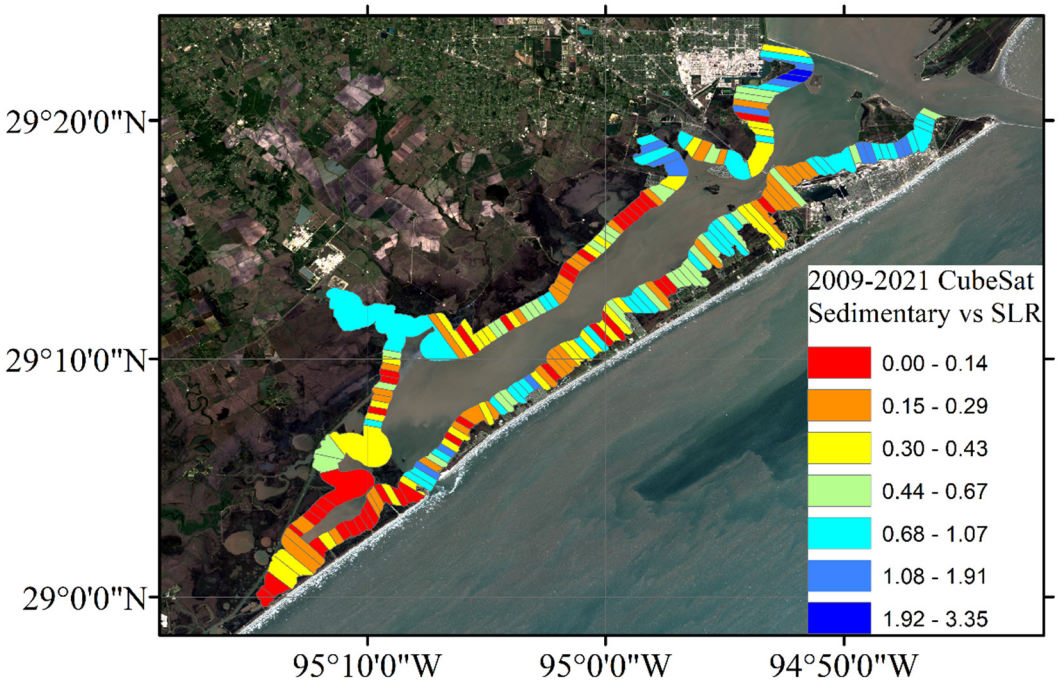

Figure 2.14: The spatial distribution of EVI, which represents the ratio of sediment erosion rate to SLR induced erosion rate

2.3.5 Relationship between wetland evolution and wetland types

The vulnerability of coastal wetland regions is not only influenced by sea level, but also the specific type of wetland (Cahoon, 2006; Sapkota & White, 2020). Vegetation within wetlands has the capacity to stabilize the soil and reduce erosion. In order to gain a better understanding of the erosion rate and its correlation with the wetland type, we conducted an analysis over 9,016 polygons adopted from the National Wetland Inventory within the west Galveston Bays. **Figure 2.15** presents the erosion rate (%/year) distributions observed between 1984 and 2020 from Landsat satellite images. The erosion rate was determined by analyzing the linear trend of wetland area changes relative to the total area in each polygon, with positive rates indicating erosion and negative rates for deposition. The average erosion rate across the domain is approximately 0.16% per year, with Christmas Bay experiencing the highest erosion rates. In contrast, industrialized areas such as Texas International Terminals exhibited slight deposition.

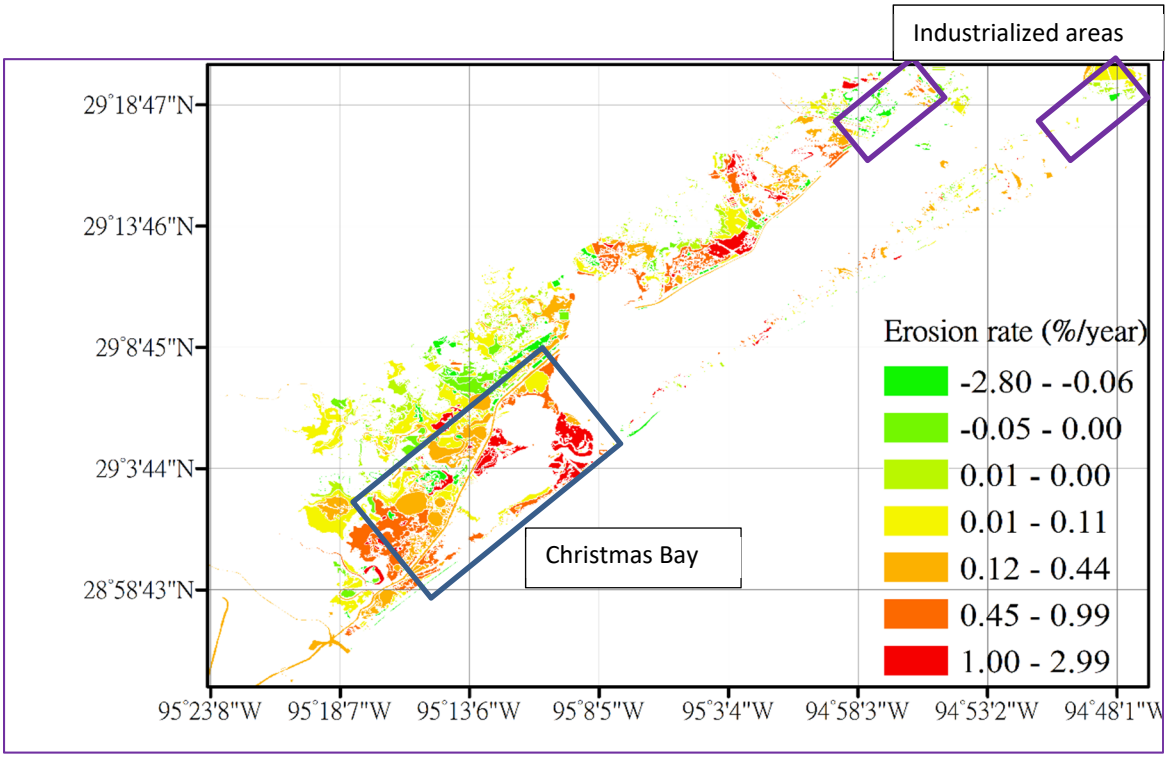

Figure 2.15: The Erosion rate on the West Galveston Bay

Seven types of wetlands are recorded by national wetland inventory in the west Galveston Bay (**Figure 2.16**). These wetland types include Deepwater (6.7%), estuarine wetland (58.3%), emergent wetland (21.0%), forest wetland (1.8%), pond (8.4%), lake (0.6%) and riverine (3.2%) classified by its substrate properties and the hydrologic characteristics. The detailed definition could be found by Wetlands Subcommittee Federal Geographic Data Committee (2013). **Figure 2.17(a)** presents the statistical analysis of the erosion rate, displaying the mean values along with ±1.96 standard deviations (95% confidence interval) for seven different wetland types. The most prominent erosion hotspots are observed in the estuarine and marine Deepwater regions (at 0.45%/year), followed by the estuarine and marine wetlands (at 0.22%/year). No significant erosion is observed in the remaining five types of wetlands. It is worth noting that the standard deviation is relatively high in the Deepwater, estuarine wetland, and lake categories, particularly in estuarine wetlands. This suggests that additional factors, such as sediment flux and wave activity, may contribute to erosion in coastal wetlands beyond the influence of wetland type. The proportion of erosion exceeding 50% of polygons was only observed in the Deepwater region (64%) and estuarine and marine wetlands (51%) as shown in **Figure 2.17(b)**. In other words, the proportion of erosion and deposition is relatively similar. However, positive mean values indicate a predominantly erosional trend and not obvious deposition in the remaining wetland (49%). Therefore, the equilibrium between erosion and deposition in these wetlands may be delicate and susceptible to disruption if the rate of sea level rise were to increase.

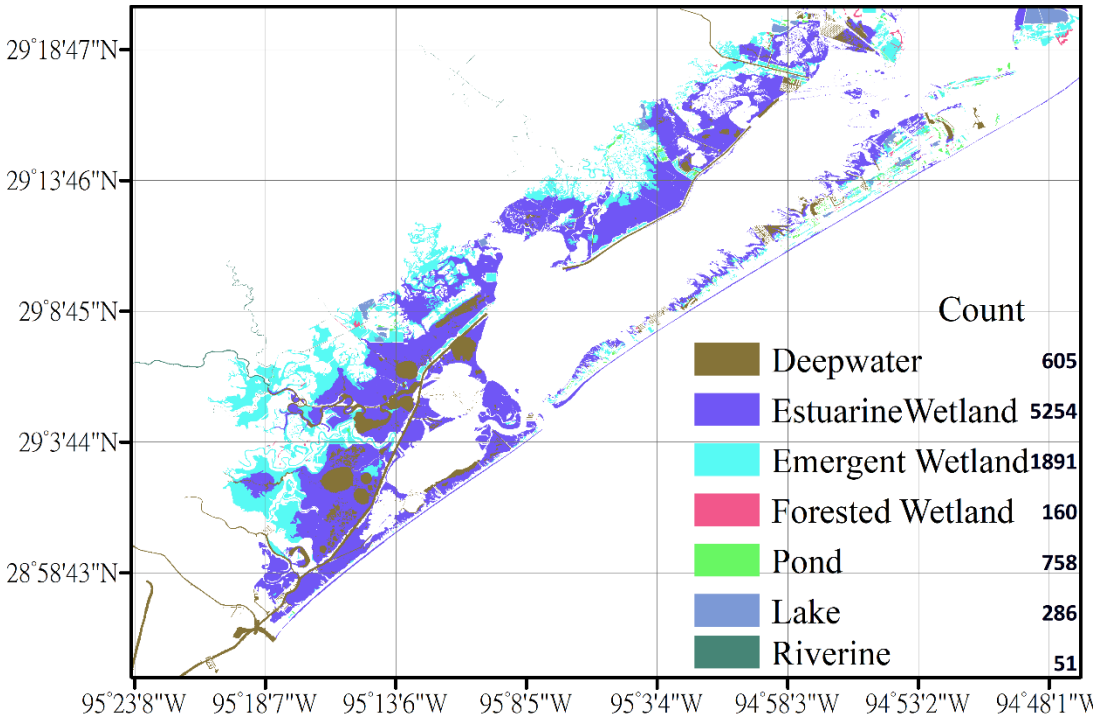

Figure 2.16. The wetland types in west Galveston Bay

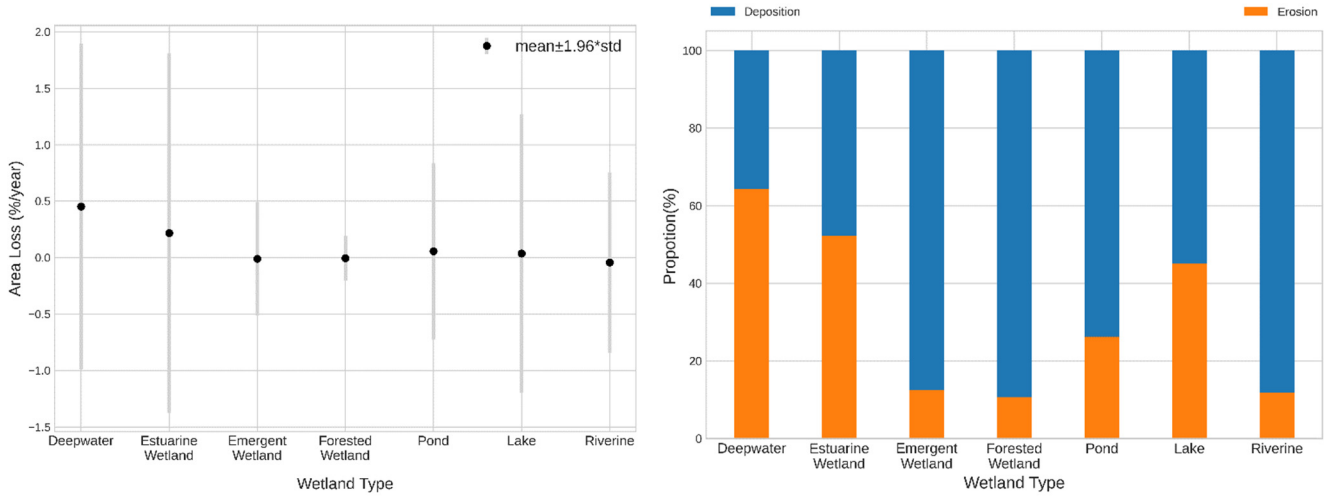

Figure 2.17: (a) Area loss and (b) the proportion of the eroded location in different type of the wetland

2.3.6 Wetland evolution during hurricanes

Furthermore, we conduct evaluations using CubeSat images with high spatial resolution to analyze hurricane impacts on the wetland area by comparing the remotely sensed wetland areas (at the same water level) before and after the hurricanes. Due to the limited availability of images after the hurricanes, we identified 20 pairs and 10 pairs of before and after images for Hurricane Harvey and Hurricane Nicholas, respectively. If more than 70% of the selected pairs in a segment have shown decreased (or increased) wetland area, this segment is defined as erosion (or deposition). Otherwise, it is classified as 'no change'. For both hurricanes, the number of the segments identified as sediment deposition was greater than as erosion, as shown in **Table 2.1** and **Figure 2.18**. The spatial distributions of the hurricane induced changes are similar for these two events in general. However, the percentage of segments identified as erosion during Hurricane Nicholas are slightly larger than Hurricane Harvey. Such erosion caused by Hurricane Nicholas is mainly found at Galveston Island. Additionally, there are more segments not impacted (i.e., no change) during Nicholas than Harvey.

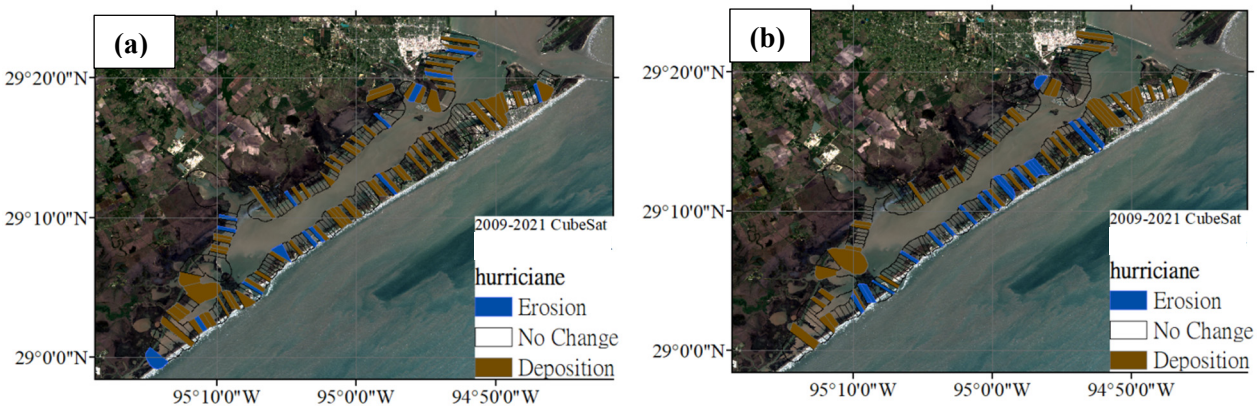

Figure 2.18: The hot spot of Erosion and Deposition during (a) Hurricane Harvey; and (b) Hurricane Nicholas

Table 2.1: The Percentage of segments with erosion and deposition

	Erosion	No Change	Deposition	Erosion/Deposition
Hurricane Harvey	7.5%	61%	31.5%	0.24
Hurricane Nicholas	9%	70%	21%	0.43

2.4 Summary

In Chapter 2, the evolution of wetlands is explored through satellite imagery. Utilizing Landsat imagery, the annual water occurrence maps are generated to estimate the long-term wetland erosion rate from 1984 to 2021. The results reveal that erosion predominantly governs the land cover changes in West Galveston Bay—especially in areas like West Bay, Christmas Bay, and Pelican Island. Within this region, the water area has expanded at a rate of approximately 0.5 km²/year, indicating a corresponding loss of land. Meanwhile, erosion is also noted in Matagorda Bay and Espiritu Santo Bay, but at a reduced rate of 0.28 km²/year. This discrepancy might be attributed to the construction of the Texas City Dike (TCD) and 31 major dammed reservoirs in West Galveston Bay.

Further detailed analysis of wetland evolution at four specific locations is conducted using CubeSat imagery. Since CubeSat satellites can provide images with high spatial and temporal resolution, the impacts of sea level rise and sedimentation on wetland boundaries can be quantified separately. An initial assessment reveals significant erosion between the wetland areas in 2009 and 2021 at the four field sites. The erosion hotspots are notably located on the north side of FS-1 and the island in FS-3, likely caused by wave erosion. This phenomenon is also reflected in the changes to the seabed, observed through the comparison of 0.2-meter imagery from 2017 and 2021. However, slight sediment deposition is observed at FS-4. Despite this, the magnitude of the sediment accumulation is too low to offset the reduction in wetland land area due to rising sea levels, resulting in a net decrease of the wetland areas.

To quantify the changes along the shoreline, we calculate the wetland erosion rate at over 900 locations. This assessment of coastal erosion is validated against the erosion rate from Paine et al. (2021). The two sets of results are in strong agreement, with an r^2 value of 0.78 and a p value of 0.015. According to the Landsat-based data in Region 1, the mean erosion rate is approximately 0.71 m/year. Most wetland areas are undergoing erosion, particularly near Christmas Bay, where rates range from 3 to 15 m/year. This trend is possibly linked to the flat slope in that area. To further understand the hotspots of erosion and deposition, CubeSat imagery is analyzed. The CubeSat-based wetland erosion rate shows a slight increase, as the erosion on the islands can be more accurately observed due to CubeSat's high spatial resolution.

In addition, we utilize high-resolution CubeSat images to analyze sedimentary changes during Hurricane Harvey and Hurricane Nicholas. By comparing the remotely sensed wetland areas at the same water level before and after the hurricanes, the impacts of these extreme events are evaluated. Generally, the spatial distributions of changes induced by the two hurricanes are similar, but the percentage of segments identified as eroded during Hurricane Nicholas is slightly higher than that during Hurricane Harvey. This erosion, specifically attributable to Hurricane Nicholas, is primarily located in Galveston Island. Moreover, there were more segments without impact (i.e., no change) during Nicholas as compared to Harvey, further distinguishing the effects of these two significant weather events.

The knowledge of long-term wetland evolution and the sedimentary change during extreme events is provided in Chapter 2. Understanding long-term wetland evolution is crucial in formulating sustainable coastal development strategies and

implementing effective measures to preserve delicate ecosystems. This represents a significant step toward a more holistic approach to managing and protecting vital coastal areas in the face of ongoing environmental changes. Furthermore, analyzing the sedimentary patterns during extreme events, such as hurricanes, is essential in crafting effective strategies to protect the shoreline. These detailed insights enable a more targeted focus on erosion-prone locations, helping to prevent potential damage in the future.

3 Establish seasonal and eventful short-term Galveston Bay wetland boundary through drone imagery

Long-term and large-scale evolution of wetland boundaries at Galveston Bay were successfully evaluated in the previous chapter through satellite imagery from Landsat and CubeSat. We also identified erosion / accretion hotspots at Galveston wetlands and assessed hurricane-induced sedimentary changes after Hurricane Harvey and Nicholas. However, remotely sensed shoreline changes through satellite imagery still suffers from its limited spatial resolution (e.g., 3-5 m for CubeSat) to provide fine-scale analysis of temporal evolution of wetland boundaries (e.g., sub-meter short-term shoreline movements).

Here, we evaluate the short-term dynamics of wetland evolution in Galveston Bay, focusing on both seasonal variations and hurricane-induced changes in wetland boundaries. We utilize Unmanned Aerial Systems (UAS) as our primary remote sensing platform to comprehensively monitor the geomorphological changes at the four select wetland sites in this report across seven field campaigns from September 2021 to July 2023. The UAS-based short-term monitoring of wetland boundary changes yields centimeter-level ground resolution and thus provides complementary datasets for satellite image-based remote sensing that offers long-term and large-scale analysis of wetland evolution but suffers from limited spatial resolution to fully evaluate the short-term changes.

Data collection methods during these field campaigns are detailed in **Section 3.1**, including the date/locations of field experiments, UAS image capture, and on-site coordinate recording using GNSS receivers. In **Section 3.2**, we elaborate on the post-processing steps applied to the collected data to generate accurate mapping products (i.e., orthomosaic maps) of the survey sites, through three-dimensional reconstruction of the UAS imagery using Structure-from-Motion photogrammetry technique. We also introduce a new georectification method utilizing Particle Image Velocimetry (PIV) technique to enhance the positional accuracy of the mapping product with large coordinate errors. Accuracy assessment of these geospatial mapping techniques and the temporal sequence of the final orthomosaic maps from the field campaigns are then statistically analyzed in **Section 3.3** to evaluate the overall shoreline change dynamics at the field sites based on hurricane event (here, Hurricane Nicholas) and seasonal changes in the wetland environments. Lastly, **Section 3.4** summarizes the results from the statistical analysis of the short-term evolution of Galveston Bay wetland boundaries.

3.1 Data collection

3.1.1 Field campaigns

We selected four field campaign sites (hereafter, FS-1, -2, -3, and -4) within Galveston Bay to monitor seasonal and event-based short-term evolution of Galveston wetlands (see **Figure 2.4** in **Chapter 2**). FS-1, FS-2, and FS-4 are located on the bay side of Galveston Island, and FS-3 is on the bay side of Bolivar Peninsula. The coordinates of each field site in latitude and longitude are listed in **Table 3.1**. We used these coordinates as base coordinates for field campaign transportation.

Table 3.1: Coordinates (latitude, longitude) of the four field sites in Galveston Bay

Field Site	Latitude	Longitude
FS-1	29°14'44.09"N	94°55'39.96"W
FS-2	29°17'5.00"N	94°58'3.95"W
FS-3	29°26'11.58"N	94°42'8.44"W
FS-4	29° 9'10.73"N	95° 2'30.52"W

We conducted the initial field reconnaissance on July 21, 2021. The objectives of the field reconnaissance for UAS mapping were twofold. First, pre-set auto-pilot routes based on available satellite maps needed to be tested due to the time gap between the latest satellite image available. For example, UAS images over regions with significant erosion activity may have large portions of water coverage in the images, which reduces the quality of the mapping products of wetlands. **Figure 3.1(a)** shows a sample UAS auto-pilot route for Route-1 at FS-3. We adjusted the auto-pilot routes on-site to minimize the water occurrence in the UAS images and used these routes for all field campaigns in this project. Second, we needed to locate flat and open areas to safely launch and land UAS and locations to install Ground Control Points (GCPs) to be easily seen in the UAS images. These drone launch locations and fixed GCPs were used for all field campaigns. **Figure 3.1(b)** shows the drone launch from a flat and open ground and recording of GCP coordinates at FS-2. However, some of the GCPs were not available after a few field campaigns since they had been washed away or buried underground due to significant erosion and sedimentation activities.

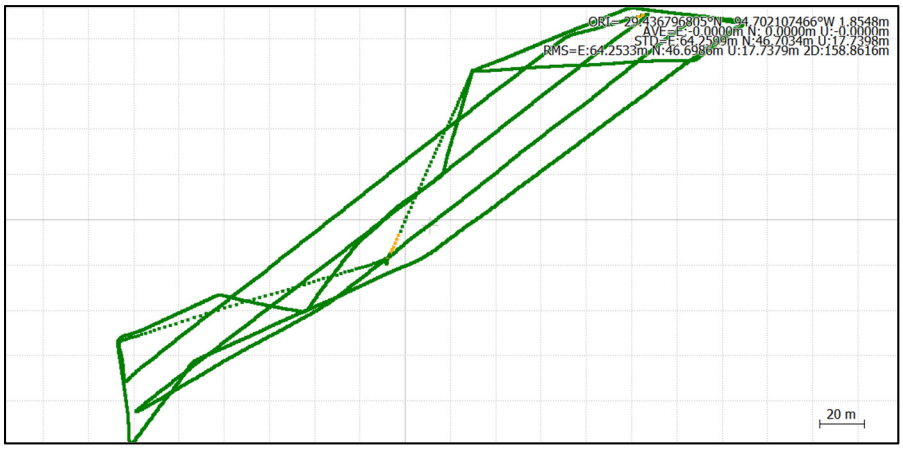

Figure 3.1: (a) A sample UAS auto-pilot route for FS-3 Route-1, (b) Drone launch from a flat and open ground

After the field reconnaissance, we conducted a total of seven field campaigns. Six field campaigns (Campaign 1, 2, 3, 4, 5, and 6) were for seasonal acquisitions of wetland boundary images, and one event was after Hurricane Nicholas (CAT 1 hurricane) in Galveston Bay area in the week of September 13th, 2021. Especially for Campaign 1H (for Hurricane Nicholas), multiple attempts to record UAS images over Galveston wetlands were made due to abrupt weather changes, such as high-speed wind and gusts, heavy rain, etc. **Table 3.2** lists the total number of UAS recordings during the field campaigns.

Table 3.2: The total number of UAS recordings during the field campaigns

Site	Drone Recordings						
	Campaign 1 (8/30 – 9/2/2021)	Campaign 1H (9/22 – 10/6/2021)	Campaign 2 (11/16 – 11/23/2021)	Campaign 3 (3/1 – 3/3/2022)	Campaign 4 (6/15 – 6/17/2022)	Campaign 5 (10/26 – 10/27/2022)	Campaign 6 (7/4 – 7/14/2022)
FS-1	4 (Route 1,2,3,4)	4 (Route 1,2,3,4)	4 (Route 1,2,3,4)	4 (Route 1,2,3,4)	4 (Route 1,2,3,4)	4 (Route 1,2,3,4)	4 (Route 1,2,3,4)
FS-2	2 (Route 1,2)	2 (Route 1,2)	2 (Route 1,2)	2 (Route 1,2)	2 (Route 1,2)	2 (Route 1,2)	2 (Route 1,2)
FS-3	4 (Route 1,2,3,4)	4 (Route 1,2,3,4)	4 (Route 1,2,3,4)	4 (Route 1,2,3,4)	4 (Route 1,2,3,4)	4 (Route 1,2,3,4)	4 (Route 1,2,3,4)
FS-4	5 (Route 1,2,3,4,5)	5 (Route 1,2,3,4,5)	5 (Route 1,2,3,4,5)	5 (Route 1,2,3,4,5)	5 (Route 1,2,3,4,5)	5 (Route 1,2,3,4,5)	5 (Route 1,2,3,4,5)

3.1.2 UAS platform with PPK module

For the field campaigns, we mainly utilized a consumer grade quadcopter, DJI Mavic 2 Pro (hereafter called as M2P), to collect aerial imagery of salt marsh edge of Galveston wetlands. This small form factor UAS platform provides a great advantage to the logistics of the field surveys with minimal space coverage, compared to large hexacopter UAS platforms with meter-scale wingspans and heavier weights. The built-in camera sensor equipped with the M2P comes with 1-inch complementary metal-oxide semiconductor (CMOS) that captures still images with resolution of up to 5472×3648 pixels in 10-bit color-depth (DJI, 2018). With 100% battery charge, the maximum flight time of the M2P with no wind is 31 minutes (DJI, 2018), and this is sufficient for drone surveys that usually take approximately 10 minutes or less.

The PPK georeferencing system incorporated with the M2P is a proprietary on-board dual frequency geodetic L1/L2 GNSS PPK receiver from TOPODRONE with built-in inertial measurement unit (IMU). This dual channel PPK receiver utilizes 184 channels to communicate with GPS, GLONASS, BeiDou, Galileo, and SBAS satellites. The reported accuracy of the PPK module is centimeter-level in x-, y-, z-direction up to 3 cm and is further assessed in **Section 3.3.1**. The logged GNSS data are available in UBX format and require further processing to obtain the actual accurate location data of recorded images.

In early field campaigns (Campaign 1 and Campaign 2), we used another consumer grade quadcopter, Phantom 4 Advanced (hereafter called as P4), to capture images over wetland boundaries. The P4 is a widely used quadcopter among researchers

for its stability during flights and cost-efficiency, providing high-resolution images up to 5472 × 3648 pixels. The P4 system was also equipped with a single-channel PPK module (Emlid Reach M+) for accurate mapping. However, our P4 system showed malfunction in the PPK georeferencing system, yielding up to approximately 1 m error in both x- and y-direction. To compensate this horizontal error in mapping results for Campaign 1 and Campaign 2, we utilized a new georectification method based on particle image velocimetry algorithm (hereafter called as PIV) that corrects the discrepancy of mapping results by linearly translating subsets of the maps using the computed displacement vectors between the image pairs. Details of this method are discussed in **Section 3.2.3**.

3.1.3 Ground control points (GCPs)

We employed a total of 16 ground control points (GCPs) with black and gray checker markers and distributed them across the four field sites. One of the GCPs at each field site was used as the base station for PPK georeferencing, while continuously operating during UAS survey. To record the coordinates of the GCPs, we used GNSS receivers, Emlid REACH RS2 (multi-band) and REACH RS+ (single-band), mounted on a 2 m height prism pole. For the reference base station, the multi-band receiver was used and logged the coordinates at the frequency of 10 Hz for at least 20 minutes for a reliable and fixed solution of the coordinate of the base station. After the completion of UAS surveys over the survey region where GCPs were distributed, the coordinates of the remaining three GCPs were recorded. For the recording of the remaining GCPs, both GNSS receivers were used. The single-band receiver logged the GNSS coordinates at the frequency of 5 Hz and was also operated for at least 20 minutes, similar to the multi-band receiver. The logged raw data were saved in RINEX format. **Figure 3.2** shows a sample GCP with black and gray checker marker and the setup for GNSS RTK receiver on GCP at FS-2.

Figure 3.2: (left) Ground control point, (right) Setup for GNSS RTK receiver on GCP

3.1.4 Flight mission

For the UAS surveys, we used the auto-pilot application, DroneDeploy, to record wetland images along the pre-determined recording routes. The UAS recording path overlapped by 70-80% while flying at the speed of approximately 4 m/s. This was equivalent to 2 – 3 second time intervals between each image recording. The initial sets of images were first recorded at nadir and later sets of images were recorded at varying angles for better 3-D photogrammetric results. The auto-pilot flight plans were designed to have around 10 minutes of UAS flights and to record about 200 – 300 images for each flight.

Overall UAS survey procedure started with installation of base stations over the GCPs, followed by recording their coordinates. Then, we conducted a compass and camera calibration procedure for the drone before UAS aerial surveys, following the manual provided by the manufacturer of the TOPODRONE PPK module. For the camera settings, the parameters for ISO, aperture, and shutter were adaptively determined within the range recommended in the manual depending on the light condition and cloud coverage. After the drone calibration, we recorded the target salt marsh edge using the UAS. After recording images, we returned the UAS to the launch location and replaced batteries after each flight.

3.2 Data processing

3.2.1 GNSS data processing

For the post-processing, we used an open source georeferencing software, called RTKLib (version 2.4.3). We downloaded continuously operating reference stations (CORS) data files from nearby CORS station (TXGA) and used them as the base station for post-processing of the raw GNSS data for the GCPs. The parameters used in RTKLib for PPK post-processing of the

GCP coordinates are listed in **Table 3.3**. Note that the GNSS receivers for GCPs were mounted on 2 m prism poles. Thus, post-processing of the GCP coordinates considered the height of the prism poles, while neglected for post-processing of the reference base station data for UAS PPK. **Table 3.4** lists the coordinates (Lat/Lon/Height) of the GCPs at each site with the two-dimensional root-mean-square error (RMSE) of the GNSS data points for each recording computed by RTKLib.

PPK post-processing of the logged UAS position data is similar to GCP data processing, but it uses the GCP reference base station data as the base station. The physical offset of the PPK antenna from the camera projection of the M2P is 0 m / -0.02 m / 0.07 m in x- (left/right) / y- (forward/backward) / z- (height) direction. The offset parameters were accounted for PPK data processing. To avoid loss of the raw data, we conducted PPK post-processing on cloned copies of the UAS position data. The parameters used for PPK post-processing of the UAS position data are also listed in **Table 3.3**. The post-processed UAS position data were then used to geotag the collected UAS images, using a dedicated plug-in within Adobe Bridge, called Drone Metadata V6.

Table 3.3: Parameters used in PPK data processing for raw GNSS data within RTKLib (Version 2.4.3)

	GCP	UAS
Positioning Mode	Static	Kinematic
Frequencies	L1 + L2	L1 + L2
Elevation Mask (°)	5 – 25 (based on signal)	15
Ionosphere Correction	Broadcast	Broadcast
Troposphere Correction	Saastamoinen	Saastamoinen
Satellite Ephemeris/Clock	Precise	Precise
Rover (Position in m)	Emlid RS+ (0.000 / 0.000 / 2.0865) Emlid RS2 (0.000 / 0.000 / 2.134)	UAS (0.00 / -0.02 / 0.07)
Base Station (Lat/Lon/Height in deg/m)	TXGA CORS station (29.327868325 / -94.772637294 / -9.2980)	Emlid RS2 (29.436513267 / -94.702269199 / -25.9393)
Base Station Antenna (Position in m)	-	(0.000 / 0.000 / 2.134)

3.2.2 Structure-from-Motion (SfM) for UAS aerial images

3.2.2.1 Data processing of Structure-from-Motion

Using the geotagged UAS images after PPK post-processing, we utilized a commercial photogrammetric software, called Agisoft Metashape, to generate digital elevation models (DEMs) and orthomosaic maps. An Open-File Report by U.S. Geological Survey (USGS) (Over et al., 2021) is publicly available as a guideline for processing the UAS images using Structure from Motion (SfM) techniques. We adhered to the guideline from this report, including general SfM processing steps and parameters used for camera optimization and error reduction process. The image input to generate SfM-based orthomosaic maps was the UAS aerial images geotagged with PPK-corrected GNSS coordinates for UAS positions.

The SfM processing began with the image alignment process, where all images collected during the survey flight were used to generate a sparse point cloud where the overlapping features among images are detected. For image sets that were recorded over survey areas with GCPs were installed, the coordinates of the GCPs were inputted to the sparse point cloud and used as the absolute correction point to georeference the SfM products by minimizing the error between the measured coordinates of the GCP center points and the extracted GCP center points during image alignment process. For image sets without any GCP presence, this step was skipped. Then, we further refined the projected sparse cloud by conducting an error reduction process built within the software, including reprojection error, reconstruction uncertainty, and projection accuracy. After this step, the refined model went through the general SfM procedure, which involves the generation of dense point cloud, DEM and orthomosaic maps. For consistency of spatial resolution, the orthomosaic maps are exported in geotiff format with 0.02 m spatial resolution.

3.2.2.2 Accuracy assessment

For accuracy assessment of the georeferencing techniques used in generating SfM-based orthomosaic maps, we compared the center points of GCPs visible in the orthomosaic maps from Campaign 2 to Campaign 6 to the measured coordinates of the GCPs using GNSS receivers. Orthomosaic maps from Campaign 1 to Campaign 1H are excluded in this accuracy assessment because of the known errors in PPK-corrected coordinates of P4 UAS platform.

We compared the accuracy by computing the mean absolute error (MAE) and root mean squared error (RMSE) in xy-direction for the remaining GCPs (GCP-2, -3, and -4) at FS-2 measured during surveys. The error analysis here was conducted, using the following equations:

$$MAE_{xy} = \frac{\sum_{i=1}^{n}\sqrt{\left(x_{i,ortho}-x_{i,GCP}\right)^2+\left(y_{i,ortho}-y_{i,GCP}\right)^2}}{n} \tag{3.1}$$

$$RMSE_{xy} = \sqrt{RMSE_x{}^2 + RMSE_y{}^2} \tag{3.2}$$

where,

$$RMSE_x = \sqrt{\frac{\sum_{i=1}^{n}\left(x_{i,ortho}-x_{i,GCP}\right)^2}{n}} \tag{3.3}$$

$$RMSE_y = \sqrt{\frac{\sum_{i=1}^{n}\left(y_{i,ortho}-y_{i,GCP}\right)^2}{n}} \tag{3.4}$$

Here, $x_{i,GCP}$ and $y_{i,GCP}$ are the longitudinal and latitudinal coordinates of GCP center points, and $x_{i,ortho}$ and $y_{i,ortho}$ are the corresponding coordinates observed in the orthomosaic maps, respectively.

3.2.3 PIV-based georectification

Particle image velocimetry (PIV) is a widely studied displacement/velocity measurement technique that is based on cross-correlation of the particle displacement within a sub-window of an image pair. PIV obtains the average displacement within a sub-window of the image pair by finding their optimum match, which is detected by the intensity peak in the correlation matrix. PIV typically involves the use of passive tracer particles for velocity extraction, but orthomaps generated from UAS aerial images do not contain such particles. In this report, land-mass structures and features of the wetlands will replace the use of tracer particles for UAS-based orthomaps.

3.2.3.1 PIV procedure

In this report, we used an open-source PIV software, PIVlab, for use within MATLAB (Thielicke and Stamhuis, 2014) to compute spatial displacement between an image pair of orthomosaic maps. Image pre-processing is required to improve the chance of extracting valid displacement vectors between an image pair. We first extracted the green channel from the original RGB orthomosaic maps. These grayscale images were inputted into PIVlab and the regions including water within the image were masked off. We also applied contrast histogram equalization (CLAHE) by using a built-in tool within PIVlab that scales every pixel intensity in the range from 0 to 216 grayscale intensity based on the global minimum and maximum values. The displacement vector extraction by PIV consisted of two passes of the PIV analysis involving three moving interrogation windows, or sub-windows, with 50% overlap (Pass 1: 1024x1024 -> 512x512, Pass 2: 512x512 => 256x256) to estimate the most probable displacement in each sub-window between the orthomosaic maps. Spurious, or erroneous PIV displacement vectors would be present in the sub-windows where landmass for cross-correlation is not enough (i.e., water, sandy beach, etc.), or significant loss/gain of land-mass is observed between the time-frame. These outliers were filtered using local median and standard deviation filters and interpolated using the built-in boundary value interpolation method.

3.2.3.2 Georectification

A new georectified orthomosaic map can be generated based on the computed PIV displacement vectors by linearly translating the images within each PIV sub-window by the according PIV vectors. To reduce the computation time, four vectors in 256x256 size sub-windows were averaged to yield one vector in 512x512 size sub-windows (i.e., 16 (column) x 16 (row) vectors in 256x256 size sub-windows were averaged to yield 8 (column) x 8 (row) vectors in 512x512 size). Using a GIS software, we shifted subsets of the orthomosaic image with 512x512 size that contain the PIV displacement vectors in the center. The extent of the linear displacement of the image subsets is equal to the magnitude of the PIV displacement vectors, but the opposite direction should be used to match the reference of frame between the image pair. The final product of PIV correction is represented in **Figure 3.3**. White lines, or gaps, are present in the final orthomosaic map due to the differences in neighboring PIV displacement vectors.

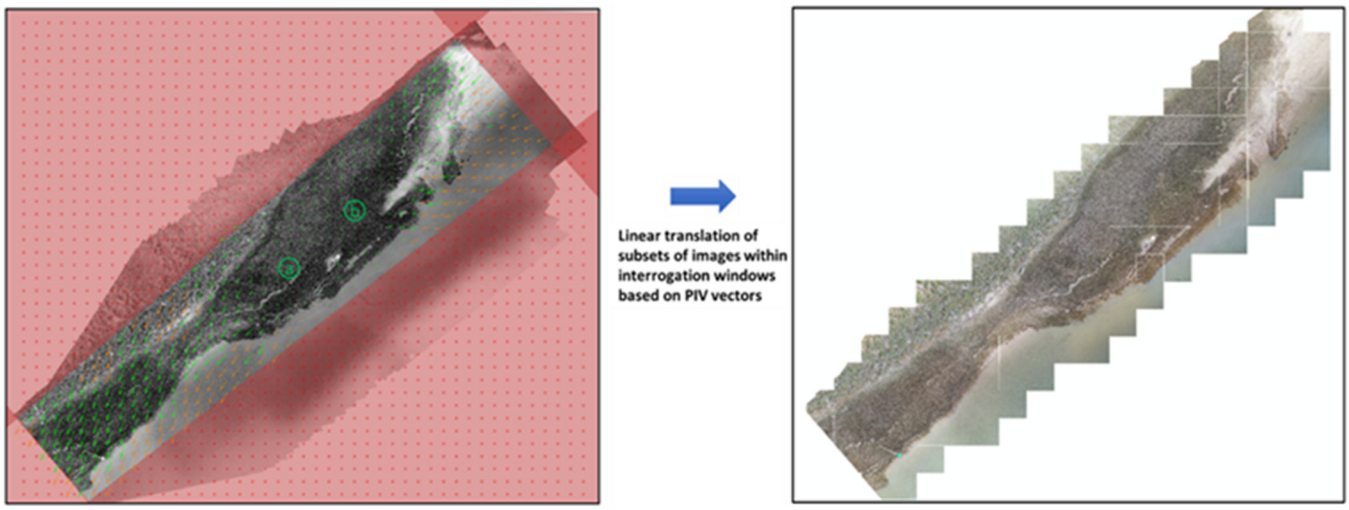

Figure 3.3: Graphical representation of the PIV-based georectification. PIV displacement vectors between orthomosaic image pair. Lettered markers in green colors (a and b) are the locations where GCPs are installed. Green vectors represent the original valid PIV displacement vectors, and orange vectors are the interpolated vectors, which are mostly present near the water and water/sand interface.

3.2.3.3 Accuracy assessment

To evaluate the performance of the PIV-based georectification method, we computed the mean absolute error (MAE) and root-mean-squared-error (RMSE) in xy-direction. Here, we compared the coordinates of fixed, stationary objects between two orthomosaic maps at Route-1 of FS-2 during Campaign 2 and Campaign 3. The fixed objects include GCPs installed on site and natural checkpoints (CPs) (i.e., strongly fixed wood blocks, boats, buckets on the ground). For GCPs, we compared the center points and for natural CPs, we compared the angle edges. Snapshots of fixed objects and their locations across the map are displayed in **Figure 3.4**. A total of 11 natural CPs and 3 GCPs (GCP-2, 3, and 4) were used to assess the precision of the PIV-based georectification method.

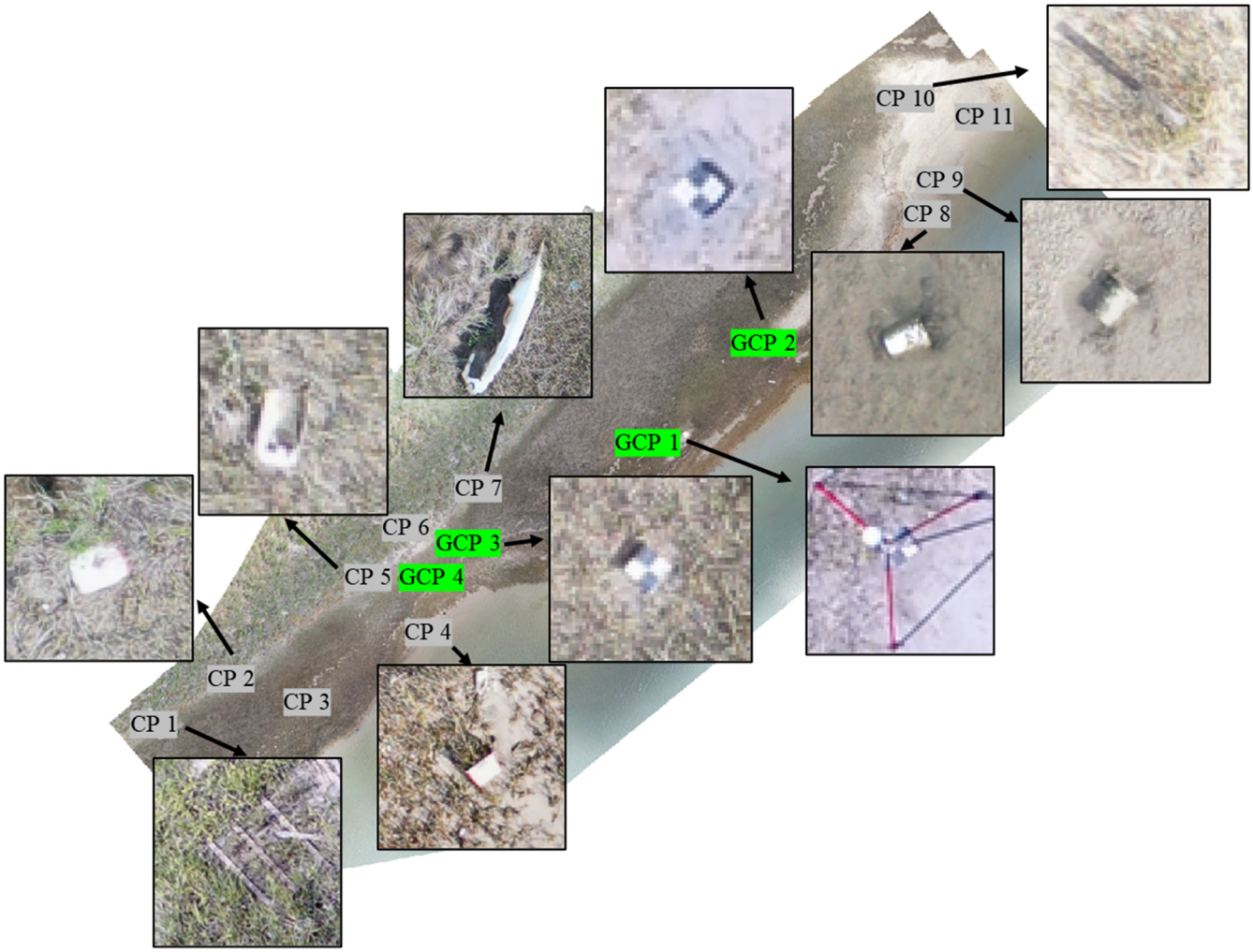

Figure 3.4: Locations and images of the identified stationary natural checkpoints (CPs) and ground control points (GCPs) to analyze accuracy of PIV-based correction method

3.2.4 Shoreline change analysis

In this section, we address the application of the Geographic Information system (GIS)-based tool, known as the Digital Shoreline Analysis System (DSAS). U.S. Geological Survey (USGS) has built a GIS-based tool to compute statistical analysis of erosion/deposition rates using a time-series of vector shoreline positions (Himmelstoss et al. 2018). The DSAS is built to work within Esri Geographic Information System (ArcGIS) software and is publicly available for applications of changes in shorelines (https://code.usgs.gov/cch/dsas). This tool provides a powerful platform for assessing changes in shoreline dynamics by the automated calculation of erosion and accretion rates through the creation of transects. The transects are projected perpendicularly from the shoreline (here, wetland boundary) to the baseline that is user-defined following the general geometry of the wetland boundaries. This allows for the computation of intersection points between the shorelines and transects and subsequent shoreline change analysis. Following the transect computations, DSAS provides the statistical analysis of the shoreline changes in various terms. In this report, we utilize End Point Ratio (EPR), which represents the temporal change of the distance between the initial and final shorelines, and Linear Regression Rate (LRR) that is determined by fitting a least-squares regression line to the intersections of each transect.

We computed the erosion/deposition rate of change in Galveston wetlands utilizing the DSAS for all times-series of SfM-based orthomosaic maps. For Campaign 1 and 1H, we used orthomosaic maps corrected by the PIV-based georectification method due to large errors in GNSS data of UAS positions during surveys. We applied the same pre-processing of the images and the input settings for the PIV analysis as described in Section 3.2.3. For all other field campaigns from Campaign 2 to Campaign 6, we used orthomosaic maps generated using PPK-corrected GNSS data and georeferenced using GCP positions, if available.

We first manually digitized the boundary of each orthomosaic map at the vegetation-water interface using Esri's ArcMap software and defined the baseline following the apparent geometry of the boundaries observed from the set of orthomosaic maps. Parameters used in the DSAS computation varied based on the geometry of the digitized boundaries and the

corresponding baselines. The DSAS settings used for each route of field sites are listed in **Table 3.4**. Then, the shoreline change rates for sequential sets of wetland boundaries (i.e., Campaign 1-to-1H, 1H-to-2, 2-to-3, 3-to-4, 4-to-5, and 5-to-6) were computed in EPR, and the overall shoreline change rate at each field site was determined in EPR and LRR.

Table 3.4: Parameters used in the transect casting procedure for DSAS computation

Parameters	Input Value
Baseline Placement	Onshore
Default Data Uncertainty (m)	1
Intersection Parameter	Seaward Intersection (Landward Intersection where seaward intersection results in false transects due to complex structures)
Maximum Search Distance (m)	7 – 35 (varied by the furthest distance between the baseline and wetland boundaries)
Transect Spacing (m)	1
Smoothing Distance (m)	7 – 15 (varied by the apparent geometry of the wetland boundaries)

3.3 Results

3.3.1 Accuracy assessment of PPK-corrected orthomosaics

To evaluate the accuracy of PPK georeferencing techniques, we picked the center points of the GCPs installed on the available sites during Campaign 2 to 6 using ArcGIS software. The coordinates of these GCP center points were then compared to the measured GCP coordinates. As mentioned in Section 3.1., GNSS recordings of some GCPs were not available due to significant erosion or sedimentation activities. Thus, the coordinates of these GCPs reported in **Table 3.5** are from the latest field campaigns they were available.

Table 3.5: Lat/Lon/Height of the ground control points at each site.

		Latitude	Longitude	Height (Ellipsoidal, m)	2-D RMSE (m)
FS-1	GCP 1-1	29.245599784	-94.927692513	-26.0312	0.0016
	GCP 1-2	29.245636417	-94.927659754	-26.1685	0.0006
	GCP 1-3	29.245466119	-94.927522218	-26.2161	0.0003
	GCP 1-4	29.246233020	-94.927072665	-26.0847	0.0013
FS-2	**GCP 2-1**	29.284921756	-94.967641627	-25.9946	0.0020
	GCP 2-2	29.285124303	-94.967390684	-26.0036	0.0017
	GCP 2-3	29.284726333	-94.968162785	-25.9375	0.0022
	GCP 2-4	29.284642881	-94.968256820	-25.9785	0.0005
FS-3	GCP 3-1	29.436513267	-94.702269199	-25.9393	0.0007
	GCP 3-2	29.436488952	-94.702347905	-25.9256	0.0009
	GCP 3-3	29.436999082	-94.701821980	-25.8529	0.0014
FS-4	**GCP 4-1**	29.152946133	-95.041684360	-25.8766	0.0010
	GCP 4-2	29.152949655	-95.041652974	-25.6835	0.0005
	GCP 4-3	29.152981935	-95.041653983	-25.2026	0.0103
	GCP 4-4	29.152686756	-95.041543919	-26.1486	0.0009
	GCP 4-5	29.152324414	-95.041267994	-26.3662	0.0098

* Bold texts for GCPS represent that GCPs were no longer available during the last field campaign (Campaign 6)

The coordinate difference in latitude and longitude between the measured GCP coordinates and their coordinates visible in the PPK-corrected orthomosaic maps showed a varying range from 0.00 m to 0.10 m. The accuracy calculation of these positional differences resulted in MAE of 0.026 m and RMSE of 0.036 m. This agrees with the reported accuracy of the PPK module (TOPODRONE PPK upgrade kit for Mavic 2 Pro), which is up to 3 cm in x-, y-, and z-direction. This result confirms that PPK-based georeferencing method provides centimeter-level accuracy, and thus is a reliable method to accurately map the survey areas without the need of on-site GCPs, when properly working without malfunctioning.

3.3.2 Accuracy assessment of PIV-based georectification

In some cases, direct georeferencing with PPK may fail to provide centimeter-level accuracy due to mechanical malfunctions,

including out-of-sync between the camera shutter and the actual UAS coordinates at the imaging time, insufficient images, or improper post-processing. The spatial deviation between orthomosaic image pairs can be detected and corrected using the PIV-based georectification method. **Figure 3.3** in **Section 3.2.3.2** represents a resulting PIV vector map computed from an orthomosaic image pair (Compaign 1 and Campaign 3, with 7 months of time gap) showing mismatch between them. Although both orthomosaic maps were generated from PPK-corrected UAS imagery with camera optimization using the known reference GCP coordinates with the deviation of only 0.023 m and 0.032 m during the SfM processing, the alignment between the image pair was only observed in the region near GCP locations, represented as miniscule PIV vectors. However, regions further away from GCP locations show deviations, marked by PIV displacement vectors. These vectors coincided with the observed spatial deviation of natural checkpoints in the orthomosaic maps.

After applying PIV-based georectification to the later time orthomosaic map (Campaign 3), we compared the observed coordinate difference among the natural CPs and GCP-2, as shown in **Figure 3.5**. The MAE of the fixed objects in the maps were reduced from 0.18 m to 0.05 m, equivalent to overall improvement of precision by 72%. Specifically, 80% of the fixed objects initially showed the positional difference ranging from 0.12 m to 0.38 m, but reduced to values below 0.10 m. This demonstrates that PIV-georectification provides additional solutions to correct the positional errors between PPK- and GCP-corrected orthomosaic maps. Also, the improvement in positional difference in the region with higher density of land mass texture was greater than the region closer to water/sand interface. This is an expected result because higher cross correlation would be deducted for the PIV cross-correlation computation in higher land mass texture regions.

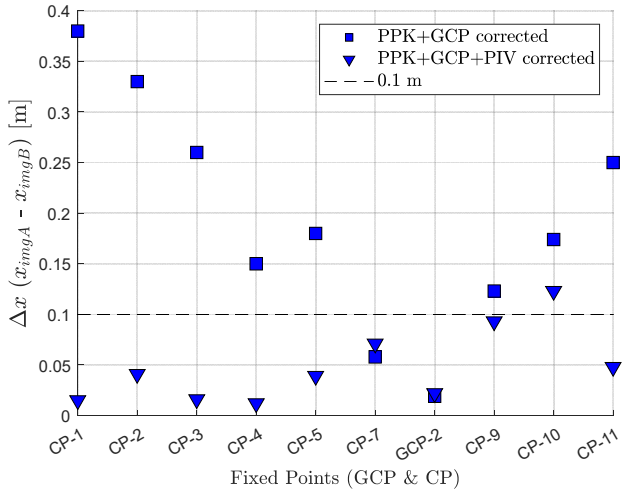

Figure 3.5: Scatter plot of the positional difference between the orthomosaic maps before and after PIV-based georectification.

To further validate the PIV-based georectification method, we assessed the precision of the PIV-based georectification method. **Figure 3.6** shows the comparison plots of coordinate precision before and after PIV-based georectification using four cases of DEM models:

(i) original UAS GNSS data only,
(ii) original UAS GNSS data with PIV-based georectification,
(iii) PPK-corrected UAS GNSS data, and
(iv) PPK-corrected UAS GNSS data with additional PIV-based georectification.

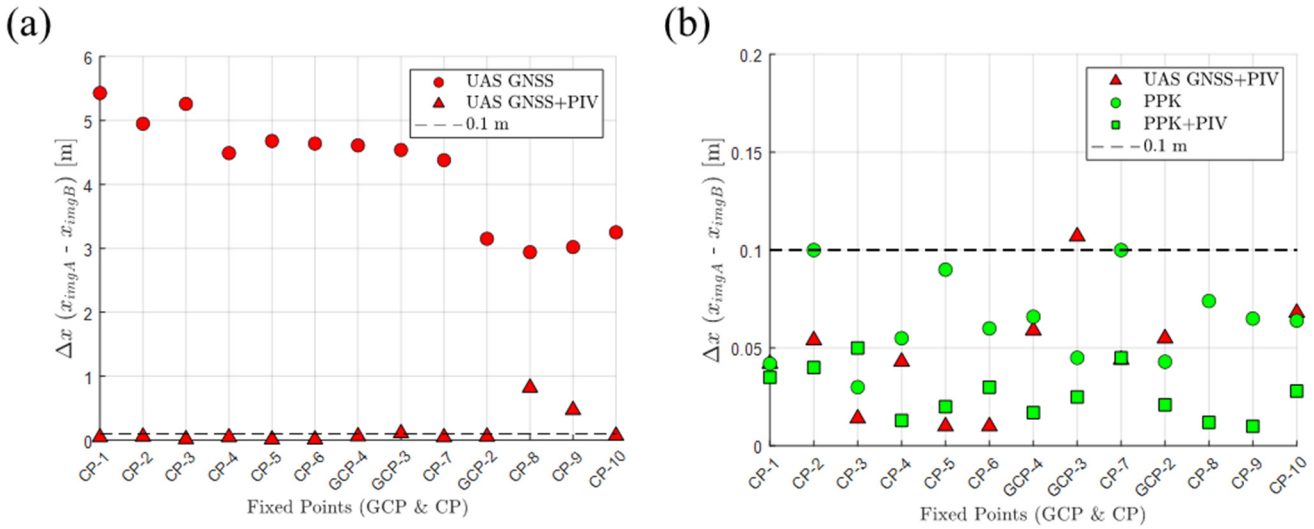

Figure 3.6: Precision assessment of PIV-based georectification using orthomosaic maps generated using (a) built-in UAS-GPS coordinates and (b) PPK-corrected coordinates. The dotted line represents the sub-decimeter level precision between the image pair.

First, we compared the pre-PIV and post-PIV orthomosaic maps to evaluate precision, using UAS-GPS orthomosaic maps, as shown in **Figure 3.6(a)**. Before PIV-georectification, the positional difference of the coordinates between the orthomosaic image pair showed meter-level precision, with the MAE of 4.13 m and the RMSE of 4.22 m. However, the precision was significantly improved after PIV-georectification, showing the MAE of 0.18 m and the RMSE of 0.31 m, equivalent to 96% improvement in precision. Except for CP-8 and CP-9 where the precision level is 0.82 m and 0.47 m, the precision of coordinates after PIV-georectification became sub-decimeter level, with the MAE of 0.046 m and the RMSE of 0.054m. The objects, marked as CP-8 and CP-9, were located in water-filled and sandy regions, where cross-correlation between image pairs is expected to be lower than regions with abundant land mass textures. This may have yielded larger deviation in PIV displacement vector computation, which, in turn, resulted in lower precision than any other GCPs and CPs plotted in **Figure 3.6(a)**.

Precision between the PPK-based orthomosaic image pair before and after PIV-georectification is also tested. **Figure 3.6(b)** shows the relative positional difference between the orthomosaic image pair for PPK-based orthomosaic map before and after the PIV georectification, as well as for UAS-GPS-based orthomosaic map after the PIV georectification for comparison. The positional difference for PPK before PIV georectification is already at centimeter-level with the MAE and RMSE of 0.07m, which was predicted from the prior accuracy assessment. After applying the PIV georectification to the PPK-based orthomosaic maps, 92% of the fixed points showed improvement in precision with the MAE and RMSE of the positional difference reduced from 0.07 m to 0.03m. This is approximately equal to 57% overall improvement in precision. Also, we can see that the UAS-GPS-based orthomosaic map after the PIV-based georectification even shows a similar level of precision with PPK-based orthomosaic maps, especially at the fixed points in the region filled with sufficient land mass textures. This confirms the PIV-based georectification as a valid method to be used for accurate quantification of geomorphological changes at coastal wetlands. Therefore, to reduce positional error of UAS GNSS data using P4 as the main imaging UAS platform, we applied the PIV-based georectification method to the orthomosaic maps for Campaign 1 and 1H using the orthomosaic maps for Campaign 2 as reference (for example, PIV between Campaign 1 and 2, and Campaign 1H and 2).

3.3.3 Marsh edge position

We delineated boundaries of a total of 105 wetland orthomosaic maps (a times series of 7 orthomosaic maps for 15 UAS survey routes) spanning a temporal range from September 2021 to July 2023 in a GIS software. Digitization of the wetland boundaries was performed by selecting multiple points with spatial steps of 0.5 to 1m along the vegetation-water interface of the wetlands. **Figure 3.7** shows sample time-series sets of the wetland boundaries that are overlayed on top of the corresponding orthomosaic maps during the latest campaign (Campaign 6). These curved lines of wetland boundaries are colored in red, orange, yellow, green, blue, purple, and light magenta, following the chronological order of the field campaigns.

Simple qualification of shoreline changes at each survey route can be done by visually interpreting the growth or retreat of these boundaries. The map figures in **Figure 3.7** have varying spatial scales from 20 m to 300m depending on the spatial

coverage of UAS flights during surveys. Significant erosion activity, typically marked by more than several meters of boundary movement, can be easily detected. For instance, **Figure 3.7(a)** (FS-2 Route-1) displays significant changes in wetland boundary positions with increase in time. In contrast, the right-hand part of **Figure 3.7(b)** (FS-2 Route-2) shows minimal changes in wetland boundary movements. This qualitatively shows that the upper part of FS-2 was more susceptible to high magnitude of erosion activity than the lower region of the site. Additionally, boundary movements at wetlands shown in **Figure 3.7(c)** and **(d)** reveal interesting activities occurring at small islands in wetlands. These figures show that the boundaries of the islands deform toward Southeastern direction, with erosion at the head (Northeast) and accretion on the other side (Southeast). Knowing that the incoming wave at this region is to the Southeast, we can qualitatively deduce that the incoming waves are the dominant factors that cause the landward deformation of these islands.

The time series sets of wetland boundaries for each site are available in shapefile format for smooth integration of the wetland boundaries within Coastal Atlas. The wetland boundaries from field campaigns 1 to 6 are projected in NAD 1983 UTM Zone 15N (EPSG: 6344) coordinate system.

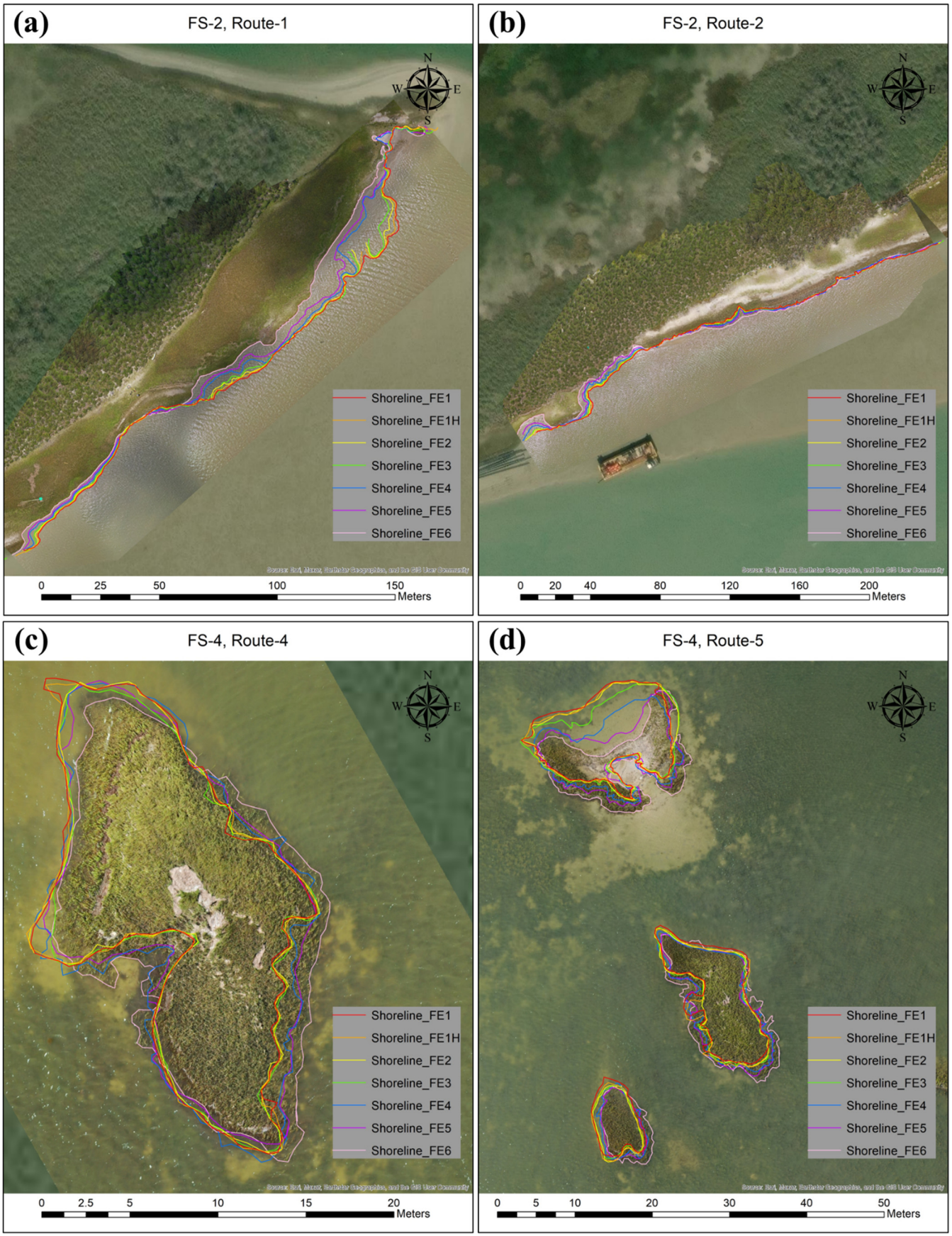

Figure 3.7: Time-series sets of shorelines at each site. Each shoreline represents the interface between wetland vegetation and water. (a) FS-1 Route-2, (b) FS-1 Route-2, (c) FS-1 Route-3, and (d) FS-1 Route-4

3.3.4 Drone image-based wetland evolution

To assess the dynamic changes in wetland boundaries over time, we employed DSAS to analyze the temporal evolution of erosion and accretion rates based on digitized wetland boundaries. We first evaluated individual shoreline change rates between each field campaign. The resulting EPR shoreline change rates for UAS survey routes across each field site are presented in **Table 3.6**. These rates were derived by averaging transect-based shoreline change rates for each route. **Table 3.6** also lists the cumulative EPR and LRR shoreline change rates spanning Campaign 1 to Campaign 6. Here, negative shoreline change rates indicate erosion, while positive values correspond to accretion or the growth of vegetation at the boundary interface. For better visual interpretation, negative rates are depicted in red, and positive values in blue. **Figure 3.8** further shows the computed individual and cumulative shoreline change rates for each route. This figure presents data points with a zero-line reference, such that data points falling below indicating erosion activities (red boxes), and those above representing accretion. The dotted blue and red lines represent the cumulative shoreline change rates from Campaign 1 to Campaign 6 in EPR and LRR, respectively.

Table 3.6: Shoreline change rate in EPR between field campaigns

		Individual						Cumulative	
		Campaign 1 to 1H	Campaign 1H to 2	Campaign 2 to 3	Campaign 3 to 4	Campaign 4 to 5	Campaign 5 to 6	EPR	LRR
FS-1	Route-1	- 0.38	- 0.63	- 0.53	- 1.15	- 0.90	- 0.24	- 0.60	- 0.66
	Route-2	2.02	- 0.92	- 0.56	0.14	- 1.32	- 0.58	- 0.54	- 0.57
	Route-3	- 1.91	- 0.56	- 0.55	0.01	- 1.34	- 1.47	- 0.92	- 0.84
	Route-4	- 0.45	- 1.27	- 0.79	- 1.43	- 1.28	- 1.70	- 1.37	- 1.39
FS-2	Route-1	- 3.19	- 2.67	- 1.00	- 7.53	- 2.49	- 3.08	- 3.42	- 3.53
	Route-2	0.52	- 1.03	- 0.09	- 1.43	- 1.24	- 0.54	- 0.54	- 0.60
FS-3	Route-1	- 1.82	- 1.06	- 1.03	- 0.53	- 0.80	- 1.46	- 1.19	- 1.11
	Route-2	- 0.87	- 1.06	- 0.38	- 0.79	- 0.93	- 0.33	- 0.61	- 0.63
	Route-3	- 0.65	- 1.64	- 0.47	- 1.22	- 0.14	- 0.22	- 0.51	- 0.53
	Route-4	- 12.21	- 4.45	- 3.22	- 2.57	- 4.06	- 5.13	- 4.53	- 4.16
FS-4	Route-1	- 0.57	- 0.63	0.14	0.09	- 0.11	0.00	- 0.07	- 0.04
	Route-2	- 0.02	- 0.98	0.15	0.43	0.07	0.12	0.13	0.18
	Route-3	- 5.54	- 1.02	- 1.75	3.67	- 0.28	0.15	0.04	0.23
	Route-4	0.40	- 0.51	- 0.15	1.62	- 0.35	0.54	0.32	0.34
	Route-5	- 1.10	- 0.70	- 0.58	- 0.69	- 0.84	0.34	- 0.31	- 0.38

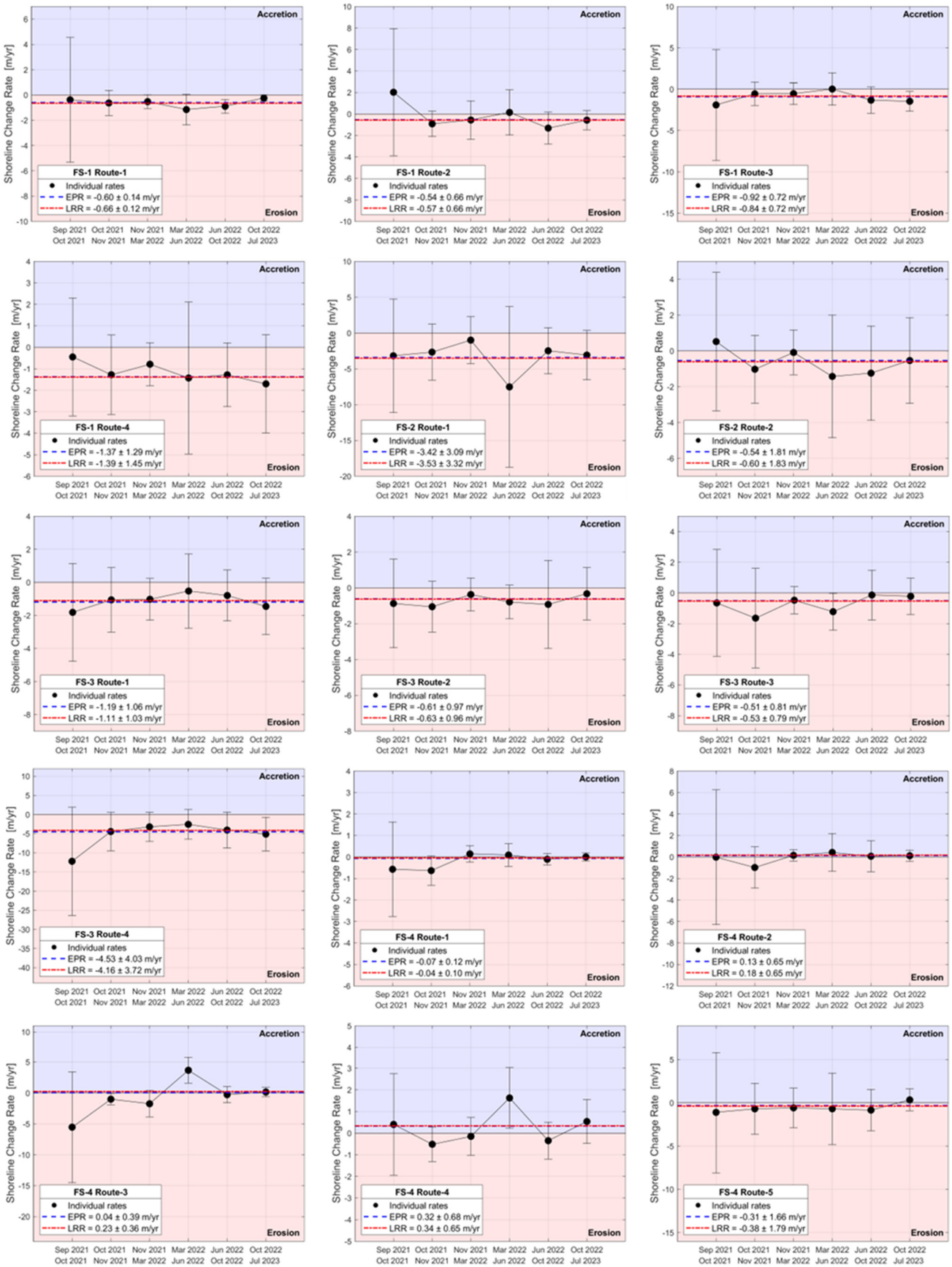

Figure 3.8: Seasonal and event-based (Hurricane Nicholas) shoreline change rates calculated at the field sites. Data points below the zero-line represent erosion activity and within the red-colored box, and those above the zero-line are accretion activity in the blue-colored box. The cumulative shoreline change rates in EPR and LRR at each route are represented as blue- and red-colored dashed lines in red and blue, respectively.

3.3.4.1 Hurricane-induced shoreline change rates

We evaluated the hurricane-induced shoreline change rates between Campaign 1 and Campaign 1H and compared them with other individual and overall shoreline change rates. The first column of the individual shoreline change rates in **Table 3.6** represents the shoreline change rates at each route during Hurricane Nicholas. These rates correspond to the first data points in plots in **Figure 3.8**.

Among the survey routes, a total of 7 out of 15 routes showed the highest magnitudes of shoreline change rates during the hurricane event, either through erosion or accretion. Notably, the erosion activity induced by the hurricane in **Figure 3.9(j)** for FS-3 Route-4 and **(m)** for FS-4 Route-3 was significantly higher when compared to that observed during the preceding field campaigns, showing 8.05 m/year and 5.58 m/year higher in erosion rate than the cumulative shoreline change rates computed in LRR. Overall, the averaged shoreline change rates induced by Hurricane Nicholas mostly showed lesser magnitudes of erosion activity at FS-1 and FS-2 and higher magnitudes of erosion activity at FS-3 and FS-4 than the cumulative shoreline change rates. Specifically, FS-3 and FS-4 experienced 493% elevated erosion activity during Hurricane-Nicholas, whereas 105% decrease in erosion activity on average was observed at FS-1 and FS-2.

Standard deviations of shoreline change rates from Campaign 1 to Campaign 1H in **Figure 3.8** ranges from 2 m/year to 14 m/year with an average rate of approximately 5 m/year and substantially exceeds that of shoreline change rates for other seasonal field campaigns. This phenomenon explains a broader distribution of erosion and accretion activities during the hurricane event, consequently inducing non-uniform shoreline changes along the wetland boundaries. Statistically, 87% of the surveyed routes (13 out 15 routes) exhibit the highest standard deviations in shoreline change rates in comparison to those of other seasonal field campaigns. **Figure 3.8(d)** for FS-1 Route-4 and **(e)** for FS-2 Route-1 only showed higher standard deviations of shoreline change rates between Campaign 3 and 4 than the hurricane event. This high standard deviation of shoreline change rates between Campaign 3 and 4 arose due to the erosion of vegetated periphery of the wetlands, which interfaces with unvegetated terrain or puddles, thereby leading to their exposure at the land-water interface.

3.3.4.2 Seasonal evolution of Galveston wetlands

This subsection aims to assess the impact of seasonal variations on shoreline change rates at the Galveston wetland sites. The analysis involves a comparison of shoreline change rates between Campaign 2 (November 2021) and Campaign 6 (July 2023). Among 60 shoreline change rates calculated for the 15 survey routes spanning Campaign 2 to Campaign 6, 77% (46 out of 60) indicated erosion-dominated shoreline changes. FS-1, FS-2, and FS-3 consistently showed erosion activities, with erosion rates ranging from -0.09 m/year to -7.53 m/year. Specifically, wetland areas along Route-1 and Route-4 at FS-1, Route-1 at FS-2, and all four routes at FS-3 demonstrated continuous erosion since Campaign 1. The most substantial erosion rates were observed in Route-1 of FS-2 (-7.53 m/year) and Route-4 of FS-3 (-5.13 m/year), likely influenced by their proximity to ship traffic and Route-4 of FS-3 acting as a barrier island, leading to significant erosion in the direction of incoming waves.

In contrast, 23% (14 out of 60) of the shoreline change rates demonstrated accretion-dominated patterns, with a majority (86%) of accretion activities concentrated at FS-4. The slight accretion activity at FS-4 was primarily attributed to the gradual slope and shallow water depth along wetland boundaries, allowing seaward growth of vegetation. Additionally, wetland areas at the interface with the water at FS-4 largely consist of small islands. In these areas, we observed simultaneous landward retreat at the boundary interface and landward accretion on the other side, compensating erosion activities along the boundaries.

Shoreline changes during different seasons and their corresponding effects on erosion and accretion rates are explored. Here, we focus on the changes in the shoreline change rates between the field campaigns (i.e., change in EPR between Campaign 2-to-3 and Campaign 3-to-4, and so on). Positive changes in shoreline change rates correspond to decrease in erosion rate or increase in accretion rate, and negative changes represent increase in erosion rate or decrease in accretion rate.

The study period encompasses different seasons, each characterized by unique environmental conditions. To understand the specific influences of these seasons, the data analysis is divided as follows:

a) Winter 2021 (Campaign 2-to-3)
   During this period, shoreline change rates using EPR exhibited decreased erosion activities in 93% (14 out of 15) of the survey routes from the preceding field campaigns (late September to November 2021). This decrease in erosion activities during the winter can be attributed to the elevated level of erosion rates during the preceding field campaigns, marked by increased erosion possibly due to multiple cold fronts and high winds/gusts. Thus, the erosion rates during

the winter of 2021 were observed to be lower than those during the latter part of the fall of 2021.

b) Spring 2022 (Campaign 3-to-4)
In this season, nearly half (7 out of 15) of the survey routes displayed positive changes in shoreline change rates, indicating a reduction in erosion rates. Among these, 6 routes (2 each at FS-1, FS-3, and FS-4) showed consistent reductions in erosion rates from November 2021 through June 2022. Notably, Route-3 at FS-4 exhibited a significant positive change, transitioning from erosion (-1.75 m/year) to accretion (+3.67 m/year) due to the revival of vegetation that had withered during the winter.

c) Summer and first half of Fall 2022 (Campaign 4-to-5)
During this phase, most survey sites experienced erosion-dominated wetland evolution. Of the 15 survey routes, 14 displayed erosion-dominated shoreline changes, with varying levels of erosion activity. FS-2 exhibited the highest erosion rate (average: -1.87 m/year), while FS-4 displayed the lowest erosion rate (average: -0.30 m/year). A comparison with the previous period (Campaign 3 to 4) revealed that 89% (8 out of 9) of survey routes at FS-3 and FS-4 witnessed an increase in the magnitudes of erosion rates.

d) Second half of Fall 2022 to early Summer 2023 (Campaign 5-to-6)
At FS-4, the trend mentioned above in (c) becomes the opposite during this period. The combined influence of the second half of the fall and winter of 2022, along with spring and early summer of 2023, led to positive changes in shoreline change rates. This shift was mostly attributed to the re-growth of vegetation on the wetland edge with gradual slopes during the spring and summer. The positive changes observed in shoreline change rates at FS-4 from fall 2022 to summer 2023 therefore indicate that the increased erosion rate measured during Campaign 5 (June 2022 to October 2022) was primarily triggered by abrupt weather changes in late September and October 2022, such as cold fronts and thunderstorms.

3.3.4.3 Overall erosion and accretion patterns

Lastly, we analyzed the cumulative shoreline changes at the field sites. The visual representation of the overall shoreline change rates overlayed on the orthomosaic maps from Campaign 6 is depicted in **Figure 3.9**. In the figure, accretion and erosion are color-coded with blue and red transects, respectively. The distribution of colors across **Figure 3.9(a)**, **(b)**, and **(c)** predominantly show red colors, signifying erosion-dominated activities in the corresponding survey regions. For these sites, the average cumulative shoreline change rates from Campaign 1 to Campaign 6 were calculated as -0.87 m/year (FS-1), -2.01 m/year (FS-2), and -1.61 m/year (FS-3).

In contrast, FS-4 exhibits a more widespread distribution of accretion activity along the wetland boundary, with sparse areas with erosion activity primarily observed around small islands. The mean overall shoreline change at FS-4 was determined to be +0.02 m/year, which is a magnitude significantly smaller than that observed at the other field sites. This discrepancy may stem from the distinctive site characteristics of FS-4, characterized by the ease of vegetation re-growth due to the gradual boundary slope and the presence of small islands facilitating both landward retreat and deposition.

Prominent erosion hotspots, indicated by bold red transects, correspond to areas with shoreline change rates in LRR exceeding -3 m/year. These erosion hotspots are scattered along the wetland boundaries and tend to prevail in regions with protruding geometry, which undergoes a transition towards flatter or smoother boundaries. For instance, in **Figure 3.9(b)**, the outer sections of the transects correspond to the wetland boundary during Campaign 1, while the inner sections represent the wetland boundary during Campaign 6. A distinct pattern emerges, demonstrating that the wetland boundaries in erosion hotspots transform from protruding geometry in Campaign 1 to smoother boundaries by Campaign 6. A possible explanation for this phenomenon may be in the vulnerability of protruding wetlands to incoming waves from various directions, making them more susceptible to erosion compared to wetlands with smoother geometry. This observation links geometric features with erosion susceptibility that, in turn, may influence the overall wetland evolution dynamics.

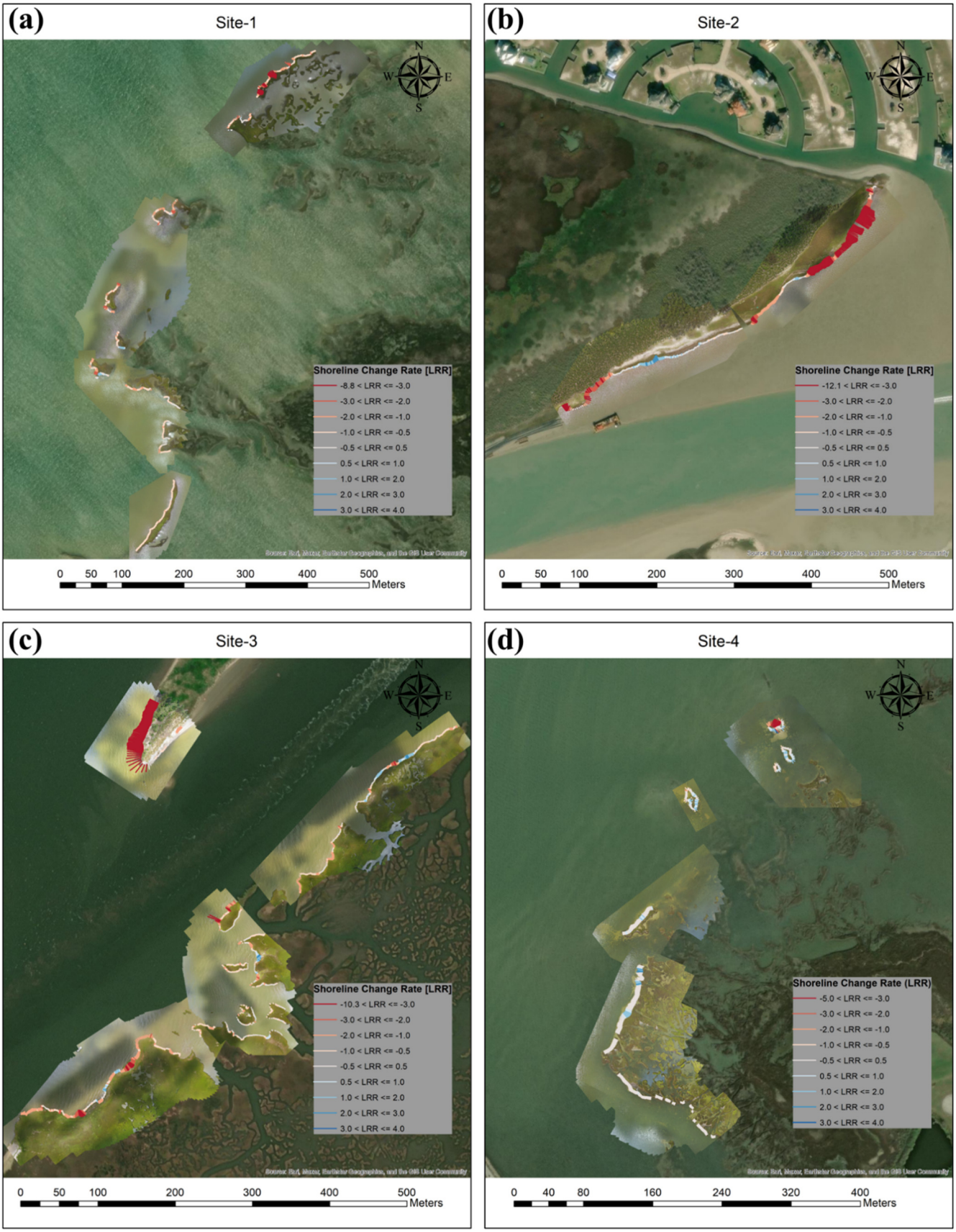

Figure 3.10: Graphical representation of the cumulative shoreline change rates in LRR at (a) FS-1, (b) FS-2, (c) FS-3, and (d) FS-4.

3.4 Summary

In this chapter, we assessed the seasonal and event-based monitoring of Galveston Bay wetland boundaries using Unmanned Aerial System (UAS) imagery. Through the implementation of Structure-from-Motion (SfM) processing of UAS aerial images, accurate digital elevation models (DEMs) and orthomosaic maps were generated using the images geotagged with accurate GNSS coordinates. The SfM-generated products with low positional accuracy were further enhanced using Particle Image Velocimetry (PIV)-based georectification methods. Accuracy assessment for both PPK-corrected orthomosaics and PIV-based georectification method confirmed their reliability in accurate UAS mapping, with PPK-corrected maps showing centimeter-level accuracy and PIV-based method offering substantial improvement in positional precision.

The short-term evolution of wetland boundaries in Galveston Bay was quantified through statistical shoreline change analysis using the Digital Shoreline Analysis System (DSAS). The PPK-corrected orthomosaic maps for four specific locations in Galveston Bay from Campaign 1 (September 2021) to Campaign 6 (July 2023) were utilized to compute the cumulative shoreline change rates at these regions. For the first two campaigns (Campaign 1 and 1H), we used orthomosaic maps further corrected using the PIV-based georectification method to achieve sub-decimeter level accuracy. The shoreline change rates were computed using the End Point Ratio (EPR) and Linear Regression Rate (LRR) metrics.

We assessed the impacts of extreme events on the shoreline change dynamics by quantifying the shoreline change rates at four select locations in Galveston Bay from Campaign 1 (September 2021) to Campaign 1H (October 2021) during which Hurricane Nicholas was prevalent. We used PPK-corrected orthomosaic maps during this time frame that were further corrected using the PIV-based georectification method to achieve sub-decimeter level accuracy. The impacts of Hurricane Nicholas on shoreline change rates were evident, with 7 out of 15 routes experiencing the highest magnitude erosion or accretion activities during the hurricane event. In comparison with the cumulative shoreline change rates, hurricane-induced erosion activity was prominent at FS-3 and FS-4 with 493% elevated erosion rates on average, while FS-1 and FS-2 showed a decrease in erosion activity by 105%, highlighting the susceptibility of FS-3 and FS-4 to extreme events. In addition, non-uniform shoreline changes along the wetland boundaries were observed at 87% of the sites, showing the most occurrence of erosion and accretion hotspots during Hurricane Nicholas.

The seasonal evolution of Galveston wetland sites was also investigated by computing the shoreline change rates from the sequential field campaigns starting from Campaign 2. Consistent erosion-dominated patterns with a range from -0.09 m/year to -7.53 m/year were observed at FS-1, FS-2, and FS-3 during all seasons, while FS-4 showed accretion-dominated shoreline changes due to seaward growth of vegetation. Detailed analyses of individual seasons demonstrated varying rates of shoreline changes. Wetland erosion was observed to peak during the second half of the fall due to abrupt weather changes, marked by elevated activities of cold fronts and thunderstorms, and gradually subsided during the winter 2021 at most of the sites. Erosion activity continued to decline at approximately half of the field locations during the spring 2022, mostly prominent at FS-4 due to the easiness of seaward growth for vegetation due to the mild slope and shallow water depth along the wetland boundary. During the combined period of the summer and first half of fall in 2022, the trend became the opposite to that of the spring, showing decreased magnitudes of erosion activity at more than half of the survey locations at FS-1, 2, and 3 combined, but elevated erosion activity only at FS-4. The increase in erosion rate at FS-4 during this period may be due to easiness of landward retreat of vegetation during abrupt weather changes toward the end of the first half of the fall 2022 (September 1 – October 25). Approaching the summer 2023, the erosion rate subsidizes again at 60% of the survey sites, specifically at FS-4 with 0.23 m/year of accretion during this period.

Lastly, we explored the overall erosion and accretion patterns to understand the complexity of wetland dynamics at the four field sites. The average temporal evolution at survey routes of each site was computed to be -0.87 m/year (FS-1), -2.01 m/year (FS-2), -1.61 m/year (FS-3), and +0.07 m/year (FS-4). This result reveals that the temporal evolution of Galveston wetlands shows erosion-dominated pattern, with an exception at FS-4 where small magnitudes of widespread accretion activities are present due to its favorable environmental and topographical conditions for vegetation regrowth. Erosion hotspots, characterized by high negative shoreline change rates, also highlighted the role of geometric features of wetland boundaries in influencing erosion susceptibility, such that protruded part of wetland may be more vulnerable to wave-driven erosion.

4 *In-Situ* Seasonal and Eventful Hydrodynamic Measurements in Galveston Bay

To better understand the forcing conditions driving changes near the wetland edges and in support of long-term (and short-term) modeling efforts, seasonal hydrodynamic field measurements were conducted simultaneously with UAS surveys at the Galveston Bay wetland sites, following a detailed deployment plan. Data were collected via multiple acoustic and optical instruments mounted in approximately 0.8 m water depth near wetland edges. The focus is on measured free-surface fluctuations at three field sites using pressure transducers (PT). These data are incorporated in model validation and forecasting of short-term wetland boundary evolution using Delft3D (see **Chapter 5**).

The measured hydrodynamic data captured one hurricane event (Hurricane Nicholas) and prevailing cold fronts throughout the year. At field site 3, located adjacent to the Gulf Intracoastal Waterway (GIW), hydrodynamics associated with ship wake patterns were observed. Wave spectral information (e.g., significant wave height, H_{m0}, and peak period, T_p) were acquired from time series of water surface elevation through time series and spectral analyses.

4.1 Field measurement campaigns

Three field sites for *in-situ* hydrodynamic measurements have been selected (see **Figure 2.4** in **Chapter 2**). They are located within Galveston Bay or Galveston West Bay and are conducive for the proposed field measurements since they contain estuarine wetland edges subject to waves with the potential for active erosion. None of the sites have substantial man-made coastal structures protecting them from wave energy in their immediate vicinity and provide reasonable accessibility via land or water. The three sites cover locations on the bay side of Galveston Island (Field Site 1 and 4) and on the bay side of the Bolivar Peninsula (Field Site 3). All sites can be reached by boat within 1.5 hours from the TAMUG campus.

Field Site 1 is the same field location as discussed by Kim et al. (2020) to make best use of already existing local knowledge and data. FS-3 is situated on the bay side of the Bolivar Peninsula bordering the Gulf Intracoastal Waterway (GIW) at a location where the GIW is unprotected from waves originating from Galveston Bay. A protective spit has been eroding over decades allowing for waves with a large fetch generated during northerly cold fronts to impact the wetland edge. FS-3 is also impacted by ship wakes from passing barges in the GIW. FS-4 is in West Bay near the western end of Galveston Island fronting a salt marsh area.

Four separate hydrodynamic field measurement campaigns were completed, each lasting about two weeks (**Table 4.1**). Individual instrument recording times, durations, as well as data availability varied somewhat within the respective campaign windows due to data storage, battery life, or other measurement limitations. The measuring campaigns covered different seasons throughout the year and include data collected during Hurricane Nicholas (Category 1) which made landfall along the Galveston coastline in September 2021.

Table 4.1: Field measurement campaign dates

Campaign	Date
Campaign 1	8/31/2021 – 9/16/2021 (including Hurricane Nicholas)
Campaign 2	11/16/2021 – 12/7/2021
Campaign 3	3/1/2022 – 3/14/2022
Campaign 4	6/2/2022 – 6/16/2022

4.2 Methods

4.2.1 Instrumentation and deployment

Water level fluctuations were recorded using submerged pressure transducers (PT) at varying distances to the respective wetland edge. Wave spectral information was derived from the recorded data using time series and spectral analysis techniques. Three different types of pressure transducers (PT) were used to record the water level fluctuations during each campaign. At each field site two RBR SoloD and/or RBR SoloD|Wave PT were deployed along a measurement transect approximately perpendicular to the wetland edge. A third PT embedded in an acoustic Doppler velocimeter (ADV; Nortek Vector) or acoustic Doppler current profiler (ADCP, Nortek Aquadopp), depending on the field site, completed the set of three PTs at each site. Bucket tests were conducted on site for each PT to aid in the translation of raw pressure data to actual water level above the sensor.

In-situ instrument deployments for each field site were accomplished using either bottom mounted or goal-post frame mounted instruments. Nortek Aquadopp ADCPs (1 MHz and 2 MHz systems) were attached to aluminum frames looking up through the water column, whereas Nortek Vector ADVs measuring 3D velocity components at a single point in the water column were fixed to downspouts attached to goal-post frames. With the internal pressure transducer, these instruments are

capable of measuring water level and velocity in burst or continuous mode. Extra battery packs and optical backscatter sensors (OBS) were used to measure suspended sediment concentrations at the field sites during the time of hydrodynamic measurements. **Table 4.2** lists details on instrument and data types collected, as well as other settings for each instrument. **Figure 4.1** shows photos of the instrument setups used in the field campaigns.

Table 4.2: Instrument types, settings, and collected data type

Instrument	Number	Sampling frequency	Raw data	Data mode
RBR SoloD PT	2	2Hz	Hydrodynamic pressure (dbar)	Continuous
RBR SoloD PT	2	16Hz	Hydrodynamic pressure (dbar)	Continuous
RBR SoloD|Wave PT	2	16Hz	Hydrodynamic pressure (dbar)	Continuous
Nortek Aquadopp ADCP1 with internal PT	1	2Hz	Velocity components (m/s) at a single point, velocity component profiles and hydrodynamic pressure (dbar)	Burst
Nortek Vector ADV1 with internal PT	1	16Hz	Velocity components (m/s) and hydrodynamic pressure (dbar) at the measuring water depth	Burst
Nortek Vector ADV2 with internal PT	1	16Hz	Velocity components (m/s) and hydrodynamic pressure (dbar) at the measuring water depth	Burst
OBS-3+ turbidity sensor	2	16Hz	Analog input (AI)	Continuous

Figure 4.1: Top row - Aquadopp ADCP / OBS bottom-mounted frame, RBRsolo PT, and OBS-3+ sensor. Bottom row - Norkek Vector ADV and mounting pole.

Figures 4.2 to **4.4** show the instrument deployment layout for the three field sites, respectively, for the example of Campaign 1. The first campaign started on August 31st, 2021. The first set of the in-situ instruments was deployed at FS-4 (farthest site from the University campus) in the morning and the second set was deployed at FS-1 in the afternoon. The last set of

instruments was deployed at FS-3 the next day. Exact instrument coordinates were measured using a real-time kinematic (RTK) GPS system.

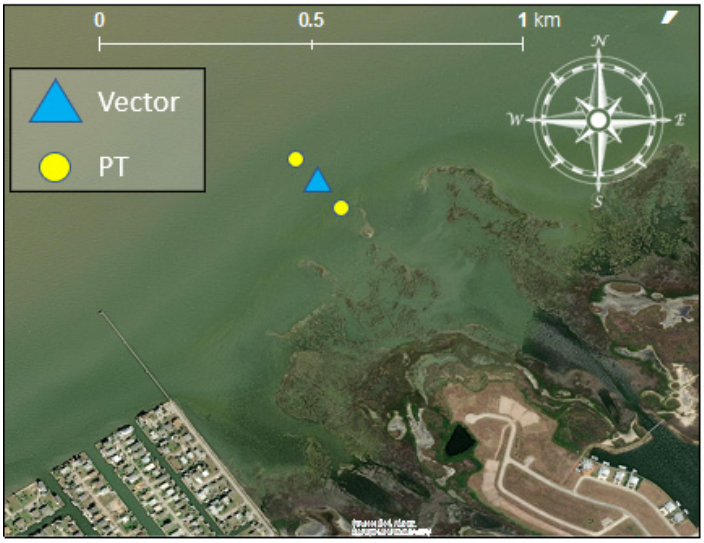

Figure 4.2: Instrument deployment layout at FS-4 (West Bay, Sea grass Lane) during Campaign 1.

At FS-4, one Vector ADV was deployed roughly at 1.2m (4 ft) depth mounted on a goal post frame looking down to record 3D velocities at a single point about 7 cm above the seabed in burst mode (16Hz sampling rate and burst interval of 40 min with 20 min measuring time). The built-in PT recorded hydrodynamic pressures at approximately 0.44 m above the seabed and one OBS was attached 7.5 cm above the pressure sensor to help estimate suspended sediment concentration. Two additional PTs were installed at separate cross-shore positions both on the landward side and seaward side of the Vector ADV to provide a continuous record of water level and wave parameters at 16 Hz sampling rate.

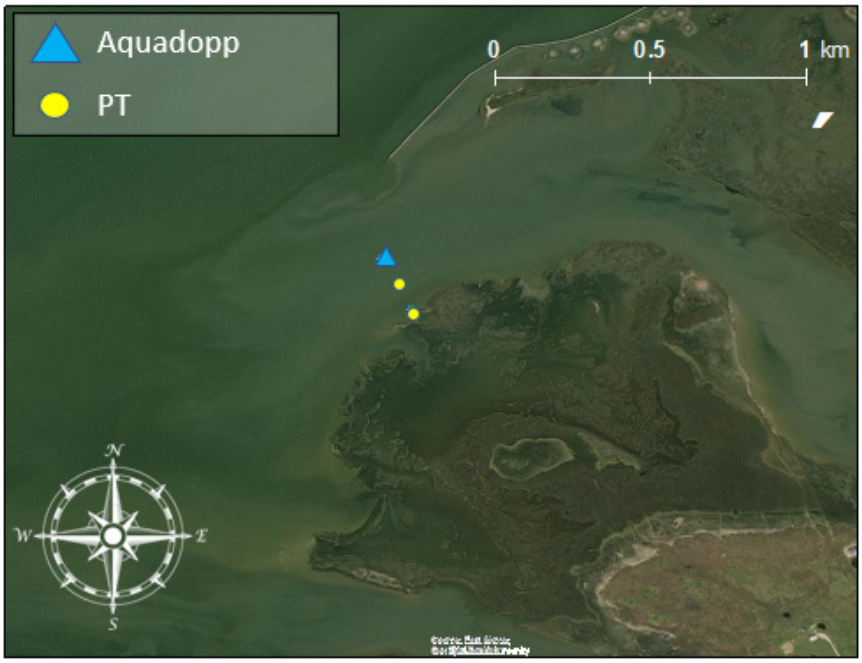

Figure 4.3: Instrument deployment layout at FS-1 (West Bay Galveston Island) during Campaign 1.

At FS-1, one Aquadopp ADCP was bottom-mounted looking up on an aluminum frame seated roughly at 1.2m (4 ft) water depth. The Aquadopp was pre-programmed to record both 3D current profiles and 3D velocities at a single point, respectively, at 1200-second measurement intervals. The current profiles consist of 10-cm vertical extent velocity bins across the 1 m water column starting from 0.32 m above the seabed. The 3D velocity point measurement is made in burst mode taking the average of 2048 samples recorded at 2 Hz roughly in the middle of the water column. The built-in PT recorded hydrodynamic pressures at about 0.27 m above the seabed and one OBS was attached about 0.5 cm above the PT. Similar to FS-4, two additional PTs

were separately installed at two cross-shore positions aligning with the Aquadopp along a profile perpendicular to the wetland shoreline to measure hydrodynamic pressure at 16 Hz and 2 Hz sampling rate, respectively, which can be calibrated to water surface elevation and to obtain wave parameters.

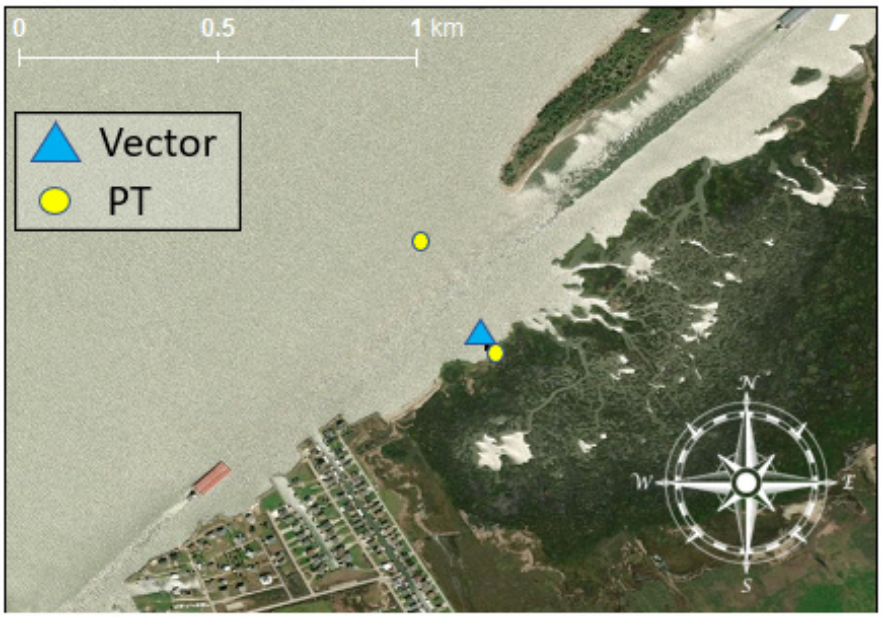

Figure 4.4: Instrument deployment layout at FS-3 (Bolivar Peninsula) during Campaign 1.

At FS-3, one Vector was deployed roughly at 1.5 m (4.8 ft) water depth mounted on a goal post frame looking down to record the 3D velocities at a single point about 0.49 m above the seabed in the same burst mode as FS-4. The built-in PT recorded hydrodynamic pressure at 0.88 m above the seabed. Two PTs were installed at separate cross-shore positions to provide a continuous record of water level and wave parameters on the landward and seaward side of the ADV Vector at 16 Hz and 2 Hz sampling rate, respectively. At this site, the 2 Hz PT was installed farther offshore to measure wave energy dissipation across the Gulf Intracoastal Waterway running parallel to the FS-3 wetland edge, as shown in **Figure 4.4.**

The in-situ hydrodynamic instruments were retrieved from the respective study sites on September 16th, 2021, two weeks after deployment started on August 31st, 2021. Each campaign used similar instrument setups and positions at each field site. However, small variations in setup were made to adjust to varying site conditions or instrument availability. **Table 4.3** lists all instrument coordinates, approximate sensor water depths of deployment, and sensor elevations above the bed for each campaign and each field site. Sampling frequencies for each instrument are also provided. All raw data were subject to rigorous quality control and post processing procedures to eliminate any outliers.

Table 4.3: Instrument coordinates

	Site	Instrument	Lat (Deg.)	Lon (Deg.)	Sensor deployment depth (m)	Sensor elevation above bed (m)	Sampling frequency (Hz)
Campaign 1	FS-1	Aquadopp	29.24655359	-94.92813003	0.90	0.32	2
		PT-1	29.24575581	-94.92779589	0.45	0.03	16
		PT-2	29.24656578	-94.92814672	0.80	0.18	2
	FS-3	Vector	29.43693370	-94.70243906	1.00	0.49	16
		PT-1	29.43679430	-94.70233533	0.50	0.055	16
		PT-2	29.43918584	-94.70378848	0.73	0.25	2
	FS-4	Vector	29.15451061	-95.04323612	1.13	0.07	16
		PT-1	29.15344438	-95.04227121	0.30	0.05	16
		PT-2	29.15396970	-95.04275698	0.48	0.15	16
Campaign 2	FS-1	Aquadopp	29.24737573	-94.92872758	0.72	0.30	2
		PT-1	29.24585142	-94.92762277	0.39	0.04	16
		PT-2	29.24666491	-94.92820349	0.60	0.28	2
	FS-3	Vector	29.43702961	-94.70256183	1.00	0.09	16
		PT-1	29.43679395	-94.70233432	0.41	0.05	16
		PT-2	29.43935683	-94.70395226	0.66	0.25	2
	FS-4	Vector	29.15559583	-95.04419933	0.90	0.12	16
		PT-1	29.15343367	-95.04225951	0.28	0.02	16
		PT-2	29.15396545	-95.04273323	0.42	0.035	16
Campaign 3	FS-1	Aquadopp	29.25083300	-94.93088508	0.72	0.26	2
		PT-1	29.24585153	-94.92762296	0.39	0.08	16
		PT-2	29.24669388	-94.92822057	0.60	0.28	2
	FS-3	Vector	29.43702807	-94.70256388	0.46	0.32	16
		PT-1	29.43679417	-94.70233432	0.50	0.04	16
		PT-2	29.43935688	-94.70395233	0.60	0.10	2
	FS-4	Vector	29.15559475	-95.04419997	0.56	0.43	16
		PT-1	29.15343392	-95.04225951	0.28	0.06	16
		PT-2	29.15396529	-95.04273334	0.42	0.04	16
Campaign 4	FS-1	Aquadopp	29.24938929	-94.93047094	0.80	0.26	2
		PT-1	29.24585150	-94.92762289	0.79	0.05	16
		PT-2	with Aquadopp	with Aquadopp	0.78	0.27	2
	FS-3	Vector	29.43694349	-94.70250896	0.82	0.26	16
		PT-1	29.43679400	-94.70233456	0.76	0.16	16
		PT-2	29.43935704	-94.70395250	0.91	0.30	2
	FS-4	Vector	29.15556670	-95.04424328	0.88	0.30	16
		PT-1	29.15343378	-95.04225946	0.63	0.095	16
		PT-2	29.15396530	-95.04273314	0.80	0.10	16

4.2.2 Data processing

To convert raw pressure data (units of dbar) to actual water level (m) above the pressure transducer, on-site bucket tests were carried out for each PT at both the beginning and the end of each campaign. During a bucked test, the sensor is submerged to a known depth in water collected from the site for up to one minute. The converting factor is calculated as the ratio of the bucket water depth D and the mean of the measured pressure sample during the bucket test. The final result α is estimated by averaging the obtained factor at the beginning α_b and end α_e of the respective campaign (see Equation 1). Converting factors vary somewhat over changing seasons due to changes in water properties, as shown in **Table 4.4**

$$\alpha_b = \left[\frac{D}{\frac{1}{N}\sum_{i=1}^{i=N} p_i}\right]_{\text{begin}} \quad \alpha_e = \left[\frac{D}{\frac{1}{N}\sum_{i=1}^{i=N} p_i}\right]_{\text{end}} \quad \alpha = \frac{\alpha_b + \alpha_e}{2} \tag{4.1}$$

Table 4.4: Factor to convert raw pressure to water level

	Site	Instrument	α		Site	Instrument	α
Campaign 1	FS-1	PT-1	1.0305	Campaign 2	FS-1	PT-1	1.0190
		PT-2	1.0099			PT-2	1.0022
	Fs-3	PT-1	1.0062		Fs-3	PT-1	1.0088
		PT-2	1.0210			PT-2	1.0421
	Fs-4	PT-1	1.0046		Fs-4	PT-1	1.0140
		PT-2	1.0504			PT-2	1.0212
Campaign 3	FS-1	PT-1	1.0550	Campaign 4	FS-1	PT-1	1.0960
		PT-2	1.0370			PT-2	1.0002
	Fs-3	PT-1	1.0690		Fs-3	PT-1	1.0381
		PT-2	1.0203			PT-2	1.0172
	Fs-4	PT-1	1.0024		Fs-4	PT-1	1.0287
		PT-2	1.0053			PT-2	1.0036

OBS sensors utilize a low-energy laser light source and optical sensor to detect diffuse reflected light from the water in a control volume close to the sensor. Calibration of the OBS sensor outputs was conducted in the laboratory using a bucket and turbulence generator setup (**Figure 4.5**). Sediment samples collected at each field site were dried and then added to a known volume of turbulent water in incremental quantities to relate the analog data from the OBS sensor to suspended sediment concentration (SSC). As expected, these tests revealed good-fit linear calibration curves between analog OBS measurements and SSC.

Figure 4.5: OBS calibration setup: OBS sensor submerged in turbulence chamber (left), power stirring device to generate turbulence in bucket (center) and incremental dry sediment quantity to be added (right).

The results of linear fit were adopted as the calibration functions for FS-1 and FS-4 (no OBS sensors were deployed at FS-3), as shown in **Figure 4.6**.

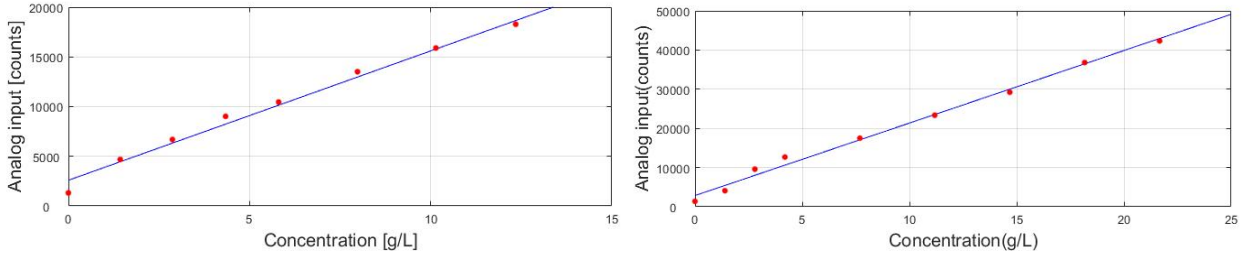

Figure 4.6: Calibration functions for FS-1 (left) and FS-4 (right). The calibration functions are: FS-1 linear fit: C = 0.0027A – 1.5411; and FS-4 linear fit: C = 0.000769A – 1.9972.

All raw data were processed using various techniques to remove outliers. Following *Goring and Nikora (2002)*, a data de-spiking method known as the Phase–Space Threshold (PST) method was employed to detect spikes and effectively eliminate outliers present in the instantaneous velocity measurements from the Aquadopp ADCPs and the Vector ADVs. Such outliers can occur due to entrained bubbles in the water or other obstacles interfering with the acoustic measurements. A flow chart of the PST de-spiking method is displayed in **Figure 4.7.** Measured points falling outside a user-defined characteristic ellipsoid in three-dimensional phase space are designated as spikes (or outliers). Good data clusters a dense cloud in phase space and can be visually inspected as such. For sporadic outliers, once spikes are detected, the outliers are replaced by local mean

values of the signal to avoid gaps (e.g., mean of the burst if the data are in burst mode or mean of 20-min data if in continuous mode). This process was repeated until the standard deviation was below the universal threshold described in *Goring and Nikora (2002)*.

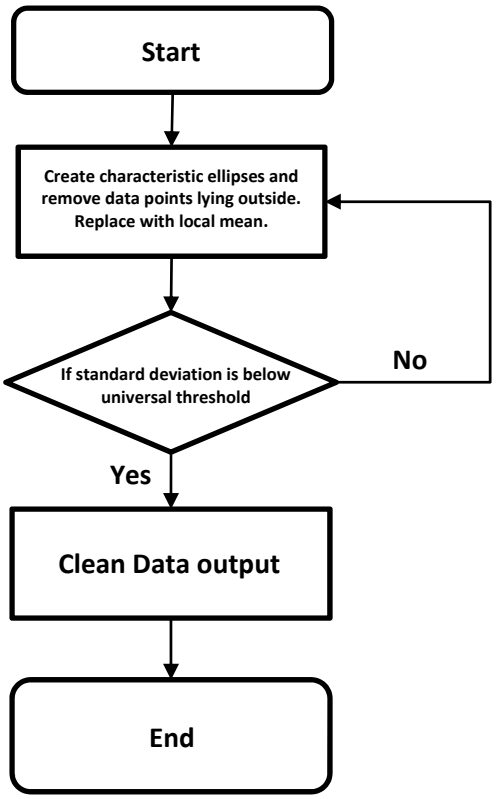

Figure 4.7. Flow chart for PST de-spiking method.

Figure 4.8 shows an example of a velocity component record before and after applying the PST de-spiking procedure to remove outliers.

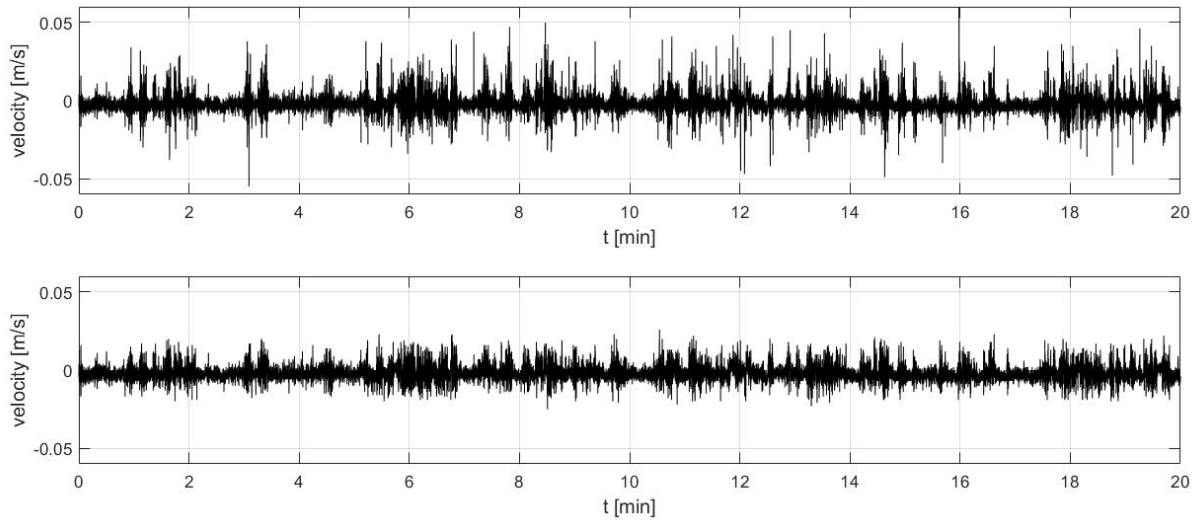

Figure 4.8: PST de-spiking method applied to a velocity time series. Top panel: contaminated 20-min record of up (+)/down (-) velocity components at FS-4 during Campaign 3. Bottom panel: same time series after outliers had been removed using the PST method.

The processed datasets encompass a time series of water surface elevation (a), velocity components (b), and suspended sediment concentration (c) organized as explained in the following. All time series data are stored as ASCII text files or MATLAB matrices accompanied by available metadata.

(a) Water surface elevation (measured by separately mounted PTs)
Column 1 – 7: Date and time (year-month-day, hour-minute-second)
Column 8: De-spiked pressure [dbar]
Column 9: Verified water depth above PT [m]
Column 10: Verified water depth above seabed [m]
(b) Velocity components
Column 1 – 7: Date and time (year-month-day, hour-minute-second)
Column 8: De-spiked east (+)/west (-) velocity component [m/s]
Column 9: De-spiked north (+)/south (-) velocity component [m/s]
Column 10: De-spiked up (-)/down (+) velocity component [m/s]
Column 11: De-spiked pressure measured by build-in PT
(c) Suspended sediment concentration
Column 1 – 7: Date and time (year-month-day, hour-minute-second)
Column 8: Raw analog input [counts]
Column 9: Verified SSC using linear calibration curve [g/L]

4.3 Field data results

4.3.1 Water free surface elevation and significant wave height

All measured time series of water level fluctuations are available as ASCII text files or MATLAB matrices including relevant meta data. At each site, data were recorded by three pressure transducers (PT1, PT2, and the internal PTs of the acoustic Doppler instruments) at high enough sampling frequencies to capture tidal variations, wind waves, and vessel wakes. In the following, water level fluctuations (η) and spectral wave data (H_{m0}) are provided for each field site and each campaign. Spectral significant wave heights are presented as a time series of 20-min averages.

Figure 4.9 shows water level fluctuations and derived spectral significant wave heights H_{m0} at FS-1 for the two RBR PTs deployed at each site. Several time periods of elevated wave activity are apparent, indicating cold front events throughout the year. Note that on September 14, 2021, Hurricane Nicholas made landfall along the Texas coast as a category 1 hurricane. Nicholas affected the Galveston Bay area with tropical-storm-force winds and rainfall from the early morning of September 13th through the end of September 15th. High wave amplitudes and elevated water levels were observed at all sites even though they are sheltered by Galveston Island and the Bolivar Peninsula.

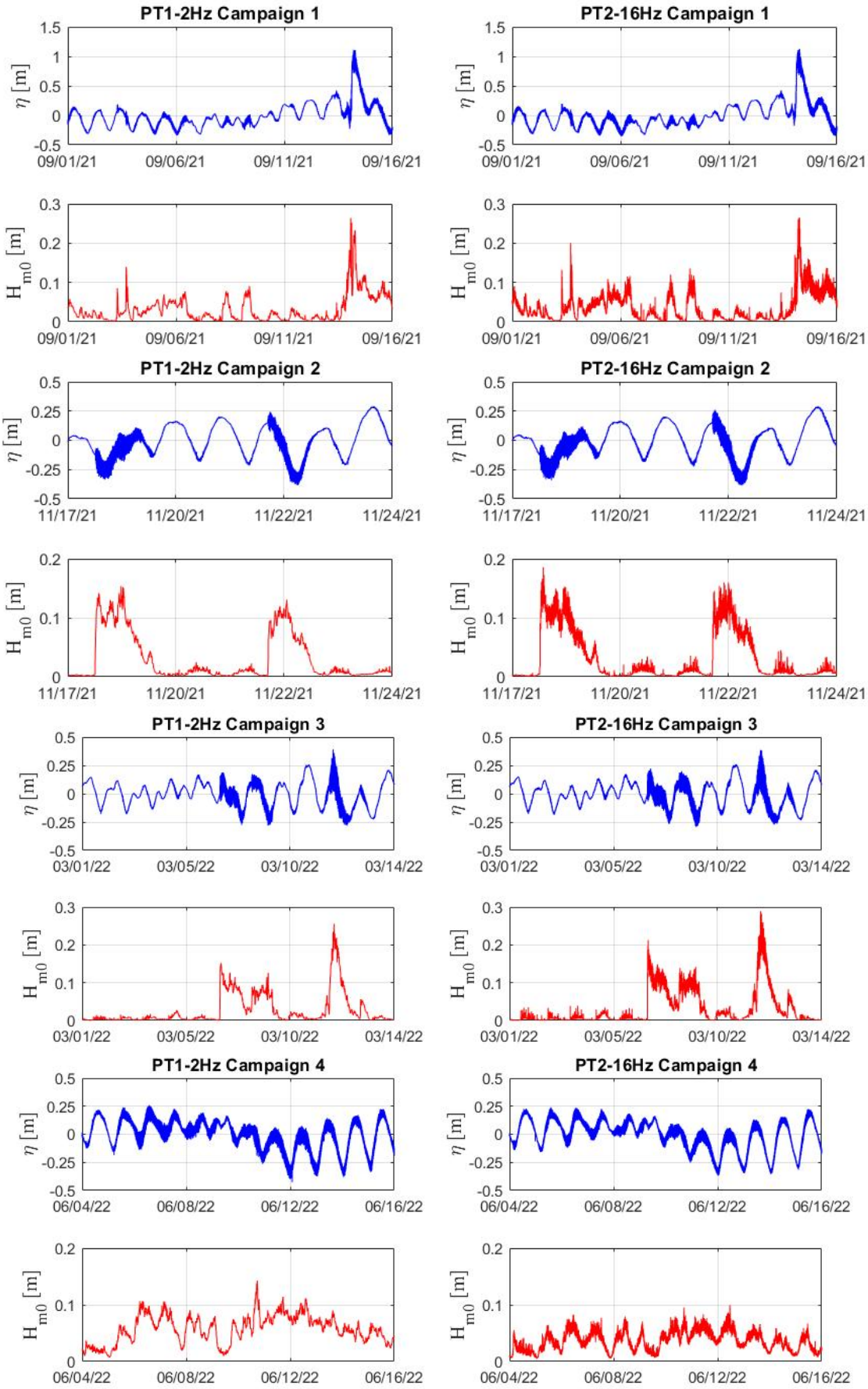

Figure 4.9: Measured water free surface elevations (η) and associated spectral significant wave height (H_{m0}) recorded by PT1 and PT2 at FS-1 for all measurement campaigns.

During the hurricane event (see measured surface elevation from Sep 13th – Sep 15th), the general tidal and storm water fluctuations are prominently displayed. Increased wave activity is visible as wider swaths of higher frequency and larger vertical range of fluctuations compared to calm conditions. The measured water level displays a rise of over 1 meter compared to pre-storm conditions while wave heights approach 0.3 m. During Campaigns 2 and 3 (see **Figure 4.9. rows 3 – 6**) multiple cold front events were captured, each persisting for approximately an entire day. The intensity of the cold front event on Mar 12th is notable as the wave height increases to 0.3 m, surpassing even the wave heights observed during Hurricane Nicholas. This can be attributed to the location of the field sites, which are sheltered from tropical systems by Galveston Island and the Bolivar Peninsula, respectively. Cold fronts feature mostly northerly winds to which all field sites are more exposed. During Campaign 4, the wave heights consistently maintained a relatively high level compared to calm water conditions, primarily due to the prolonged wind effect.

Figure 4.10 shows water level fluctuations and significant wave heights at FS-3. In addition to Hurricane Nicholas and cold front events, visible spikes in the data are signatures of vessel passages with characteristic surge, drawdown, and trailing wake patterns since this field site is directly affected by GIW maritime traffic (see photos in **Figure 4.11**). The zoom-in plots in **Figure 4.12** are visual representations of the ship wake patterns generated by passing barges.

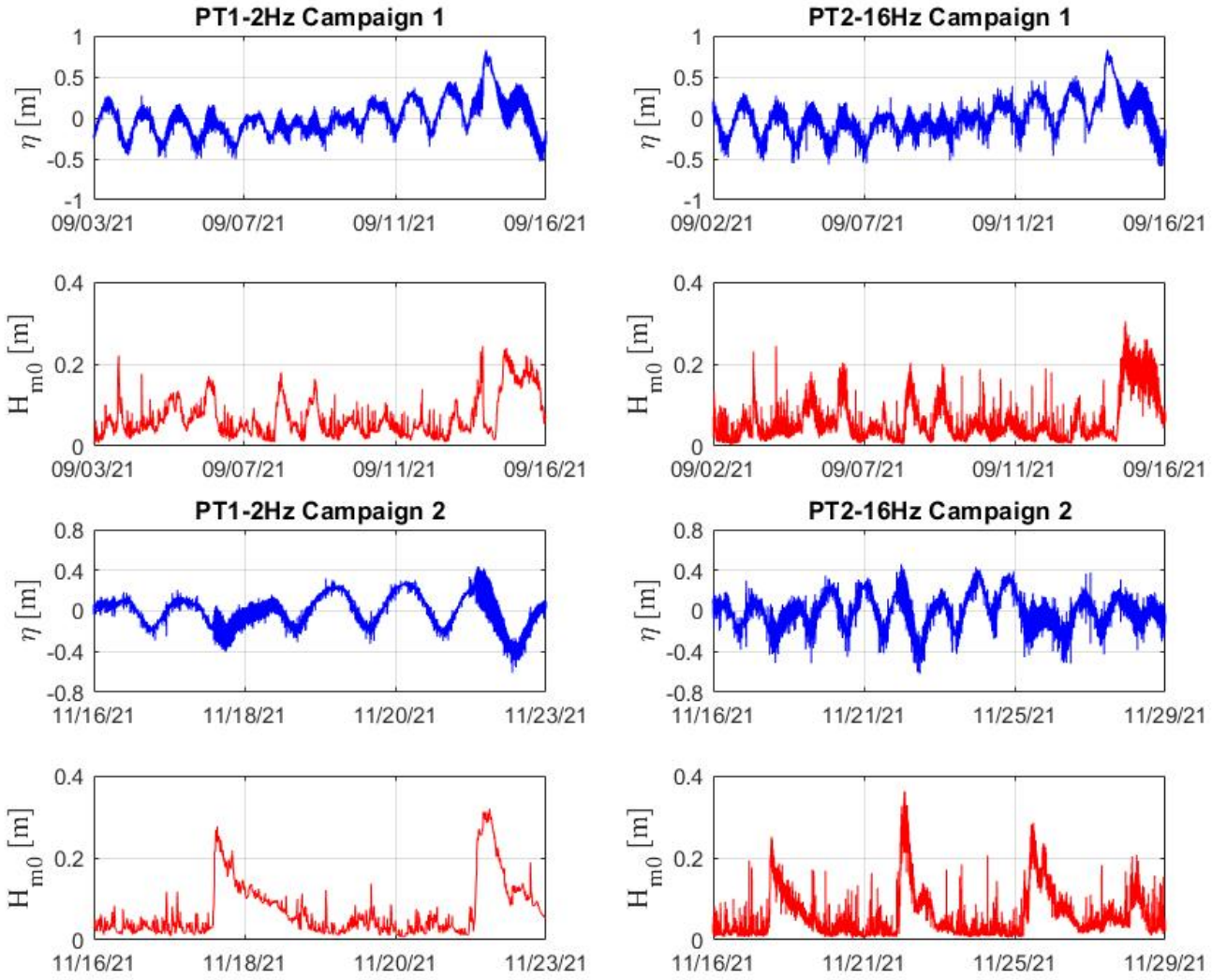

Figure 4.10: Measured water free surface elevations (η) and associated spectral significant wave height (H_{m0}) recorded by PT1 and PT2 at FS-3 for all measurement campaigns. Pink rectangle highlights the measured ship wake pattern shown in Figure 4.11

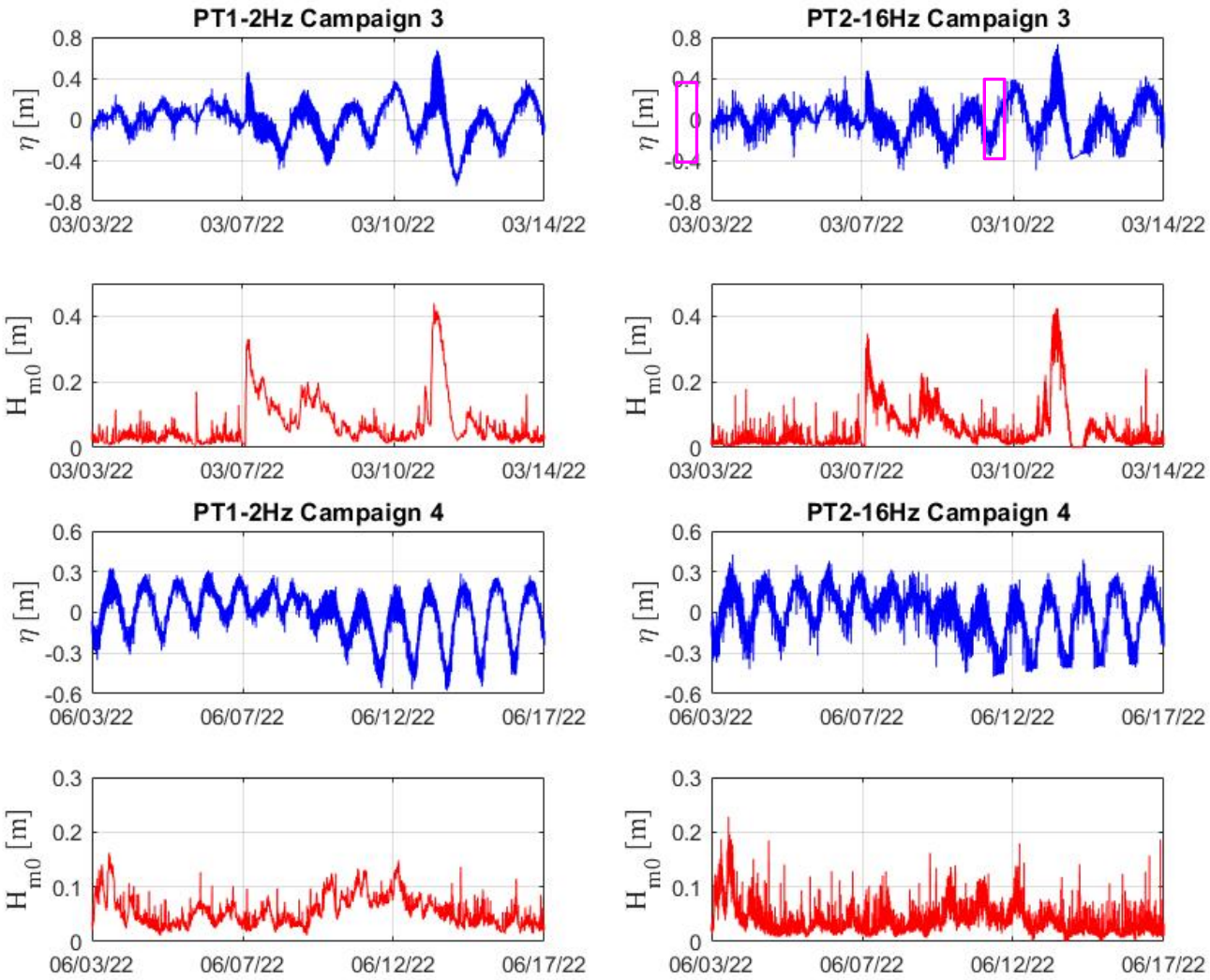

Figure 4.10: Continued.

Figure 4.11: Sequence of photos (left to right) collected by GoPro camera mounted near the wetland edge of FS-3. The images clearly show the ship passage and ship wake patterns affecting the field site.

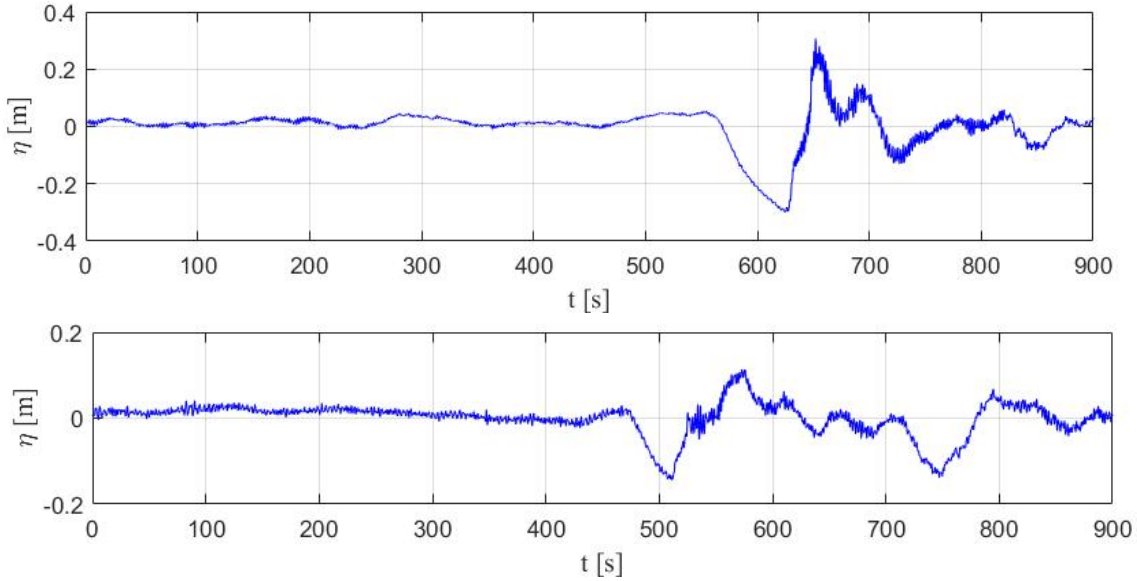

Figure 4.12: Zoomed-in windows of ship wake patterns collected at FS-3 during Campaign 3. Upper panel: single barge passage on Mar 5th; Lower panel: double barge passage on Mar 12th

At FS-3, the maximum water depth of the GIW is about 6 m and the nearby bay bed elevation is on the order of 1-2 m. Ship wakes, mainly generated by barges, produce significant wave energy when impacting wetland edges. As indicated in **Figure 4.12**, the observed maximum vessel surge exceeds 0.3 meters, a magnitude comparable to that of waves produced by the measured hurricane and cold front events at this site. This indicates that vessel-induced hydrodynamics have the potential to cause significant erosion concerns along wetland edges. Field data analysis by *Fuller (2021)* revealed that the cumulative effects of numerous vessel wakes along Galveston Bay ship channels have the potential to be a major source of energy and exacerbate erosion, making maintenance and management a great challenge.

Water level fluctuations and significant wave heights H_{m0} at FS-4 are displayed in **Figure 4.13**. FS-4 is located on the backside of Galveston Island in West Galveston Bay, closer to the western end of the island. The peak wave height during Hurricane Nicholas was 0.45 m, quite a bit higher than that at FS-1 during the same storm while water level increased by 1 m (almost the same as for FS-1). FS-4 is slightly less protected from winds produced by tropical cyclones, which might explain the increased wave energy observed at that location compared to FS-1. Similar patterns were observed for the measured cold front events (see **Figure 4.13 rows 3 – 6**) where wave heights were recorded to be between 0.2 and 0.45 m (H_{m0}).

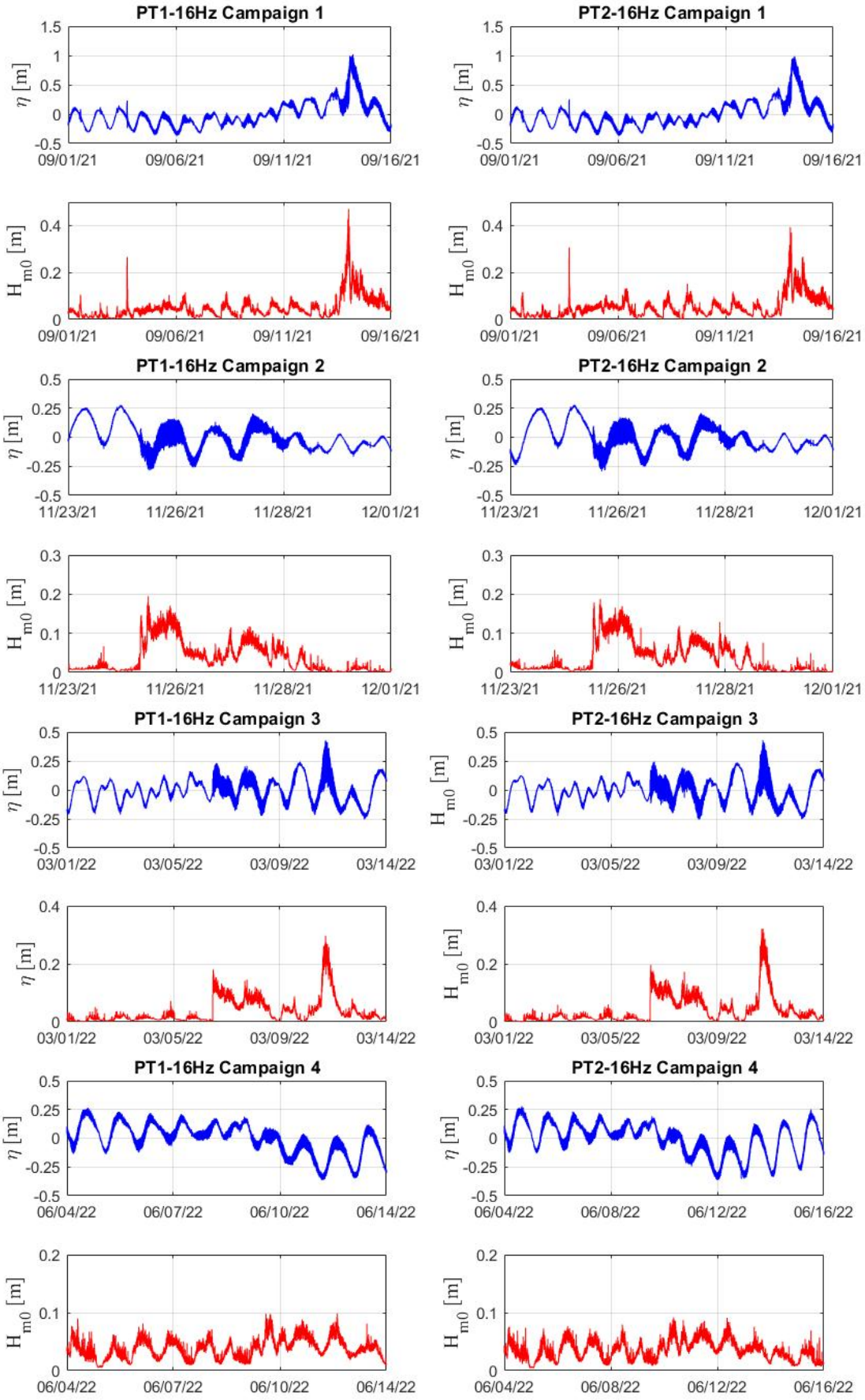

Figure 4.13: Measured water free surface elevations (η) and associated spectral significant wave height (H_{m0}) recorded by PT1 and PT2 at FS-4 for all measurement campaigns.

4.3.2 Velocity components

Examples of measured water velocity are presented in this section. East, North, and Up (ENU) velocity components and verified water depth above the seabed (indicative of free surface fluctuations) are shown for Campaign 1 at FS-3 (Bolivar Peninsula). These data were captured by the Vector ADV. This velocity time series was recorded at a high sampling frequency (16 Hz) allowing for tidal variations, wind waves, and vessel wakes to be captured.

Increases in velocity magnitude correlate with elevated wave height during Hurricane Nicholas (see **Figure 4.14** on Sep 15th) and two cold front events (**Figure 4.15** Mar 8th and Mar 12th). The magnitude of the maximum measured east/west and north/south velocity components exceeded 0.5 m/s. Vertical velocity, particularly during the occurrence of the two cold front events, exhibited significant increases owing to the increased orbital velocity under larger waves. Ship wake patterns, indicated by evident spikes, are also discernible in the velocity data.

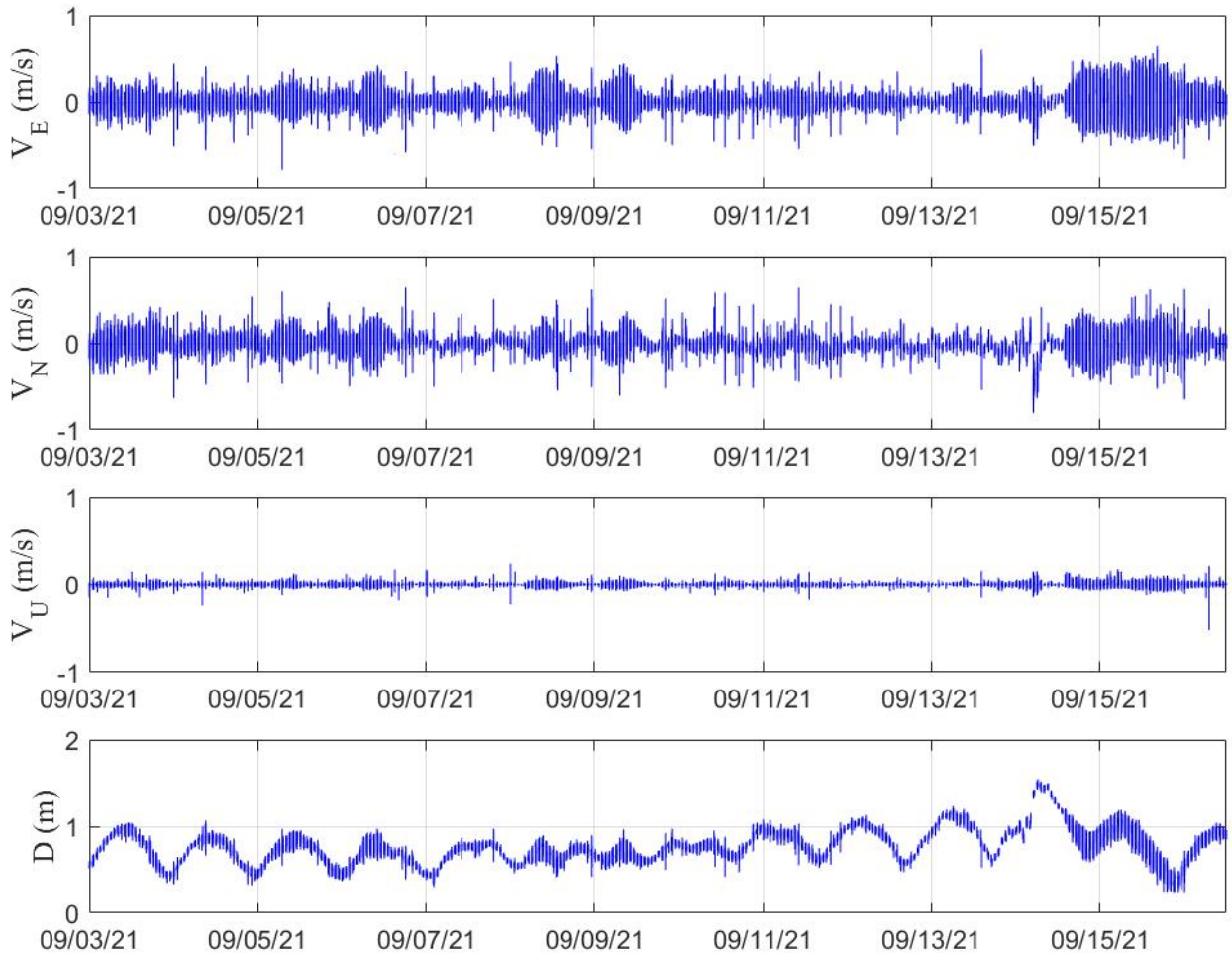

Figure 4.14: Measured E, N, U velocity components (V_E, V_N, V_U) and verified water depth (D) at FS-3 during Campaign 1 in burst mode (burst interval is 40 min with actual measuring interval of 20 min).

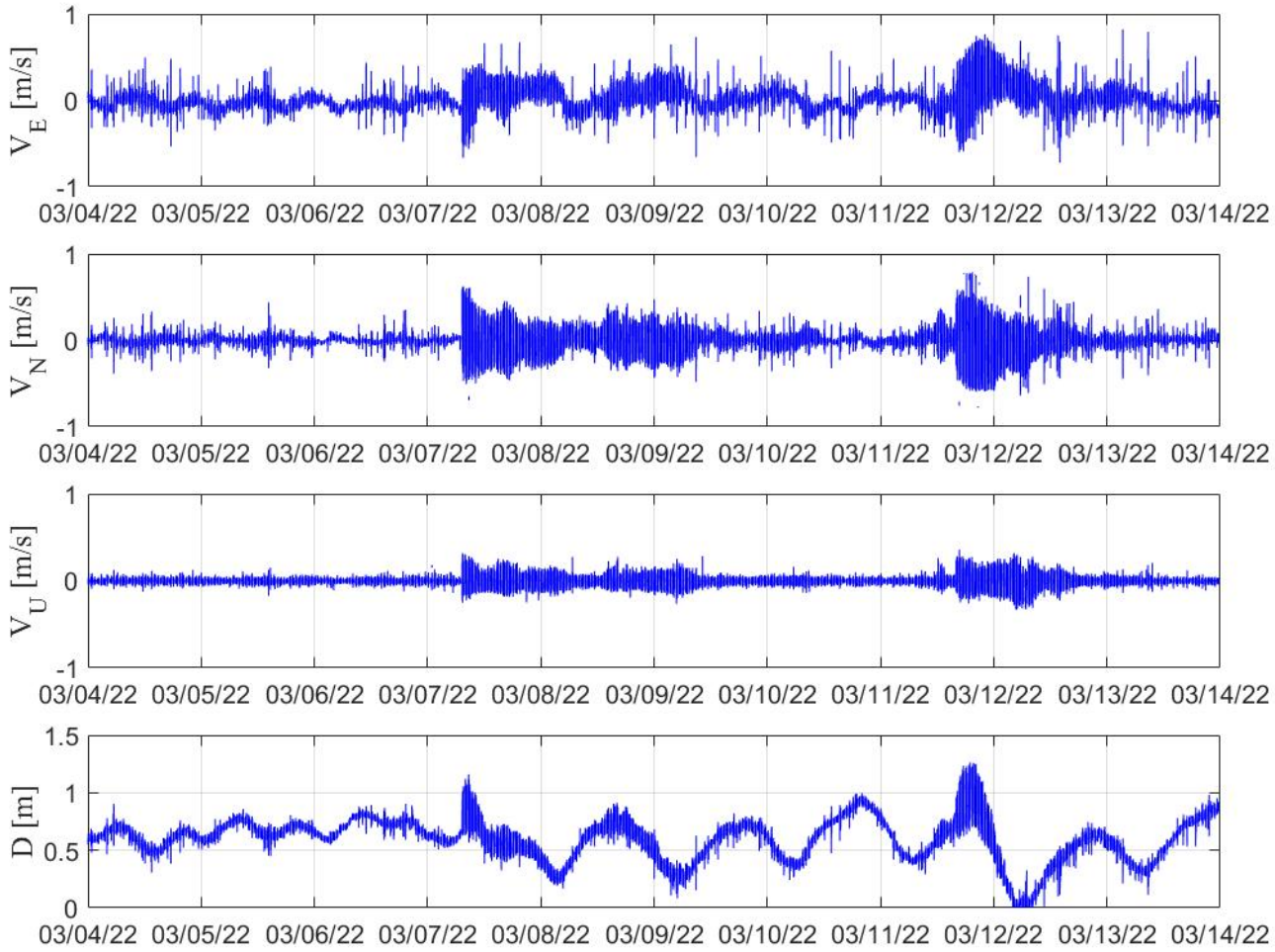

Figure 4.15: Measured E, N, U velocity components (V_E, V_N, V_U) and verified water depth (D) at FS-3 during Campaign 3 in burst mode (burst interval is 40 min with actual measuring interval of 20 min).

Velocity components maintained magnitudes at FS-4 during campaign 4 consistent with tidal flows and measured wave energy (**Figure 4.16**). This can be seen by comparing the velocity data to the measured data from the co-located PT during the same period (see bottom panel in **Figure 4.16**). Larger velocities are generally observed during maximum tidal flow (i.e., between high and low tide) and during times of increased wave activity.

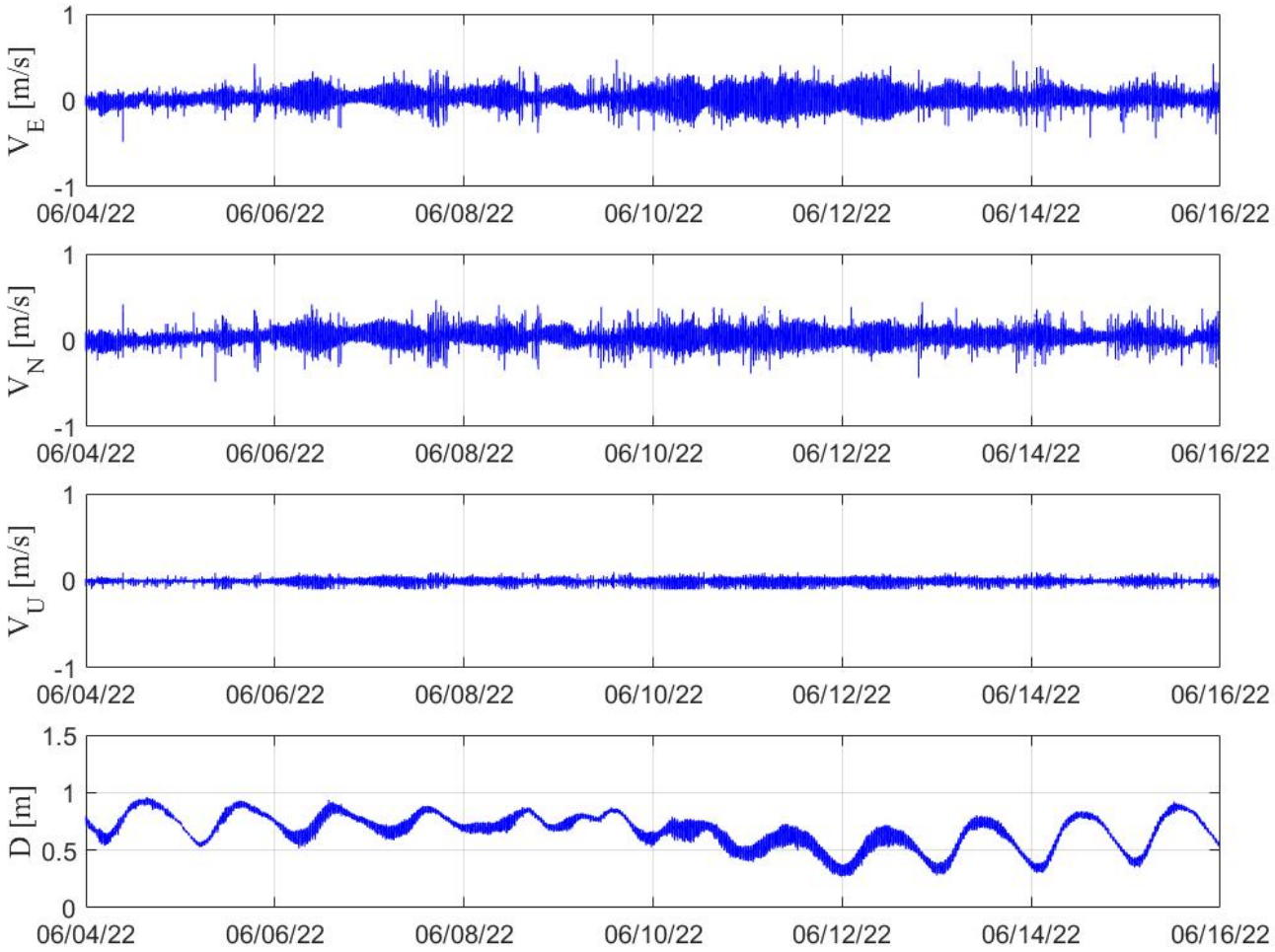

Figure 4.16: Measured E, N, U velocity components (V_E, V_N, V_U) and verified water depth (D) at FS-4 during Campaign 4 in burst mode (burst interval is 40 min with actual measuring interval of 20 min).

4.3.3 Suspended sediment concentration

Calibrated suspended sediment concentration time series are shown in this section. Field measurements conducted with optical sensors are susceptible to influences from the surrounding environment (e.g., fish in field of view or marine growth on sensor surface). In post-processing, data exhibiting such influences were removed. Marine growth issues were minimized by the relatively short duration of each field measuring Campaign (approximately 2 weeks each), which reduces the likelihood for growth to occur. **Figure 4.17** provides two examples of SSC measurements at FS-1.

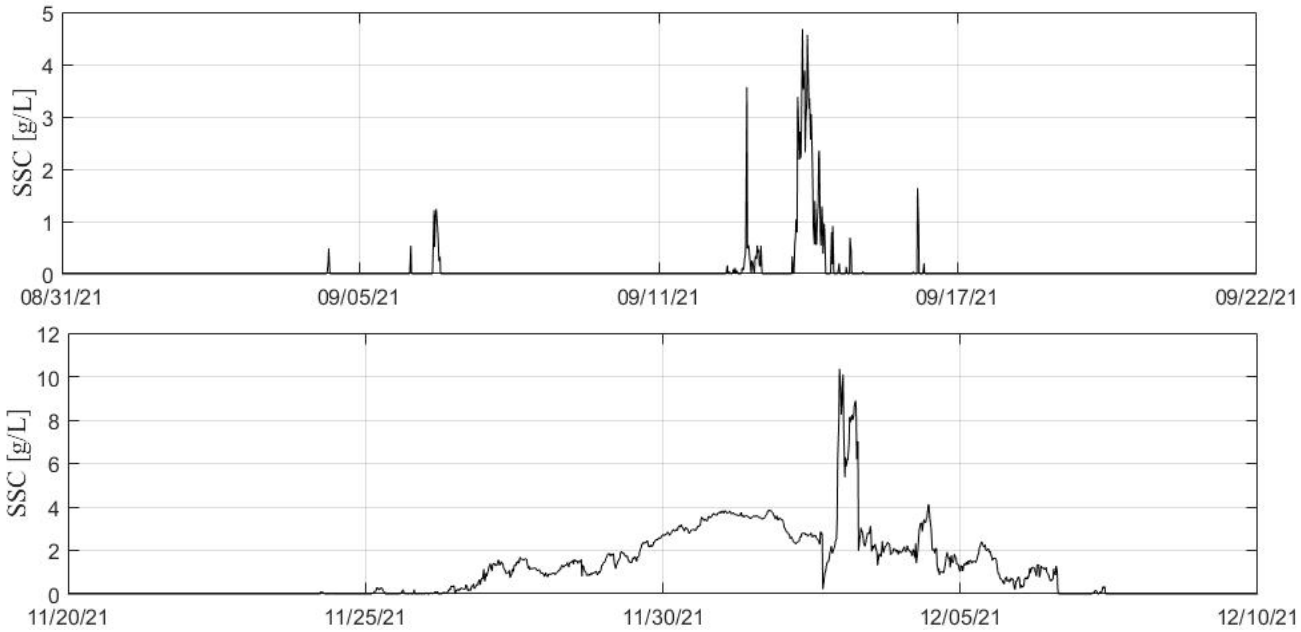

Figure 4.17: Verified SSC at FS-1 during Campaign 1 (top panel) and Campaign 2 (bottom panel).

The prominent increase of suspended sediment concentration (SSC) during Hurricane Nicholas (**top panel Figure 4.17**) and one cold front event (**bottom panel Figure 4.17**) are apparent from the plots. The peak SSC during the hurricane approached 5 g/L. During the cold front event, SSC started to increase around Nov 26th and remained at elevated levels for approximately 10 days with a peak up to 10 g/L. Measured SSC data can be combined with co-located measured velocity data to estimate suspended sediment transport rates at the field sites.

4.4 Summary

In this chapter, we focused on understanding the forcing conditions driving wetland evolutions through *in-situ* hydrodynamic measurements conducted during the four field campaigns at Galveston Bay to analyze seasonal and event-based water level fluctuations, wave energy, and sediment transport patterns. To quantify the wave energy and estimate the erosion potential, these field deployment and measurement campaigns were conducted over varying seasons from September 2021 to June 2022, one of which includes the impact of Hurricane Nicholas. To collect core datasets required in this project, we employed various hydrodynamic instruments during the field measurements: pressure transducers to measure surface fluctuations and wave parameters, ADV and ADCP for the instantaneous velocity measurements, and OBS for turbidity measurements. Instrumentation setups and deployment methods were consistent across campaigns, with minor adjustments based on site conditions.

The measured water level fluctuations (η) showed significant wave activities during Hurricane Nicholas. In comparison to the pre-hurricane conditions, we observed the rise of water levels over 1 m with wave heights approaching 0.3 m at FS-1. In addition, the measured spectral wave heights (H_{m0}) during prevailing cold front events in Campaigns 2 and 3 reached up to 0.3 m, with the most intense event showing wave heights surpassing those during Hurricane Nicholas, reaching up to 0.3 m. These observations demonstrate potential erosion risks due to the impact on wave energy induced by extreme weather events even in regions sheltered by natural barriers like Galveston Island and Bolivar peninsula.

The vessel-induced hydrodynamics were also assessed at FS-3, which is directly affected by maritime traffic in the Gulf Intracoastal Waterway. We observed characteristic surges, drawdowns, and trailing wake patterns particularly generated by passing barges with the hydrodynamic potential to cause wave energies comparable to those of storm events. This result raises alarming concerns along wetland edges due to vessel traffic.

We identified sediment transport patterns during various events using the SSC measurements. For example, we observed the peak SSC value exceeding 5 g/L during Hurricane Nicholas, indicating high sediment load during the storm. In a similar fashion, significant increases in SSC with peaks reaching up to 10 g/L during cold front events demonstrate the correlation between elevated SSC and storm events and the role of hydrodynamics in sediment suspension and transport.

5 Numerical simulations – validation and forecast of wetland boundary

The physical importance of coastal wetlands to the ecology and storm protection of an area has been discussed in previous sections. To understand wetlands evolution, it is crucial to simulate long-term water depth changes, wave energy, and sediment transport and validate these simulations with field data, to understand how they might be affected and whether they can persist in the face of increasing sea level.

Numerical modeling tools have generally been used to simulate the impact of hurricanes on coastal areas. These models include ADCIRC (*Luettich et al., 1992*), SLOSH (*Jelesnianski, 1992*), and Delft3D (*Lesser et al., 2004*). While the basic hydrodynamic equations on which they operate (the shallow water equations) are essentially the same, they differ in the implementation of the numerics and other ancillary effects (sediment transport, morphology, etc.). The ADCIRC model, for instance, is based on a finite element representation, and can be used to resolve the fine detail of local coastlines. Delft3D presently has two different numerical implementations: finite difference on a Cartesian, spherical, or curvilinear grid (Delft3D-FLOW) and a hybrid finite element / curvilinear formulation (Delft3D-FM). The hybrid nature of Delft3D-FM ("FM" for "Flexible Mesh") allows curvilinear grids to be used to resolve rivers and waterways, and finite elements to resolve the remainder of the domain. Conversely, Delft3D-FLOW uses nesting of grids (in both serial and parallel domain decomposition modes) to propagate oceanic scale phenomena toward coastal areas of interest. The nature of the model used depends on the needs of the user, the quality / resolution of the input fields (bathymetry, winds, remote water level conditions, etc.), the dominant processes in the area, and the computational platforms available.

While there has been significant focus on hurricanes and other coastal hazards in modeling studies, coastal modeling studies using future climate scenarios are far less represented in the literature. Some examples of prior work in this regard include the impact of climate change and sea level rise on the nearshore wave climate (Chini et al. 2010); climate change impacts on groundwater (El Hamdi et al. 2021), and sea level rise impacts on coastal marshes (Geselbracht et al. 2011). For these (and other similar) studies, meteorological information from future climate studies are used to force numerical models for determining coastal impact. For the most part, the models used in these studies are either fairly rudimentary or contain only the processes of interest with no other degrees of freedom. For example, Geselbracht et al (2011) used a numerical model based on a decision tree system of predicted outcomes strictly for marshes and sea level rise. Models which treat the coastal wetlands erosion problem as one of a number of impacts in a holistic manner were uncommon in this application of future effects. In contrast, we are using a sophisticated coastal model capable of simulating a myriad of ocean, coastal, and nearshore processes.

Due to prior experience (as exemplified in Kim et al. 2020) and the processes represented in the model, we used the Delft3D-FLOW model for this project. In contrast to ADCIRC and SLOSH, Delft3D-FLOW contains sediment transport and morphological evolution modules, which would allow the possibility of simulating erosion and changes to the wetlands edge. Several grids were established for the modeling of wind-induced processes (waves, surge) and tides, with these grids nesting into finer grids near the locations of interest. With this nested system, we were able to simulate the generation and propagation of wind-driven waves and surge, as well as the propagation of astronomical tides, from the overall Gulf of Mexico area down to areas of interest in the Galveston and MANERR vicinities.

Due to the computational time required to run simulations for future scenarios, different grid resolutions in the nearshore areas were used for model verification and future climate scenarios. We used data from several field deployments (listed in **Chapter 4**) to ensure the performance of the model for a wide range of conditions, then used the validated model to perform erosion predictions for Galveston Bay and MANEER areas. All computer simulations were performed on a Dell desktop computer (Intel Xeon W-1390P processor, 8 cores, 64GB memory).

5.1 Calibrated Delft3D model for long-term processes

5.1.1 Data and Methods

We utilized data from four field studies and validated the simulation results of the low-resolution model against measurements of water depth, significant wave height, and wave energy. Model grid and bathymetry setup for the Delft3D-FLOW/WAVE were performed for Galveston Bay system, its use motivated by our prior success with Delft3D-FLOW in Galveston Bay (Kim et al., 2020). In addition, the modeled domain in the vicinity of the site of interest may not necessarily benefit from the use of the more-complex Delft3D-FM. Long-term simulation of the Delft3D model for Galveston Bay was tested for the verification of wave climates affecting salt marsh edges. Cumulative wave energy for a long-term period was compared with measured marsh edge erosion rate derived by the UAV images later. Thus, a finer resolution grid in the Delft3D model for the UAV survey area (FS-4) is included since the 370 m resolution grid cannot simulate the wave condition appropriately. The details of the low-resolution model grids are as shown **Figure 5.1**. Details of the model are described in

Kim et al. (2020). This model includes Gulf of Mexico grid (N1), Galveston Bay Grid (N2) and domain decomposed grids for Field Site 1 to 4. (We note here that the N1 and N2 grids have different resolutions in these simulations than in the short-term simulations described below (and for which the grid resolutions are described in Table 5.1), despite the fact that they share the same designation).

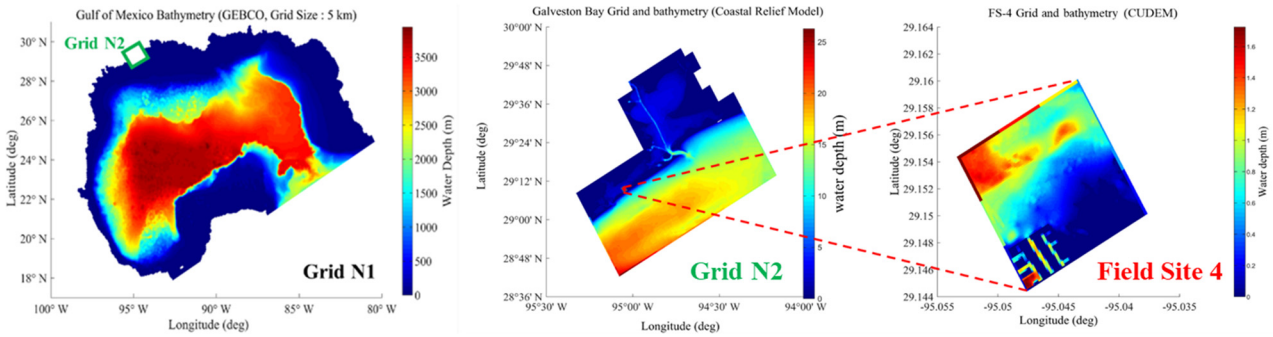

Figure 5.1: Low resolution model grid setup for long-term processes

The Galveston Bay model was validated based on 4 different *in-situ* measurements from field campaign 1 to 3. Field campaign 1 includes Hurricane passages (Hurricane Nicholas), and field campaign 2 & 3 include cold front passages. The long-term simulation from NOV 2019 to OTC 2021 was analyzed and validated. Water levels and cumulative wave energy for a campaign period were compared with measured wave data. The details of the long-term simulation that include field campaign 1 are as described below.

- Simulation period: NOV 2019 ~ OCT 2021
- Area (Grid resolution): Galveston Bay Grid (370 m) and FS-4 Grid (12 m)
- Boundary conditions: Astronomically forced from TPXO 8.0 tidal constituents
- Flow/Wave model (SWAN) time step: 1 minute / 1 hour (as communication interval)
- SWAN model directional bins: 72 directional bins of constant 5-degree width
- SWAN model wave frequency setting: 24 frequency bins, in the range of 0.05-1Hz

Water level results at Galveston Railroad Bridge tide gauge (for two years) are shown in **Figure 5.2**.

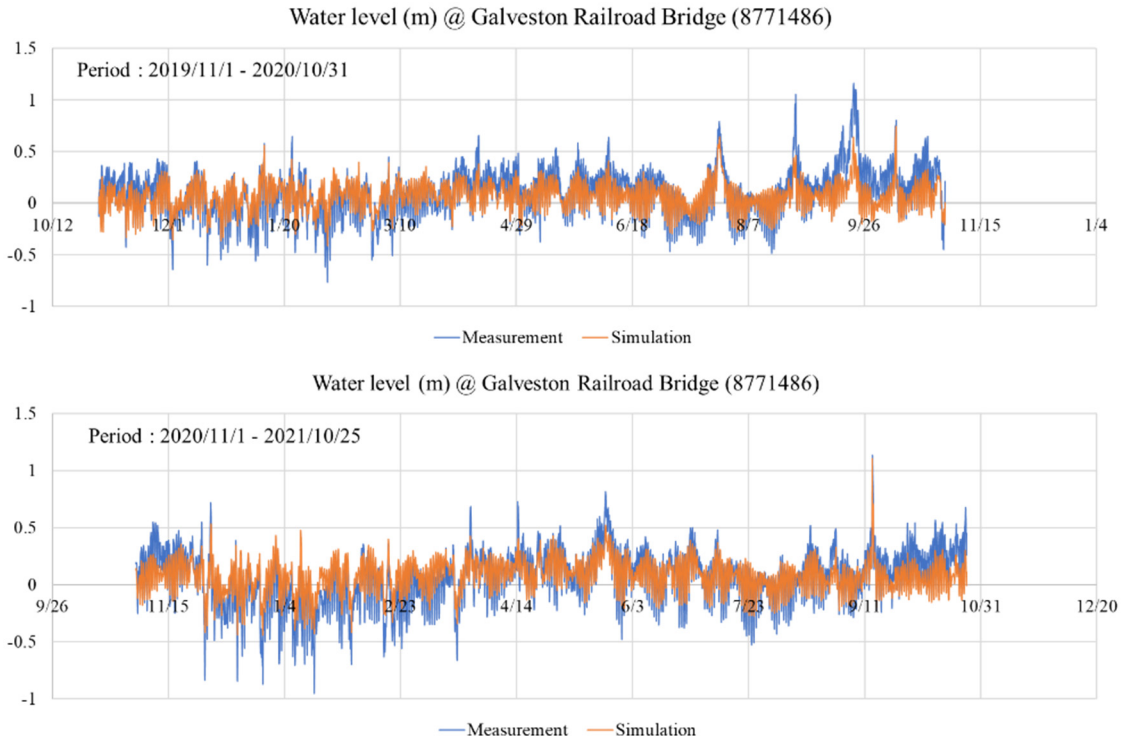

Figure 5.2: Simulated water level results at the Galveston Railroad Bridge in comparison with the tide gauge

The model simulated the increased water level during Hurricane Nicholas quite well. The significant wave height and wave power results at Site 4 from 2019/11/01 to 2021/10/25 (with corresponding histogram) are shown in **Figure 5.3**. In the location near the salt marsh edge at Site 4 (FS4-PT-NEAR), the significant wave height did not exceed 0.34 m over the two years of simulation. Also, most significant wave heights did not exceed 0.1 m during this period (**Figure 5.3c**). The magnitude of energy transport (wave power) has a peak value of 132 W/m during the passage of Hurricane Nicholas. However, most wave power estimates did not exceed 10 W/m except for cases such as hurricane/tropical storm passages. The wave power results imply that less than 10W/m ocean waves can most affect erosive activity on the salt marsh edge.

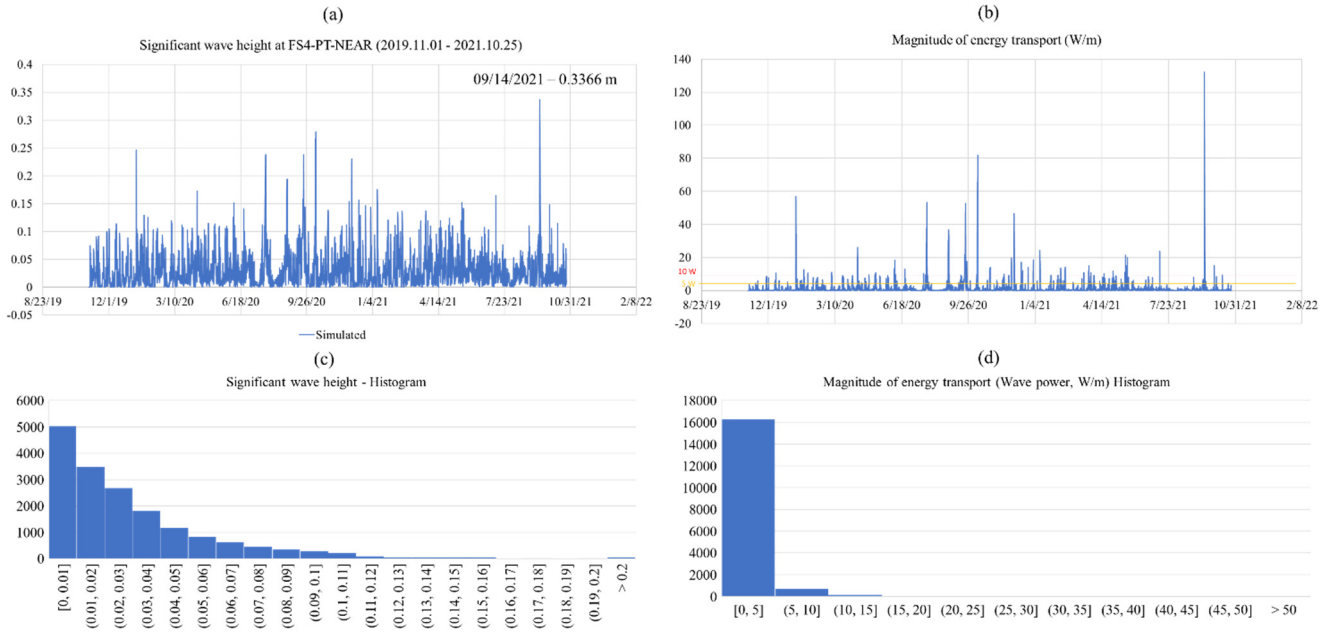

Figure 5.3: Results of (a) Significant wave height, (b) Magnitude of energy transport, (c) Histogram of significant wave height, and (d) Histogram of the magnitude of energy transport for the period of NOV 2019 ~ OCT 2021

The low resolution model was also tested for field campaigns 2 and 3 for the Galveston Bay area. As shown in **Figure 5.4**, three cold front events were observed in each of the measurement periods during Campaigns 2 and 3.

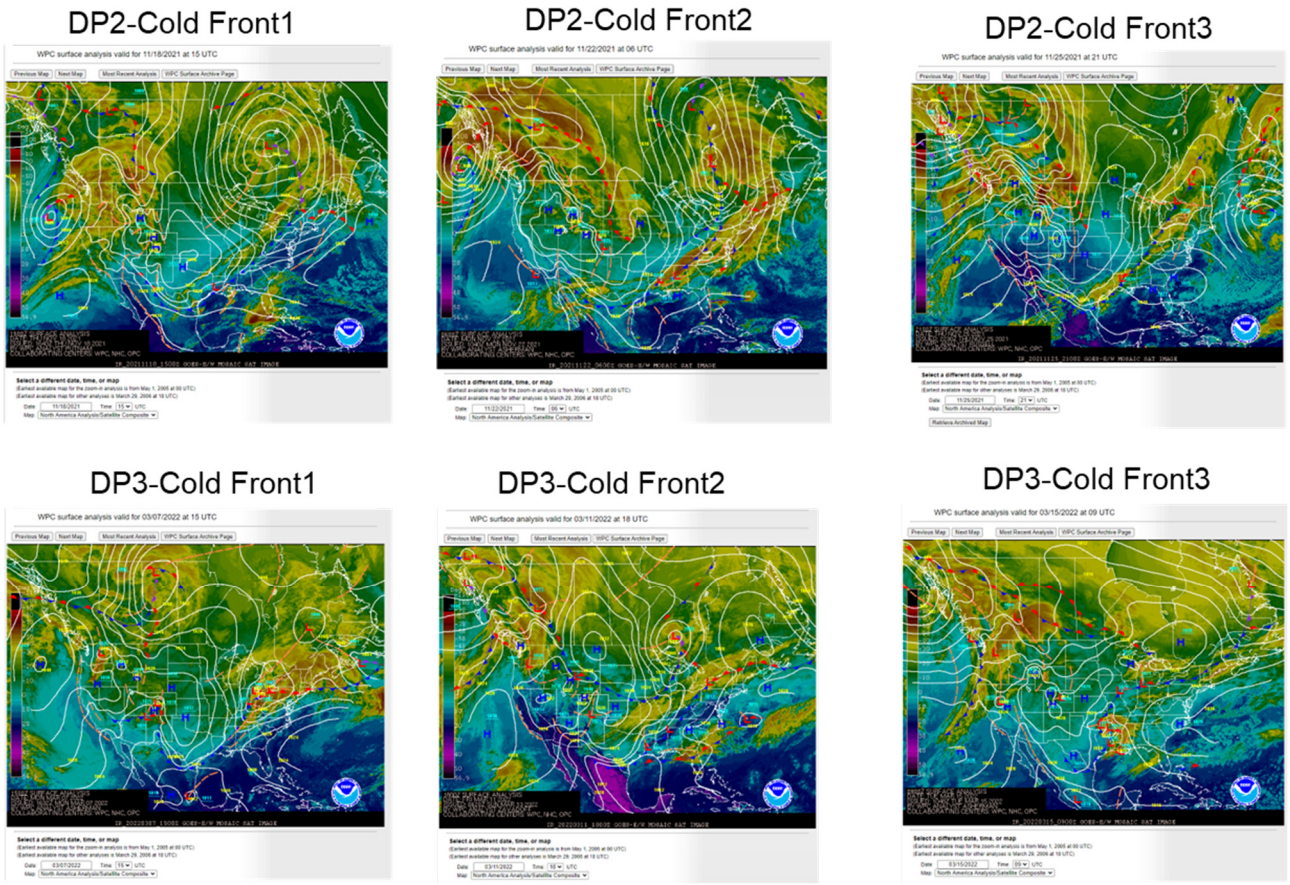

Figure 5.4: Observed pressure fields related to cold front passages during the field campaign 2 (DP2) and 3 (DP3) (Images from NOAA Weather Prediction Center Surface Analysis Archive)

These long-term simulation results from NOV 2021 to MAR 2022 (the span of time encompassing the cold fronts shown in Figure 5.4) were compared to the measurements from field campaign 2 and 3 for Delft3D model verification. **Figure 5.5** shows a comparison of significant wave height results between the long-term simulation with the low resolution model and measurements collected during Campaigns 2 and 3 in the Galveston Bay area. Significant wave height results of measurements were derived from spectrum analysis of the pressure transducers' data using the Ocean Wave Analyzing Toolbox (Oceanlyz, Karimpour & Chen, 2017).

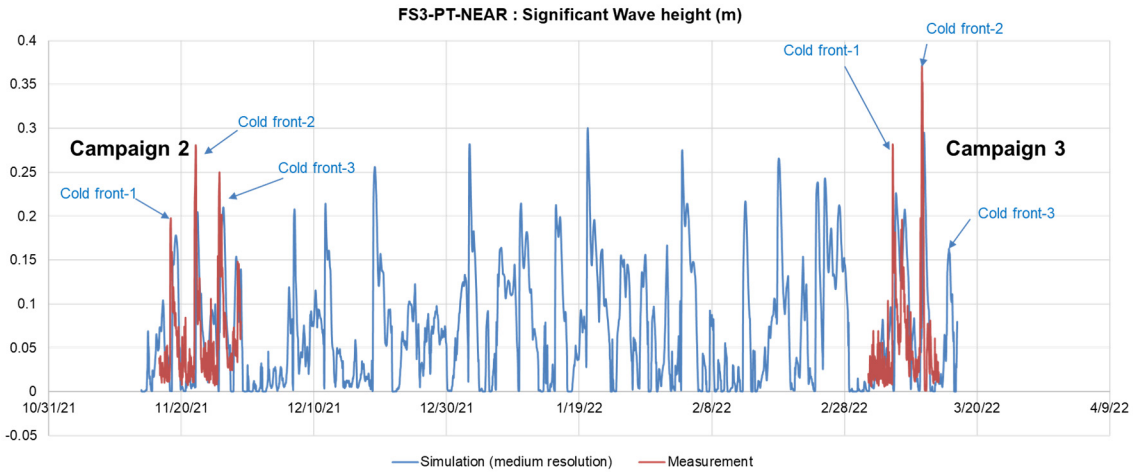

Figure 5.5: Significant wave height results comparison for field campaigns 2 and 3 at Field Site 3

The model results are in good agreement with the measured significant wave heights. Simulation results slightly underestimated the peak values of significant wave height during the cold front passages. One possible cause is the model

grid resolution used here. The long-term model is now considered to be validated, and using this model, we conducted long-term ensemble forecasts (up to the year 2100) with and without the effects of climate change for Deliverable 3.

5.2 Validated and calibrated Delft3D model for short-term processes

The short-term simulations covering field campaigns 1, 2, 3 and 4 are validated and calibrated based on the measurement at Galveston Island and Bolivar Peninsula sites. The wave power (wave energy flux) from the simulation needed to be validated since the wave power is highly correlated with wetland edge lateral erosion rate. Thus, as a validation process, we compared the wave power between simulation and measurements for the entire campaign period.

5.2.1 Data and Methods

Unlike the prior section, which detailed simulation durations of two years, here we concentrate only on the time of the field campaigns. As such we are able to use higher grid resolutions. We validate the models for short-term processes based on the simulated wave power near wetland boundaries in the Galveston Bay area during the measurement period, using these high resolution models. These high resolution models for short-term processes were developed based on the model from Kim et al. (2020).

The high-resolution model includes the Gulf of Mexico grid with nine domain-decomposed grids for Galveston Bay and identified sites of interest for the detailed simulation of the surge and wave processes. Domain decomposition is a parallel computation technique that allows smaller high-resolution grid areas to be calculated during the same computational run as a larger, coarsely-resolved area encompassing these smaller areas. The details of grids and bathymetry used are described in **Table 5.1**.

Table 5.1 Grid details in Delft3D/SWAN model

Grid number	Area	Grid resolution	DEM
N1	Gulf of Mexico	5 km	GEBCO 2008
N2	Galveston Bay	400 m	Coastal Relief Model
N3	Galveston Island and Bolivar Peninsula	125 m	CUDEM
N4	West Galveston Island	25 m	CUDEM
N5	Bolivar peninsula	25 m	CUDEM
N6	Field Site 1	2.5 m	CUDEM
N7	Field Site 2	2.5 m	CUDEM
N8	Field Site 3	2.5 m	CUDEM
N9	Field Site 4	2.5 m	CUDEM

In order to obtain an improved representation of wave and sediment transport within the simulation, the Galveston Island grids were updated to increase the resolution of most wetland areas located in the west of Galveston Island, as shown in **Figure 5.6.**

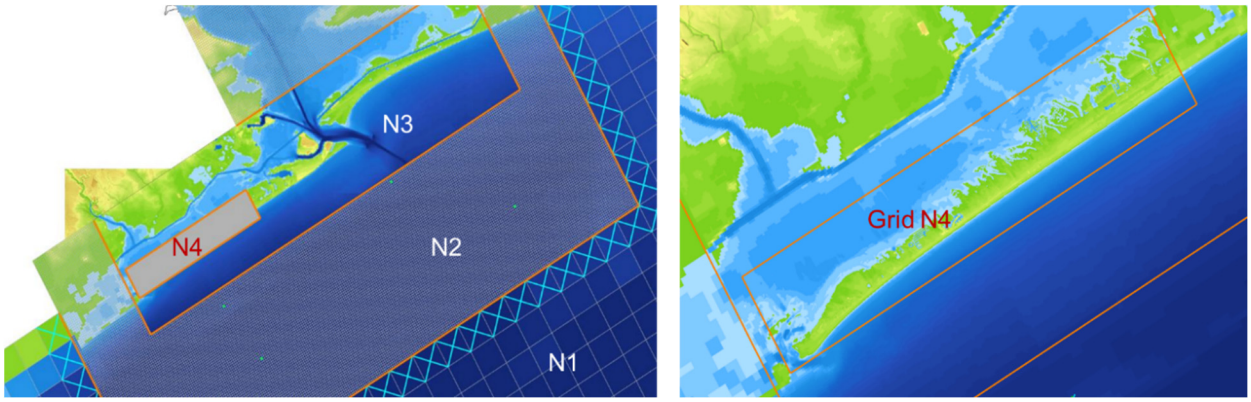

Figure 5.6: Updated domain decomposed Grid (N4) for West Galveston Island (Grid number of N4: 1042 x 217, Grid resolution: 25 m)

These model grids are connected using domain decomposition in a 2D equidistant grids framework The full model domain covers 1280 km in the N-S direction and 1440 km in the E-W direction and has tidal boundaries on the north, east and south sides of the largest grid. Tidal constituents were obtained using the Delft Dashboard model preprocessing utility (Deltares,

2015) to access the TPXO 8.2 Global Inverse Tidal Model (Egbert and Erofeeva, 2002). The SWAN model was implemented with the same equidistant grids with the smaller grids nested within the larger grids. The bathymetry was obtained from the GEBCO (30 arc-seconds resolution) model (Amante and Eakins, 2009) which has a horizontal resolution of approximately 1.80 km for the two larger grids, and from the Coastal Relief Model (3 arc-second resolution) (NOAA National Centers for Environmental Information, 2016) which has a horizontal resolution of approximately 90 m for the two smaller grids. The Continuously Updated Digital Elevation Model (CUDEM) which has a 1/9 arc-seconds resolution (CIRES, 2014) was used for the Galveston Bay area to resolve small-scale bathymetric and topographic variability near Galveston Island.

The sediment transport processes were tested for the updated Galveston Island grid (N4). The sediment parameters used in the simulation were based on the 2006 USGS usSEABED survey and are presented in **Figure 5.7(a-b)**, and preliminary erosion and accretion results of Galveston Island by sediment transport during the cold front passages simulation period are shown in **Figure 5.7(c)**.

(a)

Sediment Type	Layer Thickness (m)	D50 (mm)
Sand	5	0.1

(b)

Sediment Type	Critical shear stress (Pa)	Layer Thickness (m)	Settling velocity (mm/s)	Erosion rate (kg/m2/s)
Mud	0.1/1.0	5	0.25	0.0001

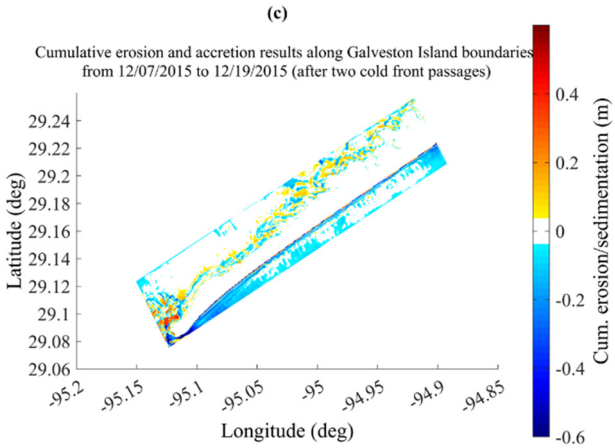

Figure 5.7: A summary of (a) non-cohesive and (b) cohesive sediment parameters used in the model and (c) preliminary erosion-accretion results of Galveston Island from 12/07/2015 to 12/19/2015

According to the results in **Figure 5.7(c)**, a significant morphological change near San Luis Pass was predicted by the model. In addition, both erosion and sedimentation were observed in the wetland and surrounding areas, with erosion reaching a maximum of 0.3 m during the two cold front passage periods. In the current Galveston model, 18 days of simulation required five days of computing with a depth-averaged model (2D model) and with the sediment transport and morphology modules engaged. In contrast, ten days with a layered model (five-layer 3D model) were required for the same simulation (CPU: Intel Xeon W-1390P, 8 cores, Memory: 64GB).

5.2.2 Preliminary model sensitivity tests

Model sensitivity tests were done related to water depth and wind input for the Galveston Bay area. Wave power was calculated and compared for both the measured and simulated wave climates to verify the model performance for estimating the current/future salt marsh boundary's retreat rate. For the verification of the Galveston Bay model, significant wave height results were compared with measurements in field campaign 1. Regarding the validation and calibration of the high-resolution Delft3D model for short-term processes, several tasks were undertaken. Initially, the model was tested using local wind data from a single location (the Galveston Railroad bridge) in conjunction with the NCEP wind field to establish a baseline. Subsequently, refined grids were incorporated for Field Sites 1 through 4. We then assessed the model's performance using the GALVESTON DEM, which was provided by NOAA in 2006. Adjustments were made to the water depth for the grids of Sites 1-4, based on records from *in-situ* pressure transducers. Further tests were conducted to evaluate the model with the ERA5 space-varying wind field. Lastly, we addressed the datum change in the Galveston Bay area DEM, transitioning from NAVD88 to MHW.

Based on the measurements, differences in water depth of 20-60 cm were seen when compared to DEM (CUDEM-NAVD88) data. The difference between NAVD88 and MHW was 30 cm for the entire Galveston Bay area. Considering this difference, a discrepancy of up to 30 cm was still present for specific sites (Site 1 and 2). Possible causes for this discrepancy include the inclusion of an old bathymetric data source for West Galveston Bay (based on 1930 data) in CUDEM, land subsidence, sea-level rise, and sea bottom sediment spill/erosion.

In addition, a new space varying wind field ECMWF-ERA5 was tested for improved representation of the hurricane wind field

for models during field campaign 1. ECMWF (European Centre for Medium-Range Weather Forecasts)-ERA5 (reanalysis) combines historical observations into global estimates using advanced modeling and data assimilation systems. The data set is one of the most recent versions of reanalyzed global wind field (2019) and has a 1-hour temporal resolution with 0.25 ° x 0.25 ° spatial resolution. ERA5 wind field and NCEP Climate Forecast System Version 2's wind field during Hurricane Nicholas's landfall are shown in **Figure 5.8.**

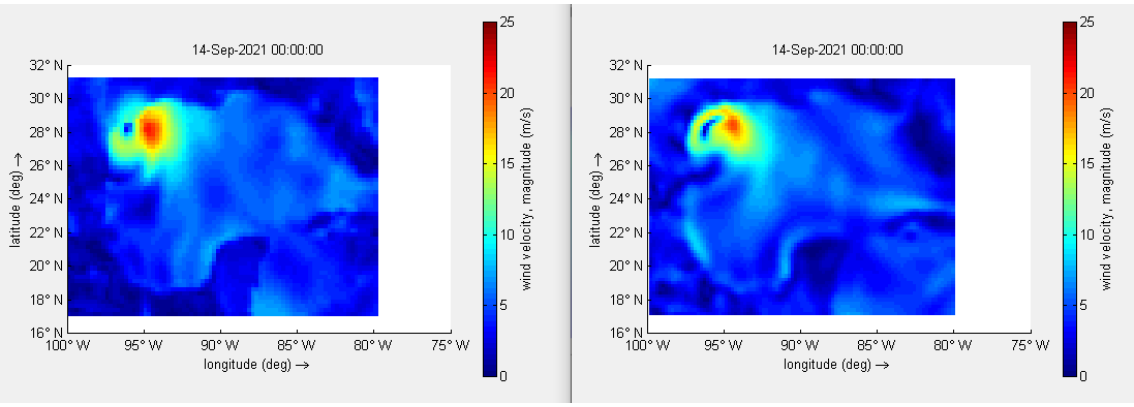

Figure 5.8: Wind field comparison during Hurricane Nicholas's landfall (Left – ERA5, Right – NCEP wind field)

The details of each calibration model are described in **Table 5.2.**

Table 5.2: Detail configurations of test models

Model	Water Depth (Galveston Area grid)	Water Depth (Site 1~4 grid)	Global wind input (Gulf of Mexico)	Local grid wind input (Galveston Area)
Baseline	CUDEM	CUDEM	NCEP	Galveston Railway bridge
Test 1	CUDEM	Adjusted to the measured depth	NCEP	Galveston Railway bridge
Test 2	CUDEM + 0.3 m	CUDEM + 0.3 m	NCEP	Galveston Railway bridge
Test 3	CUDEM + 0.3 m	CUDEM + 0.3 m	ERA5	ERA5

Modeled significant wave height results of Test 1~3 at FS1-PT-NEAR compared to measurements are shown in **Figure 5.9**.

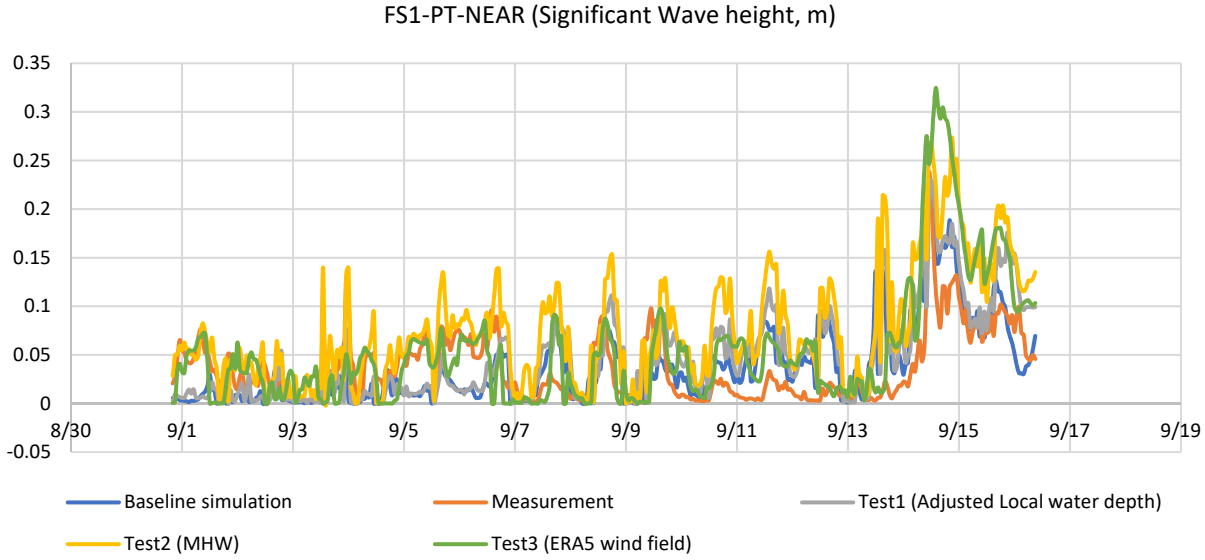

Figure 5.9: Comparison of different high-resolution models at the location of FS1-PT-NEAR

Overall, the tested models showed different predictions of significant wave height, especially during the passage of Hurricane Nicholas from 2022/9/14 to 9/16. The peak value of measured significant wave height from 9/1 to 9/13 did not exceed 0.1 m, and the use of the ERA5 wind resulted in an improved prediction for this period. Each model's performance for Site 1 was

analyzed and shown in **Table 5.3.** based on the following skill metrics, Root Mean Square Error (RMSE), Coefficient of Determination (R^2), Normalized Bias ($Bias$), Scattered Index (SI), and Mean Normalized Error (E_{NORM}).

Table 5.3: Model performance based on skill metrics

Model	RMSE (m)	R^2	$Bias$	SI	E_{NORM}
Baseline	0.03	0.28	0.01	0.03	0.73
Test 1	0.04	0.28	0.28	0.06	0.84
Test 2	0.04	0.45	1.06	0.07	1.14
Test 3	0.04	0.50	0.48	0.06	0.94

Compared to the baseline model, the difference in RSME was less than 0.01 m among the other models, and Tests 1-3 did not show improved results except for R^2 value. The R^2 value was the highest in the Test 3 model using ERA5 wind. Test 3 model performed well during the simulation period except for the overestimation of hurricane-induced significant wave height. The current Test 3 model did not use local wind for the Galveston area. In the results, ERA5 tends to underestimate cold front or sea breeze induced waves, so further investigation is needed to validate its usability in the short and long-term model.

Wave power was calculated to verify the erosive activity during the measurement period. Measured wave power was calculated from spectral analysis and linear dispersion relation, and simulated wave power was calculated by Delft3D-SWAN model results. The wave power results are shown in **Figure 5.10.** The peak value of wave power for each site was highest during the hurricane passage. However, the water level was increased by more than 1 m during the hurricane passage for the Galveston Bay area. Given the elevation of the wetlands, it can be considered that the flood of salt marsh boundaries can nullify most of the erosive activity caused by waves. The simulation underestimated the peak value of wave power. Most periods of the time, the wave power did not exceed 50 W/m. It is noticeable that some ship wake effects in Site 3 (**Figure 5.10**) can impact the erosive effect due to increased wave power.

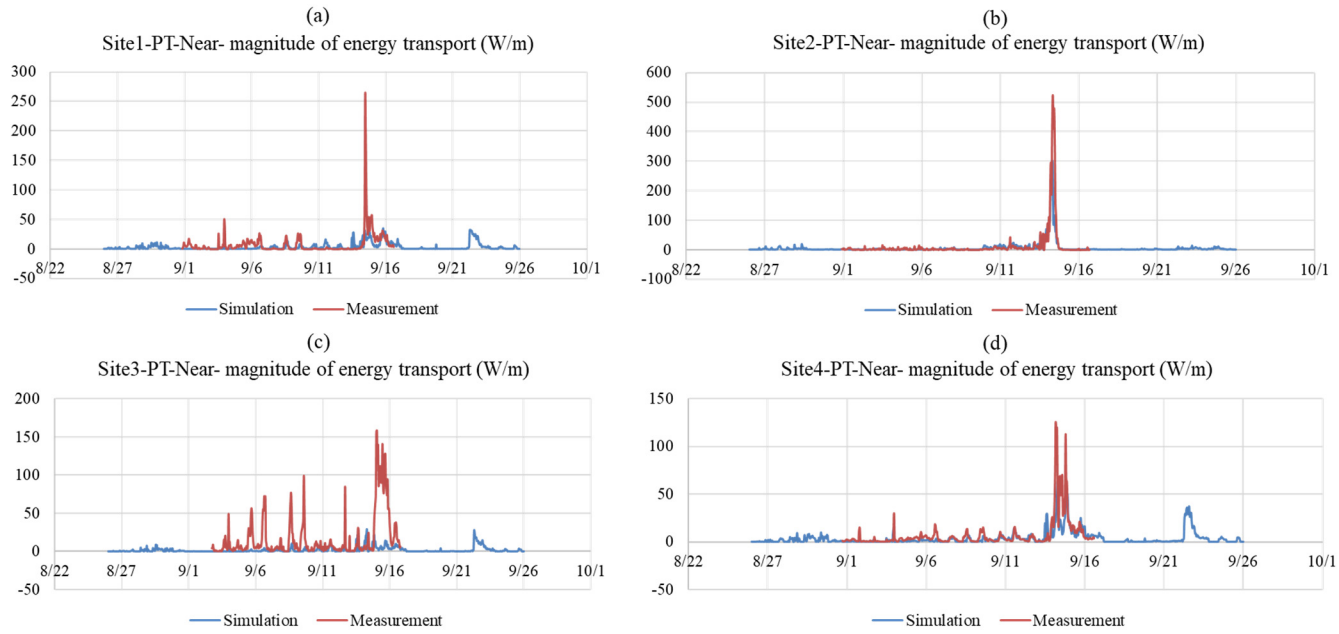

Figure 5.10: Comparison of simulated wave power with measured wave power for each site

It is of importance to ensure the accuracy of wind data generated by the hurricane to elucidate the impact of hurricanes on wetland erosion and sedimentation. We have tested HURDAT2 (Hurricane Database 2) data from NOAA's National Hurricane Center, which encompasses the precise center position of Hurricane Nicholas and respective wind speeds at various distances from the center. This data was further applied to the Holland (2010) model, facilitating the creation of a wind field representative of Hurricane Nicholas. We tested the results of the simulation forced by the Holland model winds by comparing the resulting significant wave heights to those from Buoy 42019 and the simulation outcomes derived from existing NCEP and ECMWF-ERA5 Reanalysis models. Based on the results presented in **Figure 5.11**, we confirmed that wind fields generated based on HURDAT2 data (in conjunction with the Holland model for the wind profile) can provide a more accurate prediction of significant wave height. The results highlight the need for ongoing refinement of hurricane wind data modeling and

underscores the critical role this plays in accurately predicting and mitigating the environmental impacts of such significant weather events.

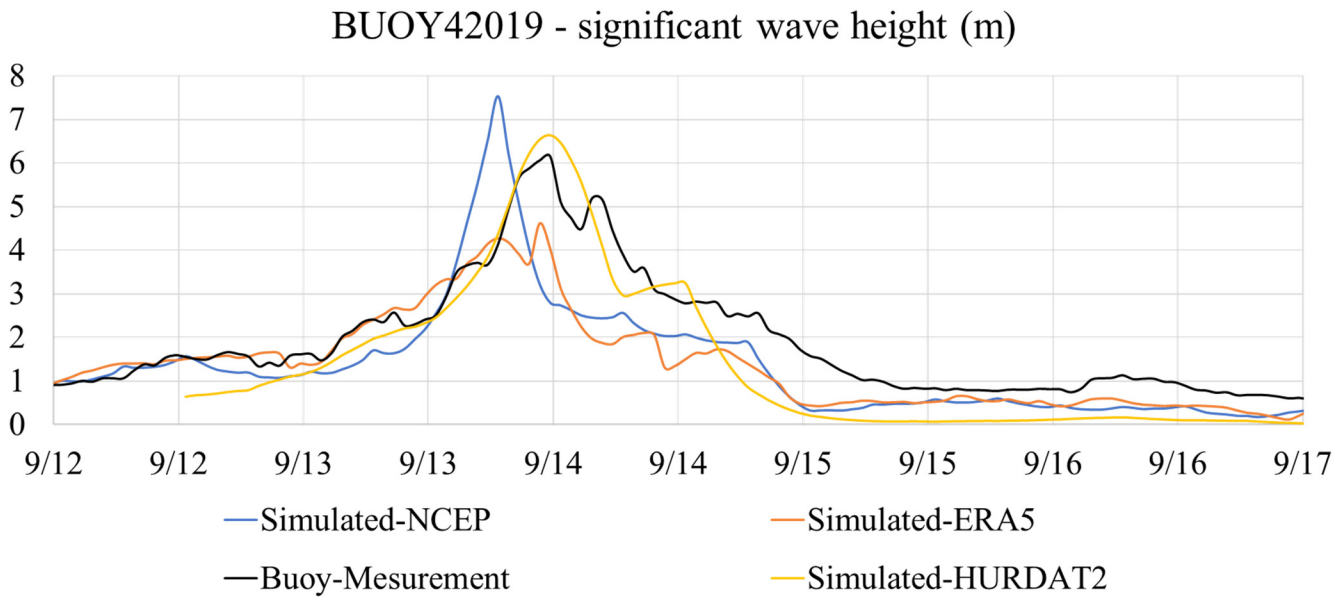

Figure 5.11: Comparison of Significant Wave Height results at Buoy42019

It is important to note the limitations of the NCEP and ERA5 reanalysis winds when it comes to hindcasting hurricane wind fields. The performance of ERA5 appears to be slightly better than that of NCEP during the passage of a hurricane, although both models exhibit potential for improvement. We will supplement these models by incorporating hurricane wind field data derived from HURDAT2 and computed via the Holland (2010) model. This model offers slightly better accuracy and captures the wind speed of hurricanes well. However, it tends to overestimate to a certain degree, which is a point of consideration for future refinements and investigations.

5.2.3 Model Results

Simulation results for Field Campaigns 1, 2, and 3 were compared to the measurement data. Wave power (energy transport) output was derived from SWAN results of the Delft3D simulation, while wave power results from measurements were derived based on spectrum analysis and the use of the linear-dispersion relation for water waves. **Figure 5.12** shows the wave power result of simulation and measurements for the field campaigns 1-3.

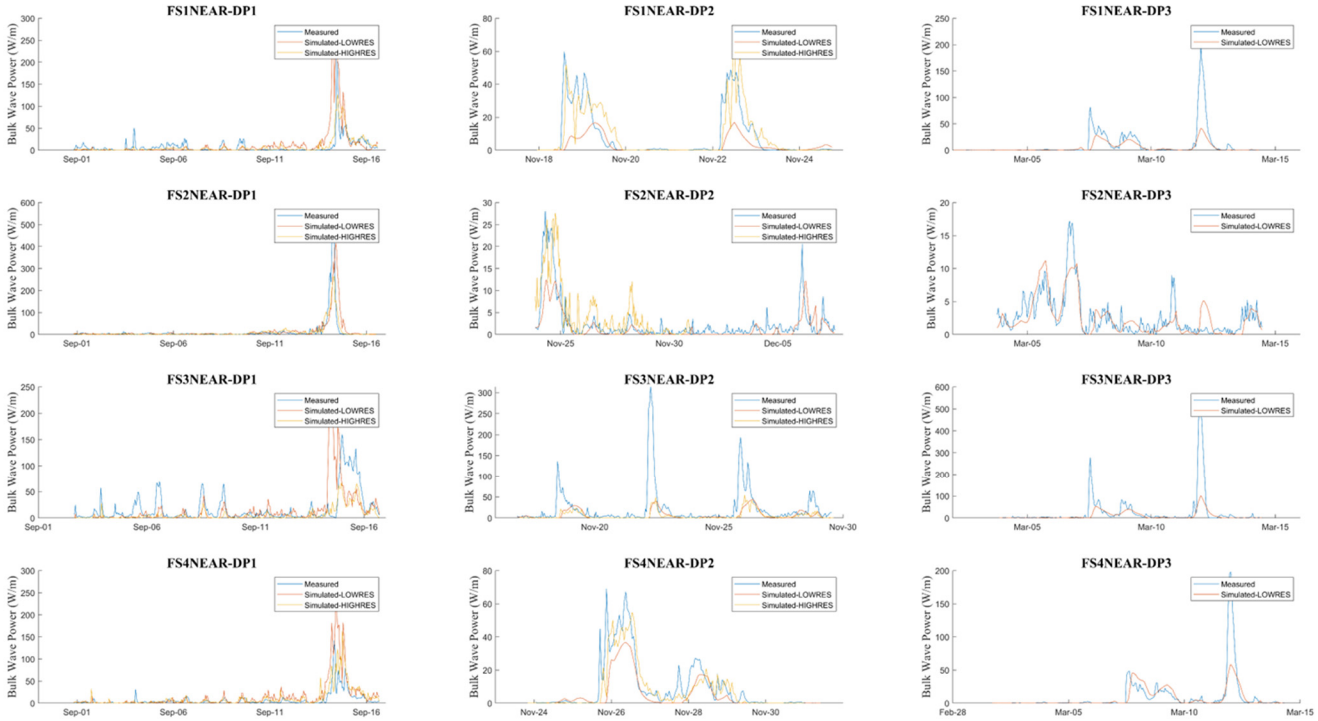

Figure 5.12: Wave power comparison between simulations and measurements for field campaigns 1-3 (DP1-3)

The simulation predicted the event-specific increased wave power during the field campaigns reasonably well, in both the high and low resolution models. During field campaign 1 (DP1) including hurricane passages, both low and high resolution models simulate averaged wave power reasonably well. The simulation underestimated the peak wave power values compared to measurements, especially at Field Site 3 for field campaigns 2 and 3 (DP 2, 3) during the cold front passages. The high resolution model showed improved prediction of peak values of wave power at Field Site 1 and Field Site 4 during the field campaign 2 when compared to the low resolution model. The possible causes of the discrepancy in wave power include the influence of wind input, differences in bathymetry and topography, model spatial grid resolution, ship wake occurrences from ship channels (Field Sites 2 and 3), and spectral resolution issues affecting the ability of the SWAN model to predict the wave period. The averaged wave power values for each field campaign are shown in **Figure 5.13**.

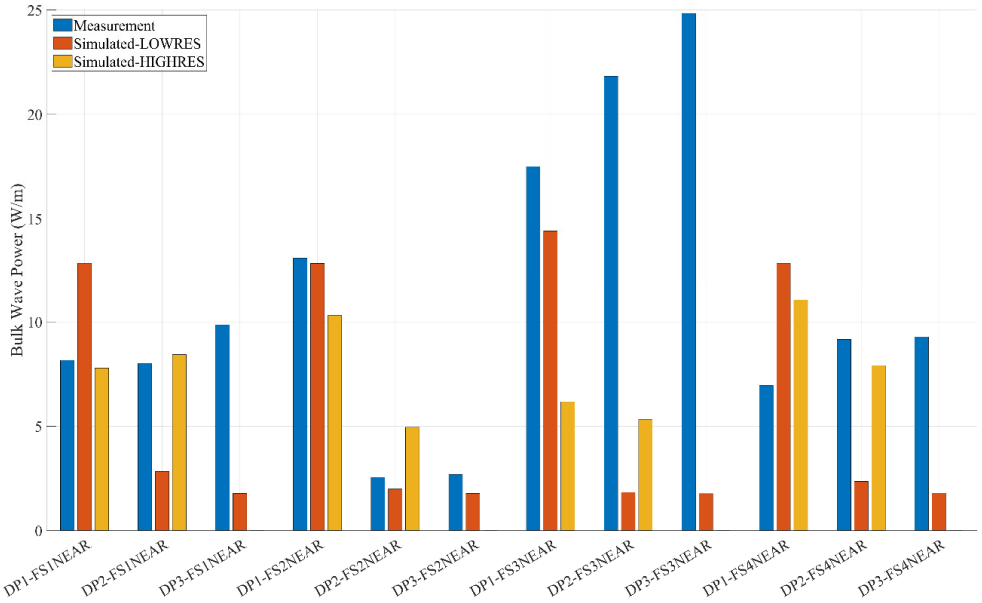

Figure 5.13: Averaged Wave power in the field campaign (DP) 1, 2 and 3

In the wave power calculations, water level, significant wave height, and mean wave period results are inputs. Thus, we verified the water level, significant wave height, and mean wave period results of the high-resolution model for the verification and calibration of the simulation model. Different wind input conditions are also tested for the high-resolution model. **Figure 5.14** shows the water level results of tide gauges near Galveston Bay.

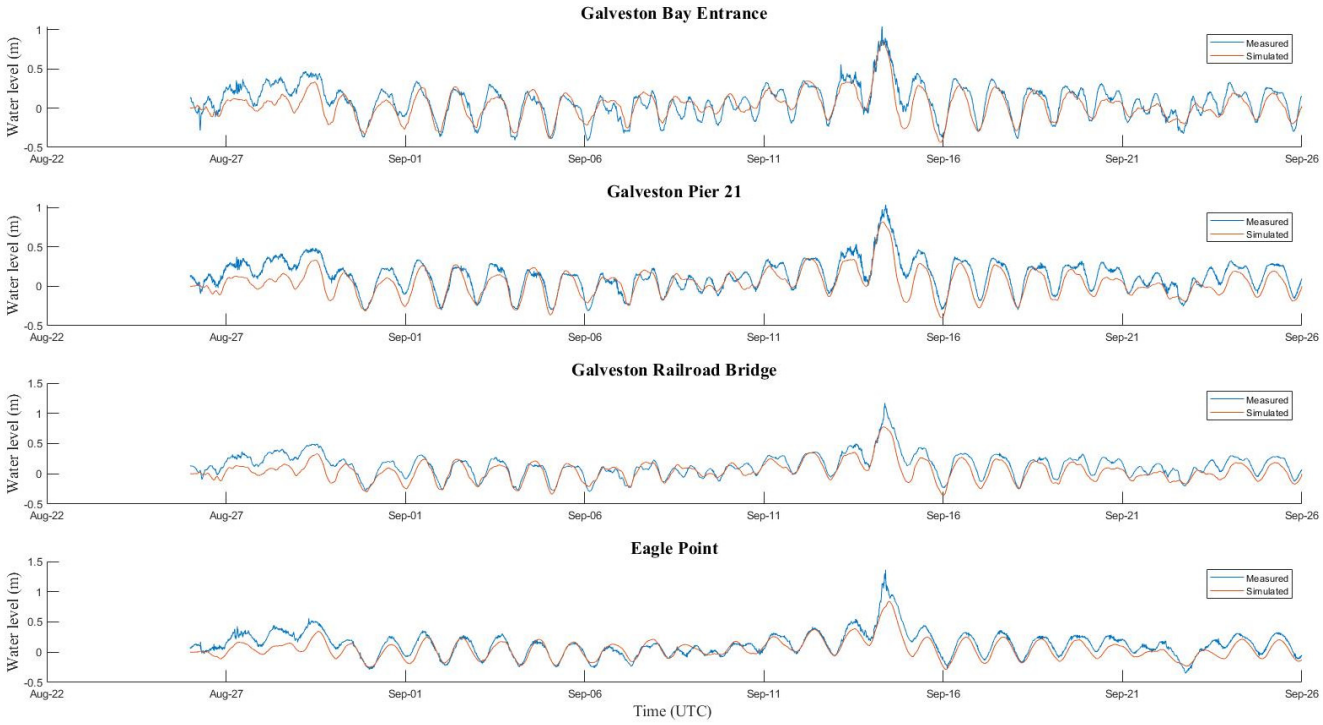

Figure 5.14: High resolution model water level results comparison with tide gauge data during the Field Campaign 1

The high-resolution model simulated tide level changes in Galveston Bay well, with low RMSE values. Model validation was quantified using the following skill metrics: Root Mean Square Error (RMSE, which is a measure of the magnitude of error, with an ideal value of zero), Coefficient of Determination (r^2, which describes how well a regression line fits a set of data, with an ideal value of one), Normalized Bias (which is a measure of the model's magnitude of overprediction or underprediction normalized to the observed value, with an ideal value of zero), Scatter Index (SI, which indicates how much the predicted variation pattern deviates from the observed one, with an ideal value of zero), and Mean Normalized Error (E_{NORM}, which is the mean error normalized by the mean observed value, with an ideal value of zero). The accuracy of model predictions of water level time series was summarized in **Table 5.4**.

Table 5.4: The accuracy of high-resolution model predictions of water level time series

Geographic location	Water level (m)			
	RMSE (m)	r^2	SI	E_{NORM}
Galveston Bay Entrance	0.09	0.73	0.0059	0.53
Galveston Pier 21	0.09	0.76	0.0004	0.56
Galveston Railroad Bridge	0.08	0.77	0.002	0.55
Eagle Point	0.07	0.81	0.0002	0.50

Mean wave period results were also compared with the measurement data as shown in **Figure 5.15**.

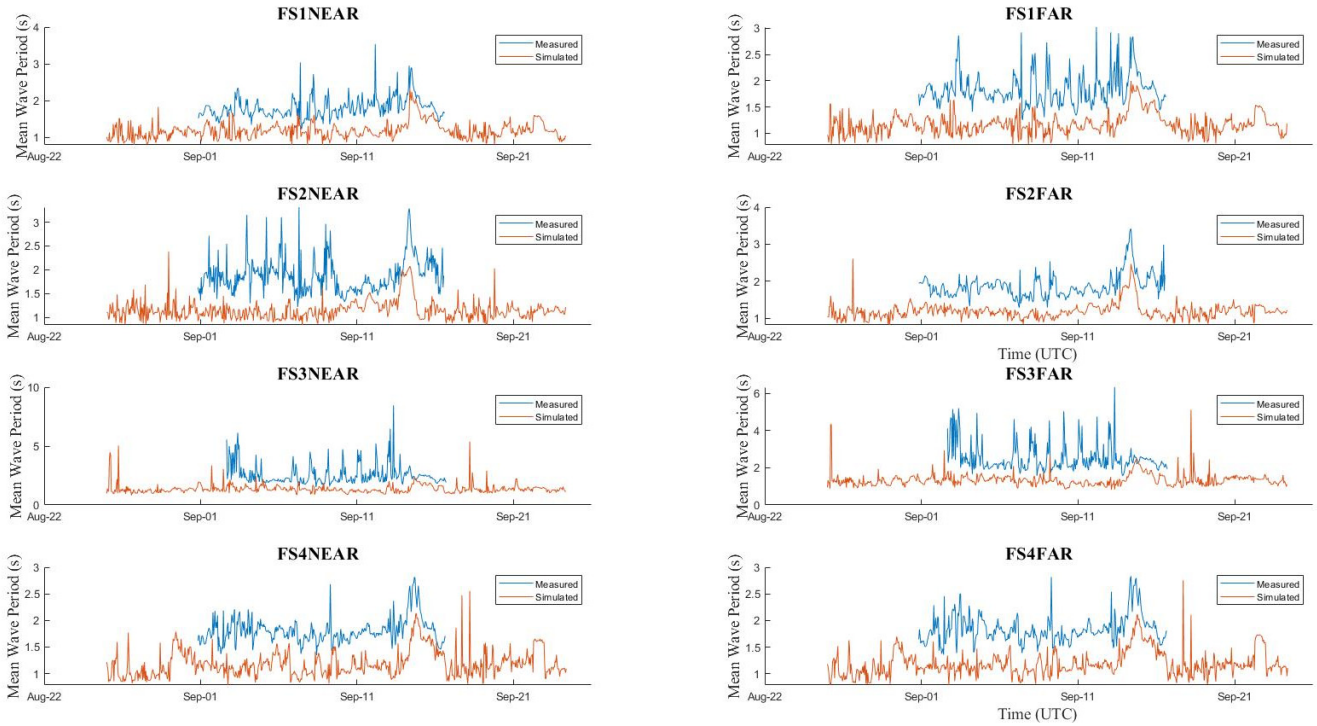

Figure 5.15: Mean wave period results from the high-resolution model in comparison with field measurements during the Field Campaign 1

Overall, the simulation overestimated the mean wave period for each measurement location. The average RMSE of all sites was 0.23 sec.

Significant wave height results were compared with different wind inputs (Local gust data and ECMWF-ERA5 reanalyzed wind forecast data). **Figure 5.16** shows the significant wave height results from simulations and measurements at each location.

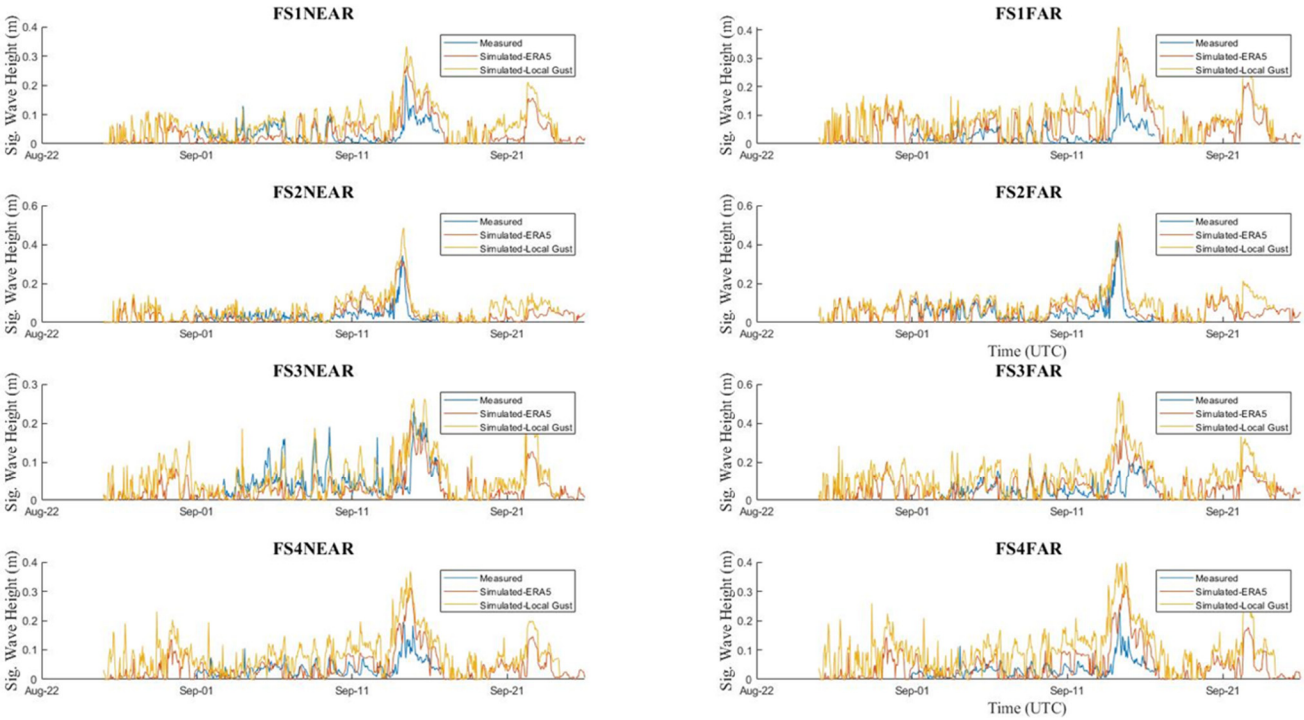

Figure 5.16: Significant wave height results from the high-resolution model with different wind conditions and their comparison with field measurements during the Field Campaign 1

Overall, the simulation estimated peak significant wave heights during the passage of Hurricane Nicholas relatively well. For the entire period, simulations slightly overestimated significant wave heights. Simulation using ERA5 wind input shows slightly better results. The average RMSE of all sites for ERA5 input was 0.046 m, whereas the average RMSE of all sites for local gust input was 0.054 m.

Modeled suspended sediment concentration estimates were compared with measurements during field campaign 1. The results of the measured suspended sediment concentrate (SSC) and the simulated SSC are shown in **Figure 5.17.**

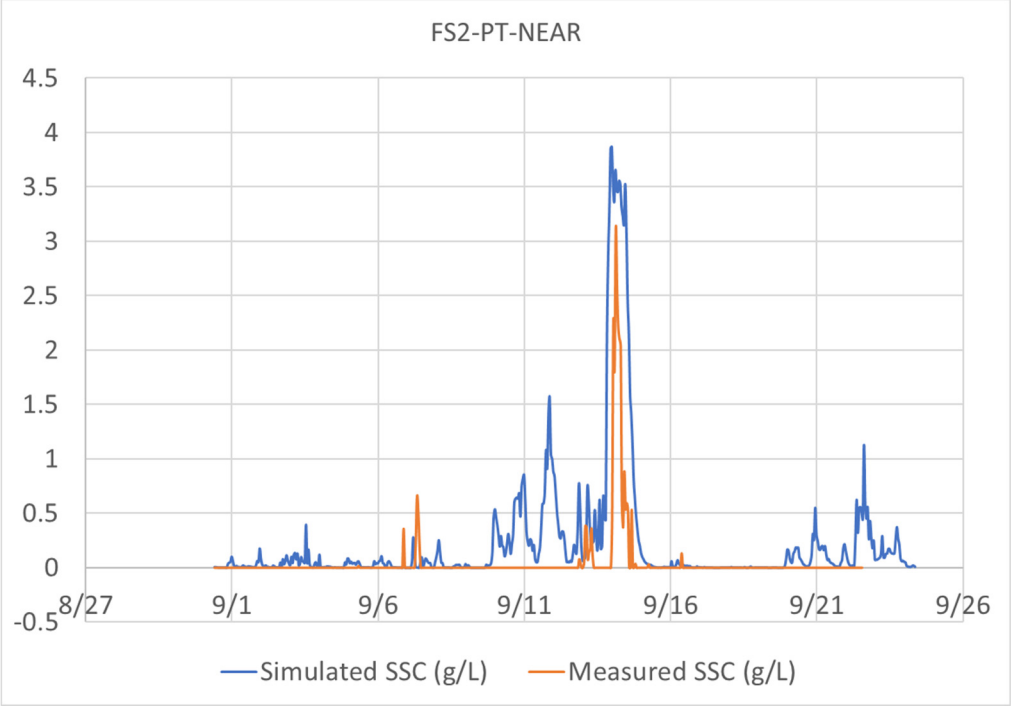

Figure 5.17: Modeled suspended sediment concentration (SSC) comparison with the measured data at Field site No.2 during the Hurricane Nicholas passage

The peak value between simulation and measurement matched relatively well during the hurricane (or tropical storm) passage. Since the implementation of the Delft3D model used is a depth-averaged model (two-dimensional horizontal), it does not accurately represent the SSC at the depth where the sensor is installed. Accordingly, we plan to validate the sediment transport model by comparing OBS data with simulated sediment transport results from other campaign periods. Furthermore, sediment properties were investigated based on the USGS's usSEABED database for Galveston Bay and MANERR area. **Figure 5.18** shows the D50 (median grain size, mm) of the sediment at Galveston Bay and MANERR area. The median grain size, sand, and mud fraction from the database can be used as an initial modeling input for sand (non-cohesive) and mud (cohesive) sediment properties information and can also be used as a parameter in erosion analysis.

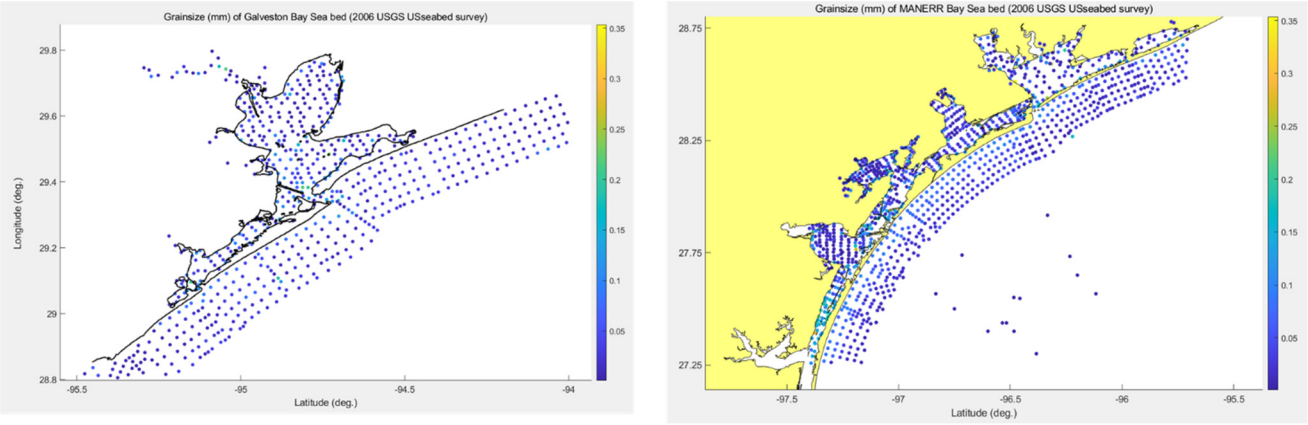

Figure 5.18: Median grainsize (mm) of Galveston Bay(left) and MANERR (right) based on the usSEABED database (https://www.usgs.gov/programs/cmhrp/science/usseabed)

Modeled significant wave height results were compared with measured significant wave height extracted from pressure transducer records in field campaign 4. The deployment period of *in-situ* measurements was from Jun 2nd to Jun 17th,2022. The results of the simulated and measured significant wave heights at FS1-FAR, FS2-NEAR, FS2-FAR, FS4-NEAR, and FS4-FAR are shown in **Figure 5.19.**

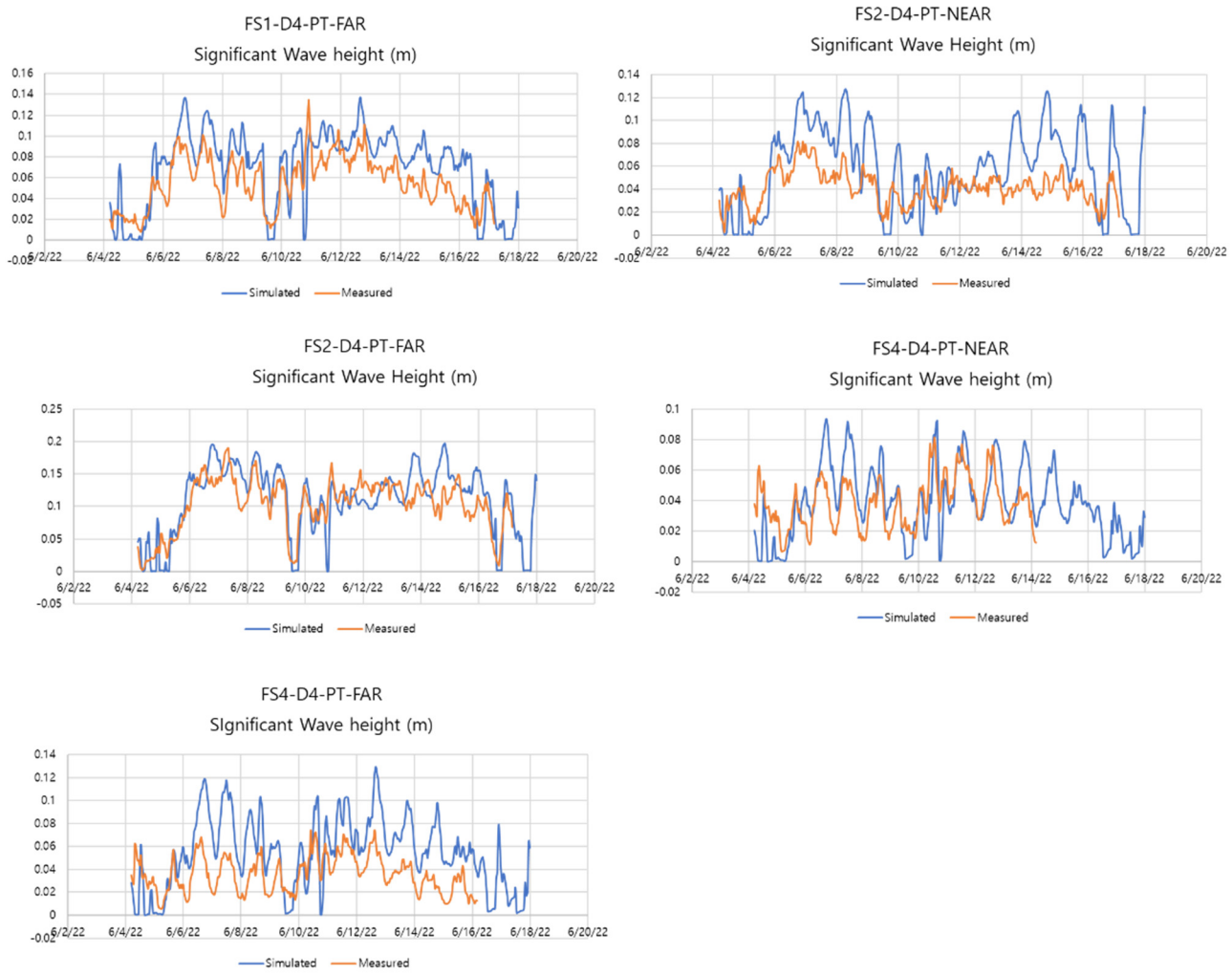

Figure 5.19: Modeled significant wave heights in comparison with the measured data at Field site 1,2 and 4 during the field campaign 4

The trends of significant wave heights between simulation and measurement matched relatively well during campaign No.4. Simulation tended to overestimate the significant wave height, especially at FS2-NEAR and FS4-FAR locations. Calculated RMSE of significant wave height at FS1-FAR, FS2-NEAR, FS2-FAR, FS4-NEAR, and FS4-FAR were 0.11 cm, 0.16 cm, 0.06 cm, 0.19 cm, and 0.16 cm, respectively. In all regions, significant wave height did not exceed 0.2 m. The place where the average significant wave height was the highest was FS2-FAR. Since Campaign 4 was conducted during the summer period, and there were no events such as cold fronts and hurricanes, overall wave energy was low. The maximum wind speed measured in the Galveston Bay area during the period was 9 m/s.

As a calibration process for the Mission-Aransas National Estuarine Research Reserve (MANERR) model, we modified the coverage of an intermediate model grid area to better encompass the location of tide gauge measurement. In addition, a portion of the model calibration process (the water level) was done with publicly available tide gauges. In the initial model of the MANERR area, this intermediate grid did not include Corpus Christi Bay and Matagorda Bay, which caused some discrepancy when modeled tide levels were compared to the tide gauge near the boundary in the initial model (i.e., 8773701 Port O'Connor, 8775237 Port Aransas). For this reason, the extent of the finer grid was adjusted to include Corpus Christi Bay and Matagorda Bay [**Figure 5.20(a)**]. Hindcast results in the model were improved in comparison with tide gauges, as shown in **Figure 5.20(b-c).**

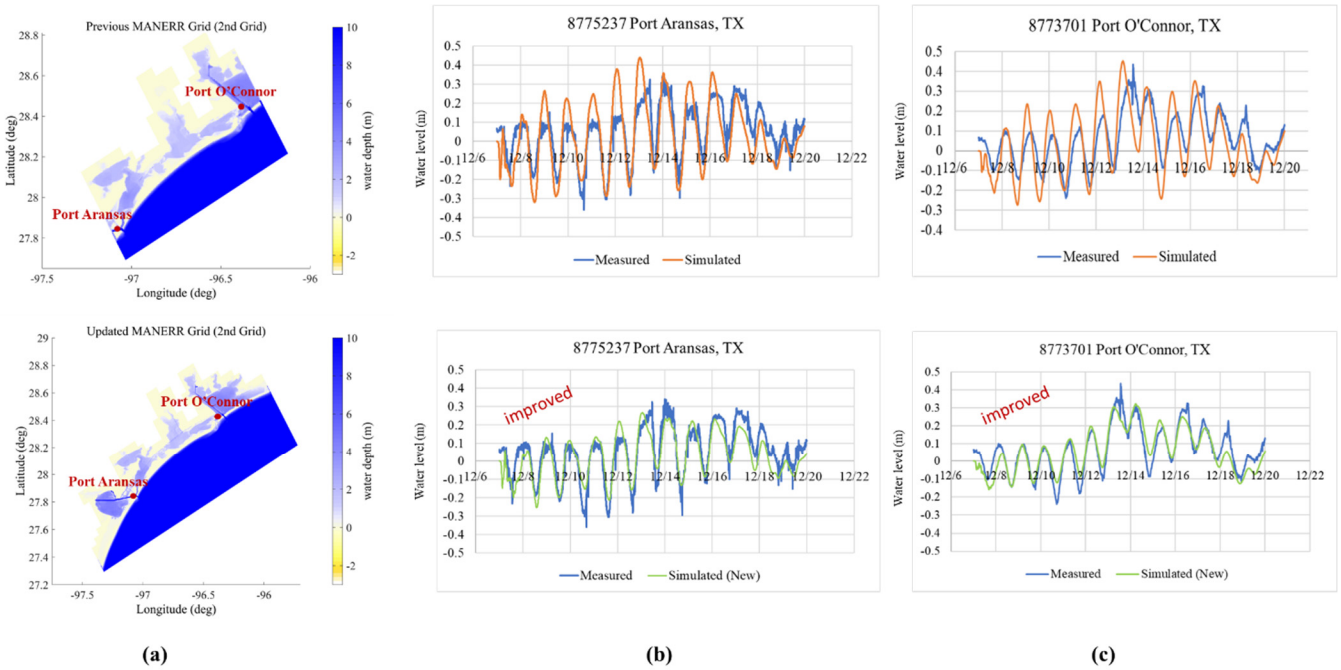

Figure 5.20: Previous and updated MANERR model grids (a) and tide simulation results with tide gauge record before (above) and after (below) grid update at Port Aransas, TX (b) and at Port O'Connor (c)

Simulation results of the Mission-Aransas National Estuarine Research Reserve (MANERR) area were compared to the wave measurement data collected by Dr. Rusty Feagin's research groups in the Department of Ecosystem Science and Management at Texas A&M University. The data collection period was from Feb 2020 to Apr 2020 for the Carancahua Pass area. Sensitivity tests for the Delft3D model covering the MANERR area were done. Originally there were two grids (Gulf of Mexico and MANERR area, **Figure 5.21**) in the simulation, and we added a domain (via domain decomposition) for the Carancahua Bay area as shown in **Figure 5.21b**. The MANERR model was tested for different wind input and grid resolutions with and without including the refined Carancahua Bay grid. The simulation results at the location of the field wave measurement were shown in **Figure 5.22.**

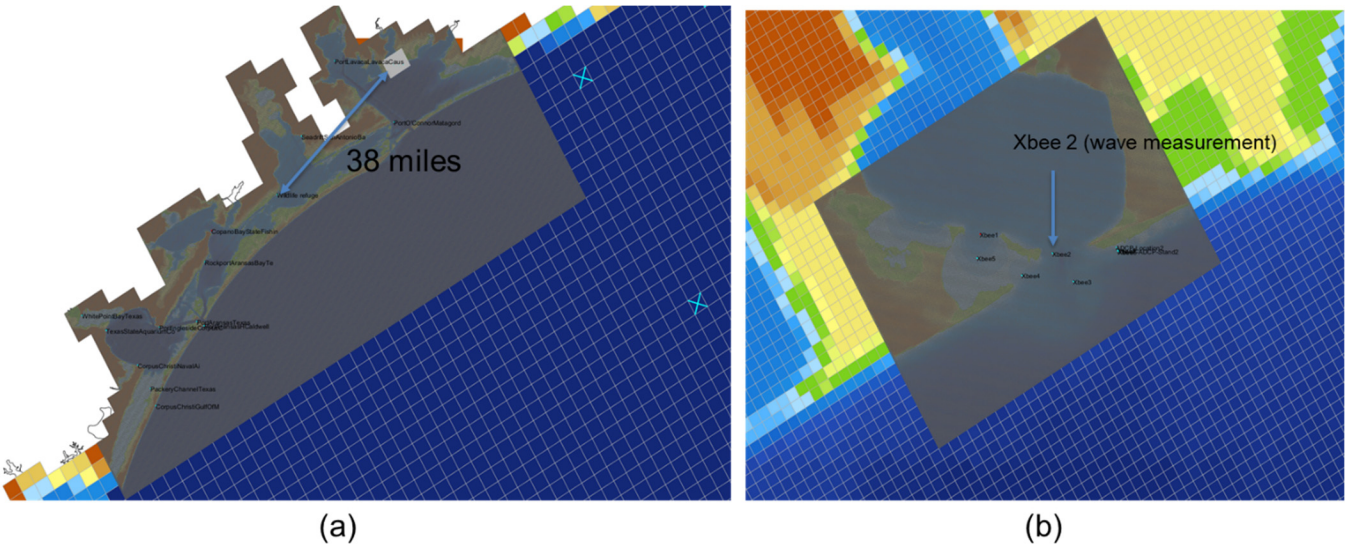

Figure 5.21: Delft3D model for MANERR area (a) including domain decomposed grid for Carancahua Bay (b)

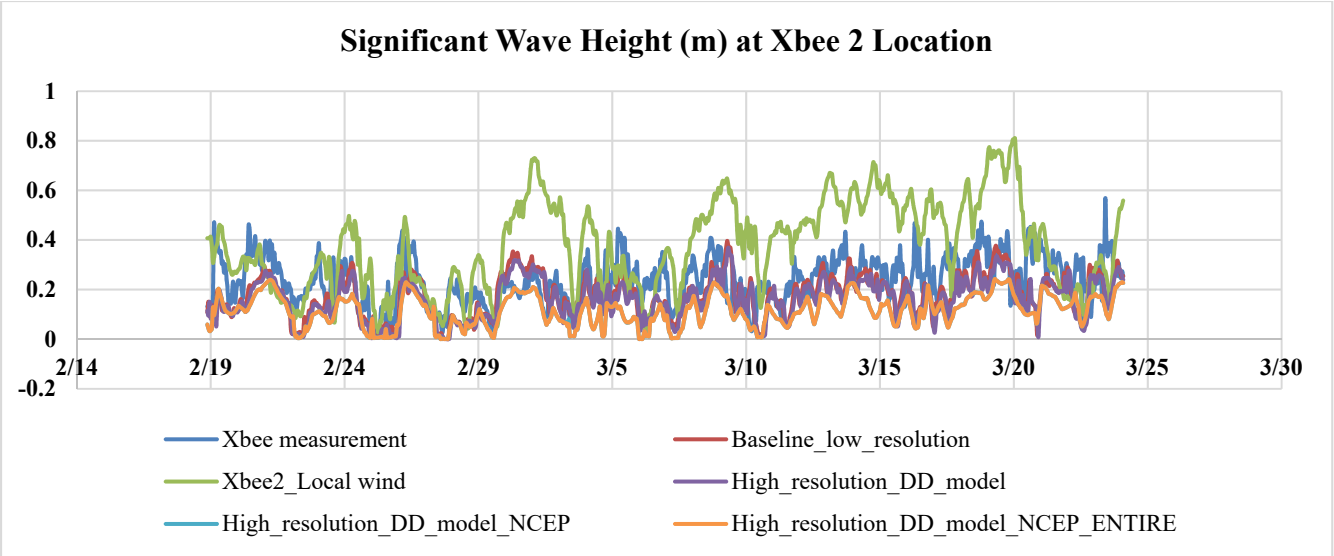

Figure 5.22: Model results of MANERR area (Carancahua pass) in comparison with measurements (Data Courtesy of Dr. Rusty Feagin)

Local wind at Aransas Wildlife Refuge (Station ID: 8774230) was used since no other adjacent wind station recorded winds during the measurement period. In the results in **Figure 5.22,** simulation using wind input from ERA5 (denoted "Baseline_Low_resolution") and NCEP (denoted "High_resolution_DD_model_NCEP") resulted in improved predictions of the significant wave height at the site than that resulting from using the local wind input ("Xbee2_Local wind results"). This is due to the fact that Carancahua Bay (the source of the local wind data) is located far away from the Aransas Wildlife Refuge wind station (38 miles, **Figure 5.21a**). Thus, the local wind data may not be representative of the wind environment at Carancahua Bay. Overall, the simulation underestimates the measurement results, and one possible cause of this is the neglected wind gust information in wind inputs from ERA5 and NCEP wind.

5.3 Long-term ensemble forecasts (to 2100) with and without climate change effects

To predict wetland erosion through the end of the present century, a one-year Delft3D simulation was conducted for selected individual years from 2025 to 2050 at 5-year intervals, and 2060 to 2100 at 20-year intervals. Wind data from a climate prediction model was used as model forcing. Three sea level rise scenarios are assumed.

5.3.1 Study area

The target regions are Galveston Bay and Mission-Aransas National Estuarine Research Reserve (MANERR), but the MANERR area has not yet been implemented due to limitations of computational resources at present. The erosion coefficient relating wave power to erosion was derived by linking the wave power result of the Delft3D simulation and the erosion estimates from satellite image analysis of the Galveston and MANERR regions. In the area where erosion values were derived from UAV images, the erosion results were predicted based on high-resolution simulation results and UAV erosion results using a domain-decomposed grid for computational efficiency.

5.3.2 Data and Methods

First, for the Galveston Bay area, a relationship between wave power and erosion from satellite images was derived based on the satellite image erosion data and long-term simulation results from the low-resolution Delft3D model. Landsat satellite images' time span is from 1984 to 2020. However, the low-resolution model can be used for year-long simulation due to the low computational cost. Thus, we used available simulation data from 2021 to 2022 (as averaged wave power data) and used erosion values by satellite images from 2009 to 2020, assuming that the annual erosion rate does not increase significantly.

For the MANERR area, we derived the wave energy transport in the MANERR area through wave simulation results. Then, we integrated the wetland erosion data, which was derived based on LANDSAT satellite imagery from 2009 to 2020. While the satellite data spans a period of approximately 10 years, simulations required more computational power to hindcast wave data over such an extended period. Therefore, we initially focused on simulating waves from February 16, 2020, to April 16, 2020, a timeframe for which we had field measurement data available for model validation. **Figure 5.23** presents the results derived from the wave power and erosion data, illustrating the rate of wetland erosion along the coast of the MANERR area.

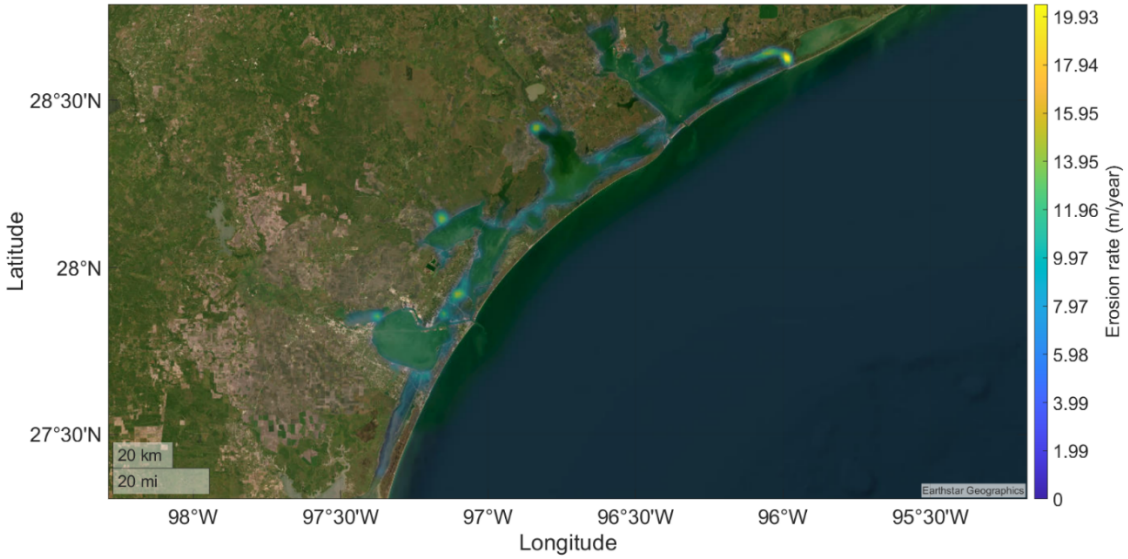

Figure 5.23: The erosion rate derived from the hindcast results of simulations and satellite images

The wave power (wave energy flux, or wave energy transport) is the major important parameter that decides the lateral erosion of wetland edges, as previously mentioned. Wave power P defined as:

$$P = \left(\frac{1}{8}\rho g H_s^2\right) C_g \cos\theta \tag{5.1}$$

where H_s is significant wave height, g is gravity, ρ is the water density, C_g is the wave group velocity, and $\cos\theta$ is mean wave direction relative to the cross-shore axis (axis normal to the shore). It is reported that the marsh erosion rate E is correlated to the averaged wave power, here we can define E as

$$E = CP \tag{5.2}$$

where C is the marsh erosion coefficient. We derived the marsh erosion coefficient C based on the Delft3D wave simulation (wave power output) with erosion data from remote sensing. The methodology to derive the erosion rate for the area is as follows: The code to derive the erosion rate iterates through each grid cell, seeking the corresponding erosion data from the satellite dataset for each cell. If data matching the cell's location is found within a predefined distance threshold (currently 0.003 degree = approximately 330 m), that erosion quantity is stored in an array alongside the wave power for that area. Subsequently, each dataset is plotted, and the erosion rate is extracted using linear regression.

In addition, space-varying erosion coefficients are also derived for application to site-specific future erosion rate estimation. **Figure 5.24** shows a schematic diagram of the process to determine the site-specific future erosion rate.

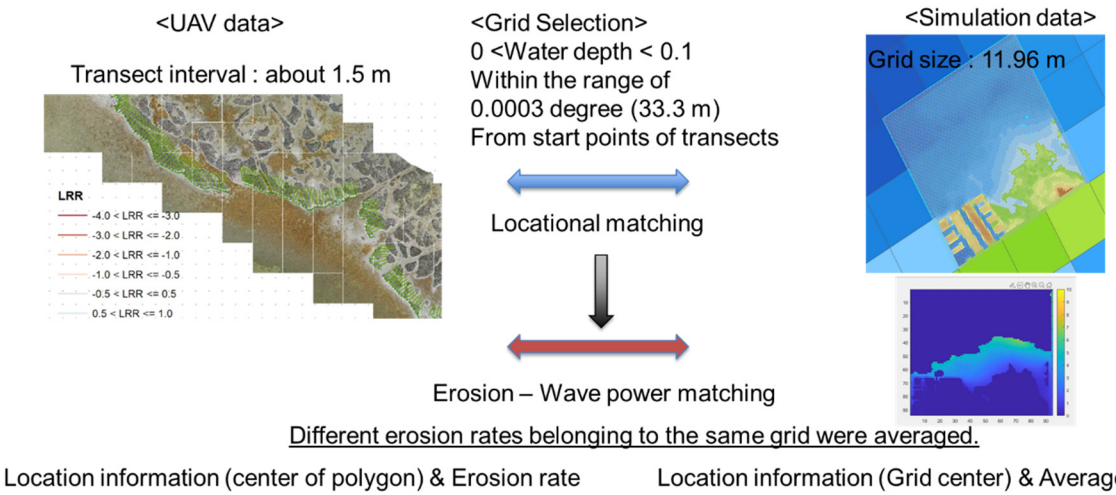

Figure 5.24: a schematic diagram of the process to determine the site-specific future erosion rate using UAV and simulation results

Figure 5.25 shows the boxplot of the erosion coefficient for Galveston Bay, Site 1, Site 2, Site 4, and MANERR area.

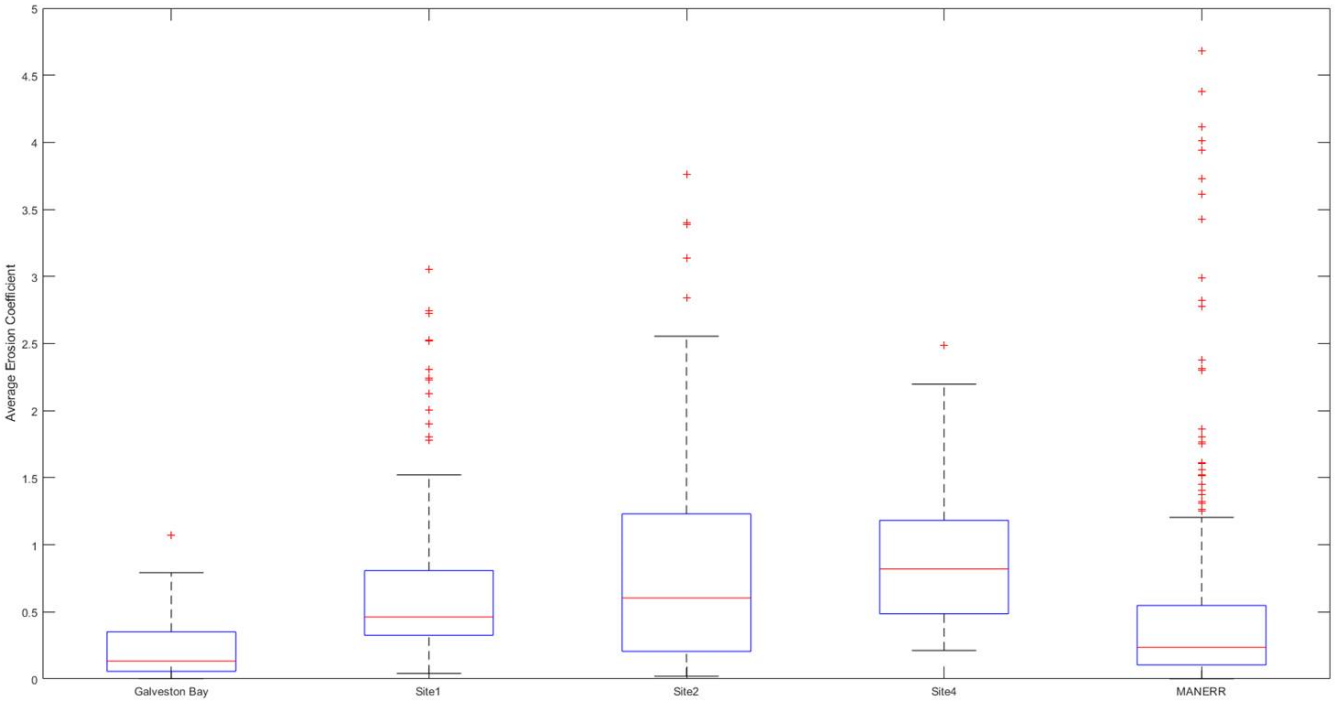

Figure 5.25: Boxplot of erosion coefficient (m^2/(W·yr)) for Galveston Bay, Site 1, Site 2, Site 4, and MANERR area.

Without filtering, no clear linear relationship was observed between wave power and erosion rate. It was necessary to analyze the spatial consistency between the data, the uncertainty of the erosion value, and the simulation resolution to provide guidance in filtering outliers. In the erosion rate–wave power locational matching, data in more than 0.5 m water depth were excluded to avoid selection of deeper water area. From the linear fit of the wave power-erosion plot, an erosion coefficient C was then determined for each area. Derived erosion coefficients for Galveston Bay, Site 1, Site 2, Site 4, and MANERR area were 0.17, 0.42, 1.11, 0.79, and 0.25 m^2/(W·yr), respectively. The erosion coefficient derived from UAV image erosion analysis with simulation tends to be higher than that derived from satellite image erosion analysis. The coefficient is then used for future simulation results to estimate the potential wetland boundary erosion.

5.3.3 Method of future simulation for long-term ensemble forecasts

We used the HADGEM3-GC31-HM (high resolution) future global forecast data to simulate future wave conditions in the Galveston Bay area. The HadGEM3-GC31 data is the third Hadley Centre (U.K.) Global Environment Model in the Global Coupled configuration 5.1.

As mentioned above, three relative sea-level rise scenarios (depicted as “no sea level rise,” “intermediate,” and “high”) are selected. The “Intermediate” scenario is based on the sea level projection data of the intermediate scenario (SSP2-4.5, 50 quantiles) from the IPCC 6th Assessment Report (AR6). The “high” scenario is based on the intermediate sea level projection data at Galveston Pier 21 from the Interagency Sea Level Rise Scenario Tool by NASA. The interagency relative sea level rise projection based on Galveston Pier 21 tide gauge includes the effects of land subsidence and vertical land motion in the Galveston Bay area (Liu et al., 2020). **Table 5.5** shows the projected relative sea level rise values for each scenario that was used in the simulation. In the year-long simulation, the corresponding sea level rise value was applied to the entire grid, and all other input and parameters were performed under the same conditions.

Table 5.5: Sea level rise projection setting for each scenario

	2020	2025	2030	2035	2040	2045	2050
No sea level rise	0	0	0	0	0	0	0
Intermediate (m)	0.049	0.071	0.093	0.118	0.142	0.173	0.204
High (m)	0.049	0.103	0.157	0.216	0.275	0.338	0.401

The global climate model (GCM) was analyzed to prepare future ocean wave simulations based on the calibrated Delft3D and

SWAN model. We generated a future wind field grid for the Delft3D model for the Gulf of Mexico region using the "HadGEM3-GC31-HM" model and primarily tested the future wind climate at the location of the Galveston Bay area. The model assesses various aspects of the historical climate system in simulations against observations. The U (west-to-east) and V (south-to-north) components of wind velocity at 10 m surface were extracted in the period from 2015 to 2050. The atmosphere grid's resolution is 50 km, and the temporal resolution is 3 hours. The model results are based on high resolution sea surface temperature/sea-ice driven CMIP5 RCP 8.5 simulations and a scenario as close to RCP8.5 as possible within CMIP6. **Figure 5.26** shows the yearly averaged wind velocity near the Galveston Bay area from 2020 to 2050.

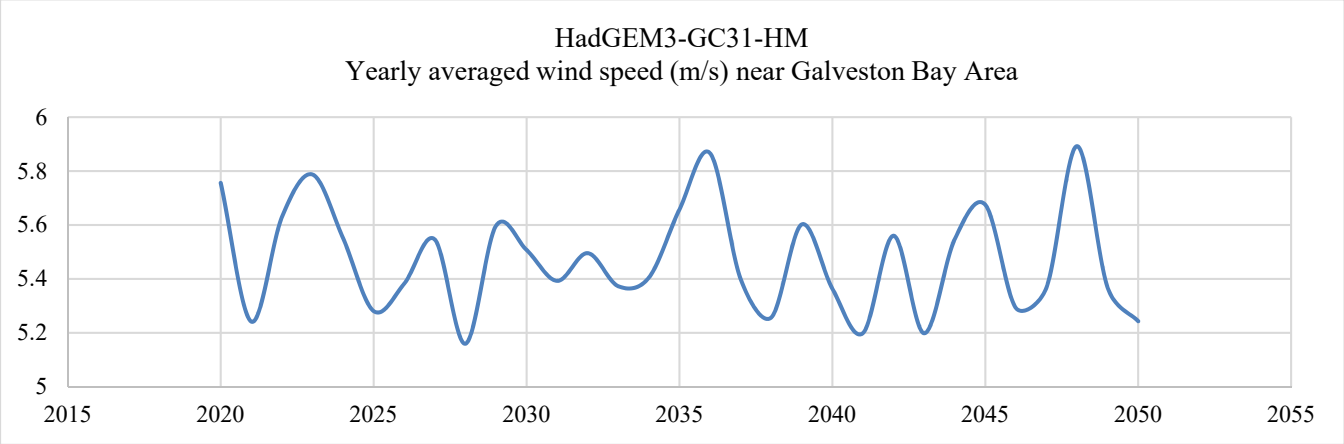

Figure 5.26: Yearly averaged future wind velocity near the Galveston Bay area

Based on the results, there is a periodic movement from 5.2 m/s to 5.8 m/s by year, and the peak value does not increase significantly even in the worst-case scenario (RCP 8.5), but the highest averaged wind speed (more than 5.8 m/s) appears as the year passes at the year 2036 and 2048.

Wave power calculation comparison was tested between "No sea level rise" and "Sea level rise" model. Test runs for 2025 using HADGEM3-GC31 with and without sea level rise were done for Galveston Bay & Gulf of Mexico. The simulation results for the significant wave height with and without sea level rise effect are shown in **Figure 5.27.**

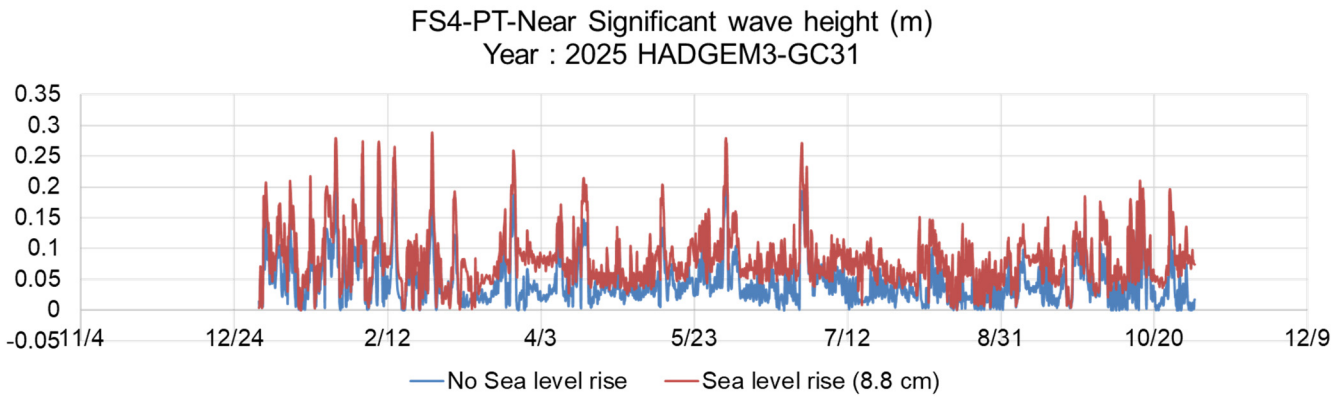

Figure 5.27: Significant wave height results comparison between No sea level rise and sea level rise model

The significant wave height of the sea level rise model was always higher than that of the no-sea-level-rise model during the entire future simulation year 2025. Averaged wave power in the future simulation was compared to hindcast results for the period of 2019-2020 and 2020-2021, as shown in **Figure 5.28**.

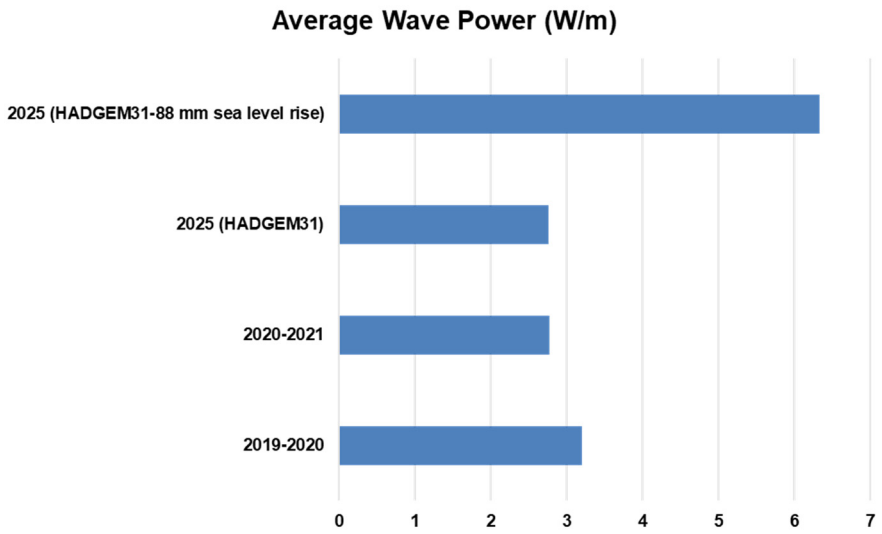

Figure 5.28: Wave power comparison between future and hindcast simulation model results at the local site (FS4)

In the yearly averaged wave power results, the averaged wave power values were similar (2.76 - 5.20 W/m) among the 2019-2020, 2020-2021 hindcast, and 2025-year future simulation as shown in **Figure 5.28**. In the sea level rise model, the average wave power doubled to 6.33 W/m. However, this calculation does not consider the effect of wave "overshooting." If the instantaneous water level is higher than the height of the edge of the wetland, the wave thrust on the wetland decreases sharply due to wave "overshoot" (Tonelli et al., 2010). We adjusted wave power by setting P = 0, during the submergence of the local wetland platform (when the water level exceeds 0.2 m) by high tide to get the effective wave power. The average wave power was recalculated based on the adjustment. The average wave power of 2025 HADGEM31 no-sea-level-rise model decreased from 2.76 W/m to 1.06 W/m and the average wave power of 2025 HADGEM31 sea level rise model (88 mm) decreased from 6.33 W/m to 0.76 W/m. The decrease of wave power in sea level rise was much higher than the no-sea-level-rise case due to the increased frequency of submergence of wetlands platform by high tides. However, the decreased amount in wave power is determined by the threshold value for wetland platform flooding, currently set as 0.20 m—further investigation of these threshold values and adjustments need to be done.

Different climate models were investigated to simulate the years from 2050 to 2100 and compare the wave energy sensitivity among different climate models with varying resolutions. Simulations for the years 2020 to 2050 for the Galveston Bay area were done using HADGEM3-GC31-HM data. Here, we compared the HADGEM3-GC31 model to NOAA-GFDL (Geophysical Fluid Dynamics Laboratory) - ESM4 (Earth System Model 4.0) model for the wind field data covering the Galveston Bay area. The GFDL-ESM4 has approximately a 1-degree resolution for future atmospheric conditions and includes comprehensive revisions of atmospheric dynamics. Wind field outputs from HADGEM3-GC31 (0.25-degree resolution) and NOAA-GFDL-ESM4 are shown in **Figure 5.29**.

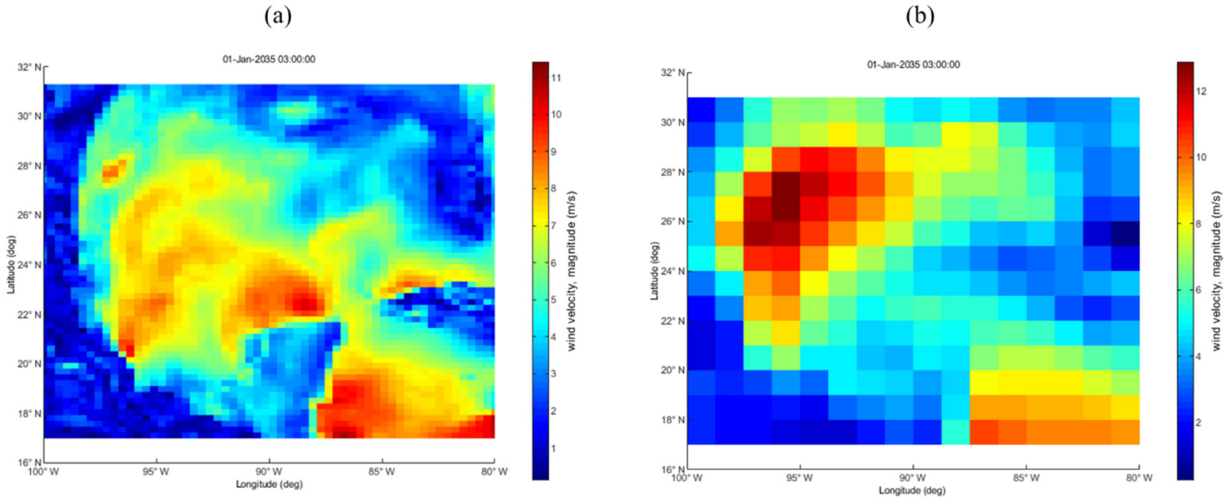

Figure 5.29: Wind field comparison between (a) HADGEM3-GC31 and (b) NOAA-GFDL-ESM4 model

Wind data of two models at Galveston Bay was compared for the future forecast year of 2035 to verify the differences by model and resolution. The average wind velocity near Galveston Bay was 5.64 m/s and 4.67 m/s in HADGEM3-GC31 and NOAA-GFDL-ESM4 models. NOAA-GFDL-ESM4 model was used for the future wave-erosion estimate of wetlands from 2060 to 2100 since these years were not available in HADGEM3-GC31 databases. **Table 5.35.2** shows the projected relative sea level rise values for each scenario from 2050 to 2100 at 20-year intervals based on the IPCC AR6 report ('Intermediate' scenario) and sea level projection data at Galveston Pier 21 ('High' scenario).

Table 5.6: Sea level rise projection setting for each scenario from 2050 to 2100

	2050	2060	2080	2100
No sea level rise	0	0	0	0
Intermediate (m)	0.204	0.262	0.403	0.556
High (m)	0.401	0.54	0.887	1.36

Each value was applied to the entire domain, including the Gulf of Mexico and Galveston Bay. Each simulation uses wind data for the year generated by the NOAA-GFDL-ESM4 future climate model. Simulations for each scenario were performed at 20-year intervals from 2060 to 2100 based on sea level rise projection in Table 5.1.

5.3.4 Results

Future projected “Intermediate” erosion rate results using constant erosion coefficient for the Galveston Bay area, Field Site 1, Field Site 2, and Field Site 4 are shown in **Figs. 5.30, 5.31, 5.32**, and **5.33**, respectively. In order to display only the area at the boundary of the wetland, only areas with a water depth between 0.05 m and 0.5 m (0 m to 0.1 m for Field Sites 1, 2, and 4) were displayed. However, it can be confirmed that the active area is changing according to the year as a result of the increase in water depth as the sea level rises. In this case, the wetland boundary may be completely inundated, so caution is required in future wetland erosion calculations. The possibility of sediment accumulation and complete inundation of wetland areas are not taken into account in the current erosion rate calculations.

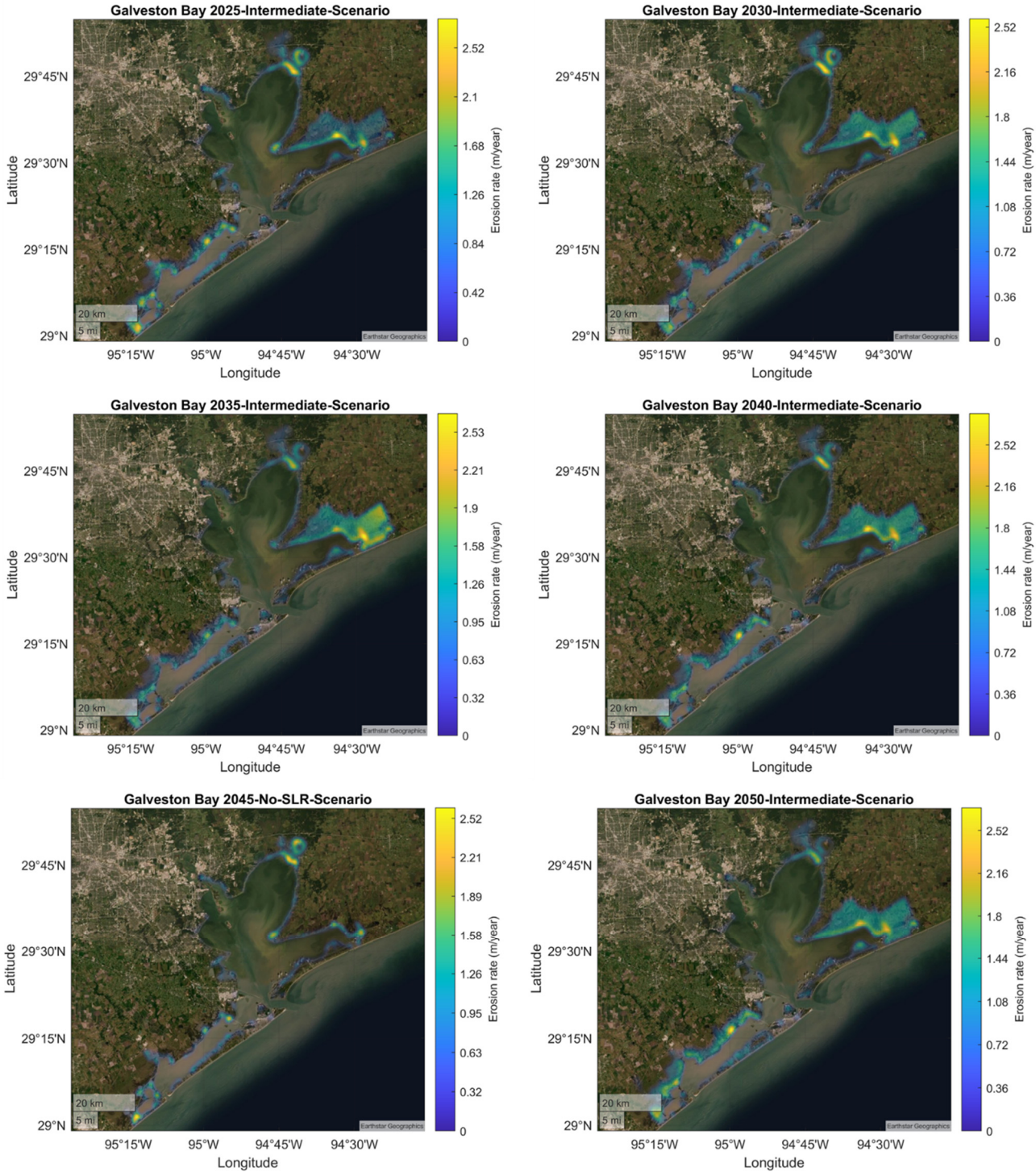

Figure 5.30: The future erosion rate for Galveston Bay based on simulations of "intermediate" scenarios from 2025 to 2050 (5-year interval)

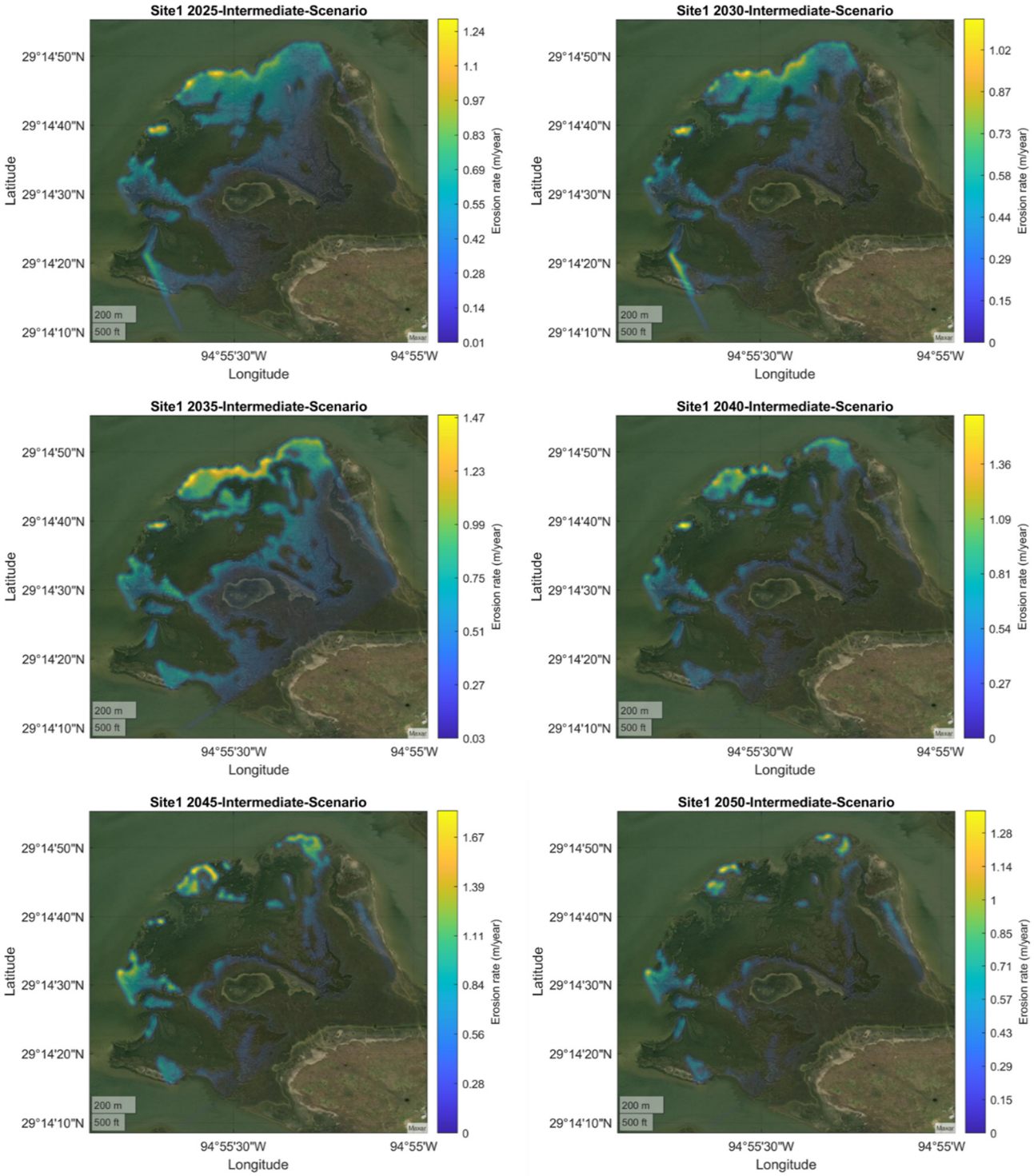

Figure 5.31: The future erosion rate for Field Site 1 based on simulations of "intermediate" scenarios from 2025 to 2050 (5-year interval)

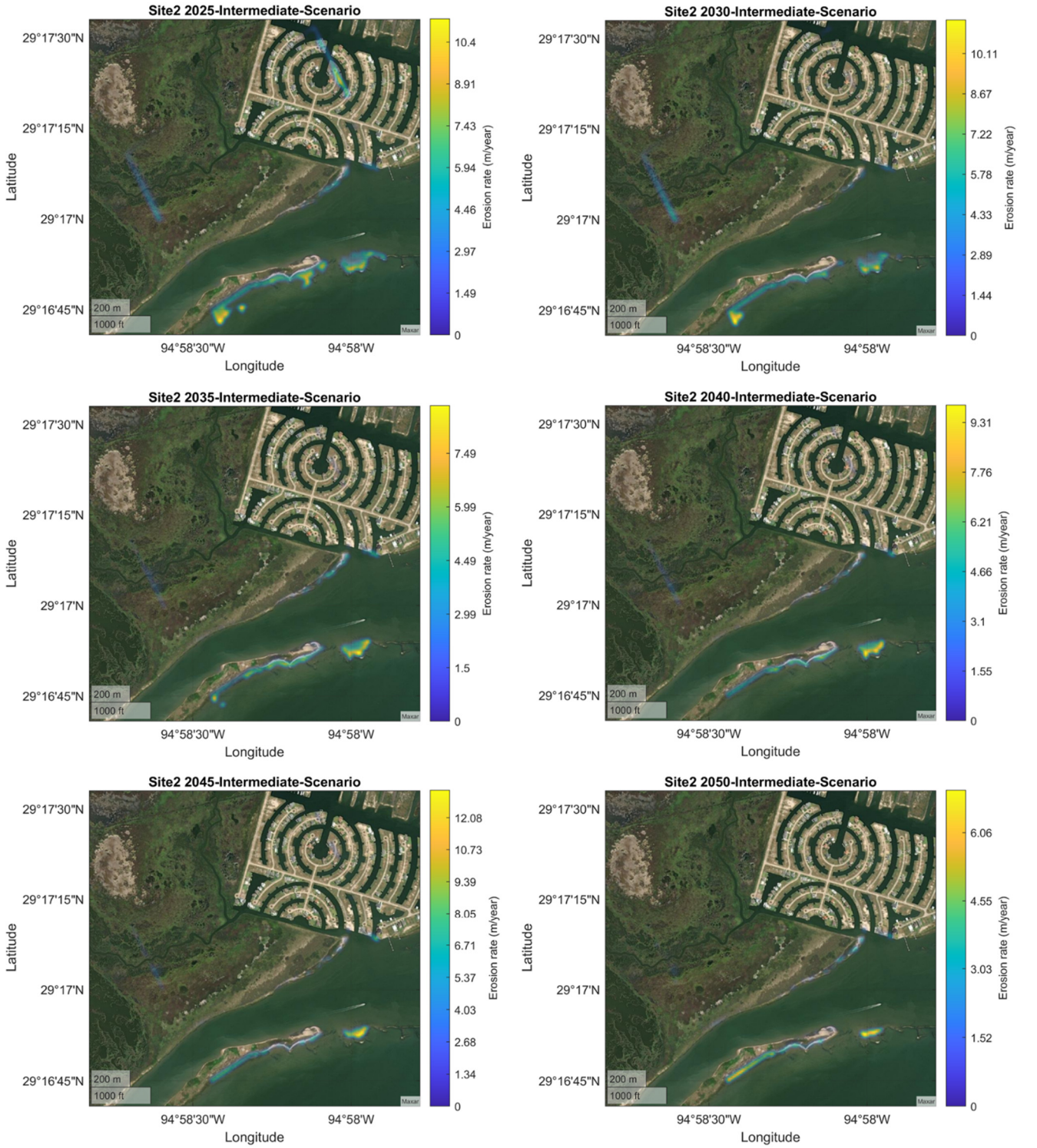

Figure 5.32: The future erosion rate for Field Site 2 based on simulations of "intermediate" scenarios from 2025 to 2050 (5-year interval)

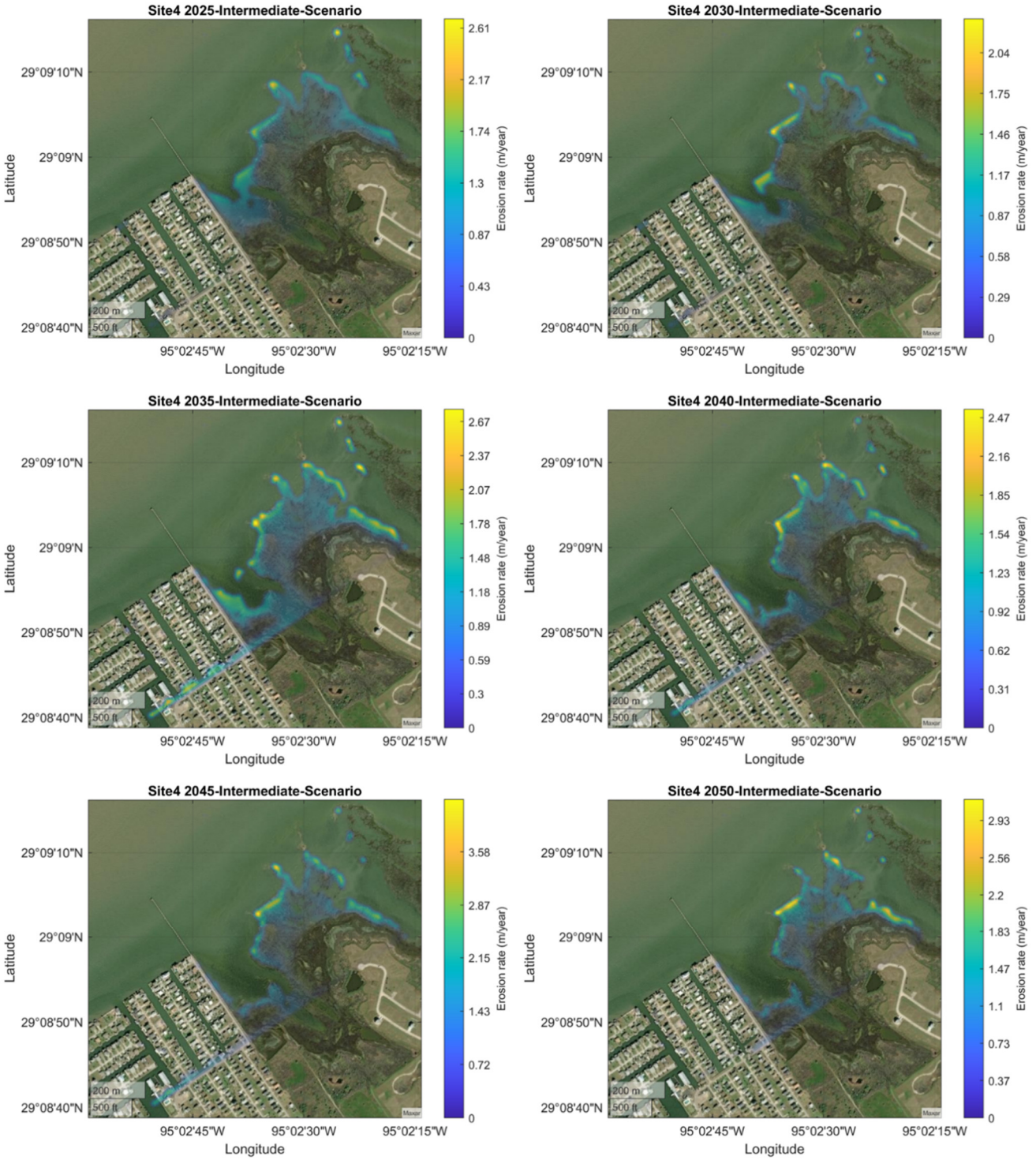

Figure 5.33: The future erosion rate for Field Site 4 based on simulations of "intermediate" scenarios from 2025 to 2050 (5-year interval)

Figures 5.34, 5.35, 5.36, and **5.37** show the average erosion rate (year/m) of the active area by scenario and year calculated for Galveston Bay, Field Site 1, Field Site 2, and Field Site 4, respectively.

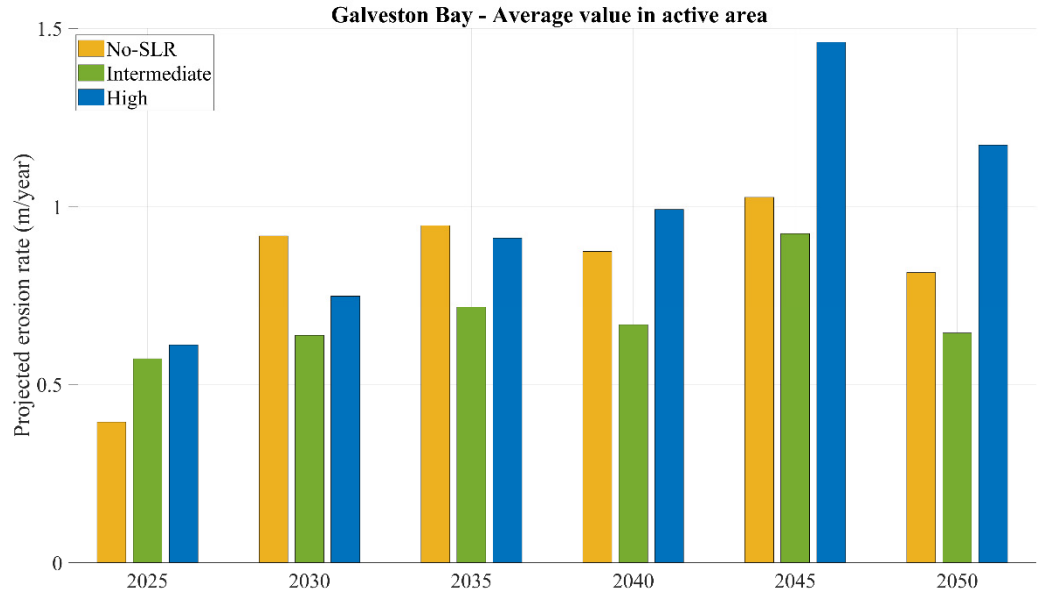

Figure 5.34: Projected erosion rate for Galveston Bay by scenario and year

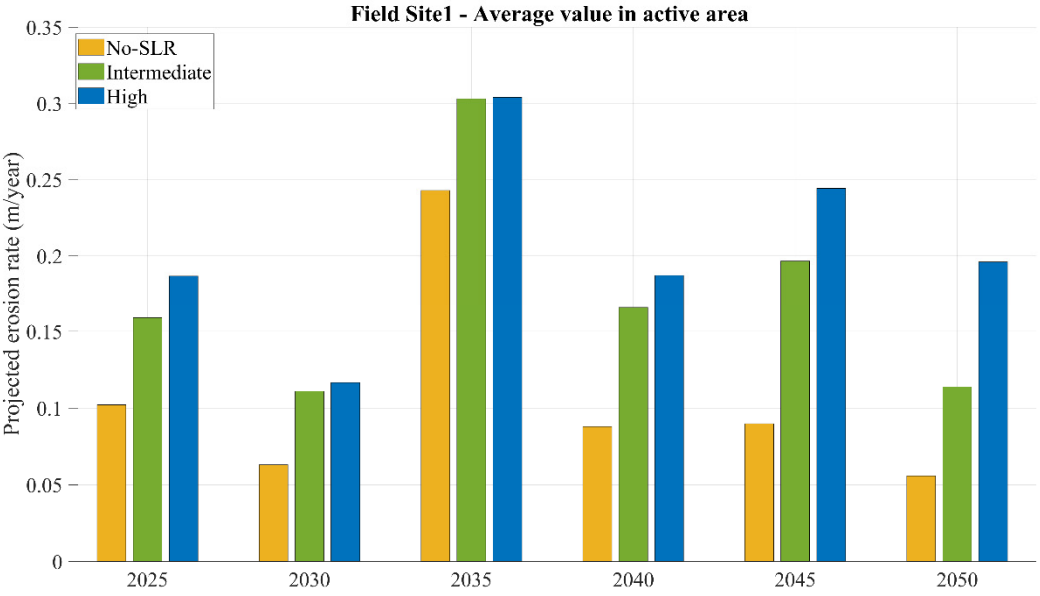

Figure 5.35: Projected erosion rate for Field Site 1 by scenario and year

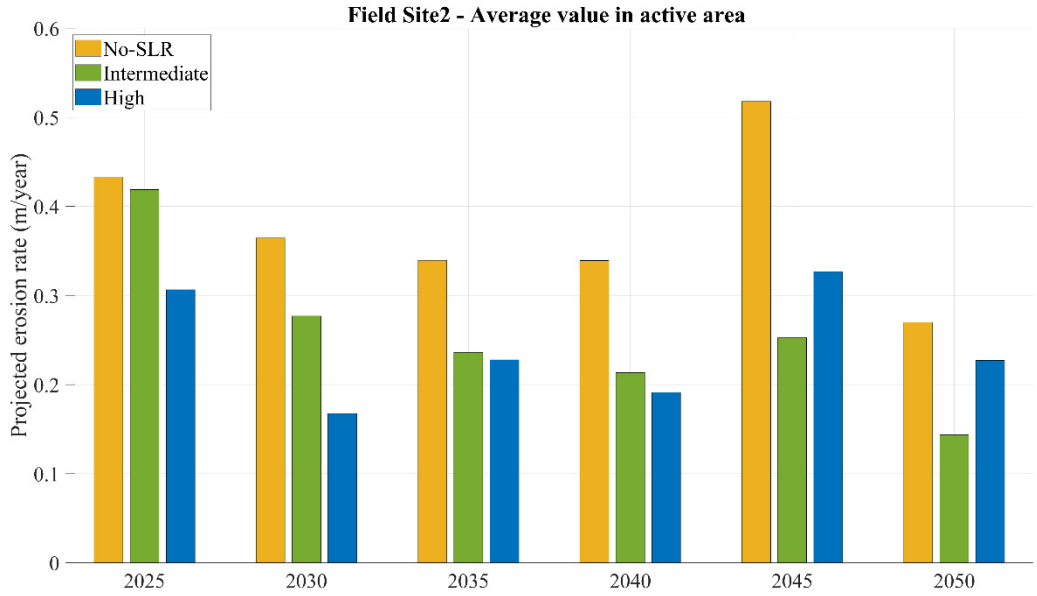

Figure 5.36: Projected erosion rate for Field Site2 by scenario and year

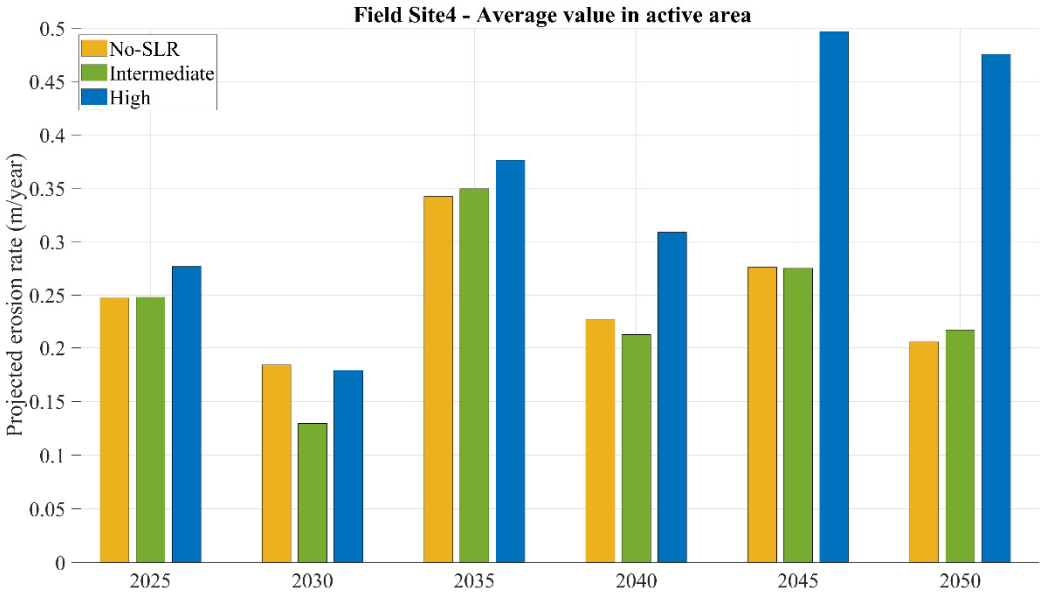

Figure 5.37: Projected erosion rate for Field Site4 by scenario and year

It was confirmed that the average erosion rate in the coastal region of Galveston Bay at a water depth of 0 to 0.5 m increased in the high scenarios of 2045 and 2050 (**Figure 5.34**). In Field Site 1 (**Figure 5.35**), the average erosion rate increased year by year with sea level rise. At Field Site 2, the average erosion rate tends to decrease gradually over the years (**Figure 5.36**). Field Site 4's average erosion rate increase due to the high scenario in 2040, 2045, and 2050 was significant (**Figure 5.37**). However, it is possible that all these results were affected by the change and reduction in the active area, so caution is needed in their interpretation. The final product considering these variables was applied to the future wetland evolution map.

Different scenarios from the Delft3D-modeled future wave climate were inter-compared at different sites, using five -year intervals spanning 2025-2050. We selected a transect aligned with our measurements (pressure transducers deployed in the field campaign) at each site and compared the averaged wave power for each year and scenario. **Figure 5.38 to Figure 5.40** show the average wave power plot along the transect in different scenarios and years at Field Site 1, Site 2, and Site 4.

(a) Delft3D Grid & Shore-normal line

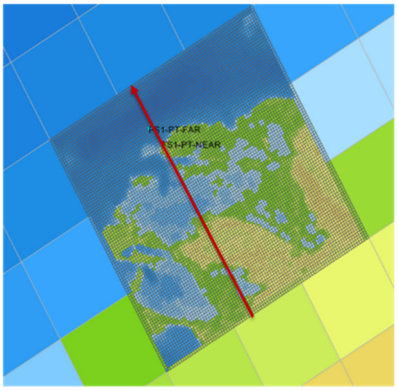

(b) Delft3D future simulation results (Average wave power plot)

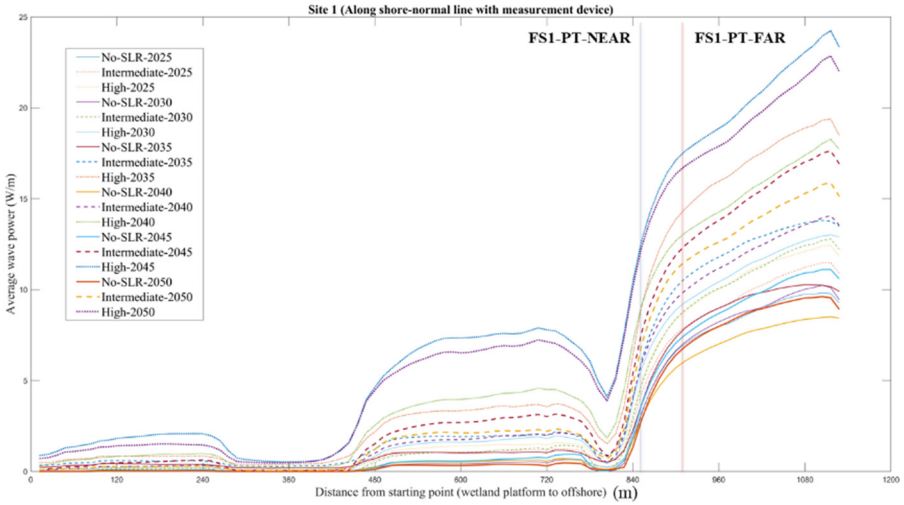

Figure 5.38: (a) shore-normal line and (b) future simulation results on the line at Field Site 1

(a) Delft3D Grid & Shore-normal line

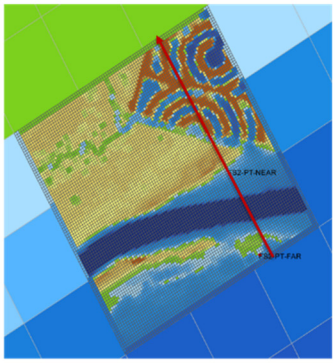

(b) Delft3D future simulation results (Average wave power plot)

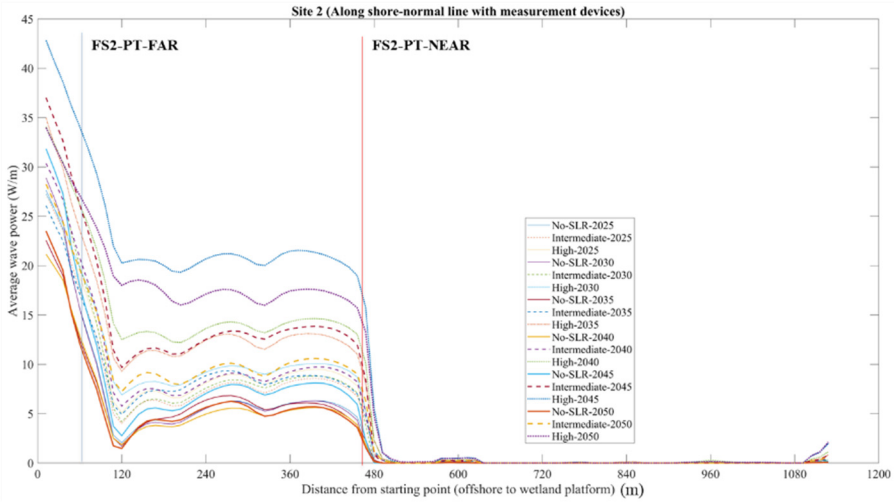

Figure 5.39: (a) shore-normal line and (b) future simulation results on the line at Field Site 2

(a) Delft3D Grid & Shore-normal line

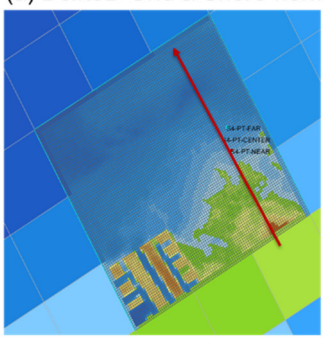

(b) Delft3D future simulation results (Average wave power plot)

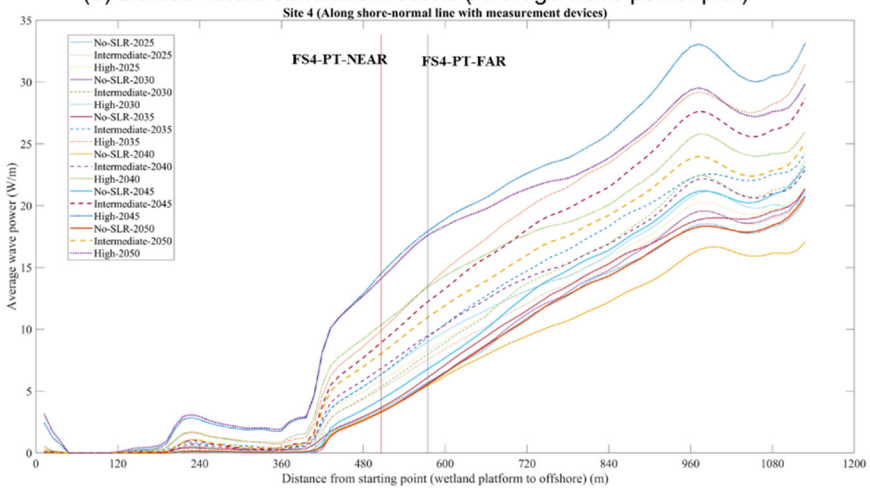

Figure 5.40: (a) shore-normal line and (b) future simulation results on the line at Field Site 4

The average wave power along the shore-normal line was highest in the "High-2045" scenario, and the second highest average wave power occurred in the "High-2050" scenario. The average wave power of the two highest scenarios significantly differs from other years and scenarios. The scenario with the lowest average wave power was "No-SLR-2040". As the sea level rises, the wave power tends to increase in the sites of interest. In the absence of sea level rise, there is no trend in the difference in average wave power values for each year.

To distinguish between wetland areas and non-wetland areas, we used a geo-database from "NOAA Coastal Change Analysis Program - Wetland Potential Layer" (https://www.fisheries.noaa.gov/inport/item/48357) and applied their classification to future ensemble forecast results. Results after the classification of wetland areas are shown in **Figure 5.41.**

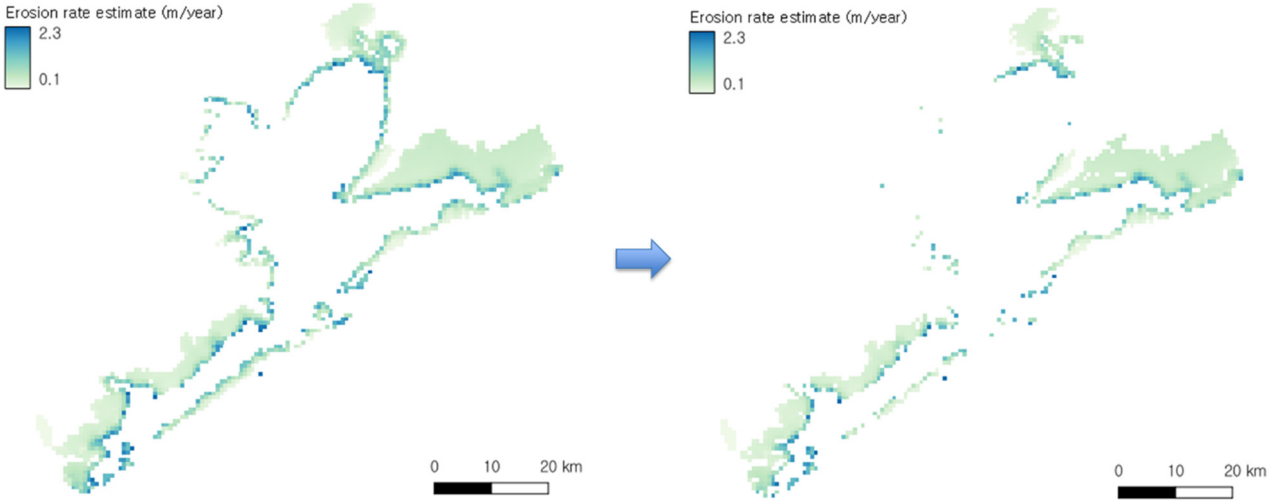

Figure 5.41: Erosion rate future estimates (2025, High scenario) before (left) and after (right) applying the wetland area classification

As for results of 2060, 2080, and 2100 simulation using NOAA-GFDL-ESM4 forcing, Future projected "No-SLR", "Intermediate", and "High" erosion rate results using constant erosion coefficient for Galveston Bay area are shown in **Figure 5.42**. The active area changes according to the year as a result of the increase in water depth as the sea level rises. The colored areas on the map represent the region between 0.05 m and 0.5 m water depth, which is set to examine the erosion coefficient of wetlands near the coast due to the wave energy caused by the relatively low grid resolution of the Galveston Bay Grid. Therefore, the active area represents the locations where wetlands might be present in accordance with scenarios, but it does not indicate the precise wetland boundary.

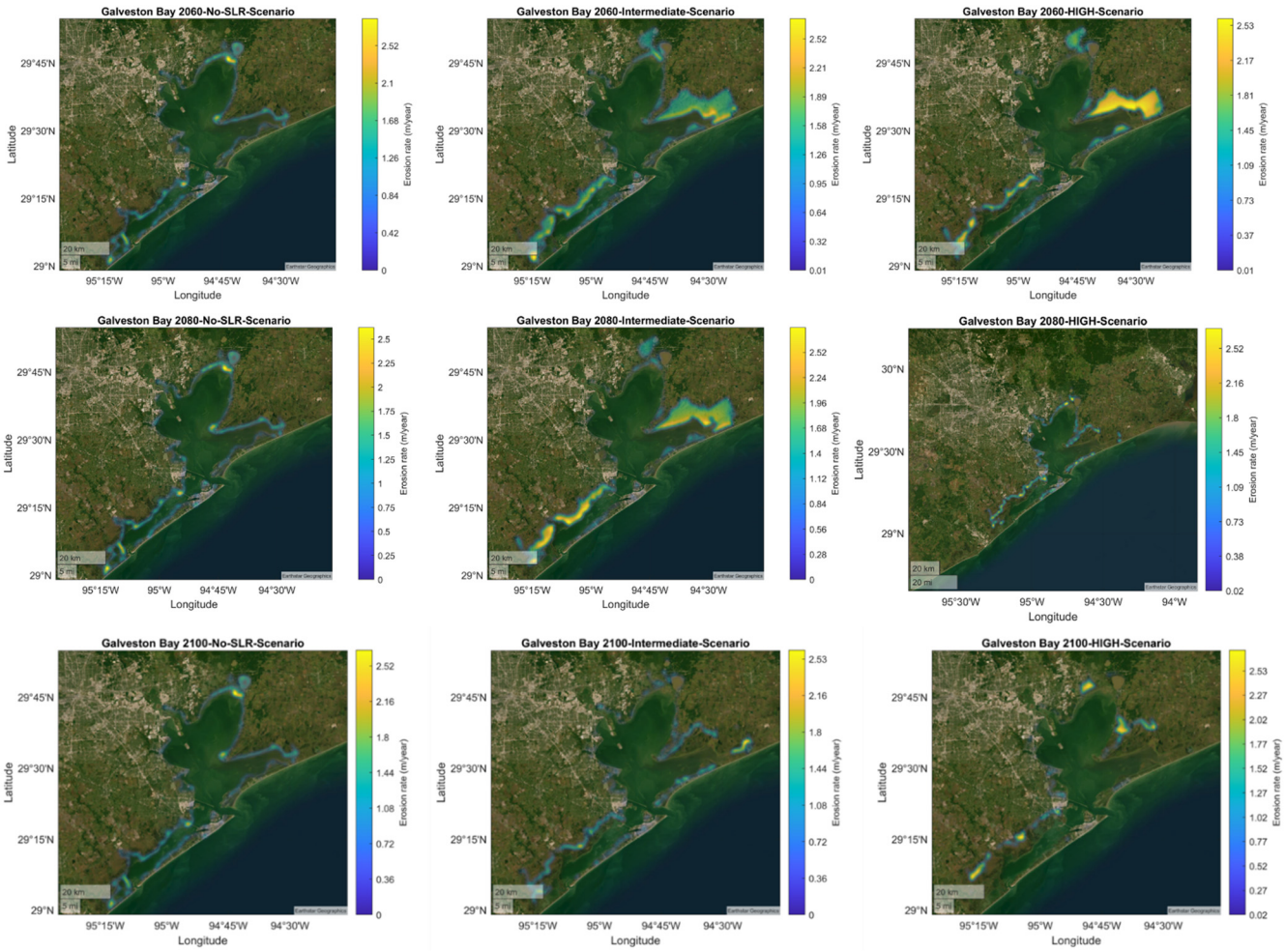

Figure 5.42: The future erosion rate for Galveston Bay wetlands based on the simulation year of 2060, 2080 and 2100

To display only the area at the boundary of the wetland, only areas containing water depths between 0.05 and 0.5m were displayed. The resulting images of the 2060-High, 2080-High, and 2100-high scenarios of Galveston Bay in **Figure 5.42** show retreated shoreline and active areas. The active area has retreated from the original Galveston shoreline, meaning that the original shoreline area is no longer above water due to inundation by sea-level rise. In the case of 2080-High, the active area was small. This occurs because most of the coastal lowlands were submerged, and the wetlands above the sea level were almost submerged. In addition, inundation areas were calculated to verify the wetland area to be inundated in the future simulation of 2080.

If the average water depth of each grid exceeds 0.1 m, the grid is assumed to be completely submerged.

Table 5.7 submergence of the wetlands at the site of interest in Galveston Bay

Sea-level-rise	0 m	0.4 m	0.88 m
Scenario	No-SLR	Intermediate	High
Site1 – grid (94x94)	2359:6477 (26.6%)	782:8054 (8.8%)	0:8836 (0%)
Site2 – grid (94x94)	3928:4908 (44.4%)	2513:6323 (28.4%)	500:8336 (5.6%)
Site4 – grid (94x94)	1425:7411 (16.1%)	659:8177 (7.4%)	259:8577 (2.9%)

The percentages in **Table 5.7** represent the unflooded area, including wetlands, in that scenario. As the sea level rises, more areas are flooded, and in the 2080 High scenario, all areas of Site 1 were found to be flooded. The numerator in the table is simply the model simulation area so ratios in the table show the relative trend of the wetland losses.
In order to analyze the change in wave energy for each scenario in each region of interest, average wave power was depicted using a box-whisker plot, as shown in **Figure 5.43**. On each box, the central mark indicates the median, and the bottom and top edges of the box indicate the 25th and 75th percentiles, respectively. The whiskers extend to the most extreme data points not considered outliers, and the outliers are plotted individually using the '+' marker symbol.

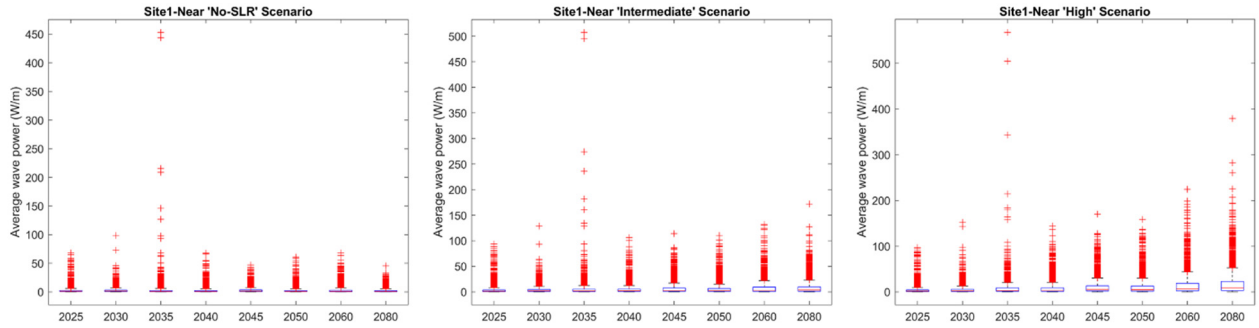

Figure 5.43: Box plot of hourly wave power for Site1-Near location in different scenarios

In the case of the 'No-SLR' scenario, there was little difference in the average wave energy, the median value of the box over time, and the average value was nearly close to 0. However, from the 'Intermediate' to 'High' scenario, as the year increases, the median value increases, the size of the box increases, and the whisker length significantly increases. Therefore, the magnitude and frequency of wave energy that can be received at the corresponding location could substantially increase as the sea level rises.

For the 'intermediate' scenario of 2100, a sea level rise of 0.56 m was assumed, while for the 'High' scenario, a sea level rise of 1.36 m was assumed, considering the expected land subsidence in Galveston Bay.
First, to consider wetland submergence due to sea level rise, the initial coastline for each scenario was plotted in **Figure 5.44.**

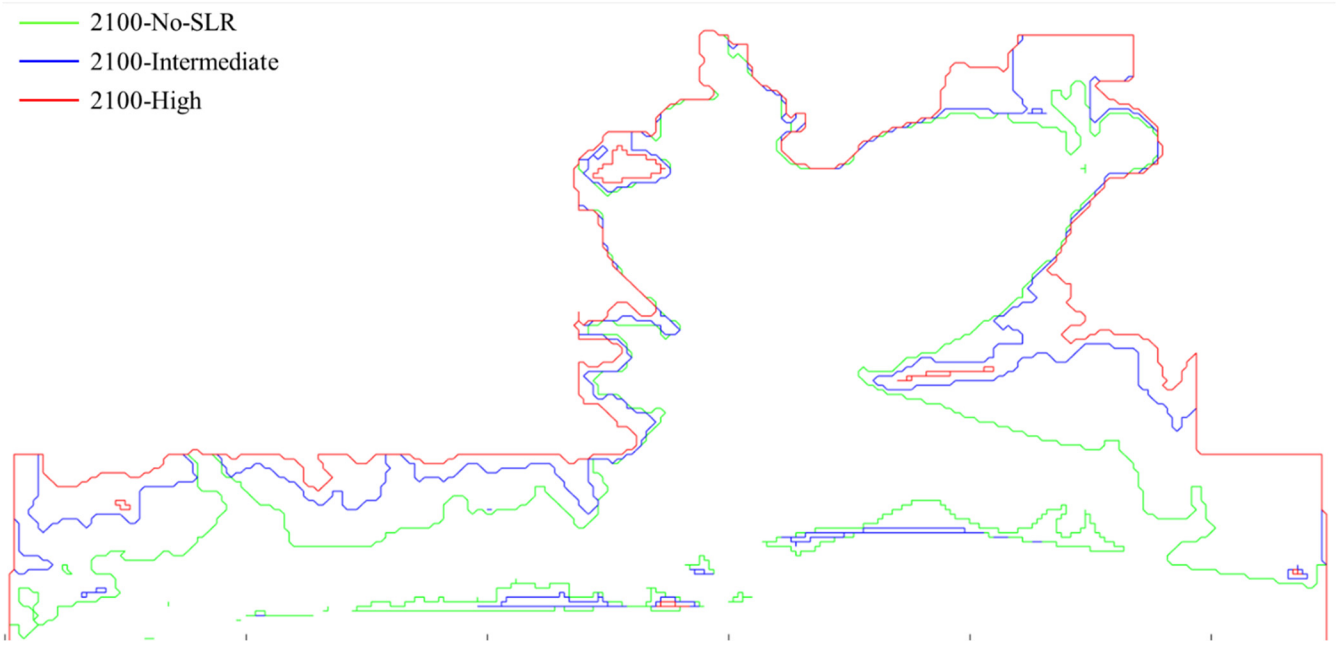

Figure 5.44: Galveston Bay coastlines for each scenario in 2100 based on the initial water depth

Figure 5.45 shows the predicted wetland erosion rates in 2100 based on the high-resolution grid (domain decomposed grid) of FS-1. The colored areas represent the regions with water depth between 0 m to 0.1 m, and for the 'high' scenario in 2100, the entire wetland area is submerged, so it is not shown in the figure.

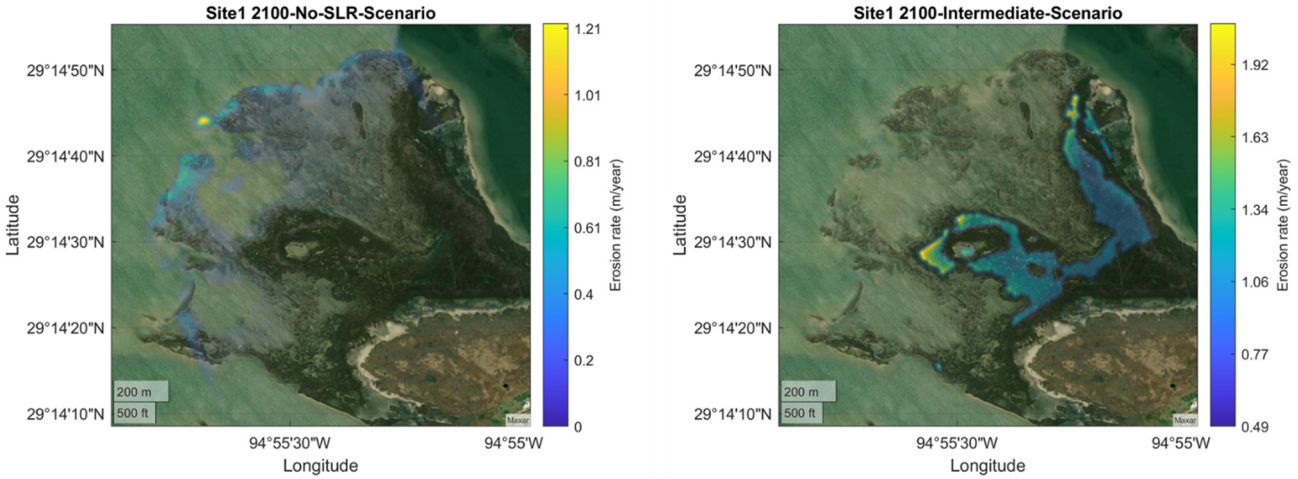

Figure 5.45: The erosion rate projections for FS-1 in the year 2100

As seen in **Figure 5.45**, most of the wetland areas are submerged due to a 0.56 m sea level rise. However, phenomena such as wetland adaptation to sea level rise-induced sediment transport changes must also be taken into account. Additionally, cumulative lateral erosion due to waves up until 2100 must be calculated simultaneously. Therefore, the results in the figure should be utilized as a map for predicting erosion rates in the area based on the 2100 wave environment. It can be observed that the maximum erosion rate under the 'Intermediate' scenario is higher, at 1.92 m/year, compared to the 'No-SLR' scenario, at 1.21 m/year.

Figure 5.46 displays the projected rates of erosion for wetlands in the year 2100, utilizing the domain decomposed grid of FS-2. The edge line that appears uniquely in the 2100-Intermediate scenario (middle image in **Figure 5.46**) is an artificially created result due to the depth matching setting between the boundary of the domain decomposition. Small islands or oyster reefs located in front of the Intra-coastal waterway in FS-2 are mostly submerged in the 'Intermediate' scenario, and wetland areas are also completely submerged in the 'High' scenario, indicating that flooding occurs in the community area located in the northwest.

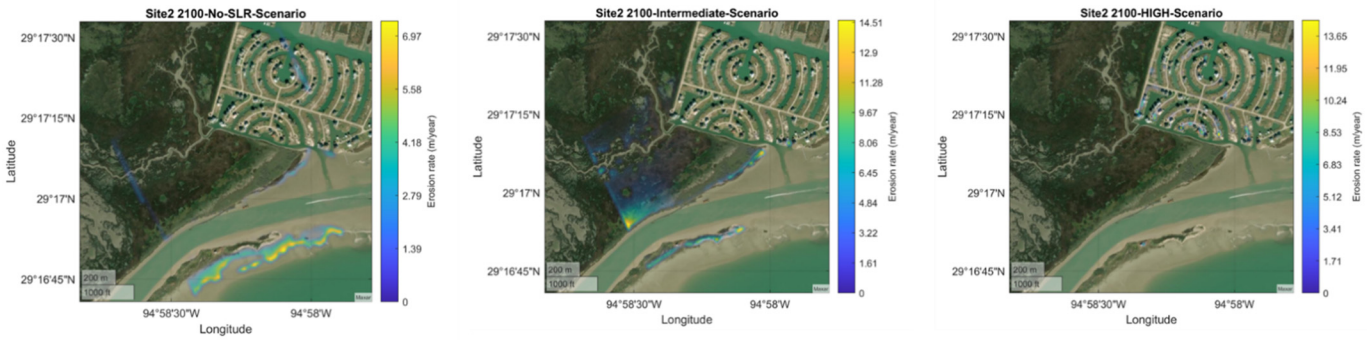

Figure 5.46: The erosion rate projections for FS-2 in the year 2100

Figure 5.47 shows the predicted wetland erosion rates in 2100 using the domain decomposed grid of FS-4. The results from the FS-4 area showed a similar trend to the results from FS-1. As sea levels respond to various future scenarios, there was a sea level rise of more than 50 cm in 2100, and as a result, most wetlands may be inundated. However, the key to maintaining at least some of the present-day wetlands will be whether adaptation scenarios can increase the elevation of wetland platforms, provide sediment, and use wave energy dissipation features to reduce wave energy – the design of which must take future climate scenarios into account.

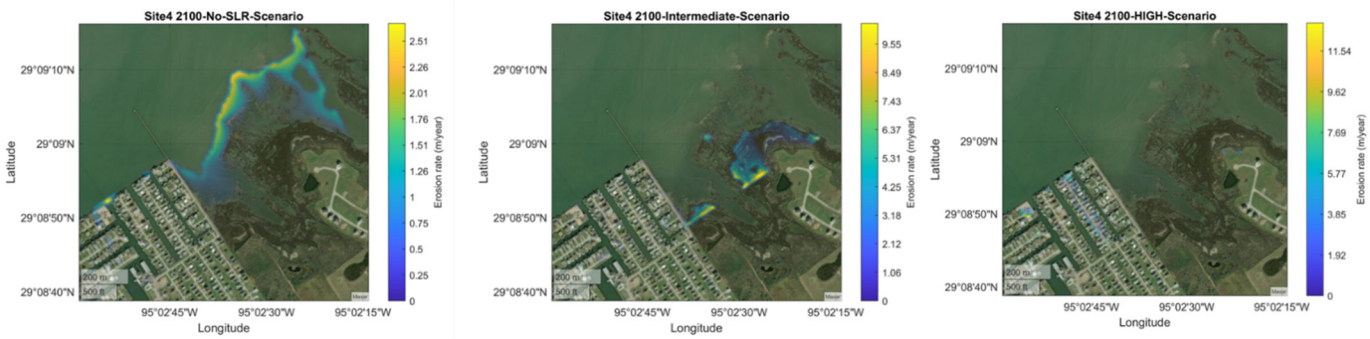

Figure 5.47: The erosion rate projections for FS-4 in the year 2100

For the visualization in the Bay Atlas Map (website), the wetland erosion rate for each polygon was derived through the following process. First, the average historical wetland erosion rate of Galveston Bay was obtained using Landsat results and simulations. Next, to obtain wave energy solely at the wetland boundaries, a range of maximum and minimum depths was defined, which were considered as nearshore wave environments near the wetland boundaries. In the case of Galveston Bay, wave simulation results for areas with depths between a minimum of 0.05 m and a maximum of 0.5 m were used. The average value of the grid area within 0.05 degrees (approximately 5.5 km) from the centroid of the polygon was employed as the representative value for that polygon. However, starting from the 2060 scenario, due to the significant sea-level rise in the 'Intermediate' and 'High' scenarios, the average depth increased and wetlands became submerged, resulting in the maximum depth being adjusted to 1 m to derive the representative value for the polygons. Additionally, there are cases where the value of a specific polygon is 0 (**Figure 5.48**). This occurs when wetlands or coastal areas are completely submerged and the current filtering used in the code is unable to derive a representative value. Therefore, when the value of a polygon is 0 under high sea-level rise scenarios, it indicates that the wetlands in that area have been entirely inundated.

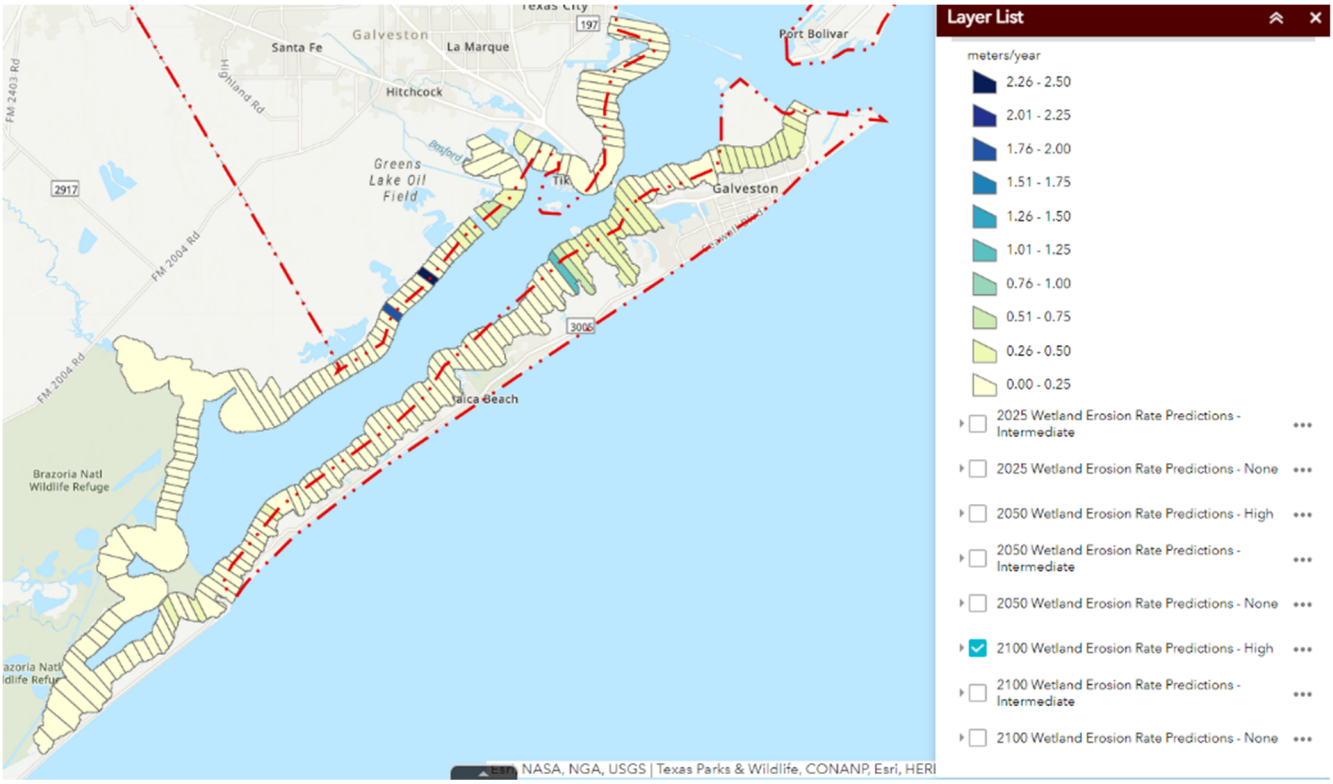

Figure 5.48: Wetland erosion rates for each polygon based on the 2100 High scenario simulation results

The current simulation is discontinuous up to the year 2100 since it only simulates representative years for one year at a time. Additionally, the grid size is low resolution (400 m), which is not sufficient to accurately represent wetland boundaries. Most importantly, the simulation for erosion rate prediction did not use a sediment transport module. As a result, aspects such as increased sediment deposition on wetland platforms that may occur with sea-level rise have been ignored. Predicting the future state of wetlands is a challenging task, but through these simulation results, we can examine the patterns of wetland

inundation along the coast under sea-level rise and how lateral erosion of wetlands changes due to increased wave energy. In the future, continuous decadal simulations incorporating a validated sediment transport model could be used to observe wetland changes under sea-level rise.

5.4 Summary

In this chapter we described the use of the Delft3D-FLOW model to quantify wave impact on wetlands in both present and future scenarios. *In-situ* data taken at four different sites in the Galveston Bay area were used to validate the model under a variety of conditions. The validated model was then used to generate future erosion rates using wave power estimates (forced by long-term predicted winds under different climate change scenarios) at the wetlands edge in conjunction with relationships between wave power and rate of wetlands retreat established under past and present-day conditions. These rates were also developed with different sea level rise predictions. To efficiently accomplish the long-term simulation and the future scenario simulations, a slightly coarser grid resolution was used, while finely-resolved grids were used to validate the model with data from the field deployments.

The long-term (2019-2021) simulations focused on the four field sites. Comparison of the model to field data was performed during times of data collection. The model performed well in capturing measured water levels at the sites. During this time, Hurricane Nicholas traversed the domain from the west, having made landfall in Matagorda County on 14 September 2021. The simulations showed that the significant wave heights at Site 4 did not exceed 0.34m at any point in the two year span, with the majority of the wave heights remaining below 0.1m. While the maximum wave power (the favored metric for determination of the erosion potential of the wave climate) reached a maximum of 132 W/m during Nicholas, it was generally always below 10 W/m.

Short term simulations, forced by winds from the NCEP and ERA5 models, were run for the time of the field deployments. In order to plan drone sorties and optimize use of remote sensing data, the morphological and sediment transport modules were engaged, which required high resolution grids. Simulations revealed erosion near San Luis Pass and a combination of erosion and accretion in the wetlands areas of interest, likely driven primarily by the cold front passages occurring during the deployment time. Maximum erosion of 0.3 meters was seen in this area in the model results. One impact of the concurrent deployment, besides model validation, is verification of the underlying bathymetry in the area. Input bathymetric and topographic information were taken from the Galveston Digital Elevation Model (DEM), which is an amalgamation of existing bathymetric and topographic surveys from 2006. Comparison of data from the deployed pressure transducers to these records showed differences as high as 60cm. Some of these differences were accommodated by changing from NAV88 to MHW datums. However, discrepancies as high as 30cm remained. For the specific time of the passage of the hurricane, the HURDAT2 data, along with the Holland profile, was used to represent the wind fields of Hurricane Nicholas. The significant wave height results from this simulation were compared to the results from simulations forced by winds from the ECMWF and NCEP wind models. While both latter data sets were able to resolve the hurricane winds, neither simulation compared as well as that of HURDAT2, likely due to the non-optimal spatial and temporal resolution of the hurricane. Wave power estimates from the model compare reasonably well to data at all sites. Some of the higher-energy events are underpredicted, likely due to bathymetric discrepancies and (in some cases) the appearance of ship wakes in the data that are not simulated by the model. In attempting to determine the cause of these discrepancies, it appeared that the mean wave period at the sites was notably underpredicted. This may be due to the fact that the area is dominated by high frequency wind wave energy, which can be poorly represented in the model. However, the significant wave heights at the sites tend to be reasonably well predicted, with some high energy overprediction at some times during the first field campaign. Since the MANERR area is one focus of future climate erosion predictions, a limited data set of wave and water level measurements in the area was used to validate the model implementation in that area. Both ERA5 and NCEP winds, as well as local winds measured from a station a distance of 38 miles away, were used to force the local implementation of Delft3D. In general, the model underpredicted the measured wave heights in the area, likely due to the lack of gust information in the modeled winds as well as the remote distance of the local wind station.

In order to predict future erosion due to climate change impacts, a relationship between wave power P and erosion rate E was derived. Erosion data was derived from satellite imagery, and the wave power determined from the Delft3D model. A presumed linear relationship between erosion rate and wave power (E=CP) was derived, where C is the "marsh erosion coefficient." The coefficient C would be attributable for each area (Galveston Bay, MANERR, and Field Sites 1, 2 and 4). The derived coefficients were: C = 0.17 $m^2/(W \cdot yr)$ for Galveston Bay; C = 0.25 $m^2/(W \cdot yr)$ for MANERR; C = 0.42 $m^2/(W \cdot yr)$ for Field Site 1; C = 1.11 $m^2/(W \cdot yr)$ for Field Site 2; and C = 0.79 $m^2/(W \cdot yr)$ for Field Site 4. Future meteorological data was taken from the Hadley Centre Global Environment Model (HadGEM3) for the years 2020 to 2050, and from the Earth Systems model from the Geophysical Fluid Dynamics Laboratory of NOAA (NOAA-GFDL-ESM4) for 2060 to 2100. In addition, three levels of sea level rise ("no sea level rise," "intermediate sea level rise," and "high sea level rise") were incorporated as well. With the

simulated wave power at the five sites of interest forced with the future meteorological conditions, it was determined that the erosion rates across Galveston and the three field sites (Field Sites 1, 2, and 4) ranged from 0.1 m/year (Field Site 1, 2025, “no sea level rise”) to almost 1.5 m/year (Galveston Bay, 2045, “high” scenario). Interestingly, the maximum erosion was not predicted for the most extreme conditions (2050, “high” scenario), as erosion is greatly reduced once the wetlands are completely submerged.

6 Conclusions

In this project, we have analyzed the temporal evolution of Galveston wetlands under seasonal and eventful environmental conditions through remote sensing techniques using satellite and UAS imagery and *in-situ* hydrodynamic measurements. We then synthesized the findings on wetland evolution dynamics derived from these analyses to validate the short-term and long-term prediction of wetland evolutions using the Delft3D-Flow model. The major conclusions in this project are as follows:

- The long-term wetland erosion rate along Galveston Bay from 1984 to 2021 was estimated through the analysis of water occurrence maps from the Landsat satellite imagery. The satellite imagery analysis revealed that the erosion activity was dominant in West Galveston Bay, particularly in West Bay, Christmas Bay, and Pelican Island. Matagorda Bay and Espiritu Santo Bay showed lower rates of erosion, possibly due to the Texas City Dike and dammed reservoirs.

- The high spatio-temporal resolution of the CubeSat satellite imagery allowed us to quantify the impacts of sea level rise and sedimentation on wetland boundaries and to capture erosion/accretion hotspots at the four specific locations discussed in this report. Significant wetland erosion in 2009 and 2021 was prevalent in all four sites with wave-induced erosion hotspots at FS-1 and FS-3. A net decrease of the wetland areas at FS-4 was also observed, with slight sediment accumulation that is compensated for by reduction in the overall wetland land area induced by rising sea levels.

- Statistical shoreline analysis using the UAS-based orthomosaic maps coupled with the Digital Shoreline Analysis System (DSAS) revealed consistent erosion-dominated patterns at FS-1, 2 and 3. In comparison, slight accretion activity was observed at FS-4, attributed to the site-specific topographic aspects, including mild slopes and shallow water depth along the wetland boundaries. These findings on wetland evolutions show good agreement with those of short-term analysis using CubeSat satellite imagery.

- Analysis of seasonal variations on wetland evolution using the UAS-based observations at sites FS-1, 2, and 3 showed that the wetland erosion is elevated during the fall at the onset of abrupt weather changes caused by multiple cold fronts and storm events. This trend tends to gradually subside until the onset of the summer. Shoreline changes at FS-4 were accretion-dominated due to seaward regrowth of vegetation during the same period.

- We demonstrated the impact of extreme hurricane events on wetland shoreline dynamics through the analyses using satellite and UAS imagery. Both analyses showed the elevation of erosion activity during Hurricane Nicholas, highlighting the susceptibility of wetlands to extreme events. *In-situ* hydrodynamic measurements also demonstrated the potential erosion risks due to the higher wave energy observed during extreme weather events. This is further corroborated by the measurement of elevated suspended sediment concentration during periods of larger water-level fluctuation.

- *In-situ* hydrodynamics measurements also revealed the potential risk of vessel-induced erosion at FS-3. Passing barges generated trailing wake patterns, associated with characteristic surges and drawdowns, and the vessel-induced wave energy was found to be comparable to that of storm events.

- Numerical prediction of wetland evolution using the Delft3D-Flow model with adaptive grid settings for short-term and long-term predictions was validated using the in-situ hydrodynamic measurements and the temporal wetland evolution results drawn from satellite and UAS imagery analyses. The validated model was used in conjunction with measured erosion estimates from satellite data to determine relationships between wave power (the incident wave metric relevant to marsh evolution) and erosion. Results indicate that the ratio of erosion rate to wave power (the “marsh erosion coefficient”) varies from 0.17 to 1.11 $m^2/(W \cdot yr)$ in Galveston Bay and the individual field sites. With these coefficients, the model system was then used to predict future wetland erosion scenarios from 2025 through 2100 under a variety of sea level rise scenarios. The resulting erosion rates under these future conditions ranged in severity from 0.1 m/year of erosion for the year 2025 (under an assumption of no sea level rise) to 1.5 m/year for the year 2045 (under the most severe assumption of sea level rise). It was also determined that the maximum predicted erosion rate did not necessarily correspond to the most severe sea level rise scenario in the most distant future year considered, since under these scenarios the present wetlands would be completely submerged and be far less vulnerable to wave-related erosion.

- The integration of historical wetland boundary data and future predictions through numerical simulations into the web-based Coastal Atlas GIS platform enables unrestricted access to the past and future wetlands extent along the Texas coast, serving as a connection point to foster public awareness and engagement with the state’s Coastal Resiliency Master Plan. Overall, the outcomes / data products from this project form a robust foundation for the development of an optimized

coastal resiliency plan. This resource also provides essential data for the USACE and the Galveston Bay Foundation to enhance their decision-making regarding the better utilization of dredged materials and the restoration of wetlands.

These conclusions above demonstrate that the over-arching objective of this project was achieved, which was to develop a robust numerical forecasting model to predict the short-term and long-term evolution of Texas coastal wetland.

References

Al Mukaimi, M. E., Dellapenna, T. M., & Williams, J. R. (2018). Enhanced land subsidence in Galveston Bay, Texas: Interaction between sediment accumulation rates and relative sea level rise. Estuarine, Coastal and Shelf Science, 207, 183-193.

Bugica, K., Sterba-Boatwright, B., & Wetz, M. S. (2020). Water quality trends in Texas estuaries. Marine Pollution Bulletin, 152, 110903.

Cahoon, D. R. (2006). A review of major storm impacts on coastal wetland elevations. Estuaries and coasts, 29, 889-898. Wetlands Subcommittee Federal Geographic Data Committee (2013) Classification of Wetlands and Deepwater Habitats of the United States: https://www.fws.gov/sites/default/files/documents/Classification-of-Wetlands-and-Deepwater-Habitats-of-the-United-States-2013.pdf

Chini, N., Stansby, P., LEake, J., Wolf, J., Roberts-Jones, J., and Lowe, J. (2010). The impact of sea level rise and climate change on inshore wave climate: a case studu for East Anglia (UK). Coastal Engineering, v. 57, 11-12.

Coops, N.C., Goodbody, T.R.H. & Cao, L. (2019) Four steps to extend drone use in research. Nature, 572, 433–435.

Dahl, T. E., & Stedman, S. M. (2013). Status and trends of wetlands in the coastal watersheds of the Conterminous United States 2004 to 2009.

DJI (2018) Mavic 2 Pro/Zoom User Manual. DJI.

Dronova, I., Kislik, C., Dinh, Z. and Kelly, M., 2021. A review of unoccupied aerial vehicle use in wetland applications: Emerging opportunities in approach, technology, and data. Drones, 5(2), p.45.

El Hamdi, M.J., Larabi, A., and Faouzi, M. (2021). Numerical modeling of salt water intrusion in the Rmel-Oulad Ogbane coastal aquifer (Larache, Morocco) in the climate change and sea level rise context (2040). Water, v13, 16.

Eltner, A. and Schneider, D., 2015. Analysis of different methods for 3D reconstruction of natural surfaces from parallel-axes UAV images. The Photogrammetric Record, 30(151), pp.279-299.

Entwistle, C., Mora, M. A., & Knight, R. (2018). Estimating coastal wetland gain and losses in Galveston County and Cameron County, Texas, USA. Integrated environmental assessment and management, 14(1), 120-129.

Fuller, W.P. (2021). Deep-draft vessel wake and wind wave hydrodynamics near a mixed-sediment embankment in Galveston Bay, Texas. M.Sc. Thesis, Department of Ocean Engineering, Texas A&M University, pp. 120.

Forlani, G., Dall'Asta, E., Diotri, F., Morra di Cella, U., Roncella, R. and Santise, M., 2018. Quality assessment of DSMs produced from UAV flights georeferenced with on-board RTK positioning. Remote Sensing, 10(2), p.311.

Geselbracht, L., Freeman, K., Kelly, E., Gordon, D.R., and Putz, F.E. (2011). Retrospective and prospective model simulations of sea level rise impact on Gulf of Mexico coastal marshes and forests in Waccasassa Bay, Florida. Climactic Change, v. 107, doi: 10.1007/s10584-011-0084-y. Holland, Greg J., James I. Belanger, and Angela Fritz. "A revised model for radial profiles of hurricane winds." Monthly weather review 138.12 (2010): 4393-4401.

Goncalves, J.A. and Henriques, R., 2015. UAV photogrammetry for topographic monitoring of coastal areas. ISPRS journal of Photogrammetry and Remote Sensing, 104, pp.101-111.

Goring, D.G., and Nikora, V.I. (2002). Despiking acoustic Doppler velocimeter data. *Journal of Hydraulic Engineering*, 128(1), 117-126.

Guannel, G., A. Guerry, J. Brenner, J. Faries, M. Thompson, J. Silver, R. Griffin et al. "Changes in the delivery of ecosystem services in Galveston Bay, TX, under a sea-level rise scenario." *Palo Alto, CA* (2014).

Himmelstoss, E., Henderson, R.E., Kratzmann, M.G. and Farris, A.S., 2018. Digital shoreline analysis system (DSAS) version

5.0 user guide (No. 2018-1179). US Geological Survey.

IPCC (2021). Climate Change 2021: The Physical Science Basis. Contribution of Working Group I to the Sixth Assessment Report of the Intergovernmental Panel on Climate Change [Masson-Delmotte, V., P. Zhai, A. Pirani, S. L. Connors, C. Péan, S. Berger, N. Caud, Y. Chen, L. Goldfarb, M. I. Gomis, M. Huang, K. Leitzell, E. Lonnoy, J. B. R. Matthews, T. K. Maycock, T. Waterfield, O. Yelekçi, R. Yu and B. Zhou (eds.)]. Cambridge University Press. In Press.

Jean-Francois Pekel, Andrew Cottam, Noel Gorelick, Alan S. Belward, High-resolution mapping of global surface water and its long-term changes. Nature 540, 418-422 (2016).

Jelesnianski, C. P. (1992). SLOSH: Sea, lake, and overland surges from hurricanes (Vol. 48). US Department of Commerce, National Oceanic and Atmospheric Administration, National Weather Service.

Karimpour, A. and Chen, Q. (2017). Wind wave analysis in depth limited water using OCEANLYZ, A MATLAB toolbox. Computers & Geosciences, 106, pp.181-189.

Khan, S. D., Gadea, O. C., Tello Alvarado, A., & Tirmizi, O. A. (2022). Surface Deformation Analysis of the Houston Area Using Time Series Interferometry and Emerging Hot Spot Analysis. Remote Sensing, 14(15), 3831.

Kim, J.Y., Kaihatu, J., Chang, K.A., Sun, S.H., Huff, T.P., and Feagin, R. A. (2020). Effect of cold front-induced waves along wetlands boundaries. *Journal of Geophysical Research: Oceans*, 125(12), e2020JC016603.

Klemas, Victor. "Remote sensing of emergent and submerged wetlands: An overview." International journal of remote sensing 34, no. 18 (2013): 6286-6320.

Lesser, G. R., Roelvink, J. V., van Kester, J. T. M., & Stelling, G. S. (2004). Development and validation of a three-dimensional morphological model. Coastal engineering, 51(8-9), 883-915.

Liu, Y., Li, J., Fasullo, J. and Galloway, D.L. (2020). Land subsidence contributions to relative sea level rise at tide gauge Galveston Pier 21, Texas. Scientific reports, 10(1), pp.1-11.

Luettich, R. A., Westerink, J. J., & Scheffner, N. W. (1992). ADCIRC: an advanced three-dimensional circulation model for shelves, coasts, and estuaries. Report 1, Theory and methodology of ADCIRC-2DD1 and ADCIRC-3DL.

McFeeters, S. K. (1996). The use of the Normalized Difference Water Index (NDWI) in the delineation of openwater features. International journal of remote sensing, 17(7), 1425-1432.

NOAA, 2021. Mean Sea Level Trend 8771450 Galveston Pier 21. Center for Operational Oceanographic Products and Services, Texas Available at: http://tidesandcurrents. noaa.gov/sltrends/sltrends_station.shtml?stnid=8771450.

Over, J.R., Ritchie, A.C., Kranenburg, C.J., Brown, J.A., Buscombe, D., Noble, T., Sherwood, C.R., Warrick, J.A., and Wernette, P.A., 2021, Processing coastal imagery with Agisoft Metashape Professional Edition, version 1.6—Structure from motion workflow documentation: U.S. Geological Survey Open-File Report 2021–1039, 46 p.

Padró, J.C., Muñoz, F.J., Planas, J. and Pons, X., 2019. Comparison of four UAV georeferencing methods for environmental monitoring purposes focusing on the combined use with airborne and satellite remote sensing platforms. International journal of applied earth observation and geoinformation, 75, pp.130-140.

Paine, J. G., Caudle, T., and Andrews, J. R., (2021), Shoreline movement and beach and dune volumetrics along the Texas Gulf Coast, 1930s to 2019: The University of Texas at Austin, Bureau of Economic Geology, final report prepared for the General Land Office under contract no. 16-201-000, 101 p.

Planet (2022) PLANET IMAGERY PRODUCT SPECIFICATION
https://assets.planet.com/docs/Planet_Combined_Imagery_Product_Specs_letter_screen.pdf

Ravens, T. M., Thomas, R. C., Roberts, K. A., & Santschi, P. H. (2009). Causes of salt marsh erosion in Galveston Bay, Texas. Journal of Coastal Research, 25(2), 265-272.

Reja, M. Y., Brody, S. D., Highfield, W. E., & Newman, G. D. (2017). Hurricane recovery and ecological resilience: Measuring the impacts of wetland alteration post Hurricane Ike on the upper TX coast. Environmental management, 60, 1116-1126.

Roberts, Malcolm J., et al. (2019). Description of the resolution hierarchy of the global coupled HadGEM3-GC5.1 model as used in CMIP6 HighResMIP experiments. Geoscientific Model Development 12.12: 4999-5028.

Rozas, L. P., Minello, T. J., Zimmerman, R. J., & Caldwell, P. (2007). Nekton populations, long-term wetland loss, and the effect of recent habitat restoration in Galveston Bay, Texas, USA. Marine Ecology Progress Series, 344, 119-130.

Sapkota, Y., & White, J. R. (2020). Carbon offset market methodologies applicable for coastal wetland restoration and conservation in the United States: A review. Science of The Total Environment, 701, 134497.

Shirzaei, M., Freymueller, J., Törnqvist, T. E., Galloway, D. L., Dura, T., & Minderhoud, P. S. (2021). Measuring, modelling and projecting coastal land subsidence. Nature Reviews Earth & Environment, 2(1), 40-58.

Sobiech, J., & Dierking, W. (2013). Observing lake-and river-ice decay with SAR: advantages and limitations of the unsupervised k-means classification approach. Annals of Glaciology, 54(62), 65-72.

Thielicke, W., and E. J. Stamhuis, 2014: PIVlab – Towards user-friendly, affordable and accurate digital particle image velocimetry in MATLAB. Journal of Open Research Software, 2 (1), e30.

Tonelli, M., Fagherazzi, S. and Petti, M. (2010). Modeling wave impact on salt marsh boundaries. Journal of geophysical research: Oceans, 115(C9).

Toth, C. and Jóźków, G., 2016. Remote sensing platforms and sensors: A survey. ISPRS Journal of Photogrammetry and Remote Sensing, 115, pp.22-36.

White, W. A., Morton, R. A., & Holmes, C. W. (2002). A comparison of factors controlling sedimentation rates and wetland loss in fluvial–deltaic systems, Texas Gulf coast. Geomorphology, 44(1-2), 47-66.

Appendix A: Data Management

Data management for this project has been published and available online for download at the corresponding DOIs (Digital Object Identifiers) for each chapter. The details of the data management are shared below.

Chapter 2. TGLO Establish Historical Long-term Wetland Boundary Evolution through Satellite Imagery
(DOI: https://doi.org/10.5281/zenodo.10034220)

This dataset includes wetland erosion rates for West Galveston, Matagorda, and San Antonio Bay. Long-term trends in wetland boundary changes are estimated using Landsat satellite imagery. Sections of the wetland experiencing the highest rates of erosion will be further investigated through CubeSat satellite observations. The format of the data is summarized as follows:

(1) Landsat based wetland evolution results from 1984 to 2020
- The Annual and seasonal water occurrence (in gif format)
- The wetland change map (in TIF format)

(2) CubeSat based wetland evolution results from 2009 to 2020
- Water occurrence maps from 2009 to 2021 for the RapidEye based bi-annual results (FSX-occurrence-yyy1-yyy2.tif) and the PlanetScope based annual results (FSX-occurrence-yyy1.tif), where yyyy represents the given year. The legend image is 'occurrence-cbar.jpg'
- Erosion maps based on the difference between water occurrence mapping in 2009 and 2021: ('FSX-occurrence-diff-2021-2009.tif'). The legend is 'occurrence-diff-cbar.jpg'
- The 0.2-meter bed counter line images based on the water occurrence maps and the tide elevation threshold from 2017 to 2021: (FSX-bed-yyy1.tif). Again, yyy1 represents the given year. The legend is 'color-bed.jpg
- The difference between the beds in the 0.2-meter bed counter line images in 2017 and 2021 at FS-1, FS-2, FS-3, and FS-4: (FSX-bed-diff-2021-2017.tif). The legend is 'color-bed-dif.jpg'

(3) Analysis of wetland boundary evolution and erosion rate
- Landsat based Wetland erosion rate from 1984 to 2020 and CubeSat erosion rate from 2009 to 2021 (data format in ArcGIS shapefile)*
- Landsat based coastlines in 1984, 2000, 2010, and 2020*
  * The dataset also shown on the Coast Atlas website (this link)

Chapter 3. Monitoring Wetland Evolution in Galveston Bay through UAS mapping
(DOI: https://doi.org/10.18738/T8/IYODKD)

This dataset includes aerial imagery collected using a UAS platform equipped with a PPK module at four select wetland sites in Galveston Bay, TX during seven field surveys from September 2021 to July 2023. GNSS data associated with the collected UAS imagery (i.e., PPK data for the UAS and on-site ground control points for validation), are also included in this data repository.

The dataset is available in the form of .zip files for better data management due to the large size of the original UAS imagery. The format of the dataset follows "Campaign_**x**__FS-**y**__Route-**z**.zip" for the UAS images and the associated GNSS data recorded from the UAS PPK module, "Campaign_**x**__FS-**y**__PPK__Base-Station.zip" for the raw GNSS data recorded from the reference base station, and "Campaign_**x**__FS-**y**__PPK__GCP.zip" for the raw GNSS data recorded at the installed ground control points.

- Field Campaigns ("Campaign_**x**")
  - Campaign-1 (8/30 – 9/2/2021)
  - Campaign-1H (9/22 – 10/6/2021)
  - Campaign-2 (11/16 – 11/23/2021)
  - Campaign-3 (3/1 – 3/3/2022)
  - Campaign-4 (6/15 – 6/17/2022)
  - Campaign-5 (10/26 – 10/27/2022)
  - Campaign-6 (7/4 – 7/14/2023)

- Field Sites ("FS-**y"**)
  - FS-1: West Bay Galveston Island
  - FS-2: West Bay Mainland Flamingo Isles
  - FS-3: Bolivar Peninsula Galveston Bay
  - FS-4: West Bay Galveston Island, Sea Grass Lane
- Imaging Routes ("Route-**z**")
  - For FS-1, 2, and 3: Route-1, Route-2, Route-3, and Route-4
  - For FS-4: Route-1, Route-2, Route-3, Route-4, and Route-5

Chapter 4. Hydrodynamic Field Data near Galveston, Texas Wetland Edges to Help Assess Storm Impacts and Erosion
(DOI: https://doi.org/10.5281/zenodo.10070373)

This dataset includes water free surface elevation measurements via submerged pressure transducers along transects near Galveston Bay wetland edges. The field hydrodynamic data collected by RBR Pressure Transducers (PT) at three field research sites in Galveston Bay, Texas, during four seasonal measurement campaigns between Aug 2021 and June 2022 are explained in "readme.txt".

Chapter 5. Prediction of Texas Wetland Erosion through Numerical Simulation
(DOI: https://doi.org/10.18738/T8/CIVAFS)

This dataset includes numerical simulation-related modeling files and results from the Texas General Land Office project (GLO Contract No. 21-155-006-C878) 'Prediction of Texas Wetland Erosion through Remote Sensing, Field Surveys, and Numerical Modeling' conducted by the Texas A&M University.

The first section deals with a calibrated Delft3D model for long-term processes for the area of Galveston Bay (Section 5.1). It includes input and output files for two time periods, spanning from November 2019 to March 2022.

The second section focuses on a validated and calibrated Delft3D model for short-term processes (Section 5.2). This section contains data related to the Galveston Bay High-resolution model and the Mission-Aransas National Estuarine Research Reserve (MANERR) area model.

The third section involves long-term ensemble forecasts (up to 2100) and assesses the impact of climate change (Section 5.3). It includes data for future erosion rate estimation in the Galveston Bay area and future simulation results based on different climate models, such as "HADGEM3-GC31-HM" and "NOAA-GFDL-ESM4."

Appendix B: Table of erosion/accretion hotspots observed in the short-term analysis from UAS (Sep 2021 – Jul 2023) and the long-term analysis from Landsat imagery (1984 – 2020)

Red-colored boxes represent erosion hotspots with erosion rates greater than 3.0 m/year, and orange-colored boxed show erosion-dominated hotspots with erosion rates smaller than 3.0 m/year. Accretion-dominated hotspots are shown in blue-colored boxes. Note that the positive value for erosion rate represents "erosion activity", and the negative value for "accretion activity".

Region	Location	Erosion rate [m/year]	Latitude / Longitude (dms)	Source
Region I	West Bay Galveston Island (Site-1)	8.3	29°14'46.45"N / 94°55'37.69"W	UAS
	West Bay Galveston Island (Site-1)	0.71	29° 14' 57.74"N / 94° 55' 5.73 "W	Satellite
	West Bay Flamingo Isles (Site-2)	10.6	29°17'6.64"N / 94°58'2.75"W	UAS
	West Bay Flamingo Isles (Site-2)	1.14	29° 16' 57.76"N / 94° 57' 17.51 "W	Satellite
	Bolivar Peninsula (Site-3)	10.2	29°26'26.90"N / 94°42'6.48"W	UAS
	Bolivar Peninsula (Site-3)	9.7	29°26'19.35"N / 94°42'2.65"W	UAS
	West Bay Galveston Island, Sea Grass Lane (Site-4)	4.3	29° 9'10.67"N / 95° 2'30.11"W	UAS
	West Bay Galveston Island, Sea Grass Lane (Site-4)	1.78	29° 8' 22.70 "N / 95° 4' 1.397 "W	Satellite
	Moodys Island	8.6	29° 4' 5.40 "N / 95° 8' 51.83 "W	Satellite
	Near Oyster Lake	3.93	29° 8' 2.82 "N / 95° 9' 18.57 "W	Satellite
	Near Dike Beach	-5.2	29° 21' 58.12 "N / 94° 51' 35 "W	Satellite
Region II	Matagorda Island	1.36	28° 14' 9.57 "N / 96° 39' 54.78 "W	Satellite
Region III	San José Island	3.17	28° 6' 10.76 "N / 96° 54' 18.68 "W	Satellite

Appendix C: Time-series of wetland boundaries at each site during the field campaigns over the orthomosaic map generated during Campaign 6

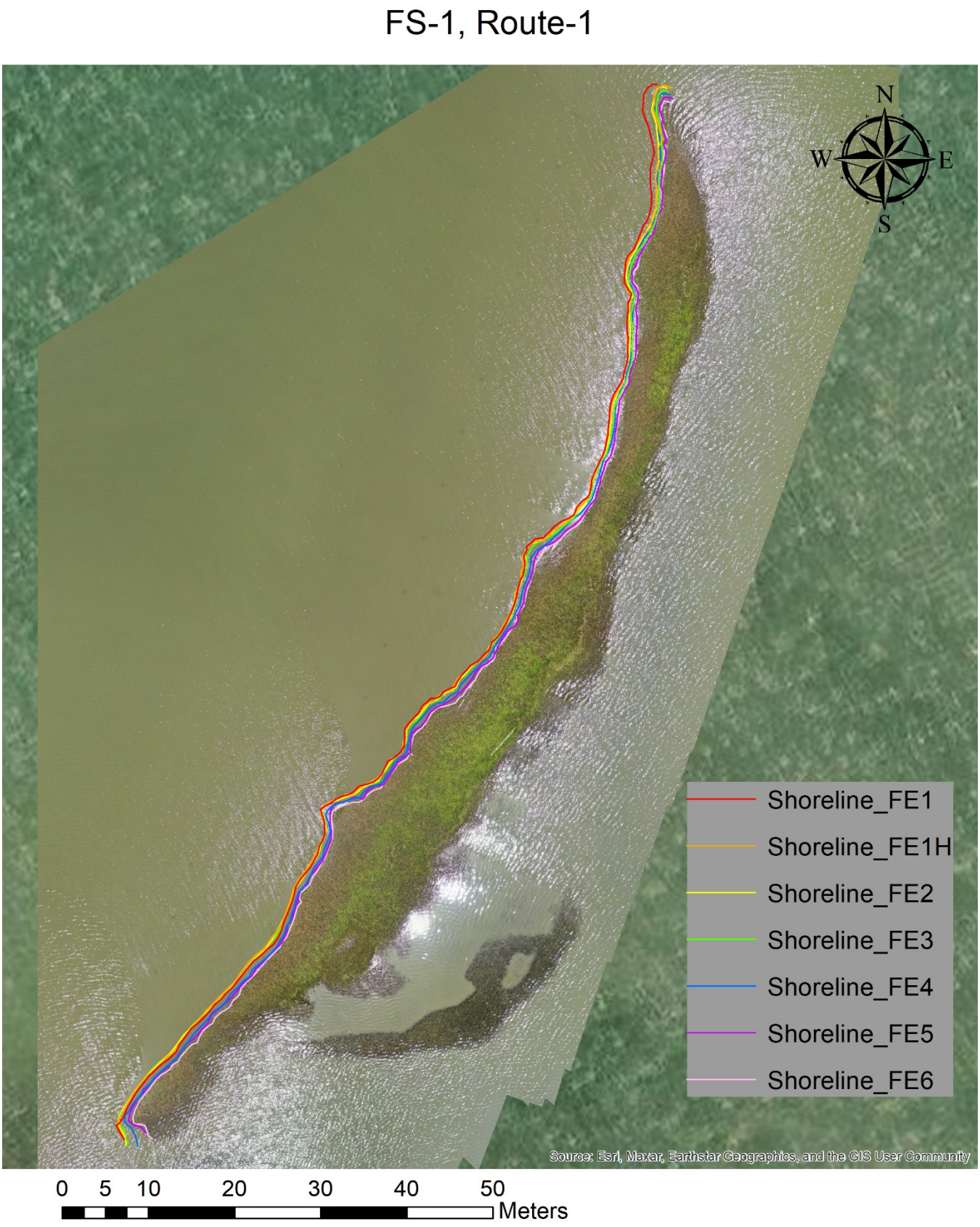

Fig. C1-1. Wetland boundaries at FS-1, Route-1

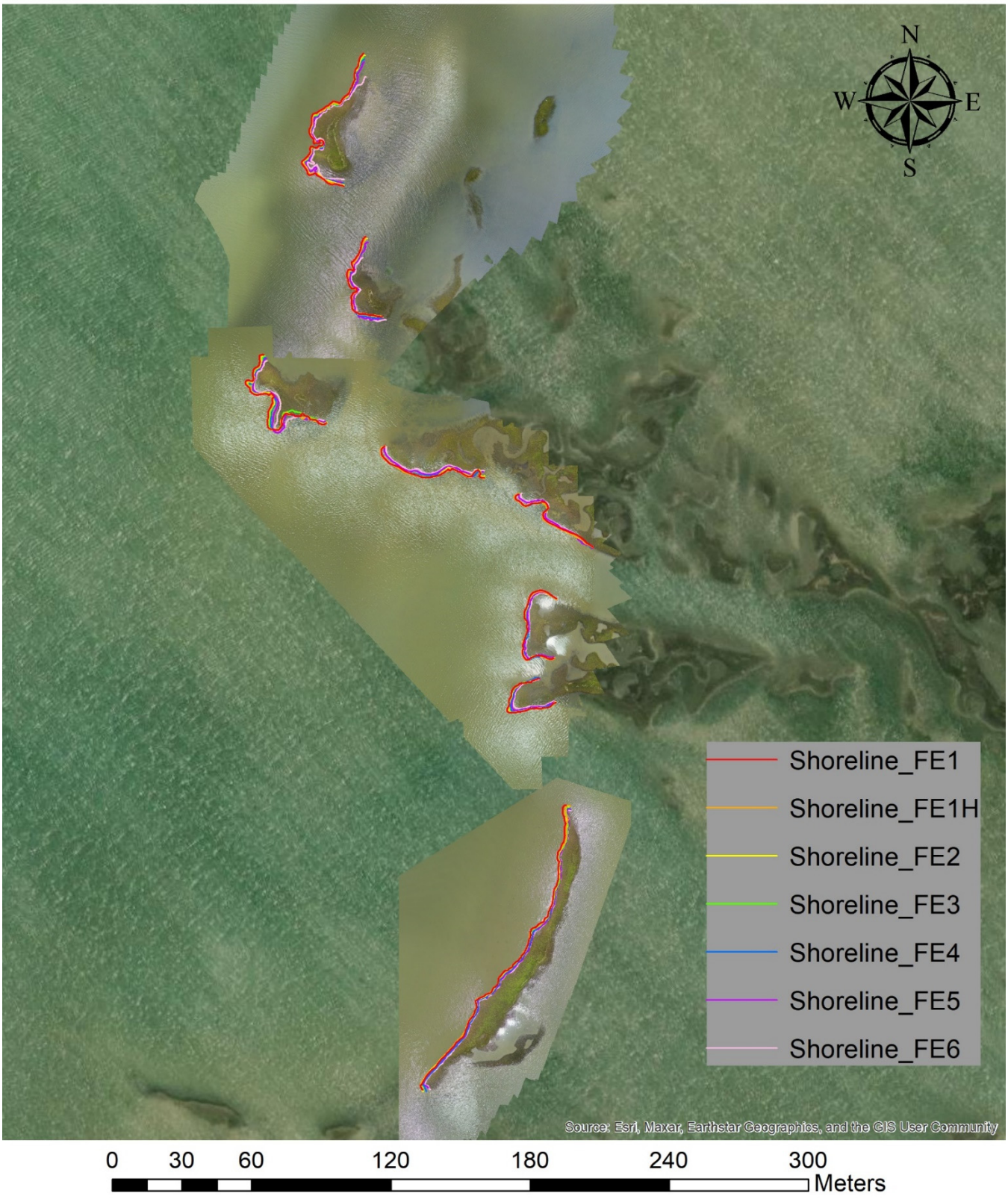

Fig. C1-2. Wetland boundaries at FS-1, Route-2

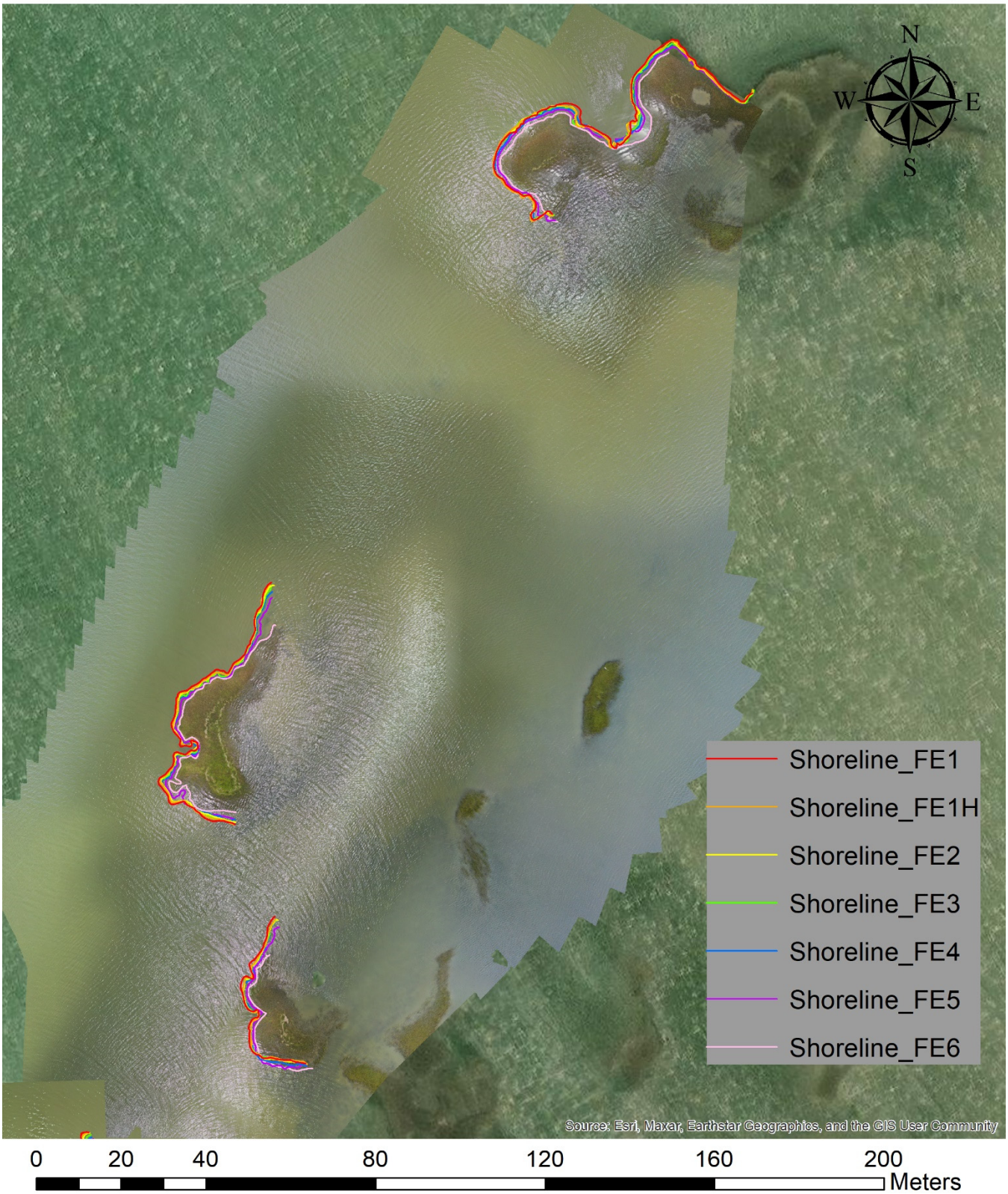

Fig. C1-3. Wetland boundaries at FS-1, Route-3

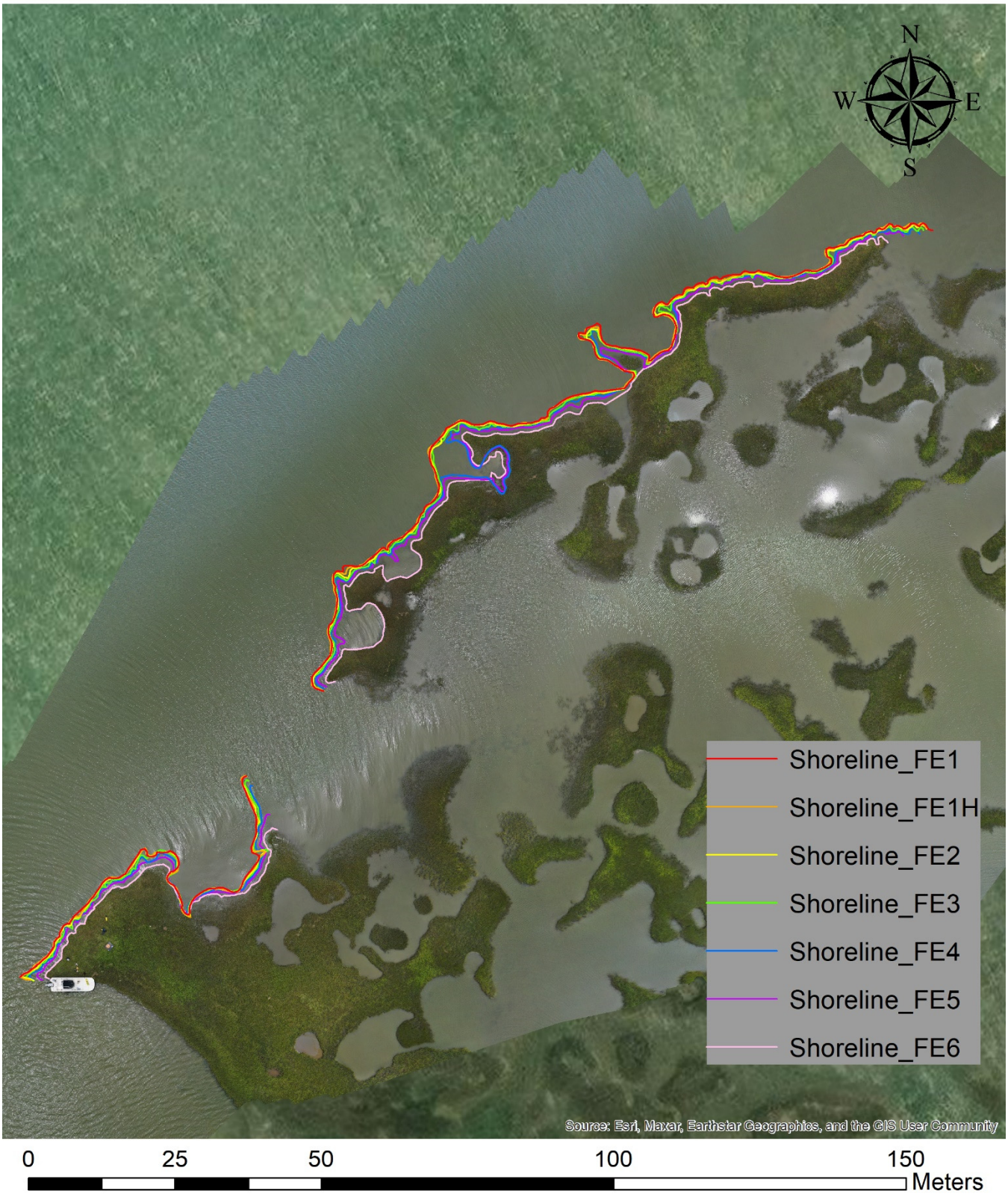

Fig. C1-4. Wetland boundaries at FS-1, Route-4

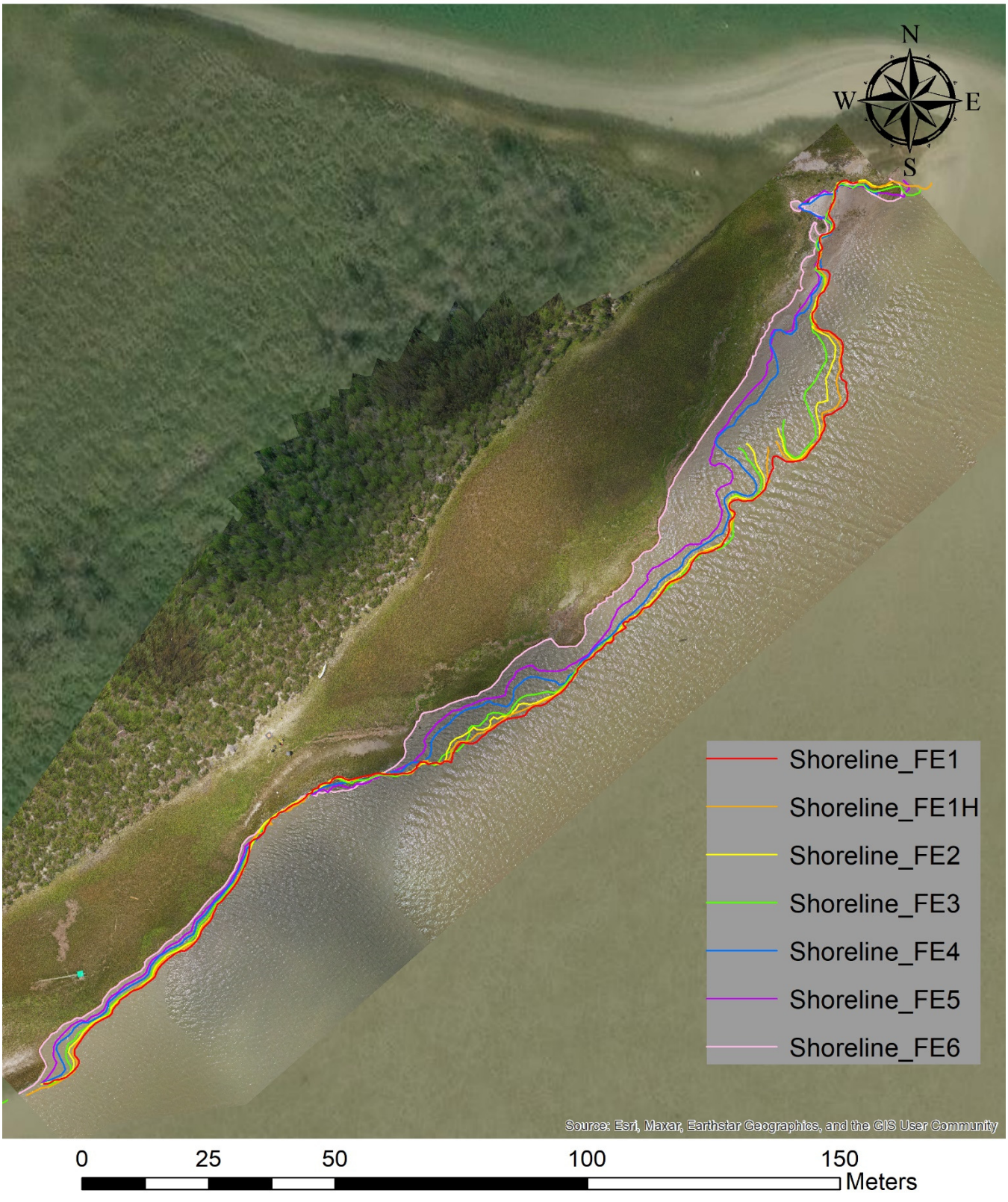

Fig. C2-1. Wetland boundaries at FS-2, Route-1

Fig. C2-2. Wetland boundaries at FS-2, Route-2

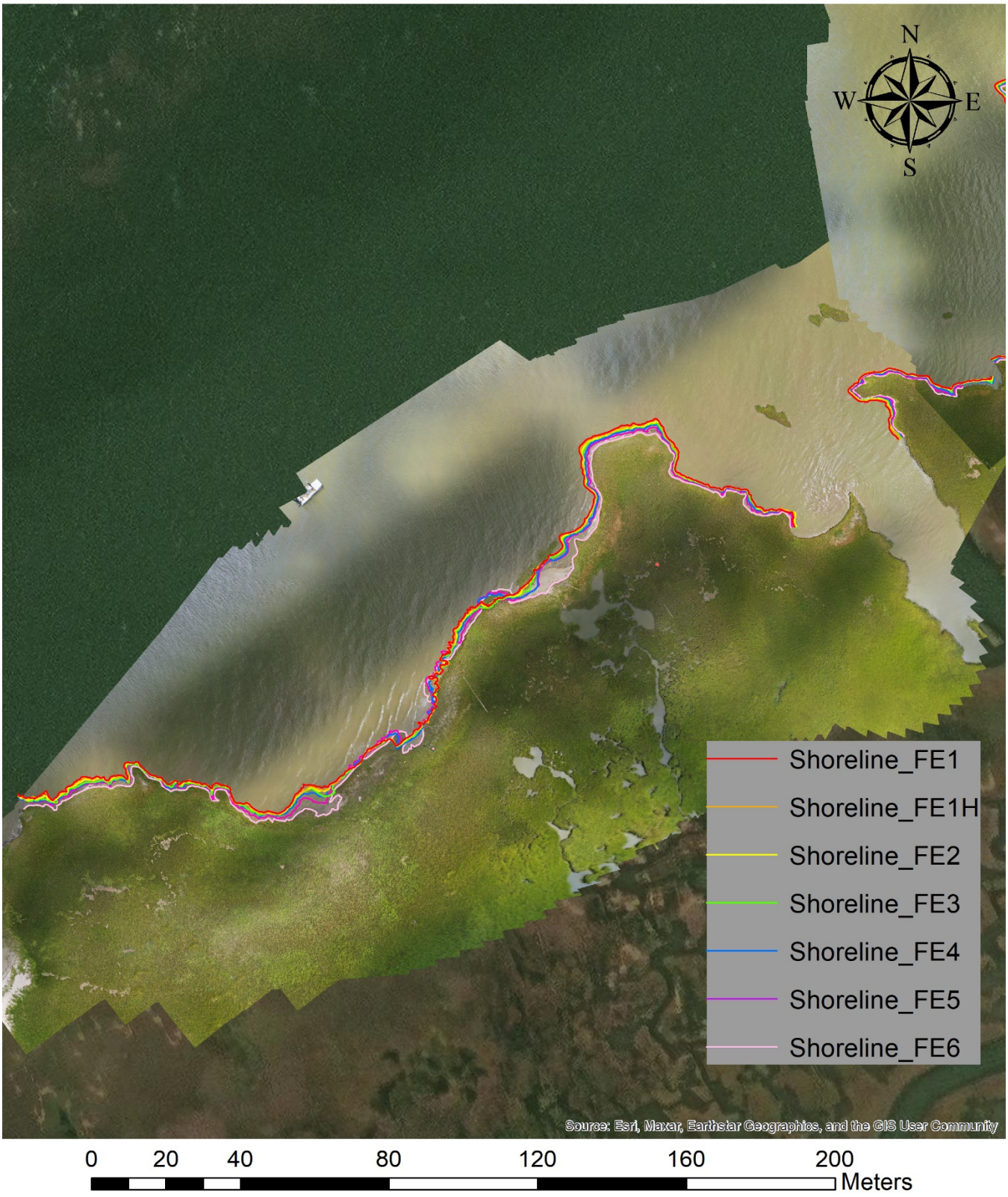

Fig. C3-1. Wetland boundaries at FS-3, Route-1

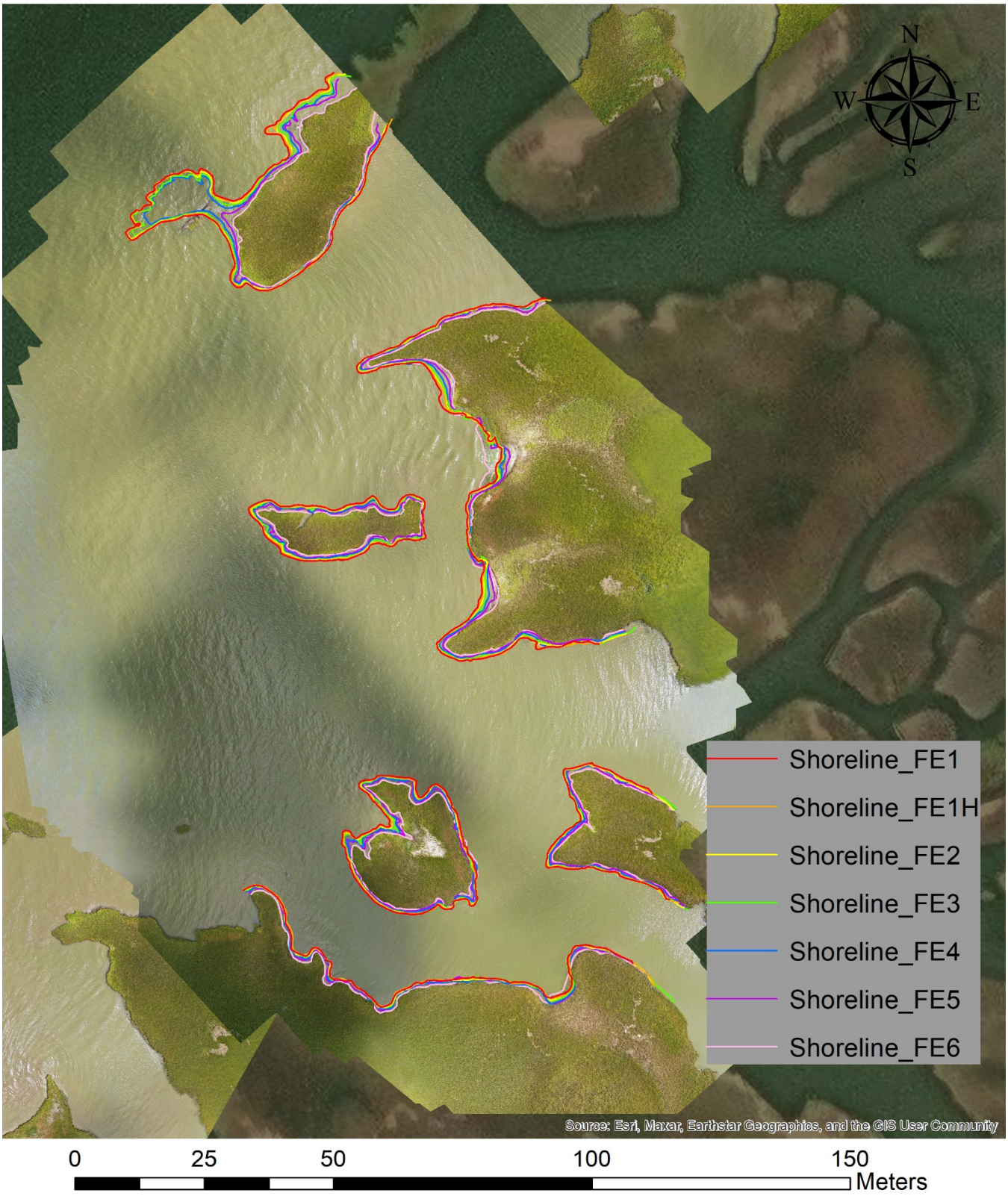

Fig. C3-2. Wetland boundaries at FS-3, Route-2

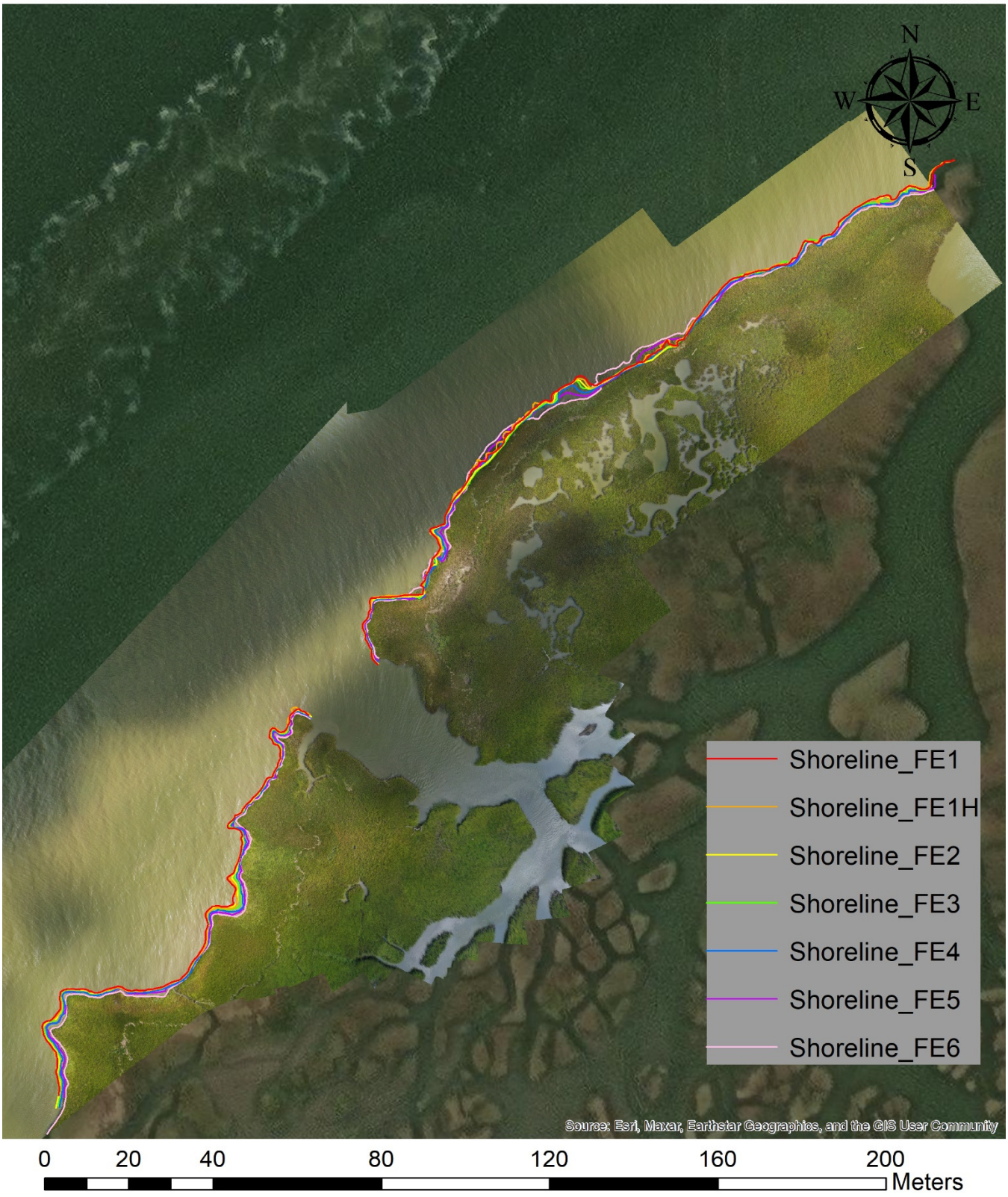

Fig. C3-3. Wetland boundaries at FS-3, Route-3

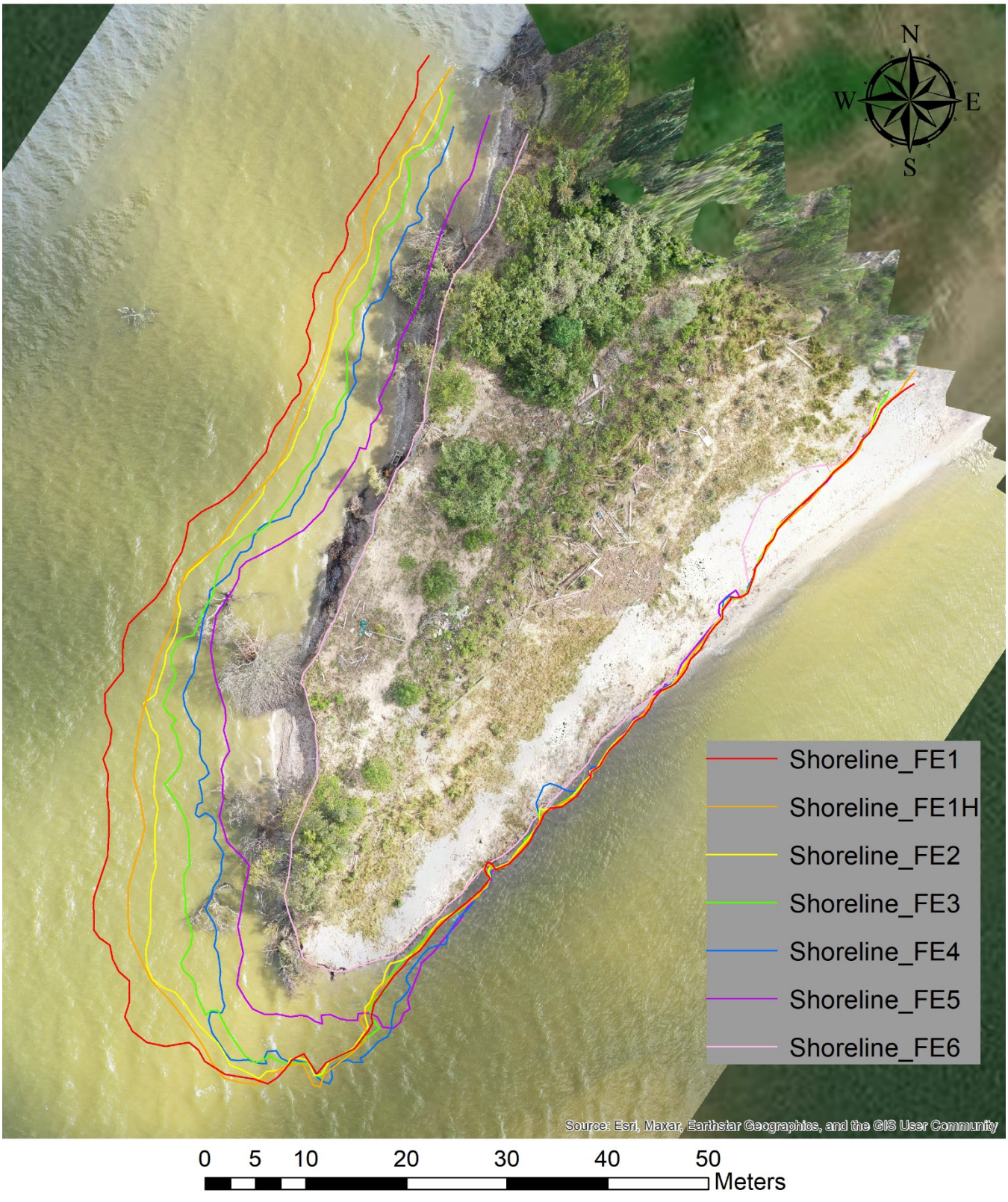

Fig. C3-4. Wetland boundaries at FS-3, Route-4

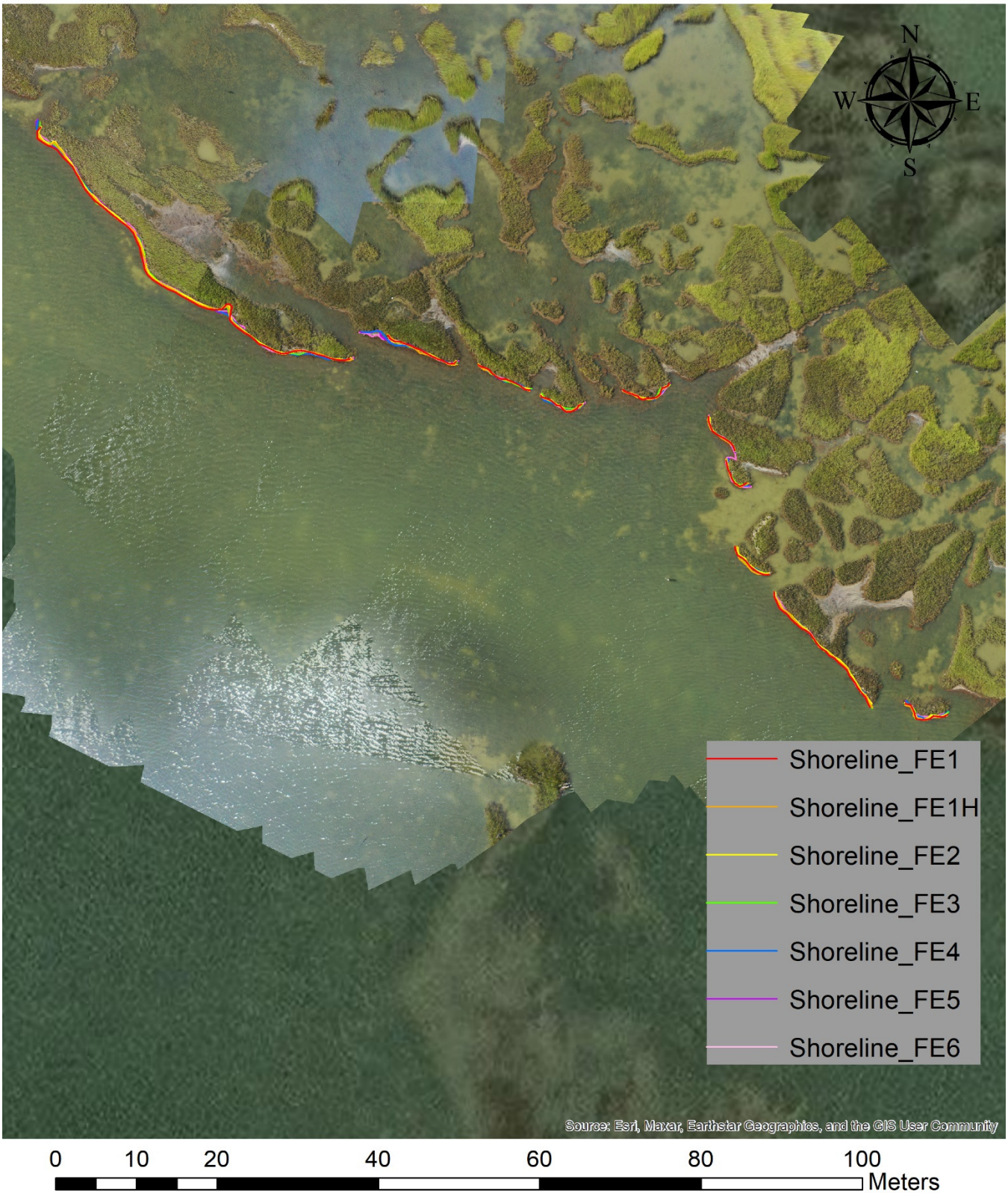

Fig. C4-1. Wetland boundaries at FS-4, Route-1

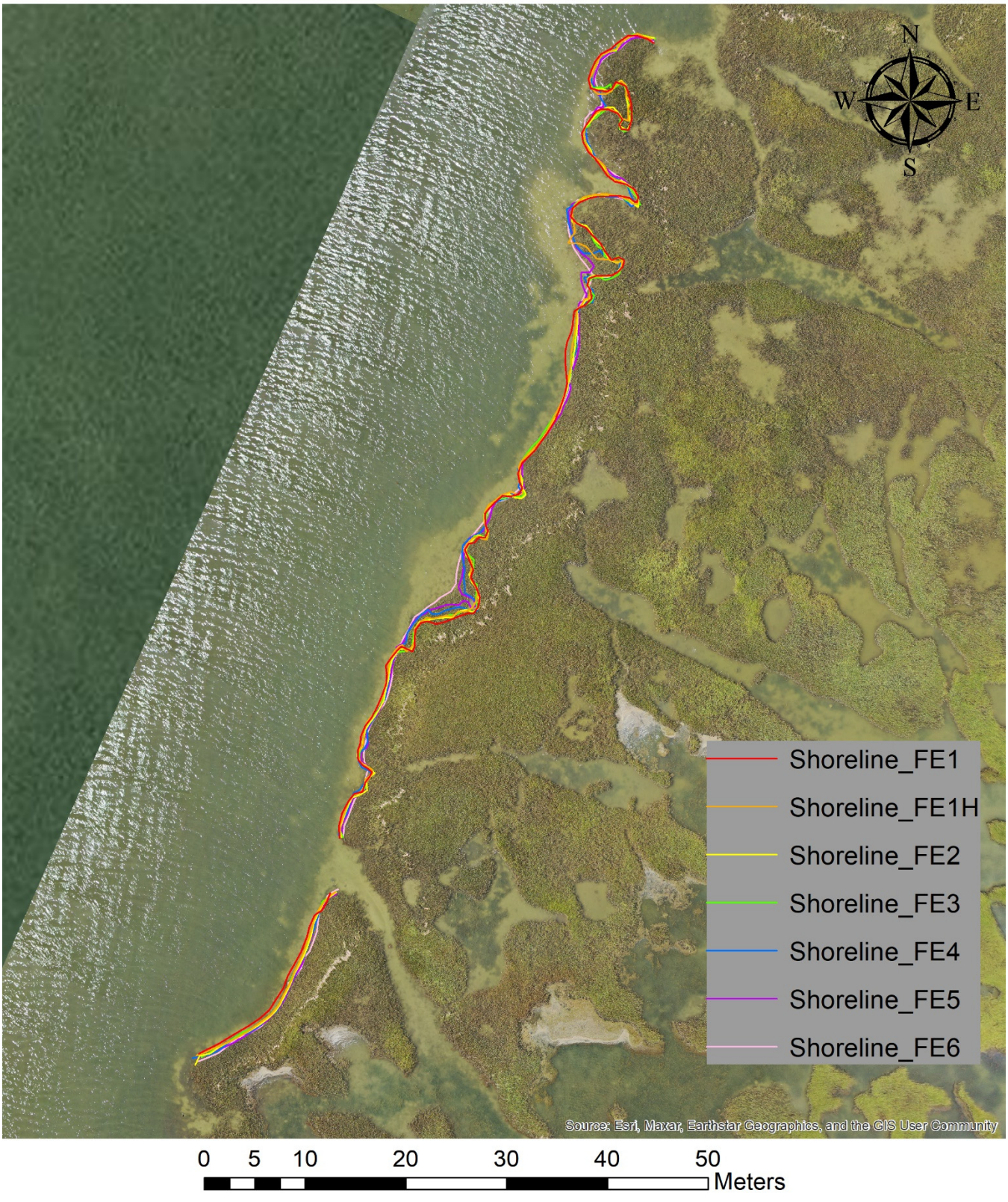

Fig. C4-2. Wetland boundaries at FS-4, Route-2

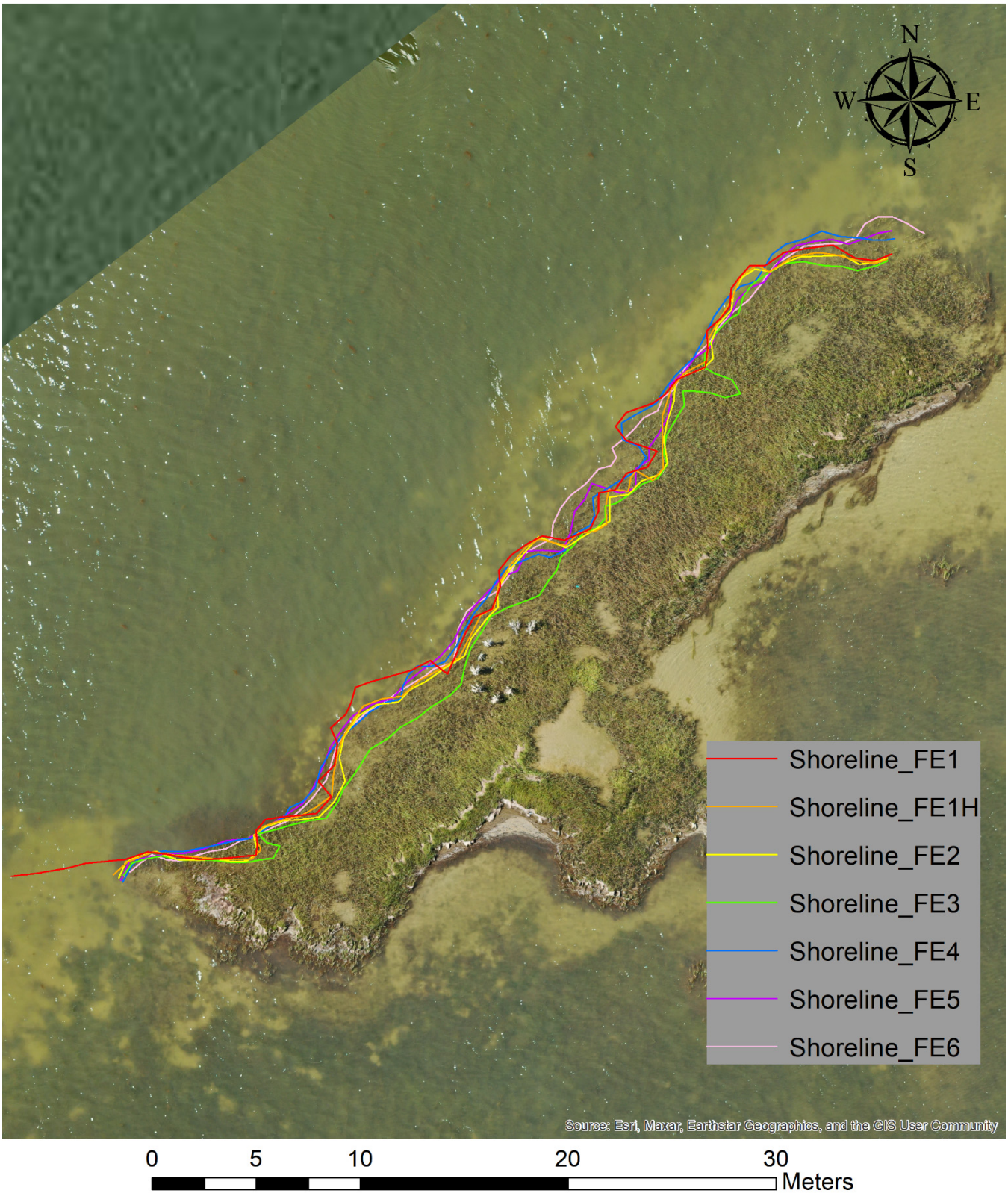

Fig. C4-3. Wetland boundaries at FS-4, Route-3

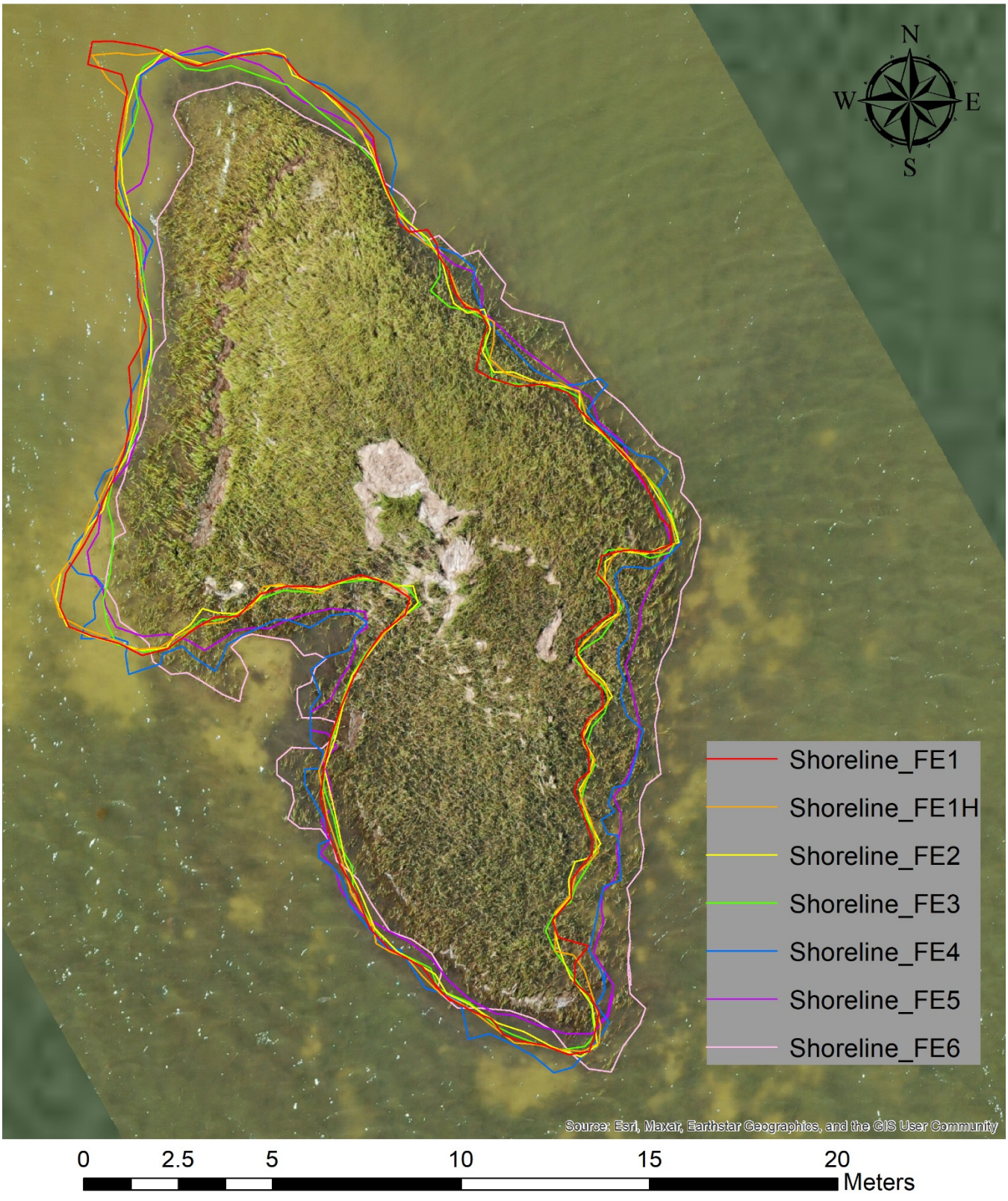

Fig. C4-4. Wetland boundaries at FS-4, Route-4

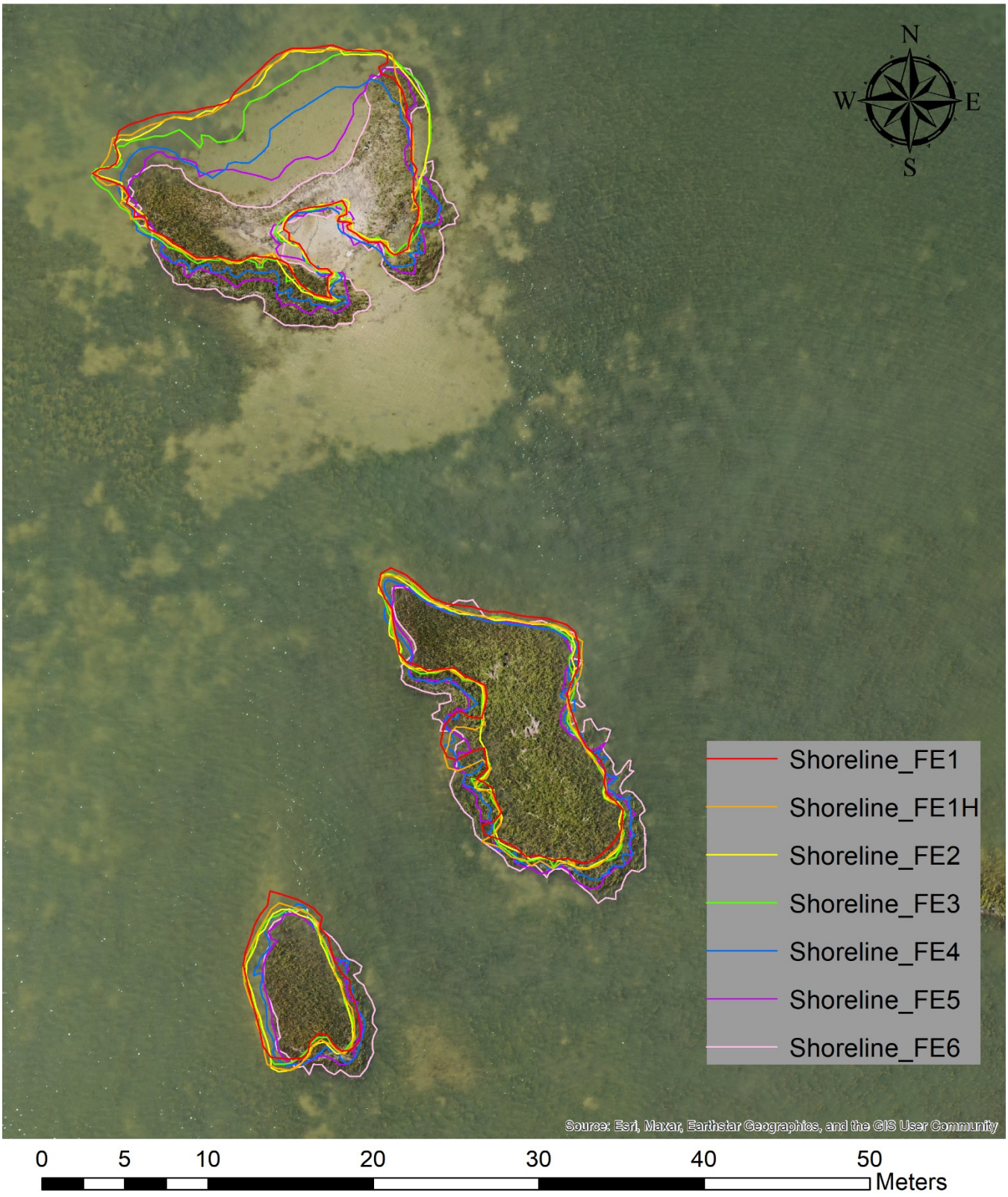

Fig. C4-5. Wetland boundaries at FS-4, Route-5

Appendix D: Cumulative statistical analysis of shoreline change rates in LRR computed for each site during Campaign 1 to 6. Red-colored transects represent erosion-dominated activities and blue-colored transects are accretion-dominated activities.

Fig. D1. Shoreline change rates in LRR at FS-1

Site-2

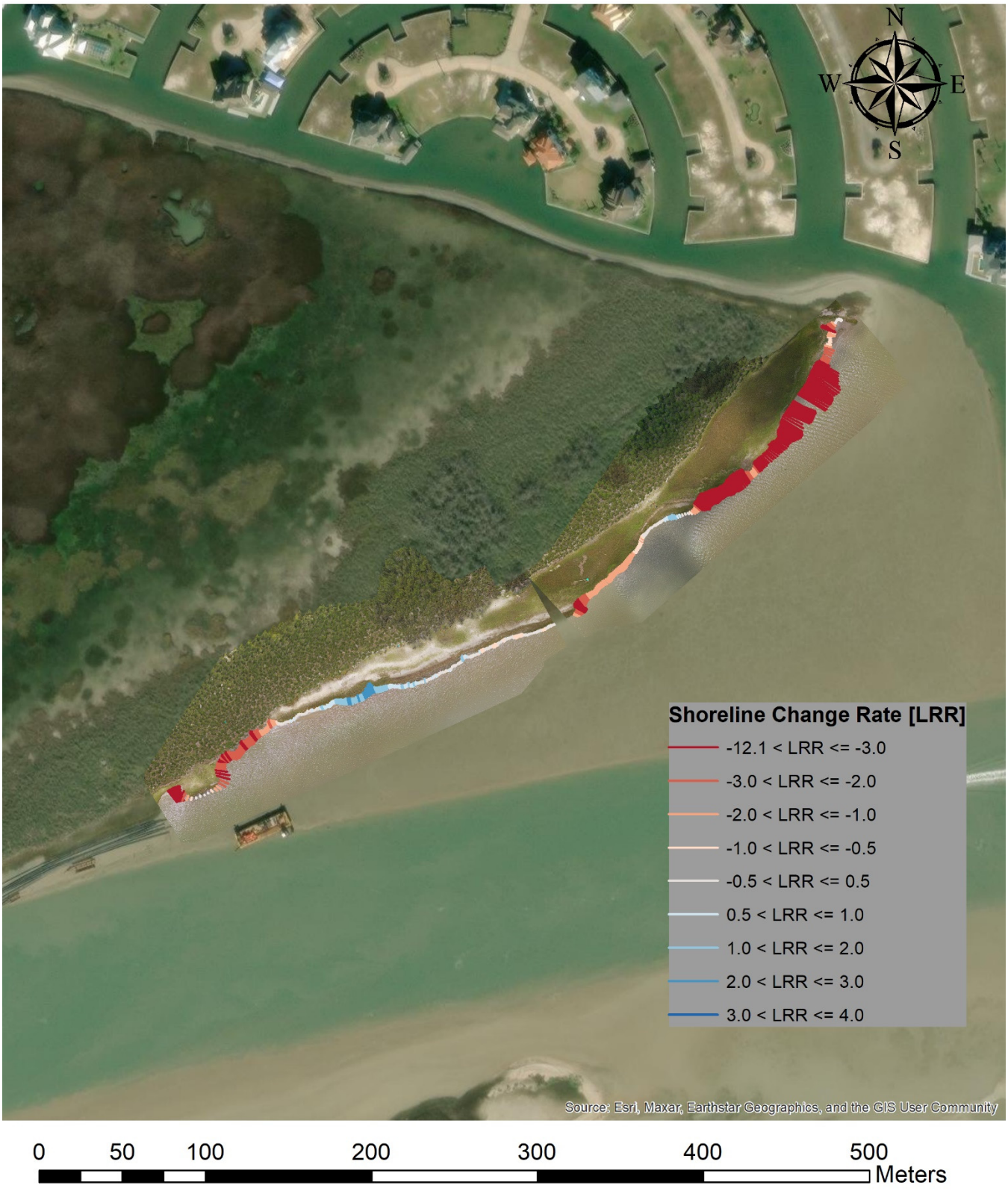

Fig. D2. Shoreline change rates in LRR at FS-2

Site-3

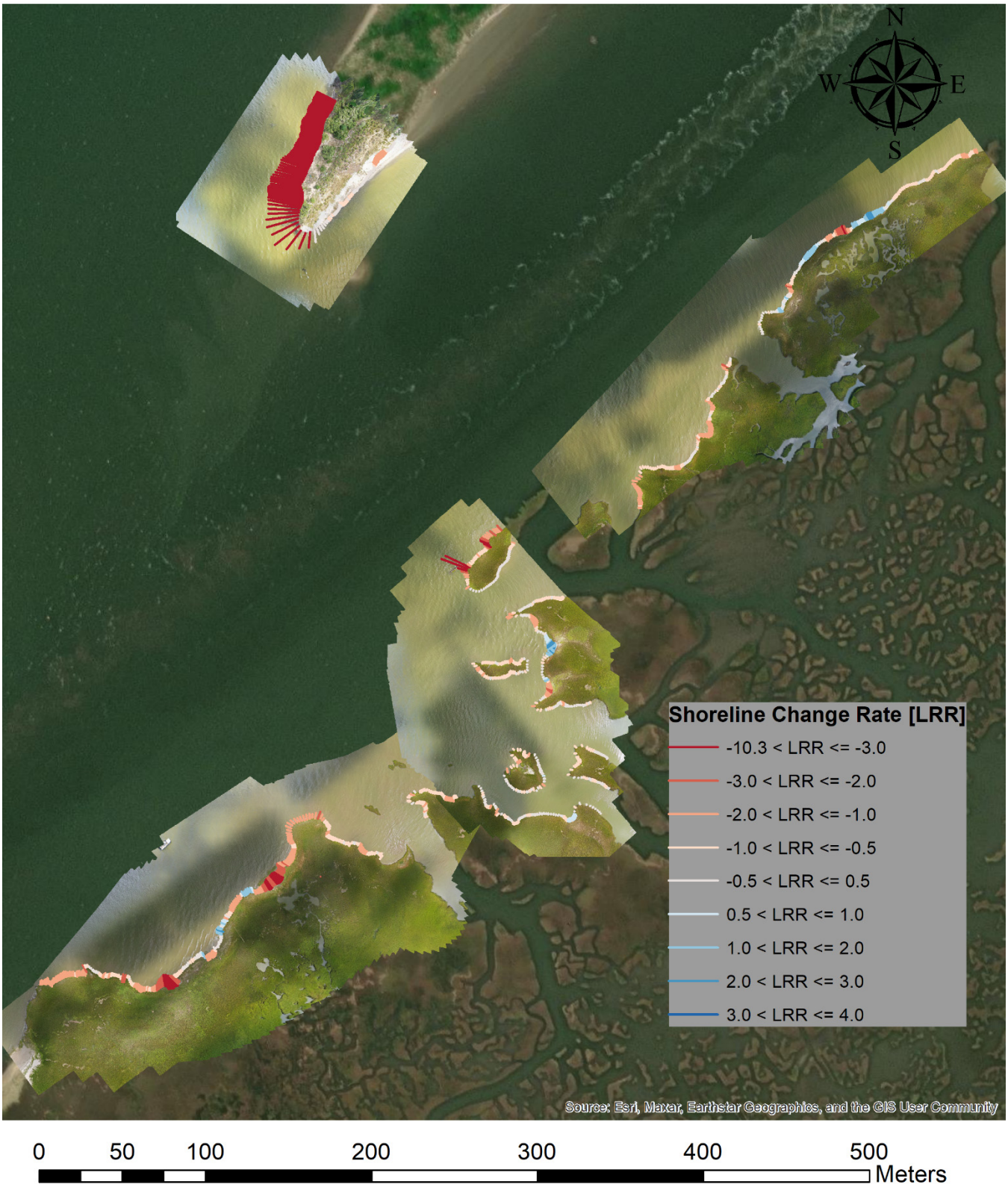

Fig. D3. Shoreline change rates in LRR at FS-3

Site-4

Fig. D4. Shoreline change rates in LRR at FS-4